Coherent X-ray Diffraction Imaging of Zinc Oxide Crystals

A thesis presented

by

Steven John Leake

Submitted in partial fulfillment of the requirements
for the degree of Doctor of Philosophy
at University College London

January 13, 2010

I, Steven John Leake confirm that the work presented in this thesis is my own. Where information has been derived from other sources, I confirm that this has been indicated in the thesis.

Supervisor: Prof. I. K. Robinson   **Author:** S. J. Leake

Abstract

Zinc Oxide (ZnO) exhibits a plethora of physical properties potentially advantageous in many roles and is why it one of the most studied semiconductor compounds. When doped or in its intrinsic state ZnO demonstrates a multitude of electronic, optical and magnetic properties in a large variety of manufacturable morphologies. Thus it is inherently important to understand why these properties arise and the impact potentially invasive sample preparation methods have for both the function and durability of the material and its devices.

Coherent X-ray Diffraction Imaging (CXDI) is a recently established non-destructive technique which can probe the whole three dimensional structure of small crystalline materials and has the potential for sub angstrom strain resolution. The iterative methods employed to overcome the 'phase problem' are described fully.

CXDI studies of wurtzite ZnO crystals in the rod morphology with high aspect ratio are presented. ZnO rods synthesised via Chemical Vapour Transport Deposition were studied in post growth state and during in-situ modification via metal evaporation processing and annealing. Small variations in post growth state were observed, the physical origin of which remains unidentified. The doping of a ZnO crystal with Iron, Nickel and Cobalt by thermal evaporation and subsequent annealing was studied. The evolution of diffusing ions into the crystal lattice from was not observed, decomposition was found to be the dominant process.

Improvements in experimental technique allowed multiple Bragg reflections from a single

ZnO crystal to be measured for the first time. Large aspect ratio ZnO rods were used to probe the coherence properties of the incident beam. The longitudinal coherence function of the illuminating radiation was mapped using the visibility of the interference pattern at each bragg reflection and an accurate estimate of the longitudinal coherence length obtained, $\xi_L = 0.66 \pm 0.02\mu$m. The consequences for data analysis are discussed. The combination of multiple Bragg reflections to realise three dimensional displacement fields was also approached.

Acknowledgements

This thesis would not have been possible were it not for the help and support of many exceptional individuals.

It is difficult to overstate my gratitude to my supervisor Ian K. Robinson, he has taught me a great deal and made great efforts to explain difficult problems in simple terms. His zest for science is truely inspiring.

I am also indebted to Ross Harder, whose friendship, support, patience, advice and stamina both on experiments and during analysis made some long experiments very enjoyable and productive. I would also like to extend my thanks to Marcus Newton, Moyu Watari, Richard Bean and Felisa Berenguer for their discussion, feedback and generating such an enjoyable working environment over the past 3 years. And Eric Dufresne for his role in the laser experiments.

My fiancée Sarahs' encouragement and support during this period cannot be exaggerated. I would also like to thank my friends and family for their help, belief and sanity during this testing time.

Contents

List of Figures

List of Tables

Chapter 1

Introduction

This chapter introduces Zinc Oxide (ZnO) the principal material studied in this thesis. An industrial nanomaterial for many decades ZnO has seen wide application in the manufacture of paints, rubber products, pharmaceuticals and sun screen amongst others. Its versatility is defined by its tunable properties, a wide direct band gap II-VI semiconductor it exhibits both n-type conductivity and when doped p-type conductivity (group V elements). When doped in a controllable way the electrical properties can be varied from an insulator through n-type semiconductor to a metal whilst maintaining optical transparency. Exhibiting both piezoelectric and pyroelectric nature, ZnO has also been identified when doped as a potential Dilute Magnetic Semiconductor (DMS) for spintronics applications. ZnO has been fabricated and studied in the bulk, thin film and nanomaterial morphologies. The literature is vast (several thousand publications per year), a concise overview of the properties of ZnO, the methods used to manipulate them and examples of application will follow.

1.1 Zinc Oxide

ZnO is a unique material and exhibits a plethora of properties applicable in many fields. A transparent semiconductor with a wide direct band-gap (E_g) of 3.37eV at 300K [175] is candidate for electronic, optoelectronic and optical applications. At present many opto-electronics devices have been fabricated using GaN, which exhibits a similar direct band gap, E_g=3.44eV [142]. ZnO is particularly interesting as it exhibits several advantageous properties, a larger exciton binding energy 60meV sufficient for ultra violet stimulated emission at room temperature [108] (28meV GaN [142]), is biodegradable and biocompatible[1] [219] and significantly cheaper to manufacture than alternatives. The inability to fabricate p-type ZnO reproducibly has hindered its application to date and resulted in hybrid ZnO devices where a different p-type material, such as ZnSe or Cu_2O, is combined with n-type ZnO. ZnO is also radiation hard making it a candidate for solar cells and satellite applications and ideal for characterisation with x-rays as they will not damage the samples.

1.1.1 Crystal Structure

ZnO can be found with either the rocksalt, wurtzite or cubic zinc-blende crystal structure. The wurtzite structure is energetically favourable at room temperature. A phase transition to rocksalt was observed at 9.6GPa, reversing at 2GPa [47, 94] and will not be discussed further. In both the wurtzite and zinc blende form each anion is surrounded by four cations

---

[1]The Materials Safety Data Sheet for Gallium Nitride states: Skin, eye and respiratory irritant. Skin contact may cause sensitization. Toxicology not fully investigated. $http$: $//msds.chem.ox.ac.uk/GA/gallium\_nitride.html$
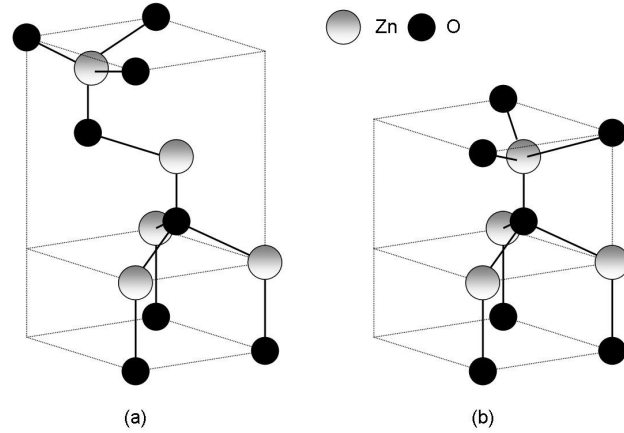
Figure 1.1: Unit cell of (a) zincblende ZnO (b) wurtzite ZnO

with tetrahedral symmetry. Jaffe et al. [89] accurately calculated the energy of cohesion for each known phase using the generalised gradient approximation (GGA). Interestingly zinc blende and wurtzite are very close, -7.679 and -7.692 respectively and could explain the observation of both structures in the tetrapod morphology due to strains induced during growth. Tetrahedral coordination is typical of sp^3 covalent bonding, however ZnO shows substantial ionic character responsible for the band gap widening beyond that expected from covalent bonding [135]. The tetrahedral coordination results in a lack of inversion symmetry and gives rise to its piezoelectric nature.

The wurtzite structure belongs to the P6$_3$mc space group and has a hexagonal unit cell with lattice parameters, $a = b$ and c, where the ideal ratio $c/a = \sqrt{8/3}$. A good agreement has been found between the lattice parameters observed experimentally and those calculated, see Table 1.1. The measured lattice parameters lie in the range, $a = 3.2498 \pm 0.0003$Å and $c = 5.2057 \pm 0.0015$Å. The zinc blende structure belongs to the F43m space group,

measured lattice parameters lie in the range, $a = 4.42 \pm 0.05$Å, see Table 1.1.

Nanoscale synthesis has produced a large variety of morphologies in the wurtzite phase, see Section 1.1.7. Combinations of both the wurtzite and zinc blende phases have been identified in the tetrapod morphology [43, 206].

Table 1.1: Lattice parameters for wurtzite ZnO both measured (X-ray Diffraction(XRD), Reflection High Energy Electron Diffraction (RHEED), Transmission Electron Microscopy (TEM)) and calculated

Wurtzite

a(Å)	c(Å)	c/a	Method
3.2496	5.2042	1.6018	XRD [97]
3.2501	5.2071	1.6021	XRD [94]
3.2498	5.2066	1.6021	Energy Dispersive XRD [47]
3.2497	5.206	1.602	Powder XRD [152]
3.286	5.241	1.595	*ab initio* [28]

Zinc Blende

a(Å)	Method
4.619	*ab initio* [28]
4.463	RHEED [10]
4.37	XRD [10]
4.47	TEM [10]

1.1.2 Surfaces

ZnO is important for gas sensor applications because point defects induce large changes in surface conductivity and has become a wide field of research. Defects will be introduced

in Section 1.1.4, here we will focus on the surface structure of wurtzite ZnO.

Wurtzite ZnO does not possess a center of inversion, hence along the c-axis an inherent asymmetry results in facets terminated with either Zn, the zinc (001) facet, or O, the oxygen (00$\bar{1}$) facet. Their polar nature suggests a surface reconstruction or relaxation to minimise the net dipole moment. Low Energy Electron Diffraction (LEED) studies confirm a (1x1) reconstruction [33, 39, 107, 187], thus atomically flat and a contraction of 0.1Å of the Zn ions on the zinc face [91]. The reason for the lack of surface reconstruction is yet to be determined. Recent theoretical frameworks have identified stabilisation due to either a reconstructed triangular defect surface structure [2] or an unreconstructed ZnO surface terminated with hydroxyl groups by density-functional calculations [99]. Experimental evidence by Kunat *et al.* suggests the saturation of dangling bonds by CH_3 or H molecules [101] measured via He atom scattering. The dominant natural growth facet is the (00$\bar{1}$).

The low-index (100) and (110) facets perpendicular to the c-axis are non polar and atomically flat with equal numbers of cations and anions in the surface plane. Both theoretical calculation and LEED I-V measurements indicate an ideal termination on the (110) facet and relaxation of the Zn ions inward by 0.4Å on the (100) facet [82]. The inward movement of the surface cation suggests a tilt of the Zn-O dimer and can be understood in a covalently bonded semiconductor by a rehybridisation of the cation from sp^3 to sp^2 moving it closer to its three anion neighbours. In ionic semiconductors charge transfer effects dominate and both the anion and cation move closer to the bulk to improve electrostatic screening and often results in a small tilt of the dimer.

---

[2]Triangular regions of Zn and O vacancies create a triangular surface reconstruction.
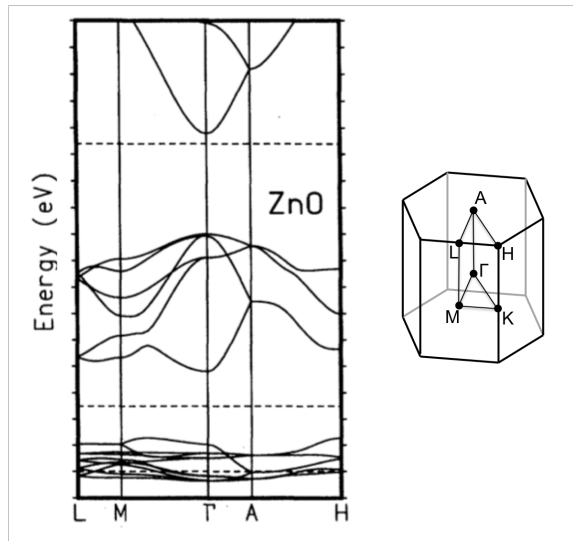
Figure 1.2: The band structure of ZnO calculated by Vogel *et al.* [195] using *ab initio* methods, the top and bottom dashed lines represent the measured band gap and the *d*-band width respectively

1.1.3 Practical Properties

Knowledge of the band structure of a semiconductor is vital in determining its electronic and mechanical properties and potential utility in devices. Typically transitions between electronic levels are determined by x-ray or ultraviolet, absorption or emission spectroscopy. The most accurate theoretical description of the measured band structure of ZnO was made by Vogel *et al.* [195] using *ab initio* methods, see Figure 1.2.

The electrical conductivity of a semiconductor is defined by its free charge carriers. In ZnO the free charge carriers are electrons whose negative charge give it the name 'n-type'. For application in electronic devices 'p-type' ZnO is required where holes (positive) are the free charge carriers. The conductivity of ZnO is n-type and can be varied by adding dopants. Increased n-type conductivity has been observed in ZnO when doped with transition metals, however p-type conductivity remains challenging. Recently, p-

type conductivity in thin films doped with N, P, and As was demonstrated [113]. Look *et al.* [111] provide a comprehensive overview of thin film developments. Xiang *et al.* were the first to fabricate p-type ZnO nanomaterials in the nanorod morphology using phosphorous pentoxide as a dopant source in a chemical vapour deposition method [214]. Later Lu *et al.* [114] used an atomic force microscope to generate 50-90mV from p-type (P doped, grown via chemical vapour deposition) ZnO nanowires compared with -5mV to -10mV from n-type nanowires. A thin film p-n junction fabricated from ZnO (n-type) and N-doped ZnO (p-type) by Cao *et al.* did not exhibit electroluminescence [27] and remains a challenge in the field.

The size of the band gap between valence and conduction states in solids determines many of their properties. Large band-gap semiconductors can support high electric fields before breaking down, which means that they can be used for high-power electronic devices. Another important affect is the temperature dependence of the population of electrons in the conduction band enabling its use at high temperatures. To date band gap tuning has been achieved through divalent substitution on the cation site. A reduction in the band gap has been observed by Makino *et al.* to 3.0eV by Cd substitution [119] up to 7% in CdZnO films using Pulsed Laser Deposition growth, Vigil *et al.* [194] and Ma *et al.* [117] confirmed a drop in the band gap of this order. An increase to 3.9eV by Mg substitution was observed by Ohmoto *et al.* at 33% Mg content in epitaxial thin films [143], Teng *et al.* observed 4.0eV at 36% solubility [178].

Optical properties of semiconductors are determined by both intrinsic and extrinsic effects. Intrinsic optical transitions take place between electrons in the conduction band and holes

in the valence band and include excitonic effects due to the Coulomb interaction. Extrinsic properties are related to defects or dopants, which can create discrete electronic states in the band gap and influence both optical absorption and emission processes. In ZnO many optically excitable transitions exist, hence identification of the physical origins of individual transitions is difficult. A photoluminescence spectra for ZnO nanowires and In-doped ZnO 'nanobelts' is shown in Figure 1.3 observed by Fan *et al.* [56]. ZnO typically produces two main characteristic bands; a sharp free exciton ultraviolet band ($\sim$380nm) and a broader green luminescence or deep level emission band (400-700nm). The presence and intensity of these bands is dependent on the growth parameters, the variation in photoluminescence is demonstrated in Figure 1.3 between two different morphologies of ZnO. For In doped 'nanobelts' a shift in the first band was evident and the second band widened with an increase in longer wavelength emission.

The lack of inversion symmetry along the c-axis leads to piezoelectric and pyroelectric behaviour in the wurtzite phase. Piezoelectric materials mechanically deform in the presence of an applied electric field. This effect was observed by Song *et al.* [172] using large aspect ratio ZnO rods of thickness $>1\mu$m and later harnessed by Qin *et al.* [151] to harvest electrical power. An overview of the field of nanopiezotronics was provided by Z. L. Wang [207]. Lee *et al.* [104] proposed the use of single crystal ZnO nanowires in scanning probe microscopy, Huang *et al.* [88] later proved theoretically that ZnO could be used for atomic force microscopy tips in contact, non-contact and tapping modes of operation. Pyroelectric materials generate electric charge when heated or cooled and are utilised as ZnO temperature sensors [86].
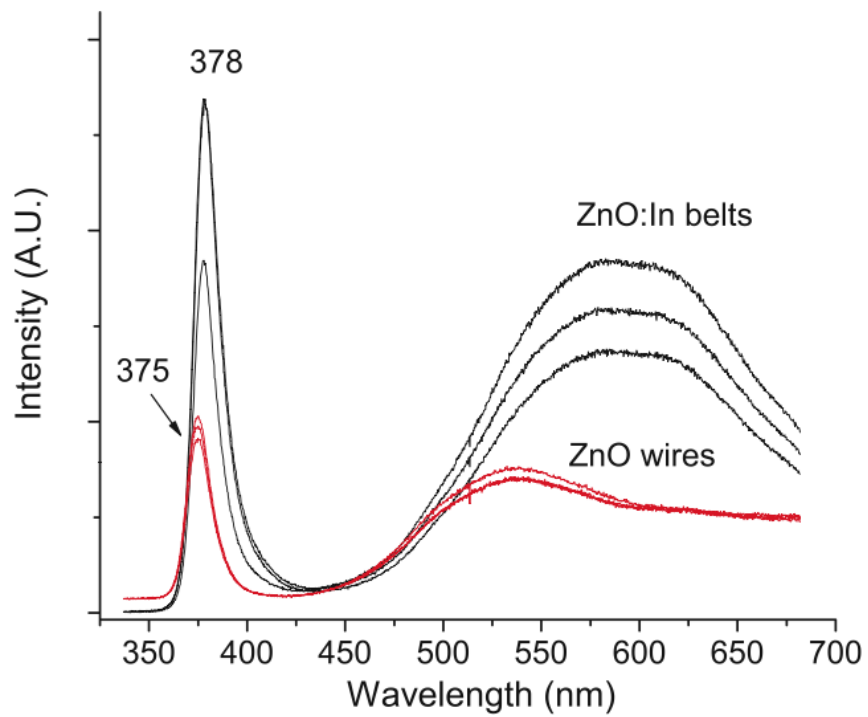
Figure 1.3: Room temperature photoluminescence spectra for ZnO nanowires and nanobelts (In-doped) grown on a SiO$_2$ layer by Fan *et al.* [56], multiple bands correspond to measurements in different regions of the substrate.

Zinc oxide is often described in the literature as a radiation hard material and is of great consequence when applied to environments where radiation damage is a factor, i.e solar cells or space satellite applications. Early work by Cordaro *et al.* [41] identified that a ZnO varistor function did not vary up to a dose of 10^5 Gy [3]. The mechanisms for irradiation damage are under debate [84, 100, 112] and few studies exist to my knowledge that have probed device operation as a function of dose. Khanna *et al.* [95] demonstrated Schottky diodes remained fully functional after radiation exposure equivalent to 100 years in a low Earth orbit. Tuomisto *et al.* [182] compared ZnO and GaN, ZnO was found to be significantly harder due to the increased mobility of ionization induced defects at low temperatures.

1.1.4 Defects

The properties discussed previously are heavily dependent on the presence of defects or dopants, control of which allows the tailoring of a variety of properties making semi-conductors particularly interesting. The presence of point defects in ZnO is well known however, the individual defects and associated mechanisms are still under debate. ZnO has a relatively open structure, in a hexagonal close packed lattice Zn atoms occupy half the tetrahedral sites. All the octahedral sites are empty. Hence there are plenty of sites for ZnO to accomodate intrinsic defects (Zn interstitials) and extrinsic dopants. It is accepted that the n-type conductivity is due to the presence of point defects. In order to maintain a Zn interstitial concentration Tomlins *et al.* found annealing in the presence of Zn vapour

---

[3]The unit of Gray (Gy) describes the absorption of 1 joule of energy per kilogram, the average radiation dose experienced on the surface of the earth is 3 mGy per year.

followed by rapid quenching was required [181].

Several studies have attempted to determine the concentration of defects. Kohan *et al.* [98] and Sokol *et al.* [169] found zinc and oxygen vacancies to be the dominant defects using *ab initio* methods. Tuomisto *et al.* [183] found neutral Zn vacancies or Zn vacancy related defects at a concentration of $V_{zn} = 2\mathrm{x}10^{-16}\mathrm{cm}^3$ in undoped ZnO and doped (Mn,As) ZnO grown via Chemical Vapour Transport (CVT). Oxygen vacancies were also seen with a concentration of $V_o = 10^{17}$ cm^3 and the partial substitution by Mn suppressed their formation. Contrary to these findings Wang et al. [203] found the presence of Zn vacancies to exceed O vacancies by an order of magnitude in bulk crystalline samples. Gopel *et al.* determined the dominant surface defects to be O vacancies [72]. Janotti and Van de Walle concluded oxygen vacancies were not responsible for n-type character via *ab-initio* calculation [90]. This agreed well with a framework outlined by Van de Walle [185] where the presence of unintentional hydrogen impurities were predicted responsible for n-type character.

1.1.5 Diffusion

The steady state diffusion of atoms in one-dimension is described by Fick's Law

$$J = -D\frac{dc}{dx} \tag{1.1}$$

where J is the flux of atoms (number crossing unit area per unit time), c is the concentration of atoms, and D is the diffusion constant.

The diffusion constant is temperature (T) dependent according to the Arrhenius relationship

$$D = D_0 exp(-E_A/k_B T) \qquad (1.2)$$

where E_A is the activation energy, the energy barrier which must be crossed to allow an ion to move. The activation energy can be split into two components; the energy required to move into a vacant site called the energy barrier against mobility, E_M, and a term corresponding to the probability of a vacant site being available for diffusion, E_V, the energy required for an atom to vacate a site and migrate to the crystal surface. The diffusion constant is proportional to the concentration of vacant sites hence $E_A = E_M + E_V$. The concentration of vacant sites is temperature dependent, at low temperature the vacant sites are defined by impurity levels and at high temperatures dominated by vacancies produced thermally. The number of vacant sites n in a lattice with N sites containing atoms can be expressed simply by minimizing the free energy [50].

$$n = N exp(E_V/k_B T) \qquad (1.3)$$

The diffusion mechanisms for defects in ZnO are also under debate. Several studies using Secondary Ion Mass Spectrometry (SIMS) have reached different conclusions. Haneda *et al.* [77] working with polycrystals of pure ZnO proposed an interstitial mechanism for oxygen diffusion. Sabioni *et al.* [162] determined oxygen diffusion rates in ZnO between 900°C and 1000°C and confirmed the interstitial mechanism for oxygen diffusion [161]. On

the other hand, Tomlins *et al.* [180] proposed a vacancy mechanism for oxygen diffusion. For Zn diffusion a vacancy mechanism was determined by Tomlins *et al.* [181] who built on theoretical work by Mahan [118] and Binks [21].

1.1.6 Doping

A recent review by Davies *et al.* [45] regarding the doping of ZnO describes the present state of the field. Here we focus on the transition metals Fe, Ni and Co due to recent observations of improved luminescence [11], conductivity [184] and calculation suggesting room temperature ferromagnetism [48]. Based on the electronegativities of Fe, Ni and Co being larger than Zn, see Table 1.2, these elements should substitute at the Zn site upon annealing.

Table 1.2: Electronegativity based on the Pauling Scale for deposition metals [6]

Element	Zn	Fe	Ni	Co
Electronegativity [146]	1.65	1.83	1.91	1.81

A variety of methods have been used for fabrication including ion implantation, sol-gel, pulsed laser deposition and solid state methods. An array of conclusions has been drawn regarding the solubility of these transition elements into the ZnO lattice. Several thin film studies show dopant concentrations between 0 and 30 at.%[4] [93, 120, 184, 210]. In both bulk and powder samples concentrations of Fe at 2-7 at.% [16, 200] at 500°C-800°C beyond which secondary phases Fe_2O_3 and Fe_3O_4 were observed. Similar observations were made

---

[4]Atomic percent, number of atoms of one element relative to the total number of elements in that compound.

in Co doped ZnO thin films, up to 50 at.% [5, 120], compared with powder samples, up to 6.5 at.% [16, 160] again the onset of diffusion occurred at 500°C. Dumont studied ZnO bulk crystals and the diffusion of Co into the surface layers, at 550°C Co substitution for Zn atoms was observed [51]. Rout *et al.* noted an increase in photoconductivity when Co diffused into the surface [160]. Few studies exist to my knowledge of Ni integration into the ZnO lattice, in thin films a 3 at.% was observed by Mandal *et al.* [120] and in bulk crystalline samples Bates *et al.* reported 1 at.% [16].

1.1.7 Synthesis

Z. L. Wang provides a comprehensive overview of the growth methods, properties and corresponding applications of ZnO nanomaterials [205] along with detailed discussion of the variation in nanostructures synthesised to date [204]. Synthesis methods include; Chemical Vapour Transport Deposition (CVTD), Metal-Organic Chemical Vapour Deposition (MOCVD) and solvent based methods which will be introduced in Chapter 3. Focus will be placed on the CVTD method [136, 137] which can be tuned to produce nanorods, nanowires, platelets and tetrapods; nanoscale branched structures, demonstrated with SEM[5] in Figure 3.2 and Figure 1.4 highlights some more exotic nanostructures of ZnO grown by Wang *et al.* [204].

The morphologies are dependent on several factors; substrate, catalyst, source material, dopants, oxygen partial pressure and heating rates. Closely matching lattice parameter substrates such as sapphire [202] and GaN [173] produce epitaxial crystal growth, well

---

[5]Carl Zeiss XB1540 "Cross Beam" focussed-ion-beam microscope at London Centre for Nanotechnology, specification: http://www.london-nano.com/content/lcnfacilities/crossbeam
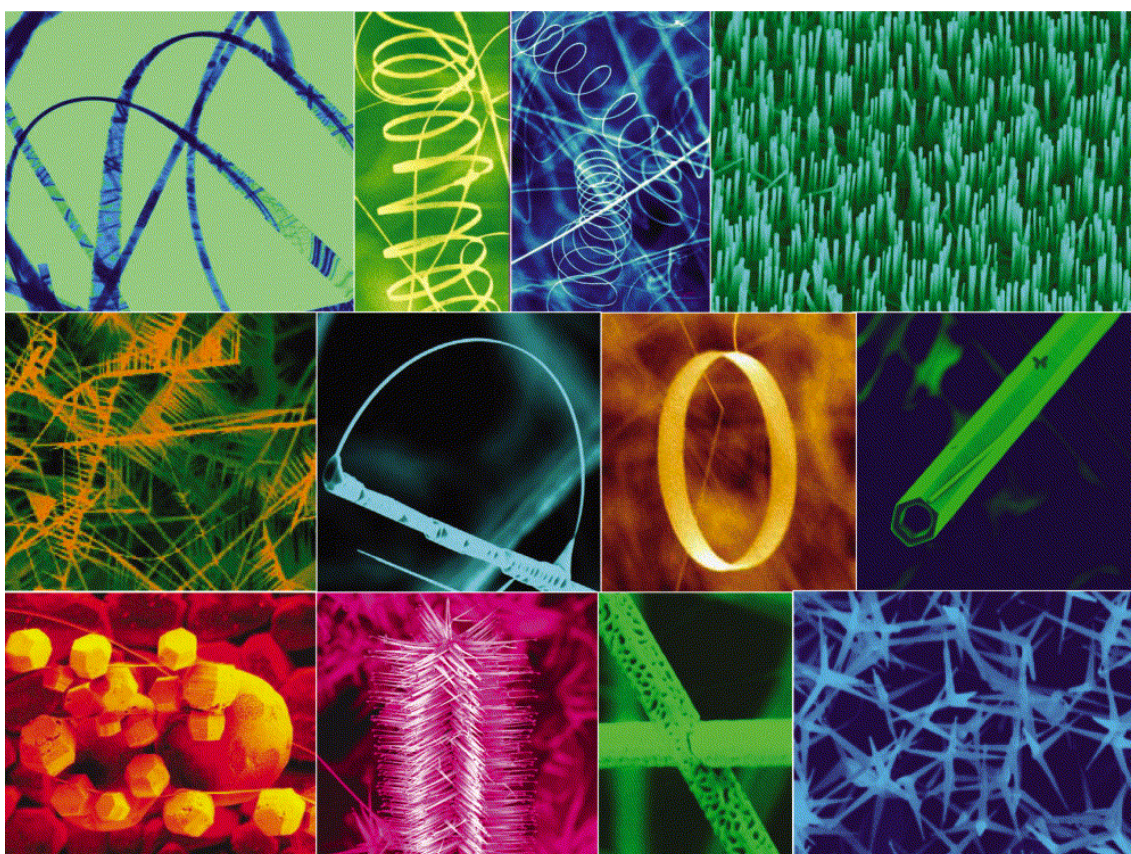
Figure 1.4: Variation in ZnO nanostructures grown by Wang *et al.* [204]. From left to right, top to bottom nanobelts, nanohelices, nanosprings, nanorod arrays, nanosaws, nanobows, nanorings, nanotubes, nanospheres, nanopropellers, nanocages and tetrapods.

aligned ZnO nanorod arrays have been fabricated on GaAs substrates [103]. The introduction of catalysts or defects affects growth morphology, Au [57,87,140,201,202,216,218] and Sn [69] are common catalysts and In has been observed to change morphology from nanowire to 'nanobelt'[6] [55,56]. Careful control of the electrostatic interaction energy and chemical activity on the polar surfaces can lead to a number of nanostructures including 'nanosprings', 'nanorings', 'nanohelices' and many more [145,204]. Zn powder in an oxygen atmosphere produce the tetrapod morphology [43] as does CVTD [139]. In essence a close control over the experimental variables can yield a variety of different morphologies, the variables will be discussed further in Section 3.1.

The tetrapod structure in Figure 1.5, is of specific interest as it has been proven via Transmission Electron Microscopy (TEM) [49] to possess both known phases of ZnO, wurtzite arms and a zinc blende core [139]. The main advantage of using CXDI to investigate tetrapods is that different structures and crystal orientations produce different Bragg peaks which can be measured independently. This would allow the independent measurement of each side of an interface, in this case the Zinc blende core and the four wurtzite arms, see Figure 1.5A. The experimental sample manipulation procedure prior to this work was not accurate enough to map several Bragg peaks from a single crystal. If the orientation of two crystals at a single interface is known and the experimental accuracy improved the experiment is feasible. Tetrapods have been fabricated into Schottky diodes by Newton *et al.* [136,139] using a Focused Ion Beam (FIB) to connect a single tetrapod to contacts on a substrate, see Figure 1.5C. This fabrication method raises questions about the damage induced by FIB and the effect it has on the properties of a material so sensitive

---

[6]The nanobelt morphology grows along the 100/110 crystal directions as opposed to the traditional $00\bar{1}$ growth facet and determined by growth variables.

to defects.
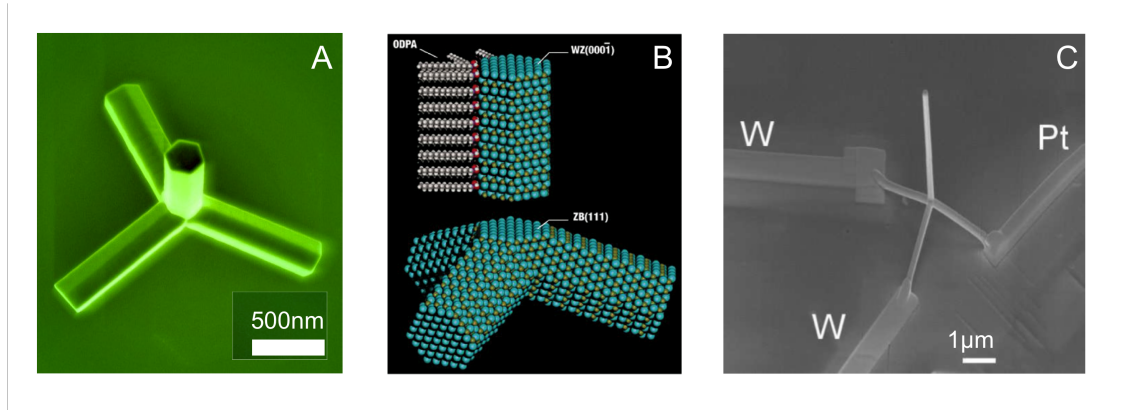
Figure 1.5: ZnO Tetrapod (A) produced via CVT on Silicon (100) substrate imaged with Scanning Electron Microscopy (SEM) (B) predicted structure [121] (C) Schottky diode fabricated by Newton with W and Pt contacts produced via FIB [136]

1.1.8 ZnO Goals

A detailed understanding of the structure of the crystals is required in order to determine if the doping is uniform. Coherent X-ray Diffraction Imaging (CXDI) will be introduced in Chapter 2, the technique is sensitive to lattice displacements on the angstrom scale. First, the crystal synthesis will be tailored to grow nanostructures of ZnO uniform in both size and morphology suitable for device applications (nanorods, nanowires, tetrapods). Sample manipulation methods and the CXDI technique will be developed to measure the samples grown and carry out *in situ* solid state reaction experiments. The measured lattice parameters are shown for Fe concentrations in ZnO in Table 1.3. When doped to the maximum 7 at.% uniformly throughout a 1μm crystal a 1.5nm expansion would be seen which is well within the resolution of the technique. A solid state reaction method would be implemented in vacuum *in situ* with deposition of Fe, Co and Ni layers at 200°C onto ZnO nanocrystals sufficient to dope the crystals to their maximum observed solubility.

Upon step wise annealing the diffusion of the element into the ZnO structure would be expected and mapped.

Table 1.3: Lattice parameters for $Zn_{1-x}Fe_xO$ synthesised via a sol-gel method with different concentrations of Fe estimated by Rietveld refinement from x-ray diffraction patterns, * corresponds to solid state method Rietveld refinement.

x	$a_0(Å)$	$c_0(Å)$	Reference
0.01	3.2494	5.2031	[4]
0.03	3.2526	5.2066	[4]
0.03	3.252	5.205	[3]
0.04	3.2525	5.2025	[22]
0.05	3.2538	5.2067	[4]
0.07	3.2547	5.2063	[4]

The piezoelectric effect can be intimately studied using CXDI, bringing about a distinct structural change in the crystal through the application of an electric field. In device applications where the crystals are fixed to a substrate large internal strains will result during operation. This topic will not be approached in this thesis but remains a long term aim of the work.

1.1.9 Device Applications

Nanorods are also of interest for applications other than those previously mentioned throughout this chapter, a comprehensive overview of their growth, properties and applications is given by Yi *et al.* [217], Ozgur [144] and Schmidt-Mende *et al.* [165]. ZnO is fabricated over 10 orders of magnitude with high crystalline quality. Highlights of the work

to date include; the fabrication of a Schottky diode with a single ZnO nanorod by Heo *et al.* [83]. Several sensors have been developed including hydrogen [199], ethanol [197], glucose [209] and O_2, NO_2 and NH_3 [58, 59]. On the nanoscale the total surface area is large relative to the volume and defects in the surface, such as absorbed gases, have a stronger influence on electronic properties. Liao *et al.* [109] demonstrated how the diameter of nanorods affects the properties of a gas sensing device; those rods with smaller diameters possessed larger compressive stress and increased surface defects, which made them more sensitive to oxygen adsorption. The first single nanowire ZnO Light Emitting Diode (LED) was demonstrated by Bao *et al.* [13] and exhibits broad sub-bandgap emission at room temperature; an LED consists of a p-n junction; p-type silicon and n-type ZnO in Baos' case. The necessity of a dopant for p-type conduction was shown by Xiang *et al.* [214] in the synthesis of the first p-type ZnO nanowires. It is expected to pave the way for pure ZnO LEDs and transistors.

1.2 Summary

The functionality of ZnO has been outlined. The ease at which nanoscale morphologies are synthesised and its exceptional physical properties make ZnO a prime candidate for future device applications. The defect chemistry is still debated and extrinsic dopants have widened the interest in ZnO in recent years.

Chapter 2

Coherent X-ray Diffraction

2.1   Diffraction

In this Chapter the basic principles of x-ray diffraction will be reviewed and the Coherent X-ray Diffractive Imaging method introduced. The objective is not to extend the theory of diffraction but to employ it in an already well documented way. Where necessary quantitative discussion will ensue however a formal treatment will be referred to qualitatively and not derived as it can be found elsewhere.

> The word "diffraction" is derived from the Latin dis, meaning "apart" or "asunder", and frangere, "to break". The term "diffraction of light" signifies a certain breaking-up which a beam of light undergoes in passing an obstacle, and also signifies other types of breaking up which are fundamentally related to the one mentioned.
>
> Charles F. Meyer [127]

2.1.1 X-ray Diffraction

X-rays are a type of electromagnetic radiation with wavelengths shorter than visible light and were discovered in 1895 by Wilhelm Conrad Röntgen [159]. Their wavelengths range from soft x-rays (6-100Å) to hard x-rays (0.1-6Å) and their energies 150-2000eV (electron volts) and 2-120KeV respectively. High energies mean deeply penetrating radiation capable of probing the electron density of the material through either absorption or scattering to determine atomic structure. This has allowed x-rays to be applied to many fields, including; crystallography, radiography, astronomy and material science. Specifically, wavelengths of the order of atomic spacings in materials crystallographers have studied bulk and surface structures of a wide range of materials with atomic scale resolution by probing the electron density.

The experiments we describe utilise hard x-rays with a wavelength of 1.39Å (8.9KeV) and a bandwidth of 1eV. We employ the exceptional coherence properties and brightness of x-rays produced by third generation Synchrotron sources to study displacement fields in crystal structures with sub-angstrom resolution. To introduce these methods we begin with two assumptions, firstly the incident x-rays are a plane wave and secondly, each x-ray scatterers elastically and only once, known as the 'Kinematical' limit.

Consider two parallel planes of atoms in a crystal lattice. When an incident plane wave of x-rays is elastically scattered from an electron in a plane a spherical wave results. An interference pattern between spherical waves generated from x-rays scattered by electrons in both planes is understood by the Bragg Law [23]:
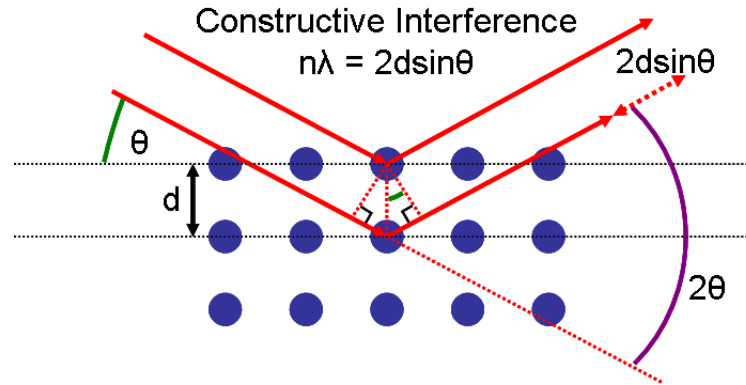
Figure 2.1: Bragg Scattering Geometry; the path length difference (2dsinθ) between x-rays incident on a set of parallel planes can determine the interatomic layer spacing, d, when a constructive interference pattern is observed in the far field at a detector, see eqn 2.1

$$n\lambda = 2dsin\theta \qquad (2.1)$$

The Bragg angle 2θ (relative to the incident radiation) describes the experimental geometry for constructive interference to be observed at a detector between x-rays scattered from different parallel planes in a crystal. The x-rays incident to the sample are equivalent in amplitude and phase, and when scattered from different planes, separated by a distance d, an optical path length difference results (2dsinθ). Thus, constructive interference occurs when the phases are equal, i.e when the path length difference is an integer number of wavelengths. Every 2θ angle at which constructive interference occurs is called a Bragg peak.

Thus far we have assumed the incident x-ray phases are equal, this is not always true as the bandwidth of the incident x-ray beam and source size play a role. The distance over which the phases are equivalent defines the spatial coherence of the incident x-ray

beam, and will be discussed further in Section 2.2.1. If the sample dimensions exceed the spatial coherence an averaging over the illuminated volume of the sample results and small scale local structures are averaged out. Whereas when coherently illuminated an interference pattern results which is sensitive to local structures. Third generation synchrotron facilities have improved the spatial coherence properties sufficiently to probe sub-micron sized samples with coherent x-ray radiation.

2.1.2 Scattering from a perfect crystal

A full derivation will not be provided, for comprehensive overviews refer to texts by Warren [208], Als-Nielsen and McMorrow [7], Coppens [40] or Guinier [76].

A crystal is a 3-dimensional periodic structure and can be built from a unit cell or the 'basis' (a description of atoms within the unit cell) found at each point on a 3-dimensional uniform lattice of points. This describes a convolution operation, originally called the 'folding' operation, and is one of the most important concepts in Fourier Theory.

Mathematically, a convolution is defined as the integral over all space of one function $f(x)$ at a position x' multiplied by another function $g(x)$, reversed and shifted, at $(x - x')$. The convolution, denoted by $\otimes$ is defined as

$$(f \otimes g)(x) = \int\limits_{\infty}^{-\infty} f(x')g(x - x')dx \qquad (2.2)$$

The convolution theorem can now be expressed in two ways; the Fourier Transform (FT) of the product of the two functions is equal to the convolution of the FTs of the individual

functions, or, the FT of the convolution of two functions is equal to the product of the FTs of the individual functions, written respectively as

$$\mathcal{F}(f \cdot g) = \mathcal{F}(f) \otimes \mathcal{F}(g) \; ; \quad \mathcal{F}(f \otimes g) = \mathcal{F}(f)\mathcal{F}(g) \tag{2.3}$$

Thus for a finite crystal we convolve the lattice, the basis and an envelope function (S_{shape}). The envelope function is a binary function which defines the boundaries of the crystal, i.e the lattice positions where unit cells exist. The 3-dimensional lattice of points is defined by a set of vectors, $\mathbf{R}_n$,

$$\mathbf{R}_n = x\mathbf{a} + y\mathbf{b} + z\mathbf{c} \tag{2.4}$$

where x, y, z are integers and $\mathbf{a}, \mathbf{b}, \mathbf{c}$ are the primitive unit cell vectors. The unit cell scattered amplitude is described by the structure factor, $F(Q)$, which is the Fourier Transform of the electron density inside the unit cell. $\mathbf{Q}$ defines the wavevector transfer local to the Bragg peak[1].

$$F(Q) = \sum_{j=1}^{N} f_j(Q)e^{i\mathbf{Q}\cdot\mathbf{r}_j} \tag{2.5}$$

For j atoms inside a unit cell at positions $\mathbf{r}_j$ with atomic form factor $f_j(Q)$, which is the FT of the electron density of an atom. The corresponding intensity observed ($I(Q)$) is derived in Appendix A.5.2.

[1] $\mathbf{Q} \equiv \mathbf{k}_f - \mathbf{k}_i$, where $\mathbf{k}_i$ and $\mathbf{k}_f$ are the incident and scattered wavevectors (where λ is the wavelength of the incident radiation, $|\mathbf{k}_i| = \frac{2\pi}{\lambda} = |\mathbf{k}_f|$).

$$I(Q) \ \propto \ \frac{sin^2(N_1\frac{\mathbf{Q}\cdot\mathbf{a}}{2})}{sin^2(\frac{\mathbf{Q}\cdot\mathbf{a}}{2})} \cdot \frac{sin^2(N_2\frac{\mathbf{Q}\cdot\mathbf{b}}{2})}{sin^2(\frac{\mathbf{Q}\cdot\mathbf{b}}{2})} \cdot \frac{sin^2(N_3\frac{\mathbf{Q}\cdot\mathbf{c}}{2})}{sin^2(\frac{\mathbf{Q}\cdot\mathbf{c}}{2})} \tag{2.6}$$

where N_1, N_2 and N_3 define a parallelepiped envelope function, the number of unit cells along $\mathbf{a}$,$\mathbf{b}$ and $\mathbf{c}$ respectively. For a large crystal Equation 2.6 the sum of phase factors is small compared to when all of the phases are equal to $2\pi m$, where m is an integer. Therefore intensity is observed when

$$\mathbf{Q} \cdot \mathbf{R}_n = 2\pi m \tag{2.7}$$

To solve this we construct the reciprocal lattice with a set of basis vectors $\mathbf{a^*}, \mathbf{b^*}, \mathbf{c^*}$ which obey the following equations

$$\mathbf{a} \cdot \mathbf{a}^* = 2\pi h \ ; \quad \mathbf{b} \cdot \mathbf{b}^* = 2\pi k \ ; \quad \mathbf{c} \cdot \mathbf{c}^* = 2\pi l \tag{2.8}$$

where h, k, l are integers, also known as Miller indices. These are the Laue equations. The points of the reciprocal lattice are defined by the vectors, G,

$$\mathbf{G} = h\mathbf{a^*} + k\mathbf{b^*} + l\mathbf{c^*} \tag{2.9}$$

Hence, when the Bragg reflection is met, $\mathbf{Q} = \mathbf{G}$, the equations in 2.8 are satisfied, this is the Laue condition[2]. The equations in 2.8 are the Laue equations and it can be shown

---

[2]This relation is dependent on the structure factor, $F(Q)$, being non zero, these reflections are known

when simultaneously satisfied define a vector space where

$$\mathbf{a*} = 2\pi \frac{\mathbf{b} \times \mathbf{c}}{v} \; ; \quad \mathbf{b*} = 2\pi \frac{\mathbf{c} \times \mathbf{a}}{v} \; ; \quad \mathbf{c*} = 2\pi \frac{\mathbf{a} \times \mathbf{b}}{v} \tag{2.10}$$

where the volume of the primitive unit cell is $v = |\mathbf{a} \cdot (\mathbf{b} \times \mathbf{c})|$, [3]. Returning to the convolution argument in equation 2.3; the reciprocal lattice is defined by the FT of the direct space lattice, each point by a vector $\mathbf{G}$, and the FT of the envelope function is copied to every reciprocal lattice point. The resulting periodic function exhibits local inversion symmetry at the origin of reciprocal space.

2.1.3 Ewald Sphere

The Ewald sphere is a geometric construction which defines a spherical shell of radius $\frac{2\pi}{\lambda}$ in reciprocal space, or a circle in two dimensions as shown in Figure 2.2, where the incident wavevector, $\mathbf{k}_i$, and scattered wavevector, $\mathbf{k}_f$, are related in the kinematic limit by $\mathbf{k}_i = \mathbf{k}_f = \frac{2\pi}{\lambda}$. At every point on this shell where a reciprocal lattice point resides a Bragg condition is met, $\mathbf{G} = \mathbf{Q}$, and the diffraction pattern corresponding to the envelope function observed.

as forbidden reflections

[3]In wurtzite ZnO the basis vectors are not orthogonal $\mathbf{a}$ and $\mathbf{b}$ at 60° and $\mathbf{a*}$ and $\mathbf{b*}$ at 30°.
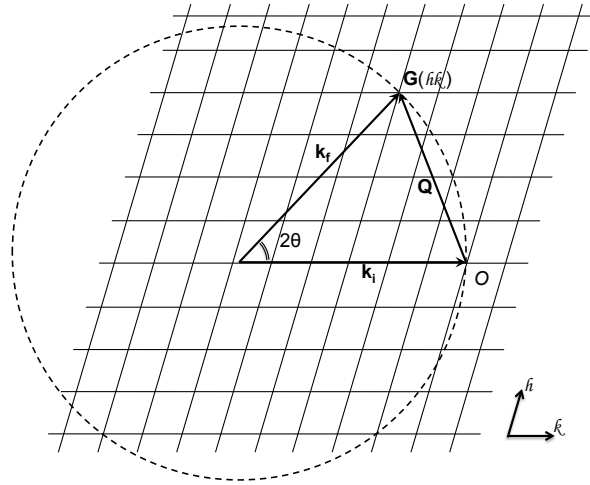
Figure 2.2: 2D Ewald circle construction, the Bragg condition is satisfied for any point on the circle which overlays a point on the underlying reciprocal space lattice point, **Q(hk)**=**G**(hk), extends to a sphere in 3D, **Q(hkl)**=**G**(hkl)

2.2 Coherent X-ray Diffraction Imaging

CXDI is applicable when a finite crystal is illuminated completely by the coherent portion of a beam of x-rays; a coherent beam is achieved when all scatterers (electrons) within the crystal see the source with the same relative phase. In the Kinematical limit scattering from the whole volume of the nanocrystal will interfere at the detector, therefore the intensity (I(Q)) surrounding each Bragg peak represents the shape of the electron density (envelope function) and is given by:

$$I(\mathbf{q}) = |A(\mathbf{q})|^2 \qquad (2.11)$$

$$\simeq |\int \rho(\mathbf{r})e^{i\mathbf{q}\cdot\mathbf{r}}|^2 \qquad (2.12)$$

where $\rho(r)$ is a complex function describing the electron density of the sample at the point $\mathbf{r}$. If the reciprocal space amplitude and phase could be measured experimentally, an Inverse Fourier Transform (IFT) could be used to obtain the diffracting electron density distribution. The diffraction signal is detected as photons, the resulting intensity measurement (square modulus of $\rho(\mathbf{r})$ in equation 2.12) destroys all phase, $\alpha = \mathbf{q}.\mathbf{r}$, information in reciprocal space; the inherent 'Phase Problem' of X-ray Crystallography. One solution is to sufficiently sample a bandwidth limited intensity measurement akin to diffraction from a finite crystal and solve the phase problem using iterative methods. Iterative methods use algorithms with constraints built from *a priori* information of the diffracting object and converge to find the lost phase information.

If a finite crystal was truly real (i.e a perfect equilibrium lattice), the dependence of the intensity on the FT of the shape function would produce a locally symmetric diffraction pattern about each Bragg peak. In reality crystals have defects, which lead to atomic displacements away from the equilibrium lattice positions. Assuming in the close vicinity of Bragg peak, $q = Q$, and the displacements are small the resulting change in shape function can be described by the phase factor, $\phi = \mathbf{Q}.\mathbf{u}(\mathbf{r})$, where the displacement field, $\mathbf{u}(\mathbf{r})$, describes the relative displacement from an equilibrium lattice. The complex shape function $S'_{shape} = S_{shape}e^{i\phi}$ in direct space propagates as asymmetry in the observed diffraction patterns[4]. Thus the technique is potentially sensitive to all crystal defects which result in atomic displacements. The derivative of this displacement can be sought to describe a component of the strain tensor and rigid body rotation.

---

[4]The symmetry of reciprocal space is not broken, the corresponding inverse Bragg peak about the origin will exhibit the exact opposite asymmetry maintaining the overall symmetry of reciprocal space.

$$\varepsilon_{ij} = \frac{1}{2}\left(\frac{\partial u_i}{\partial x_j} + \frac{\partial u_j}{\partial x_i}\right) \ ; \ \tau_z = \left(\frac{\partial u_y}{\partial x} - \frac{\partial u_x}{\partial y}\right) \qquad (2.13)$$

where u represents the displacement field of the objects configuration, the difference between the objects current configuration and its natural state.

2.2.1   Coherence

For the coherent illumination of a finite crystal the incident x-ray beam must be sufficiently coherent in all of the crystals dimensions. The coherent x-ray volume defines a 3-dimensional region of space, a coherent volume and is dependent on two factors; firstly, the reliability of the x-ray source to produce a coherent beam, and secondly, the focussing optics required to get the beam to the sample without distorting the wavefront. Until recently the brightness (x-ray flux) and coherence properties of the source were the predominant factors, third generation synchrotron source facilities have provided sufficient x-ray flux to illuminate extremely small volumes and coherence properties of the order of the samples measured. The x-ray flux defines the smallest size ($\sim$100nm^3) a crystal can be in order to measure an interference pattern at a Bragg peak and requires the beam to be focussed. For the experiments we have carried out focussing was not possible, hence we use larger crystals to obtain sufficient scattered intensity but the coherence properties begin to limit our capability.

The coherence length of a beam of light is split into two components, the transverse and longitudinal (temporal) coherence lengths (ξ_T and ξ_L respectively). The transverse

coherence is dependent on the source itself and is split into two components the horizontal and vertical creating the 3D coherent volume. A synchrotron source consists of incoherent emitters confined to a space size d. Two points within the sample will see the source with the same relative phase up to a separation distance ξ_T,

$$\xi_T = \frac{\lambda D}{2d} \tag{2.14}$$

where D is the distance from the source to the sample. This is demonstrated in Figure 2.3; two waves (A and B) of equal wavelength and different propagation directions coincide at the point P. The propagation direction is dependent on the source size, two points at the extents of the source will have the largest divergence angle and set the limit on ξ_T. ξ_T is the distance traveled along the wavefront A from point P in both directions at which destructive interference occurs [7, 186].

ξ_L is dependent on the bandwidth of the monochromator ($\frac{\Delta\lambda}{\lambda}$) attributed to the thickness of the monochromator crystal via the Darwin width [7, 208]. It is coupled to the Optical Path Length Difference (OPLD) of scattering rays through the sample and can be described by the equation,

$$\xi_L = \frac{\lambda^2}{2\Delta\lambda} \tag{2.15}$$

This is demonstrated in Figure 2.4; two waves of wavelengths λ and $\lambda + \Delta\lambda$ propagate in the same direction from point A and destructively interfere (π out of phase) at point

B, at a distance ξ_L. When the OPLD is smaller than ξ_L the sample is said to be coherently illuminated and meets the required conditions for CXDI measurements. It is important to note the OPLD is coupled to the Bragg angle. For a typical synchrotron source; $\xi_{T-horizontal} = 10\mu$m ,$\xi_{T-vertical} = 50\mu$m $> \xi_L = 0.7\mu$m therefore the longitudinal coherence length is the limiting factor for successful CXDI measurements. The coherence lengths are sufficient to investigate micro/nanosized objects with nanometer precision.
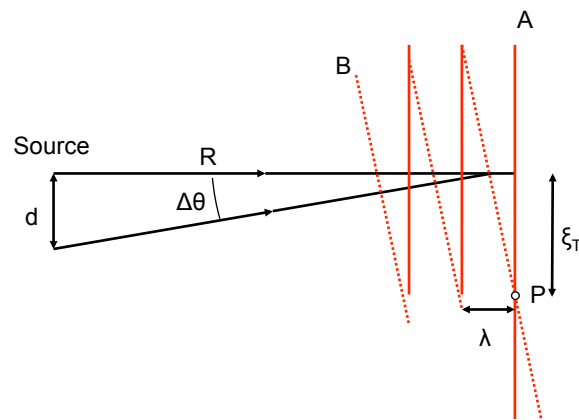
Figure 2.3: ξ_T described by the interference between two waves propagating from a source size d at point P, adaptation of figure from [7]
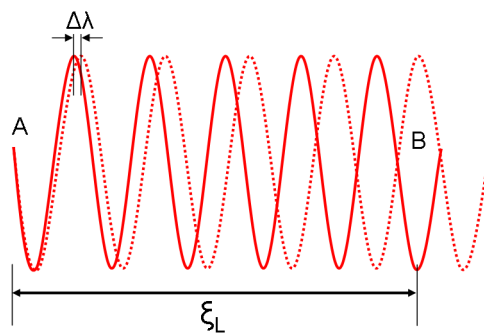
Figure 2.4: Interference between two waves with different wavelengths $\Delta\lambda$ propagating from the same point A are out of phase at point B a distance ξ_L from the source, adaptation of figure from [186]
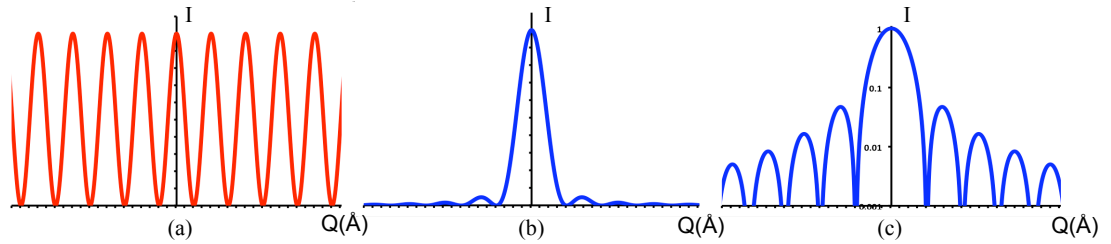
Figure 2.5: Scattered x-ray interference patterns observed in the Fraunhofer regime for (a) two point scatters and (b) all the scatterers inbetween the two points, a slit function, (c) the data from (b) plotted with a log scale

2.2.2 Degree of Coherence

As CXDI is reliant on the coherence properties of the incident x-ray beam in 3D it is important to understand how coherent the beam actually is, this cannot be measured directly but can be estimated from the diffraction patterns. The degree of coherence in its simplest form is a measure of the normalized correlation between two electromagnetic fields; zero being completely incoherent, and where the two fields are effectively identical, equal to one. If in fact they were identical x-rays scattering from two points, the interference pattern that would result is a cosine function, Figure 2.5(a). The fringe spacing corresponds to the distance d between the scatterers through $\frac{\lambda D}{d}$, where D is the distance from the scatterer to the detector. The degree of coherence between the two scattered x-rays can be measured directly by the visibility (V); defined as the contrast of the fringe intensity maxima (I_{max}) and minima (I_{min}) of the interference pattern,

$$V = \frac{I_{max} - I_{min}}{I_{max} + I_{min}} \tag{2.16}$$

For the coherent illumination of two point scatterers the visibility of the interference

pattern would be equal to 1 for all fringes, and drop to zero as the two fields are varied to the state where they are π out of phase.

So far we have considered two point scatterers, the intensity distribution expected is shown in Figure 2.5. Practically a finite crystal consists of many scatterers. In 1D a finite crystal is a chain of atoms whose diffracted intensity distribution is similar to the sinc function, see Figure 2.5(b). The length of the chain can be determined by the interference maxima spacing, equivalent to the spacing between slits for Youngs double slit experiment. Therefore if we extend to three dimensions and sample the interference fringes which correspond to each set of parallel facets in the crystal, the fringe spacing determines the size of the crystal facet to facet in the corresponding direction. Equation 2.16 is still valid and in the presence of perfect coherent illumination a visibility of one is expected. Derivation for both distributions can be found in Appendix A.5.

2.2.3 Synchrotron Radiation

The Advanced Photon Source (APS) Synchrotron facility operation begins with the generation of electrons by a thermionic emission electron gun (tungsten oxide cathode at 1100°C). The emitted electrons are then accelerated by a linear accelerator (LINAC) using microwaves produced by Radio Frequency (RF) cavities, and further accelerated in the booster ring to 7GeV[5]. The RF cavities in the LINAC force the electrons to bunch into pulses, these are used to fill a single 'bunch' in the storage ring, the number of bunches is dependent on the length of a bunch, the size of the ring and the frequency of the RF cav-

---

[5]The booster ring is used to economise on both space and equipment as a linear accelerator would be considerably larger than the synchrotron

ities. When sufficient current is accumulated in the booster ring the electrons are fed into the storage ring, here they are guided in a circular orbit actually made up of 40 straight sections and 40 bending magnets. In the straight sections Insertion Devices (ID) are placed, they employ an array of magnets to produce an alternating field in the horizontal plane and force the electrons to oscillate. Upon changes in direction of the electrons radiation is emitted, as electrons further down the ID are oscillating and progressing down the ID slower than the radiation emitted amplification of the x-ray beam results. The Undulator ID simply ensures that the radiation emitted by an electron turning through one period in the undulator is in phase with the radiation emitted at all other periods, Als-nielsen and McMorrow [7] treat this comprehensively mathematically. The key point is the radiation is in phase and quasi-monochromatic (a single wavelength and its harmonics[6]), therefore suitable for CXDI experiments

2.2.4 Optics

The optics on a beamline required to maintain a coherence volume large enough to analyse crystals using CXDI has been realised in the last 10 years [153]. Practically getting the beam from the source to the sample is experimentally challenging, optical components must handle heat load, vacuum environment and be stable enough to maintain ξ_L (the limiting coherence property). Improvements in the quality of monochromator crystals have enhanced the longitudinal coherence length set by equation 2.15. Longer longitudinal coherence lengths can be achieved using crystal reflections with smaller darwin widths but a smaller x-ray photon flux results. Equally different monochromator crystals could be

---

[6]Harmonics are removed from the beam using a mirror.

used, for example diamond $(111)(\frac{\Delta\lambda}{\lambda} = 5.95 \times 10^{-5})$ [75] provides ξ_L twice that of Silicon but cannot be fabricated as flat which distorts the wavefront of the incident beam.

In addition to coherent beams third generation synchrotron sources provide enough intensity to obtain sufficient statistics for CXDI measurements from finite nanocrystals. The flux is spread across a relatively wide beam (several hundred microns) and for sub micron crystals leads to the introduction of focussing optics. Common choices include Fresnel Zone Plates, Kirkpatrick-Baez (KB) mirrors and compound refractive lenses. Their use is dependent on the size of the focus and intensity required. Robinson et al. [154] discuss the advantages and disadvantages of each method concluding KB mirrors are the most suitable for finite nanocrystal CXDI for optimization of both flux and coherence. The introduction of more optics has a significant impact on the coherence properties of the incident beam, traditionally in a CXDI beamline as few components are used as possible to maintain the coherence properties of the incident beam.

2.2.5 Beamline Setup

The synchrotron at the Argonne National Laboratory called the Advanced Photon Source (APS) was used for our experiments. Beamline 34-ID-C uses a beam splitting mirror to direct the x-ray beam produced by the undulator onto a silicon (111) double crystal monochromator. The monochromator was used to select 8.9keV monochromatic x-rays (λ = 1.39Å) with a bandwidth (1eV) small enough to provide a longitudinal coherence length ($\xi_L \simeq 0.7\mu$m) according to equation 2.15. There are two principle modes of operation defined by the size of the sample in the transverse directions:
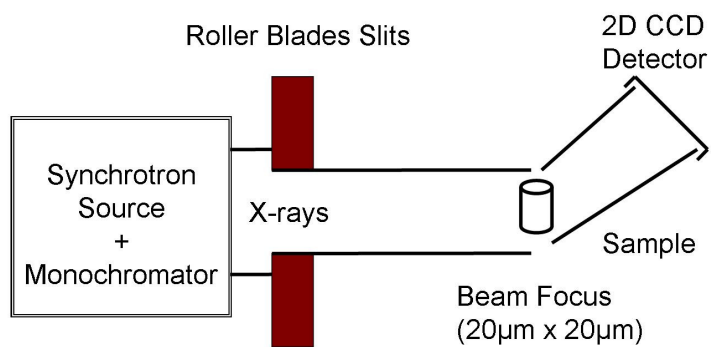
Figure 2.6: Schematic of unfocused mode of beamline operation
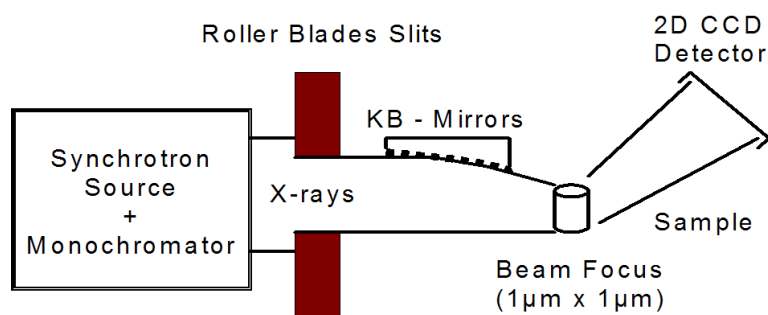
Figure 2.7: Schematic of focused mode of beamline operation

Unfocused setup : the beam is selected using Roller Blade slits, depending on the crystal density on the sample surface the required area of sample illumination can be set comfortably to (20-100μm x 20-100μm).

Focused setup : the beam is again selected using Roller Blade slits (100μm x 100μm) and is focussed using Kirkpatrick-Baez (KB) mirrors to a square approximately 1μm x 1μm, providing a significant increase in intensity compared to the unfocussed approach, thus is favourable for smaller crystals which require a greater photon flux.

Sample stages move the sample into the beam, illuminating all crystals in the beam footprint. The beam footprint on the sample is incident angle dependent; from large angles to grazing incidence the illuminated area on the sample will increase accordingly. The footprint is varied to locate and isolate crystals on the substrate; for a sample with a low crystal density a large footprint illuminates the few crystals that satisfy Braggs law for a particular crystal orientation. Figure 2.8(a) shows a schematic view of a sample with multiple randomly oriented crystals which all satisfy the Bragg condition akin to a traditional powder ring. If the sample is densely populated and multiple diffraction peaks from different crystals are detected, see Figure 2.8(b), the beam size and footprint can be decreased until a single crystal in the required orientation is illuminated.

For ZnO rods two orientations are probable, rods stood on end and rods lying on their sides at random rotations relative to the samples surface plane. By choosing a specific orientation of the crystal; in this case a rod stood on end, the Roper Scientific direct-detection Charge-Coupled Device (CCD) detector is placed 1-3m behind the sample and is moved to the correct Bragg angle for in this case the brightest (101) ZnO reflection.

(a)

φ=0°

φ=1°

φ=2°

φ=3°

φ=4°
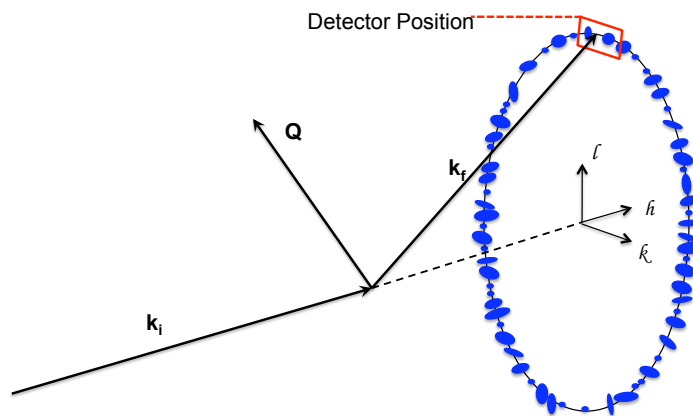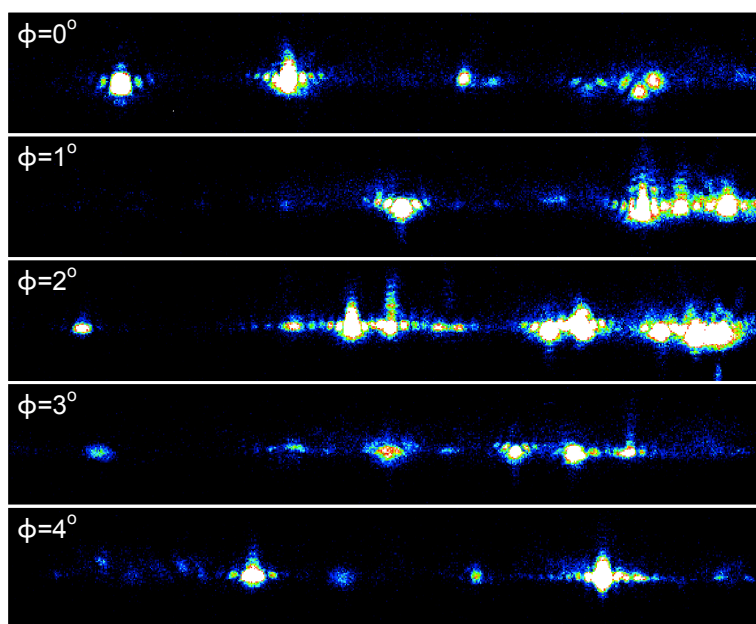
(b)

Figure 2.8: The (002) ZnO powder ring (a) reduces to individual intensity distributions due to low crystal density, (b) for four one degree ϕ rotations crystals move in and out of diffraction according to the Bragg condition, intensity measured on a Charge Coupled Device. Dataset No. 140 (Aug 2009), frames 5,25,45,65,85.

The sample is translated in the beam until a crystal on the sample happens to have the right orientation and adjustments to both the sample position and the detector arm to allow the diffraction pattern to be centred on the detector. The distance to the detector defines the rate at which the data is sampled, governed by the oversampling rule, see Section 4.2.2. Through rotation of the sample in the surface plane (θ) rocking curves are taken through the Bragg peak, reciprocal space is rocked through the stationary detector and 2-dimensional diffraction patterns, see Figure 2.9, are concatenated to produce a 3-dimensional dataset, see Figure 2.10. The cut planes in Figure 2.10 highlight the fringes resulting from coherent illumination of a crystal terminated by parallel facets of a finite single crystal.
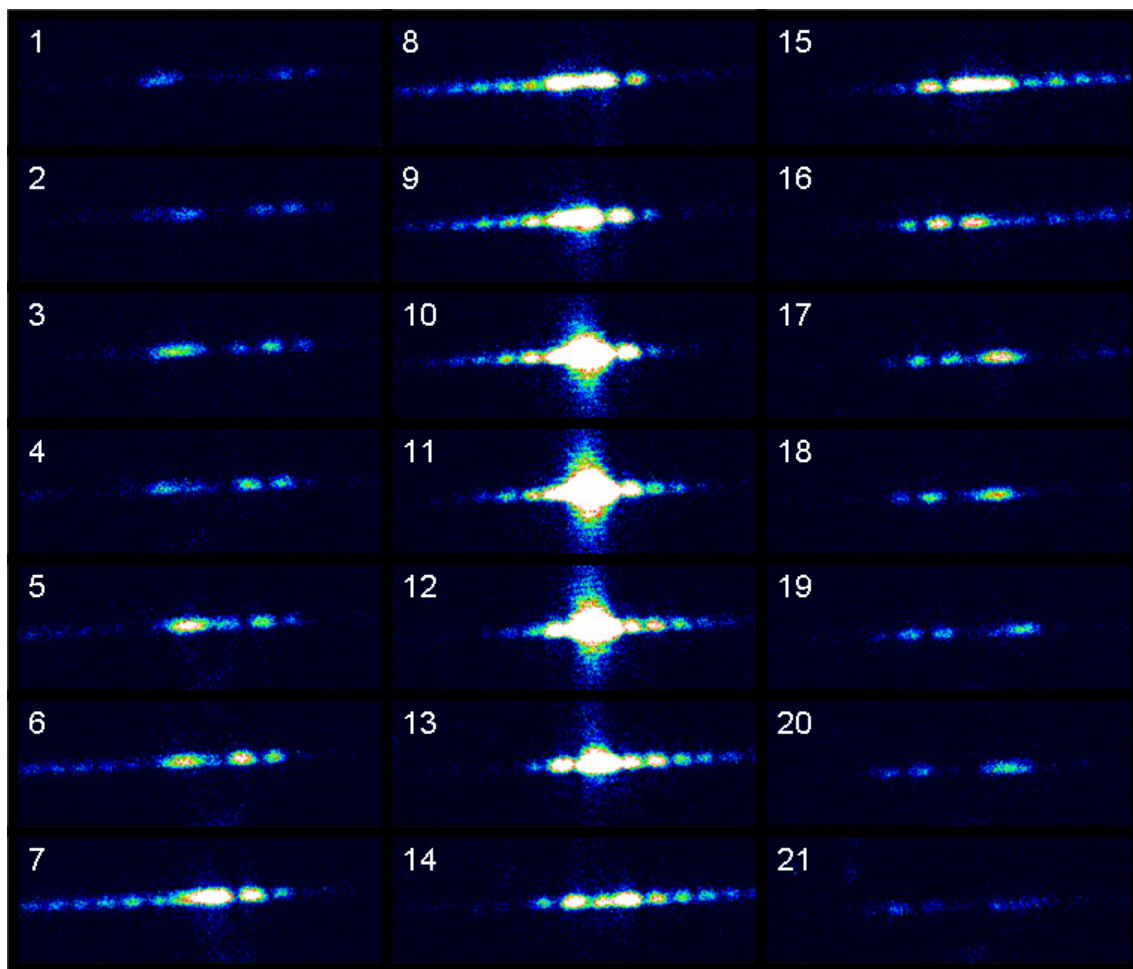
Figure 2.9: Twenty one 2D diffraction patterns collected in the CCD at consecutive steps of a rocking scan of a ZnO (101) Bragg peak
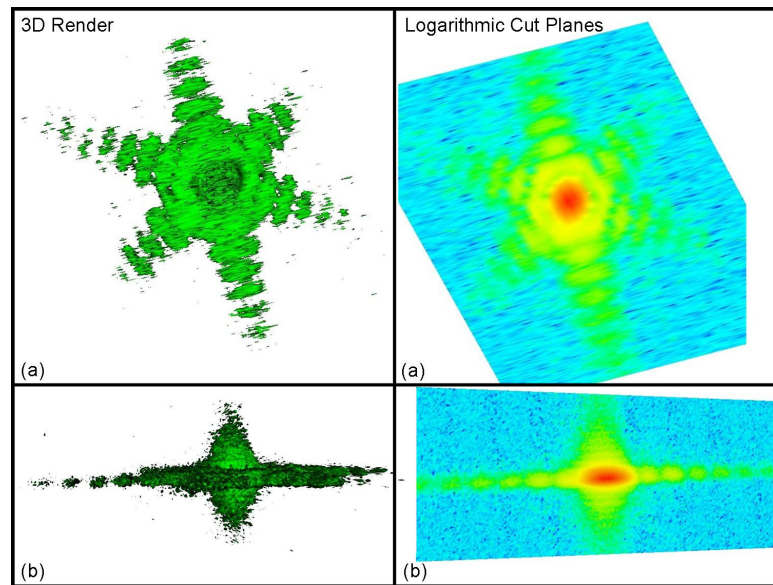
Figure 2.10: Three dimensional render of slices in Figure 2.9 using the MayaVi Data Visualizer, (a) Side, (b) Top view and Logarithmic scalar cut planes for corresponding views

Chapter 3

ZnO crystal synthesis

In this chapter the Chemical Vapour Transport Deposition (CVTD) method employed

for ZnO crystal growth will be introduced and alternative routes to synthesis reviewed.

The processing of ZnO nanomaterials post growth will be discussed to achieve the sample

requirements for successful CXDI measurements. A description of experimental set up for

post growth, *in-situ* annealing and metal evaporation in high vacuum is provided.

3.1   ZnO synthesis routes to crystal growth

The huge variation in ZnO crystal morphologies available via several different synthesis

methods was identified in Section 1.1.7.

Several 'control' parameters were optimised for sample synthesis. For a measurable diffrac-

tive signal from a crystal both high crystalline quality and sufficient diffracting volume

were required. Control over the morphology, aspect ratio, size, orientation, crystal den-

sity and location ensure a coherent illumination of a nanocrystal. Substrates with closely matching lattice parameters and catalysts can provide orientation and location control, however this often results in epitaxy; advantageous for locating diffraction but isolation becomes problematic and substrate diffraction can interfere when aligned with the substrate lattice. The final consideration was the adhesion of measured crystals to substrates, crystals simply deposited on substrates were unstable and prevented measurement by CXDI hence a solution was sought.

3.1.1 Chemical Vapour Deposition

Chemical Vapour Deposition (CVD) is reported to proceed via the Vapour Liquid Solid (VLS) mechanism [196]. When applied to ZnO, ZnO vapour reacts on the surface of a substrate, typically a catalyst is used to control the growth in the form of Gold (Au) [57, 87, 140, 201, 202, 216, 218] or Tin (Sn) [69] for nanowire/nanorod morphologies and Indium for the nanobelt morphology [55, 56]. Solidification occurs when the liquid seed layer is enriched until saturated. A multitude of experimental variables influence the growth mechanism and subsequently change the dimensions, crystal quality and morphologies of the grown structures. The thickness of the catalyst layer can determine the nanowire dimensions [87]. At high temperatures the Au dewets the surface, the thickness determines the size of coagulated Au and the size of the catalyst determines the size of the seeded ZnO crystal.

For the large scale fabrication of nanoscale devices the growth needs to be controlled at desired locations; the nucleation of several different ZnO morphologies has been success-

fully controlled using substrates with closely matching lattice parameters, such as sapphire c-plane (Al_2O_3), GaN and Silicon (111). The next step is to apply lithographic techniques to control the catalyst location, a consequence is control over the volume of the catalyst material and therefore its size. This was demonstrated initially over a wide area [74] with Au catalyst (50-200nm squares) at regular intervals several nanowires were grown at each catalyst location. Fan et al. [57] implemented a Au nanotube membrane method to pattern the catalyst and grow individual rod structures from each catalyst location.

3.1.2 Metal-organic chemical vapour deposition

Metal-Organic Chemical Vapour Deposition (MOCVD) is traditionally used in thin film growth. Desired atoms are combined with complex organic gas molecules. The gas passes over a hot semiconductor substrate and breaks up, depositing atoms onto the surface, layer by layer. Capable of almost atomic scale precision and orientation with substrates has been applied to ZnO in thin film applications for decades, but rarely nanowires. Lee et al. [105] demonstrated MOCVD of ZnO nanowires on GaAs substrates without catalysts. The physical properties of the crystals were found to be similar to those in thin films, suggesting high crystalline quality. The inability to seed growth leads to high crystal density, this combined with orientation to the substrates was deemed unsuitable.

3.1.3 Hydrothermal growth

Hydrothermal growth methods, also referred to as aqueous solution methods were first showcased by Andres Verges et al. [8] in 1990. The growth proceeds in liquid at relatively

low temperatures ($<150°$C) and result in homogeneous coverage of substrates over a large surface area (>1cm^2). A wide variety of morphologies are again available, particularly advantageous for the manufacture of highly aligned arrays of nanowires/nanorods [73, 165, 174, 193]. Alignment of wires in close proximity make them unsuitable for study with CXDI at present, therefore this method was not employed for synthesis and will not be discussed further.

3.1.4   Electrodeposition

Electrodeposition has also been implemented to grow ZnO columnar structures [29, 30, 32, 110, 124] and thin films [44, 54]. The reaction proceeds by deposition of material onto an electrode (substrate) from a Zn containing solution and dissolved oxygen in deionized water. Films grown in this way are being applied to photovoltaic applications. Typical dimensions of ZnO columns between 100 and 300 nm in diameter and 400 to 900 nm in height are obtained depending on the electrodeposition parameters [30], at low temperatues ($<100°$C). The structures grown with this method are extremely dense and aligned with their substrate and unsuitable for study with CXDI.

3.1.5   Chemical vapour transport deposition

The CVD process discussed earlier in this chapter, Section 3.1.1, described growth seeded at the substrate. We employed a variant CVTD method where the growth proceeds in the gas phase and the grown crystals are deposited on a substrate downstream. The set up is shown in Figure. 3.1. A mixture of zinc carbonate ($ZnCO_3 \circ 2Zn(OH)_2 \circ H_2O$)
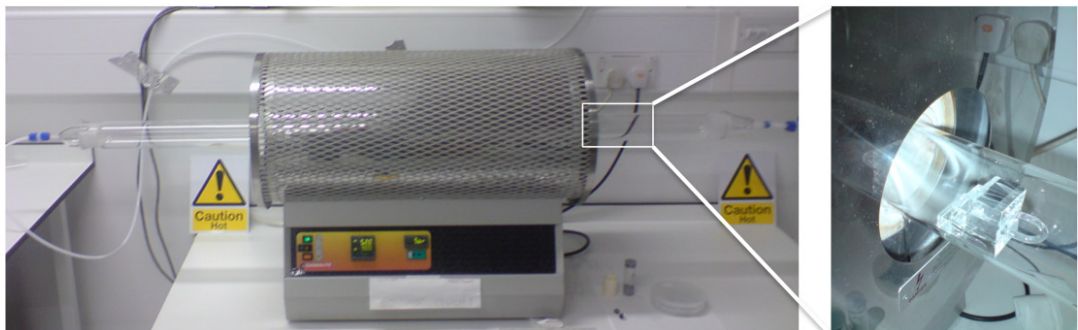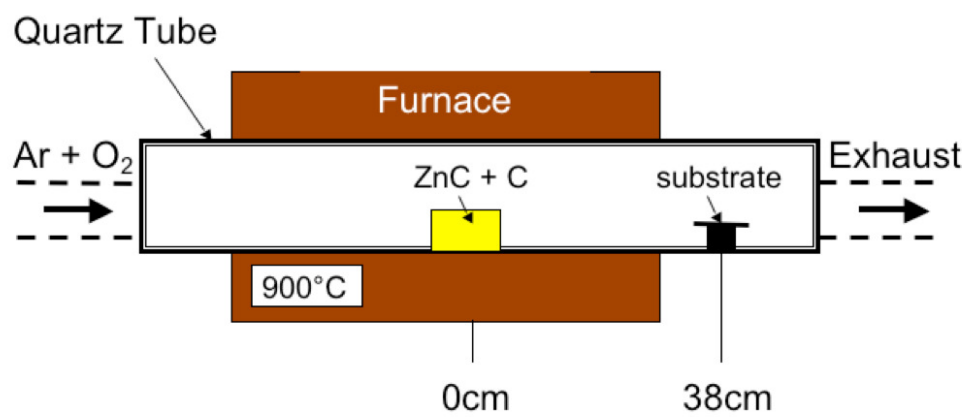
Figure 3.1: Schematic and photograph of ZnO furnace set up, zoomed photograph of silicon substrate location and mount with white ZnO deposition

and graphite powder; weight ratios of (5:1) and (10:1) were placed in a silica boat in the center of a quartz tube surrounded by a Carbolite[1] furnace. Argon carrier gas was introduced at a flow rate of 500-700 Standard Cubic Centimetres per Minute (sccm) with oxygen concentration in the range 3%-5%. The furnace was heated to 900°C, the reaction proceeds via the carbothermal reduction of zinc carbonate, $ZnCO_3$:

$$ZnCO_3 \xrightarrow{Heat} ZnO + CO_2 \tag{3.1}$$
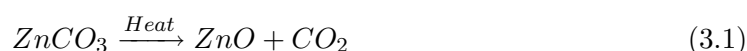
The decomposition begins at low temperature (<100°C), is considerable between 240°C and 320°C and complete by 400°C. The zinc hydroxide component breaks down at low temperature ($\sim$100°C) producing ZnO and water:

$$Zn(OH)_2 \xrightarrow{Heat} ZnO + H_2O \tag{3.2}$$
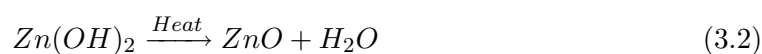
At higher temperatures there are several energetically favourable reactions[2], they include:

$$C + 1/2O_2 \longrightarrow CO \tag{3.3}$$

$$2ZnO + C \longrightarrow 2Zn + CO_2 \tag{3.4}$$

$$ZnO + CO \longrightarrow ZnO_x + CO_2 \tag{3.5}$$

$$ZnO + C(CO) \longrightarrow ZnO_x + CO_2 \tag{3.6}$$

---
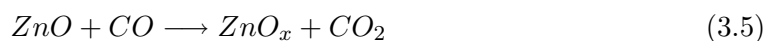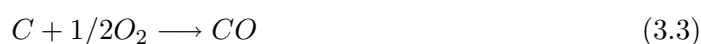
[1]Carbolite Tube Furnace (CTF:12/65/550), http://www.carbolite.com
[2]For Gibbs free energy calculations, see [46] for eqn. 3.3, [60] for eqns 3.4 and 3.5, and [136] for eqns 3.1 and 3.6.
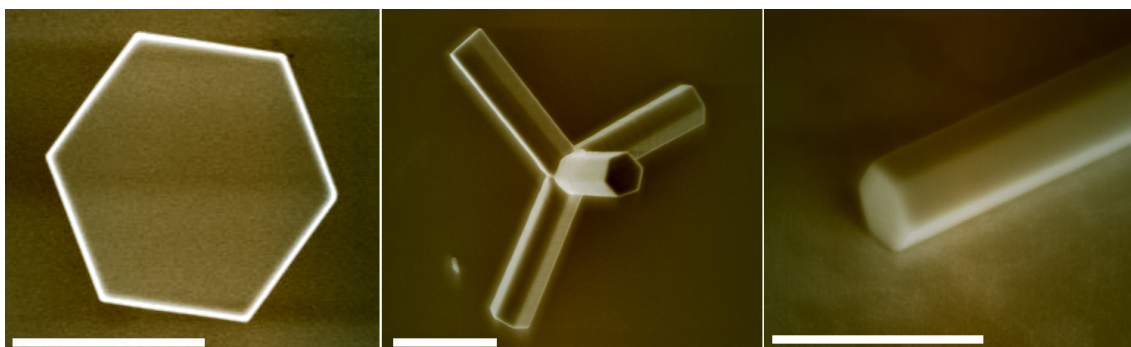
Figure 3.2: SEM micrographs of a) hexagonal plate b) tetrapod and c) nanorod morphologies synthesised previous to this work by Newton [136]; Scale Bar = 1μm

The carbon within the mixture promotes a deoxidation reaction, the resulting sub oxides of ZnO formed through reactions 3.5 and 3.6 nucleate and oxidise to form nanocrystals. The growth proceeds in the gas phase or on the walls of the furnace near the source [216]. The crystals are deposited on a substrate positioned downstream, observed as a white layer of material on a Silicon (111) substrate (150°C) parallel to the gas flow, see Figure 3.5(a). The crystals grown are dependent on several variables; temperature, partial pressures of Zn^{2+} and O^{2-}, source material, the shape of the source boat and substrates used. A wide variation in morphologies are made available and crystals can be suitably tuned to each experiment. The cleaning procedure carried out before each run can be found in Appendix A.7.

The nanocrystals synthesised by Marcus Newton previous to this project are shown in Figure 3.2, they include hexagonal plates (200nm thick x 1-2μm), nanorods (0.2μm x 1μm) and tetrapods; multiarmed wurtzite ZnO structures joined at a central zincblende core, growth parameters can be varied to produce both tapered and uniform hexagonal arms at higher pressures.

The growth mechanism is not clear, it is reported to be both vapour-solid [43, 125, 215] and vapour-liquid-solid [69, 196], this could explain the large variation in parameters as both are valid. A distinction needs to be made, not between the mechanism but where the mechanism occurs for this study. The crystals are grown in the gas phase or on the furnace walls at high temperature [3] and are deposited at a lower temperature downstream, they therefore do not adhere or align to the substrate in anyway and cannot be grown longer by increasing the growth time. This has several advantageous implications for the CXDI measurements.

3.2   CXDI sample preparation

CXDI requires the coherent illumination of an almost perfectly crystalline sample in a known orientation. In the two modes of set up with a high density of crystals on the substrate, accentuated when aligned with each other, diffraction patterns from multiple crystals can interfere with each other thus a lower density was preferable. In theory if they are coherently illuminated they will interfere and the problem is still resolvable. However with limiting coherence lengths of the incident radiation it is probable they will be incoherently illuminated relative to one another and their diffracted intensities will average out any information we had hoped to gain. With this in mind randomly oriented crystals are useful, unless the distance between crystals can be guaranteed larger than the beam footprint.

Misalignment of crystals with the substrate lattice is preferable, some level of epitaxy can

---

[3]Post growth, removal of the quartz tube showed heavy deposition of ZnO around the source. Between synthesis cycles this was removed using Hydrochloric acid, Acetone and Isopropanol cleaning
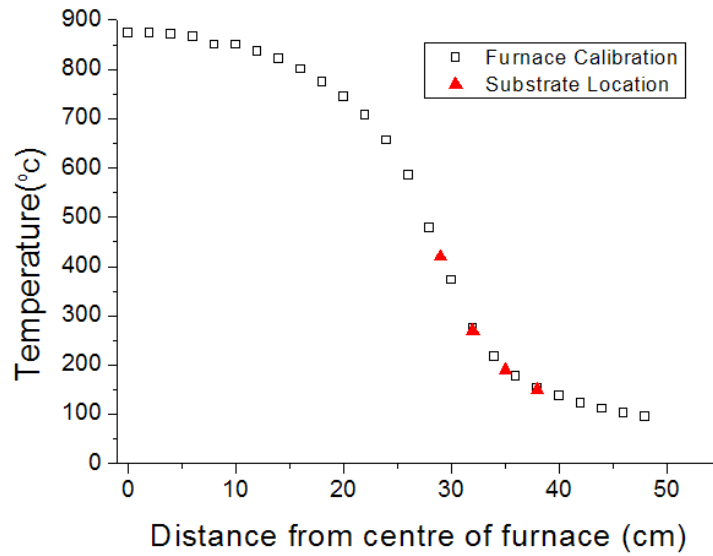
Figure 3.3: Temperature profile of the furnace system used to grow ZnO and red triangles mark locations of samples subsequently characterised with SEM in Figure 3.4

be useful. Crystal Truncation Rods [9, 153] produced by interference between scattered X-rays from the substrate reside at the same position in reciprocal space as they have the same structure overlap diffraction from an illuminated crystal on the substrate.

CVTD produces misoriented crystals loose on a substrate. Due to the strong ionising power of the x-ray beam loose crystals can move when placed in the incident x-ray beam. Several post growth processing steps were required for successful CXDI measurements, see Section 3.3.

3.2.1 Synthesis Results

The CVTD method used has been characterised.

There are many variables which determine the morphology and size of crystals grown,

mentioned in Section 1.1.7. To an extent they all determine the partial pressure of Zn supersaturate which oxidises in the gas phase to produce crystals. For uniform growth the amount of supersaturate needs to remain relatively constant for the growth duration, otherwise a taper was observed. In practice this was very difficult as the source quickly became depleted. The conditions found to produce the most uniform crystals were 700sccm oxygen, 45sccm Argon, 1.5grams of 10:1 zinc carbonate to carbon ratio and the substrate positioned at 150°C. Examples of the variation in morphology of samples deposited at different temperatures is shown in Figure 3.4, a close up of one of the crystals is shown in Figure 3.5 high crystalline quality can be identified from the well defined hexagonal and end facets and was later confirmed by x-ray diffraction.

The temperature profile of the furnace is shown in Figure 3.3. Four red triangles identify samples positioned at different temperatures subsequently characterised using SEM. The rod morphology is deposited at 150°C (A) with little variation in size and morphology, upon increasing temperature a larger variation in structure was observed. At 190°C (B) few rods are deposited, balls of ZnO (up to 500nm) are observed in lines up to 10μm in length. At 270°C (C) nanowires (<100nm in width and up to 60 μm in length) are observed amongst other morphologies and at 420°C (D) high yields of ZnO whiskers are observed (tapered nanowires several microns long and less than 40nm in width). Growth at the substrate was not observed at any growth temperature, contrary to other findings [216].

The main drawbacks of vapour phase growth is the general lack of control. The material deposited was found to be heavily dependent on the gas flow dynamics in the tube[4],

---

[4]It is important to note the furnace system was moved to a new location (Jospehson Laboratory, London Centre for Nanotechnology) and the strength of the exhaust severely affected the morphology of the crystals. Maintaining atmospheric pressure with a needle valve favoured the rod morphology and
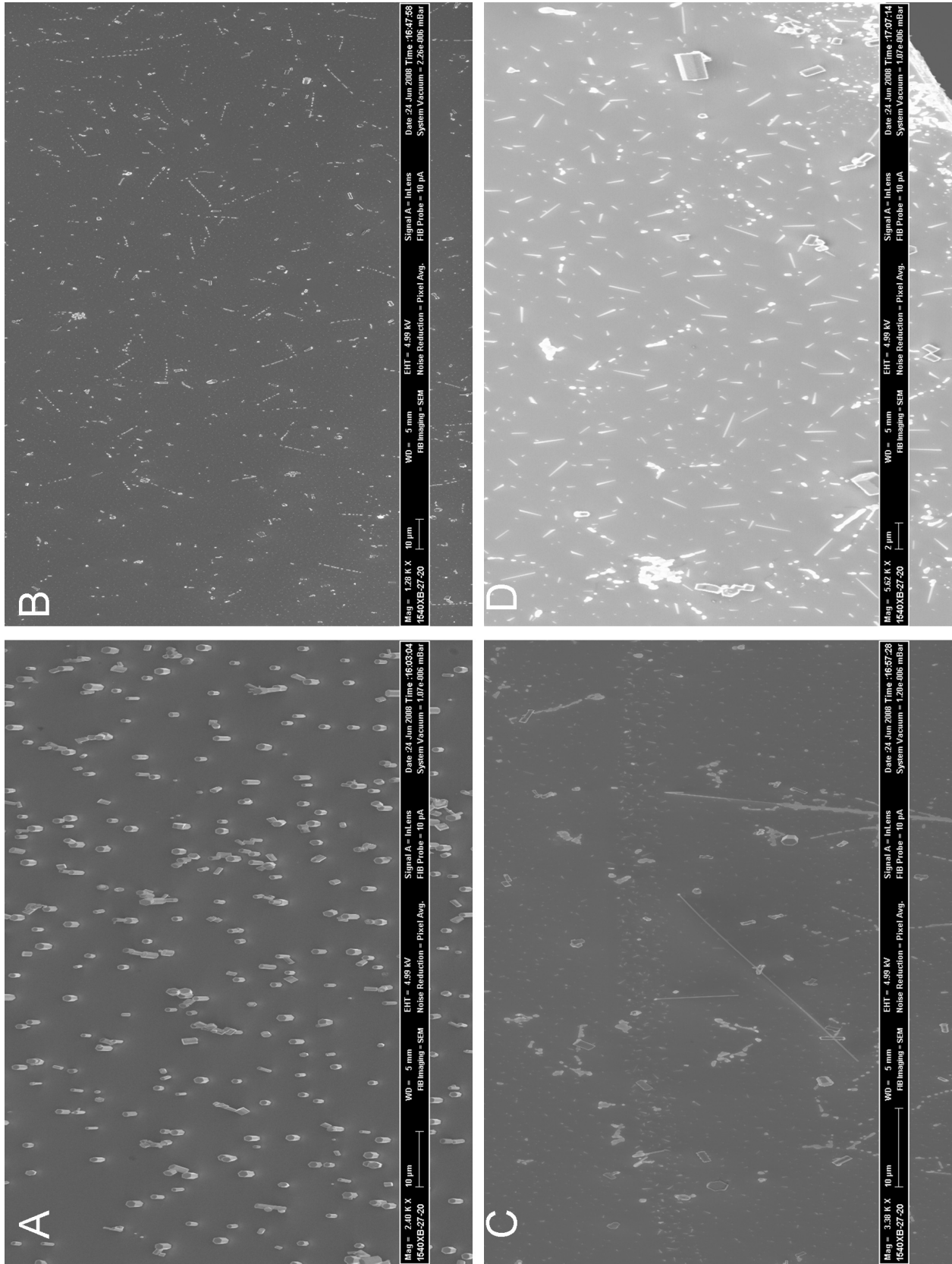
Figure 3.4: SEM micrographs of deposition structures at varying substrate positions (A) 150°C (B) 190°C (C) 270°C (D) 420°C

additional substrates in the tube caused turbulence and deposition to change at different temperatures. Newton et al. [139] highlighted this by using baffles to aid mixing of the supersaturate, producing the tetrapod morphology under the same conditions, in the same furnace.

To overcome the crystal adhesion problem the obvious solution discussed previously was to catalyse the growth. Attempts to seed the growth in a furnace operating at atmospheric pressure using different substrates (Indium Tin Oxide(ITO), sapphire, Si(111),Si(100)) and Au catalysts proved unsuccessul. The majority of the Zn supersaturate had oxidised prior to arriving at the substrate. In general CVD approaches that seed substrate epitaxial growth require low pressure (10^{-3}Torr [216]) to ensure the Zn supersaturate gets to the substrate before nucleating.

3.3   Post Growth Sample Preparation

Several methods were tested to adhere the crystals to the surface without changing their morphology, they include; (i) evaporate a layer of Titanium (nm) onto the crystals; (ii) fabricate on substrates with matching lattice parameters e.g Si (111) and sapphire c-plane, (iii) previously Liang et al. [126] had used glues and paints, these proved to be unstable as they did not fully crystallise; (iv) grow the oxide layer on the substrate to encase the base of the crystals.

---

tuning of the variables allowed rods of dimensions in the range 0.2-2μm in diameter x 2-5μm in length to be grown. These wires did not grow epitaxially and were easily broken by the electron beam in the SEM. The inability to adhere the smaller morphologies to the substrate prevented measurement by CXDI in this case.

3.3.1 Silicon dioxide growth

Growing the oxide layer post synthesis proved the most successful method for adhering samples to the substrate, combined with improvements in the stability of the beamline allowed individual crystals to be analysed for several days. As the oxide layer was grown the substrates colour changes (to blue for an additional 80nm of oxide layer). Gradients in the oxide layer were avoided by increasing the oxygen flow rate and placing the sample in the hottest region of the furnace where the temperature gradient across the sample was the lowest (effectively zero) $\pm$8cm about the center of the furnace, see Figure 3.3. It is important to note an interaction between the crystals and the oxide layer was expected and was observed in Figure 3.5 (b) as a lighter halo region around each crystal on the substrate. Energy Dispersive x-ray Spectroscopy (EDS) confirmed a gradient of Zinc was present here. Further evidence is shown in the side on view, Figure 3.5 (c), an undercut at the base of the crystals confirmed a breakdown of the facets at the contact point with the substrate, an increase in relative SiO_2 growth in this region is also clear.

3.4 Energy Dispersive x-ray Spectroscopy of ZnO post oxide growth

A 5keV electron beam excites an electron from the inner shell of an atom, an electron from an outer shells decays into the hole producing an x-ray of energy defined by the energy difference between the two states. An elemental analysis results, the method is called Energy Dispersive x-ray Spectroscopy (EDS). A ZnO crystal with a grown thermal oxide
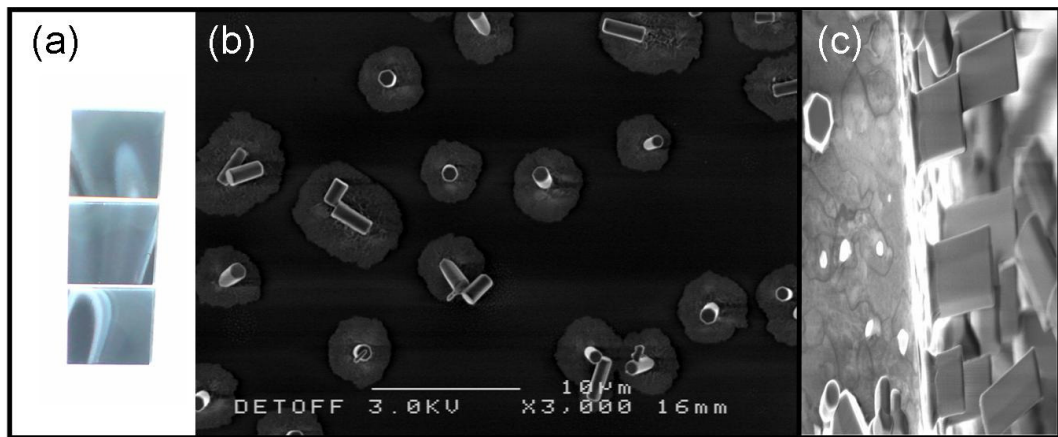
Figure 3.5: (a) Photograph of 3 (10x10mm) silicon substrates post CVTD growth, white deposition lines are evident due to system gas flow dynamics, and SEM micrographs of (b) top view and (c) side view of multiple nanorods on a Si(111) substrate with a post synthesis oxide layer growth. Note in (b) a halo is evident around each crystal , Energy Dispersive x-ray Spectroscopy(EDS) confirmed a gradient of Zinc was present. In (c) an undercut at the base of the crystals confirmed a breakdown of the facets during post growth oxidation, an increase in relative SiO_2 growth in this region is clear

layer was characterised via EDS and SEM simultaneously. Starting where the ZnO crystal was known to be several measurements were made at regular intervals through and beyond the observed 'halo' of roughness surrounding the crystal. Figure 3.6D shows the weight percentage of Zn(L edge) drops dramatically at the edge of the crystal and the Si(K edge) increases in contrast as expected. At approximately 600nm from the crystals edge 20% Zn is still present a shallow gradient is observed until the edge of the observed 'halo', beyond the halo a negligible amount of Zn (<1Wt.%) was observed. Considerable diffusion of Zn into the substrate, an accurate quantification was difficult. Figure 3.6B shows the imprint left by the electron beam on the sample, the area sampled was considerably larger than expected due to the beam size but less than 300nm in diameter and sufficient to rule out tails of the electron beam exciting the end of the ZnO rod in all measurements.[5]

Initially experiments were carried out in the focussed mode of operation and required small crystals. Further experiments incorporated an *in-situ* approach which could only operate in unfocussed mode, it was necessary to tailor the rods to larger sizes to get enough intensity from the samples to make successful CXDI measurements.

3.4.1 Micro-manipulation

The vast number of crystals present on a substrate meant it was virtually impossible to find the crystal measured with CXDI with alternate imaging techniques such as SEM. Novel methods were needed to fiducialise the samples to achieve this and extend the CXDI technique so that multiple Bragg peaks could be measured from the same crystal.

---

[5]The electron microscopy was accomplished at the Electron Microscopy Center for Materials Research at Argonne National Laboratory, a U.S. Department of Energy Office of Science Laboratory operated under Contract No. DE-AC02-06CH11357 by UChicago Argonne, LLC.
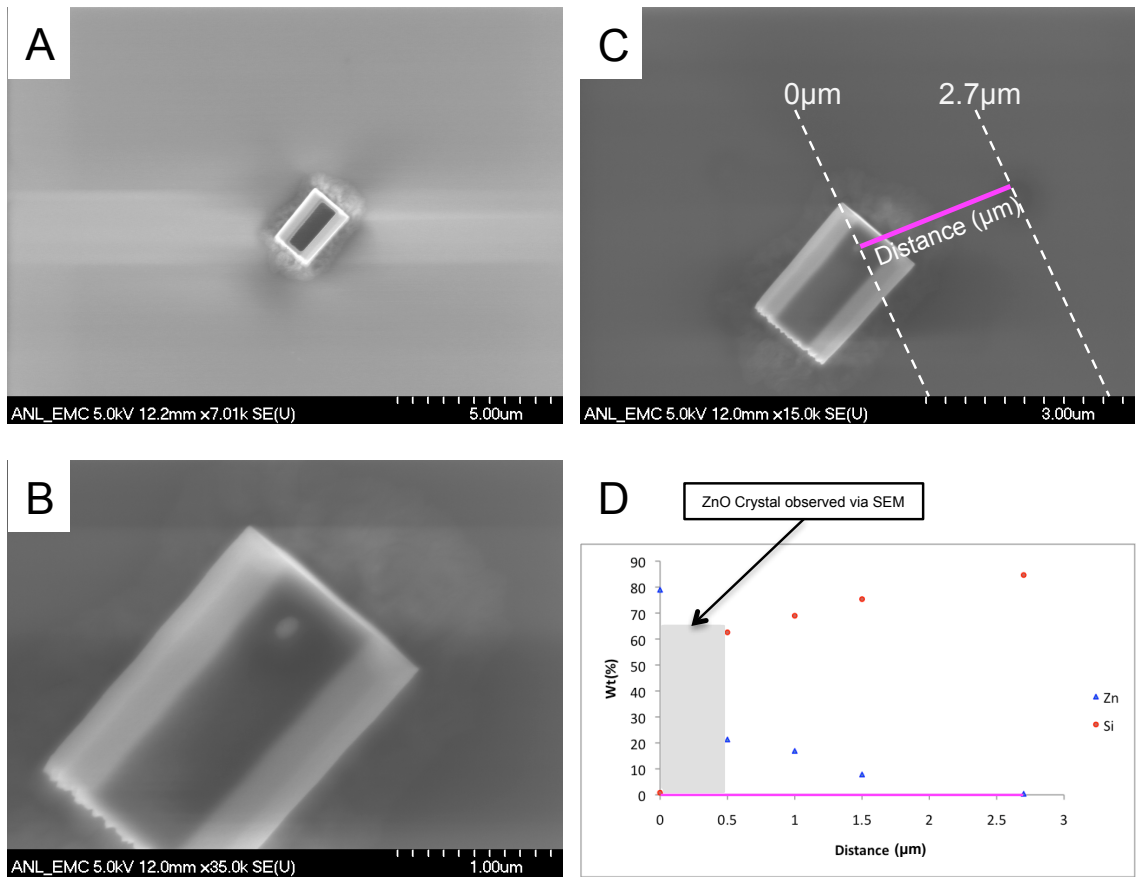
Figure 3.6: A ZnO crystal (A) SEM post thermal oxide growth, (B) a zoomed SEM image of distortion in the crystal post EDS, (D) EDS Wt% for elements present at intermediate positions along the pink line identified in (D).

A Silicon (001) wafer was cut in 10x10mm squares and a cross scored through the centre of each die. An individual ZnO rod was placed in a marked corner quadrant as close to the centre as possible using a micromanipulator [6]; electrostatic forces attract the chosen rod to the manipulation probe, contact with the surface being sufficient to deposit the rod. It is then possible to identify the rod easily using SEM with the larger scored structure providing a point of reference, see Figure 3.7, and utilise the roughness of the silicon to guarantee illumination of the crystal. The additional information provided by SEM allowed an accurate estimate of the orientation of the crystal on the substrate. A search was then embarked upon to locate the specular reflection in this case ZnO (100), once found the position is logged and a second search initiated for a second reflection. Upon the realisation of a second reflection a full orientation matrix is achieved and further reflections are easily found.

Multiple Bragg reflections could be independently measured for a single crystal. This provided two new realms of contemplation, the first, the potential for 3 dimensional displacement fields of single nanocrystals and, the second, a direct test of the reliability of phase retrieval algorithms to find the correct solution (discussed further in Section 4.2.4). Independent reconstructions should show similar features as they all represent different components of the same three dimensional displacement field.

---

[6]A-Zoom-2 light microscope combined with two Narishige MMO-202ND Three-axis Hanging Joystick Oil Hydraulic Micromanipulators, London Centre for Nanotechnology Cleanroom

CVTD ZnO Crystals	Micromanipulate & Deposit	Thermal Oxide Growth
Morphology & Size Control	Isolate in known location	Adhere to substrate
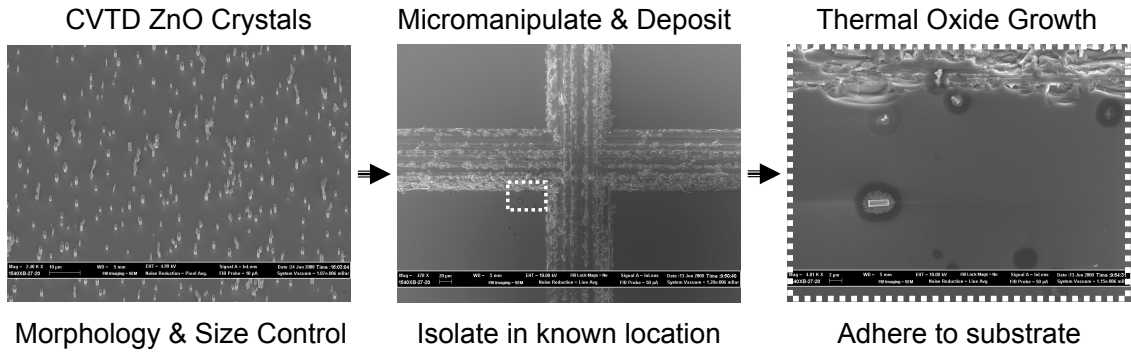
Figure 3.7: Micro-manipulation procedure: CVTD produces thousands of loose crystals, a single crystal is removed and positioned next to a scored cross hair on a bare Silicon substrate, finally, the oxide layer is grown in order to adhere the crystal to the substrate.

3.5 Confocal Microscope

The method outlined in the previous section has been optimised using a confocal microscope. Integrating this into the beamline setup to reside above the sample as it is illuminated with x-rays. Alignment of the x-ray beam with the focal spot of the confocal microscope allows any crystal to be oriented in either the unfocussed or focussed modes of CXDI operation. Multiple Bragg reflections can therefore be measured from much smaller crystals with minimal effort. Realised close to the end of this project the potential applications for the technique are discussed in Section 8.2.1.

3.5.1 In-situ Coherent X-ray Diffraction Experiments

Vacuum Chamber Setup

The unfocused setup discussed previously in Section 2.2.5 can be implemented in-situ; both for annealing and metal deposition evaporation experiments. The samples were
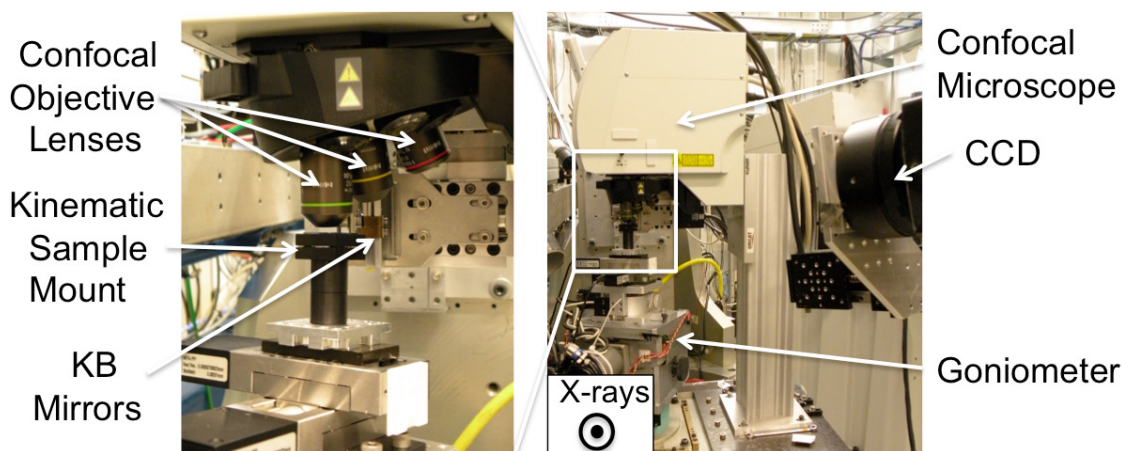
Figure 3.8: Photographs of the confocal microscope at the APS, beamline 34-ID-C, positioned above the goniometer provides live observation of the illuminated sample and allows alignment on user defined crystals

prepared on diced Silicon substrates (10x10mm) which were clamped to a ceramic heater, capable of 1000°C with tantalum clips, Figure 3.9 (b). A thermocouple was spot welded to one of the clamps for temperature calibration. The sample mount was inserted into the base of the vacuum chamber, Figure 3.9 (a), and the diffractometer moved to provide vertical (z), rotation (θ) and tilt (ϕ) translation when sealed into the vacuum chamber and fastened to the goniometer. The metal evaporator was mounted through an access port and loaded with Ni, Fe and Co sources. The sample was raised and aligned in the x-ray beam, diffraction from crystals on the sample exit the chamber through the large beryllium window shown in Figure 3.9 (b) and were recorded using the CCD detector. A crystal quartz monitor could not be mounted into the chamber, deposited layers were estimated using Dektak[7] and SEM observations of the sample cross section.

---

[7]A stylus was placed in contact with, and then dragged along the surface of the substrate. The vertical deflection measures the change in step height and can map the profile in up to three dimensions. Veeco Dektak 8 profiler, London Centre for Nanotechnology Cleanroom Facilities, 1nm minimum achievable step height.
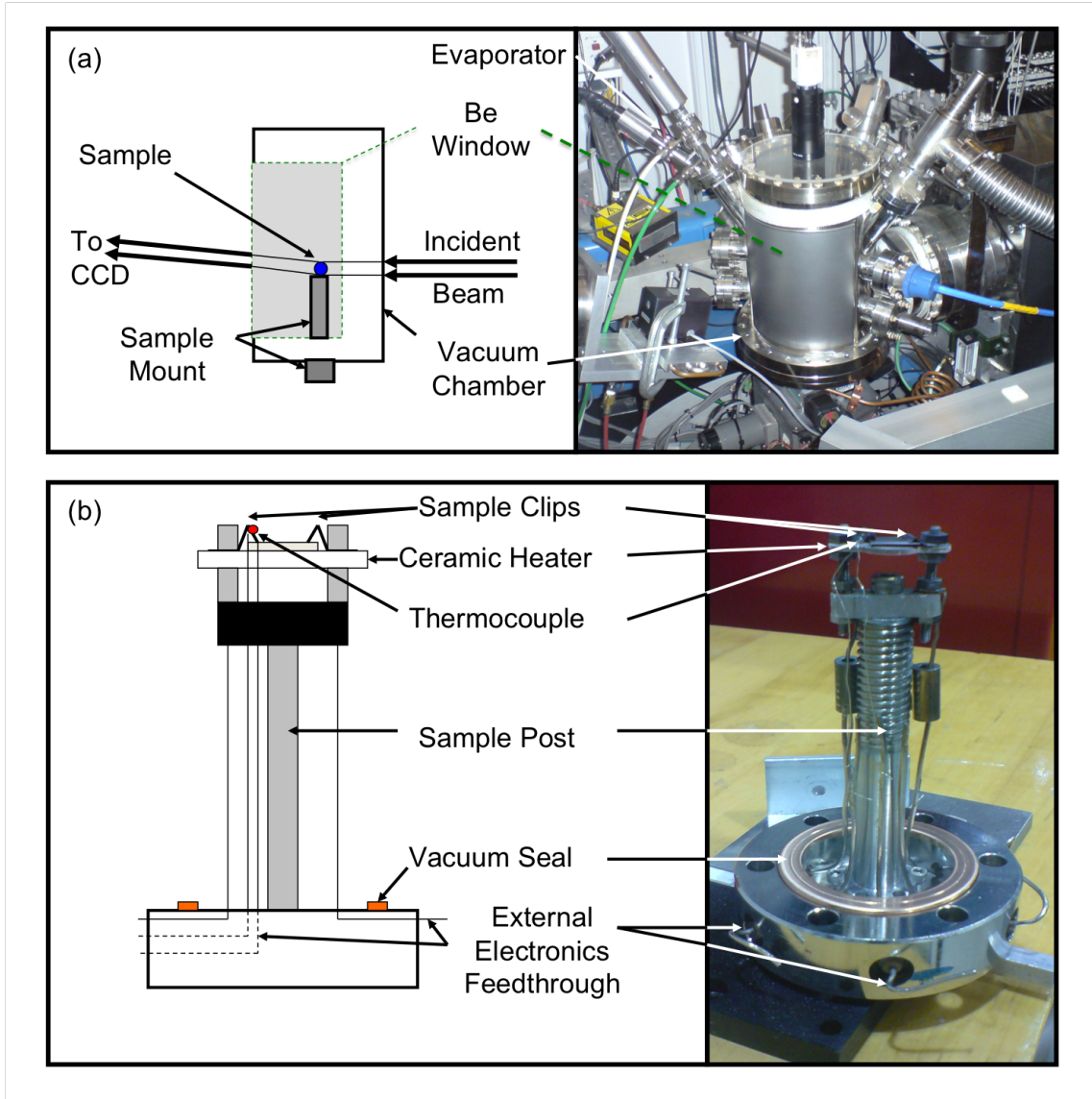
Figure 3.9: Schematic and corresponding photograph of (a) vacuum chamber set up and corresponding (b) sample mount for in-situ annealing and metal evaporation experiments at the APS, Beamline 34-ID-C

Evaporation Procedure

Before each experiment the evaporator was serviced and sources materials checked to prevent shorting. The evaporator was mounted, the vacuum chamber sample mounting procedure followed and when the chamber pressure was $\leq 1 \times 10^{-8}$mbar or lower evaporation could commence. The evaporator was water cooled during and for 15 minutes prior to the evaporation. The procedure identified in the User Manual[8] was followed, the guides for power to deposition rate proved inaccurate hence the Dektak and SEM methods discussed previously were used to estimate deposition.

The evaporation angle was $60°$ to the horizontal, hence for a rod stood on end would see deposition on the top facet and half of the a-b plane facets (3 of 6 facets). Unlocking the sample rotation circle on the diffractometer allowed a rotation through approximately 180 degrees ensuring deposition on all six a-b plane facets, consequently the top facet deposition layer was approximately twice as thick.

Evaporation Goals

The aim was to evaporate several different transition metals on to ZnO nanocrystals. Using transition metals with known solubility in ZnO anneal and observe the solid state diffusion of the deposited metal into the crystal structure using CXDI *in-situ*. The diffusion will result in a lattice parameter expansion in the deposition region, estimated in Section 1.1.6 to be resolvable with CXDI.

Assuming a uniform evaporation layer, a crystal of diameter 1μm and length 2μm, typical

---

[8]OXFORD APPLIED RESEARCH, Mini e-Beam Evaporator EGN4, http://www.oaresearch.co.uk

size and aspect ratio for those measurements made. The total surface area upon which a layer is deposited is $9.464\mu m^2$ for the asymmetric deposition (top facet and 3 a-b plane facets) and $18.928\mu m^2$ for the symmetric deposition(top facet double thickness and 6 a-b plane facets). The volume of the crystal is $6.928\mu m^3$ hence assuming maximum solubilities of Fe, Ni and Co described in Section 1.1.6, Table 3.1 demonstrates the required deposition thickness for each metal in both evaporation cases.

Table 3.1: Estimated deposited film thickness required to achieve maximum doping in ZnO with Fe, Ni and Co for both the symmetric and asymmetric deposition cases.

	Deposition Film Thickness (nm)	
	Asymmetric Case	Symmetric Case
Fe	13.7	6.8
Ni	2.2	1.1
Co	29.2	14.6

3.5.2 Summary

A detailed description of the employed CVTD synthesis method and a review of alternative synthesis routes was provided. The variation in morphology as a function of temperature was demonstrated and a level on control was achieved, the parameters outlined for a high yield of ZnO nanorods (700sccm oxygen, 45sccm Argon, 1.5grams of 10:1 zinc carbonate to carbon ratio and the substrate positioned at $150°C$). A thermal oxide layer was grown to adhere crystals to the substrates, EDS identified a gradient of Zn in the substrates due to diffusion. The high vacuum set up used for solid state diffusion experiments, evaporation procedure and required deposition thicknesses defined.

The micromanipulation method used to isolate and locate a individual ZnO crystals for combination with alternate characterisation methods was described. Subsequent advances in beamline set up that have led to routine operation in this mode of operation were discussed

Chapter 4

Phase Retrieval

4.1   Introduction

The phase retrieval process tackles a typical inverse problem, given a measurement iden-
tify what is responsible for it. In this case, given the measured intensity $I = |F(q)|^2$
from a crystal of density, $f(r)$, find the phases of complex scattered amplitude $F(q)$ lost
in the measurement so $f(r)$ can be found simply by IFT. This is an example of a gen-
eral phase problem encountered in many fields including microscopy, astronomy, protein
crystallography and optics. In crystallographic problems Millane was the first to note
that crystallographic problems were analagous to imaging problems [132]. A series of
constraints were developed to overcome ambiguities Crowther [42] proposed an efficient
computational approach to solve the problem of internal non-crystallographic symmetry
identified by Rossman and Blow [192]. Solvent Flattening [198] set the region outside of
the object to a constant value and atomicity confined the electrons to a small volume close

to the core of the atom.

Alternate methods have been studied, Maximum Entropy Methods (MEMs) employ Bayesian statistics to solve structures [24] and are utilised in many fields including; in x-ray crystallography, astronomy, medical tomography and electron holography amongst others [25,71]. MEMs isolate the global minimum and ensure the uniqueness of the solution. Baikova [12] demonstrated a MEM method applied to the phase retrieval problem in two dimensions and concluded upon increasing complexity that image reconstruction ran into the thousands of iterations. In order to improve the efficiency of the method the MEM was used to seed alternate iterative methods that will be discussed later in this chapter. The inability of the applied algorithm to reconstruct relatively simple 2D structures does not bode well for the 3D problems we encounter. Direct phase retrieval via x-ray holography using a known reference wave has also been employed [67].

Here, we limit ourselves to the imaging of finite sized non periodic objects, a method first approached in 1997 by Miao et al. [128] where vast progress has been made since. The first example of coherent x-ray diffraction imaging was a one 1D study of Silicon surfaces [155,189] and later Cu_3Au [188]. The first demonstration in 2D was made by Miao et al. [129] with a non-crystalline test object made up of an array of gold (Au) nanocrystals at 75nm resolution. Vartanyants and Robinson [156,188] identified the application of the method to map strain fields in finite crystalline samples. Vartanyants et al. [190] predicted the partial coherence effects associated with measurements of this nature and Robinson et al. [157] used CXDI around a $11\bar{1}$ Bragg peak to recover the shape of a single Au nanocrystal and confirmed the coherence effects predicted. This was soon followed by

the successful recovery of a pseudo 3D test object [131] and a 3D Au nanocrystal by Williams *et al.* [157, 211, 212] at 50nm resolution. Since then a large number of test objects and samples have been successfully recovered from both x-ray [1, 15, 79, 92, 148] and electron [68, 220] diffraction data. Those most relevant to CXDI of nanocrystals in the Bragg geometry are detailed. Favre-Nicolin *et al.* [62] reconstructed the shape of a single Silicon (100nm diameter) nanowire with 15nm resolution and discussed the effects of the beam interacting with the sample, the observation of wires 'breaking' whilst in the beam implies radiation damage is a serious limitation. Chamard *et al.* [31] identified, via simulation, the reciprocal space features exhibited by nanowires with stacking faults. Minkevich *et al.* [134] studied arrays of silicon lines and concluded, by inspection with finite element models, the origins of reciprocal space features attributed to large internal strains.

In the transmission geometry reconstruction of individual Au nanocrystals (sub 100nm) has been achieved by Schroer *et al.* [166] at 5nm resolution and Ag nanocubes ($\sim$100nm) at 3nm resolution by Takahashi *et al.* [176]. At present obtaining sufficient intensity at high spatial frequencies limits the resolution and is dependent on the photon flux delivered to the scattering volume. Bismuth (Bi) buried in Silicon was studied by Song et al. [170], observation of the difference between reconstructions above and below the Bi M_5 absorption edge. The first example of *in-situ* CXDI in the forward scattering geometry was demonstrated by Takahashi *et al.* [177], although potential extensions to the phasing algorithms were not discussed. We will demonstrate measurements of this nature for CXDI in the Bragg geometry and discuss the implications for the phasing operation, see Chapter 6.

Alternative applications of coherent diffraction methods include; Biological imaging, Shapiro *et al.* [168] used soft x-ray diffraction microscopy to image yeast cells to 30nm resolution. Nishino et al. imaged a dried human chromosome [141] and Song *et al.* imaged an unstained virus [171]. Direct Holographic Inversion of a magnetised film [52] overcomes the central problem of phase retrieval by using a nanoscale pinhole reference aperture[1] close to the sample which phases the interference pattern, He et al. [80] have also demonstrated this method. In these cases iterative algorithms can be used to further enhance the spatial resolution of the image.

So far, only the recovery of finite objects has been discussed, it is possible to measure extended objects using a combination of CXDI and microscopy methods called 'ptychography' [61, 158]. The basis for this method is measuring multiple diffraction patterns from overlapping regions on a sample, the subsequent overlap provides a constraint strong enough to reconstruct the illuminated region of the sample. Here the successful reconstruction of a Zone Plate was demonstrated by Thibault et al. [179]

The CXDI technique is also a strong candidate for future X-ray Free-Electron Lasers (XFELs), high intensity coherent pulses of femtosecond duration allow single shot imaging, see Appendix A.6.

4.2   Iterative Approach to the Phase Problem

An iterative mathematical approach is employed to solve our 'Phase problem' and gives rise to its name 'lensless imaging'. Moving from direct space to reciprocal space and back

---

[1]The size of the reference aperture/source defines the resolution.

again, *a priori* information about the crystal is used to constrain each iteration until a set of amplitudes and phases are found which are consistent with the measured intensity around a Bragg peak. In this chapter the methods used to solve the phase problem will be introduced and a critical analysis of the phasing method employed made in Chapter 5.

The successful retrieval of phase for a measured diffraction pattern is dependent on overcoming several experimental and analytical hurdles; specifically sampling the diffraction pattern sufficiently to retrieve all the information in the signal and the broader problem of finding unique solutions and identifying ambiguous solutions (enantiomorphs).

4.2.1 Equation Counting

A discretely sampled continuous diffraction pattern represent scattering from a direct space function $f(x, y, z)$ which when complex has $2N_1N_2N_3$ unknowns, where x, y, z are discrete coordinates and N_1, N_2, N_3 the extents of the coordinate space in pixel dimensions. To solve for these unknowns a matching number of known equations are required which corresponds to the number of sampled points in reciprocal space. The modulus of inverse Discrete Fourier Transform (DFT) is computed as

$$|F(q_x, q_y, q_z)| = |\sum_{x,y,z} f(x, y, z) exp(\frac{2\pi i}{N}(q_x x, q_y y, q_z z))| \tag{4.1}$$

where q_x, q_y, q_z define the corresponding coordinates in reciprocal space and yields a total of $N_1N_2N_3$ equations. Hence to solve the problem we need to sample reciprocal space by a factor of $t \geq 2$ to ensure there are $\geq 2N_1N_2N_3$ equations.

4.2.2   Oversampling

The ability of the phase retrieval method to find a solution depends on the sampling ratio; the rate at which the intensity is sampled. A signal or function is bandwidth limited if it contains no energy at frequencies higher than a defined bandwidth. Hence, it is constrained in terms of how rapidly it changes in time and consequently how much detail it can convey inbetween discrete instances of time. The sampling theorem [167] states that uniformly spaced discrete samples are a complete representation of the signal if this bandwidth is less than half the sampling rate. For example, a signal with a maximum frequency f_{max} needs to be sampled at a frequency of at least $2f_{max}$, the Nyquist critical frequency, to be resolved. In the case of x-ray diffraction measurements Sayre [163] observed that if the square modulus of the signal was measured, the intensity from equation 2.12, the sampling rate required is oversampled by a factor of two, i.e $(4f_{max})$. The oversampling ratio is defined in direct space in each dimension as

$$\sigma = \frac{Array\ Size}{Crystal\ Size} \tag{4.2}$$

With this in mind, all data is measured with an oversampling ratio of approximately 3 to ensure the data can be solved mathematically and corresponds to 3 pixels per fringe.

It is important to note the oversampling requirement is controversial in 3-dimensional problems; Miao et al. [130] suggest the limit does not apply to each dimension individually but to the entire measured volume, hence the object fills a volume half the volume of the array. Millane suggests [132] σ=2 in each dimensions and the corresponding support

$1/2^3(1/8^{th})$ the total volume measured.

4.2.3 Aliasing

The phenomenon of 'Aliasing' arises when discretely sampling a continuous function that is not bandwidth limited to less than the Nyquist critical frequency. In this case all of the power spectral density that lies outside of the frequency range ($-f_c < f < f_c$) is spuriously moved into that range and would be expected in the Miao case. There are two ways to overcome Aliasing; i) sample at a sufficient rate to obtain two points per period of the highest frequency present, ii) identify the natural bandwidth of the signal or else enforce a known limit by analog filtering of the continuous signal before it is sampled.

In our case by padding the diffracted intensity grid with zeroes, higher frequencies which would overlap between unit cells are given room to be reconstructed and any overlap significantly reduced.[2]

4.2.4 Uniqueness

It was Bruck & Sodin [26] who first identified uniqueness in multiple dimensional phase retrieval problems and later discussed fully by Bates [17]. The constraints imposed must be sufficiently tight to ensure there is no function g(r) other than f(r) which satisfies $|G(q)|^2 = I = |F(q)|^2$, where $\mathcal{F}\{g(r)\} = G(q)$, i.e the solution $f(r)$ is unique. The discrete nature of the measurement leads to ambiguous solutions. A problem with N knowns

---

[2]High frequency amplitudes tend to overlap when two parallel facets lie parallel to the sides of the sampled grid. A rotation of the crystal away from this condition will reduce overlap and is fulfilled by interpolating the measured intensities onto a rotated grid

(amplitudes) and N unknowns (phases) potentially has many solutions, the application of *a priori* knowledge provides sufficient constraints for the algorithms to identify the correct solution. This is not always satisfied. One can envisage a solution space whereby once an algorithm finds a local minima, where some of the constraints are met but others are not. The solution remains there as the changes its constraints impose upon it are insufficient to find an alternate solution and this is the definition of 'stagnation'. The global minima is defined as the actual solution where all constraints are met and can never be achieved in the presence of noise. At present distinguishing between local minima and the global minimum is difficult and depends on the phase retrieval algorithms discussed in Section 4.3.

Barakat and Newsam [14] identified the uniqueness of the solution is not guaranteed if the measured intensity is factorisable. Although prevalent in one dimensional problems, Barakat and Newsam concluded multiple non-equivalent solutions in phase retrieval problems in more than one dimension are rare. They exhibit only when the convolution [66] of two or more non centrosymmetric intensity distributions is equivalent[3]. Thus we would expect to find a unique solution, however, limited prior knowledge and the presence of noise can increase the likelihood of multiple solutions and can exhibit as stagnation in the algorithm operation.

Once overcome the problem of multiple ambiguous solutions of a direct space function ($f(r)$) remains, whereby rather than finding a single solution, a set of direct space solutions are obtained where the Fourier Moduli are identical. The equivalent cases include; $f(r+r_0)$

---

[3] Two direct space functions g(r) and h(r) when convolved produce the measured intensity, $|G(q)H(q)|^2 = |F(q)|^2$.

a shift in the position of the diffracting object, *f*(-r)* the complex conjugate of the electron density (enantiomorphs) and $e^{i\phi}f(r)$ a phase factor applicable to the entire function.

There are several solutions presented in the literature for overcoming the uniqueness problem and the existence of ambiguities. Random starts provide an insight into the reproducibility of the reconstructions and identify uniqueness [35,168] through the identification of ambiguous solutions. The error between the equivalent solutions provide a measure of the resolution of the function in the form of a Phase Retrieval Transfer Function (PRTF).

$$PRTF = \frac{|\langle A_{calc}e^{i\alpha}\rangle|^2}{\sqrt{I_{meas}}} \tag{4.3}$$

where A_{calc} are the calculated reciprocal space amplitudes and α their corresponding phases. Solutions must be averaged correctly by accounting for ambiguous solutions to identify which spatial frequencies are reconstructed consistently.

4.3   Phase Retrieval Algorithms

The algorithms are introduced using a theoretical language described by Levi and Stark [106] each iteration is described as a projection in a Hilbert space ($\mathcal{H}$). Defining constraints in both direct space and reciprocal space as sets, the algorithms proceed to find solutions that intersect these sets by projecting the current best estimate onto each set and measuring the distance between them with an error metric. A solution has been achieved when it belongs to all sets simultaneously. For example, a solution set which describes all
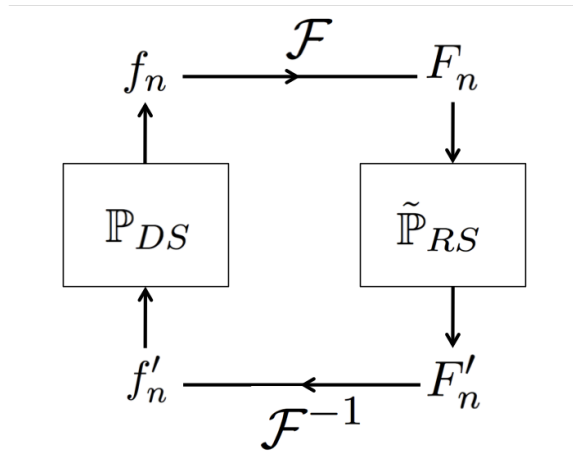
Figure 4.1: Iteration scheme for basic algorithm

objects that are constrained within a given volume in direct space (finite crystal approximation) and the modulus set, all possible objects with a given diffraction pattern. We define the N point discrete object $\rho_n(r)$ as a N dimensional vector $f_n(r)$ in $\mathcal{H}$. The object can be described by a linear transformation in any n-dimensional orthogonal bases. In our case a Fourier Transform describes the transformation between bases where constraint sets are implemented. Parseval's theorem states the distance between two points in an n-dimensional space is independent of the Fourier transformation of the bases.

We define a projector $\mathbb{P}$ as an operator that takes to the closest point of a set from the current point . A repetition of the same projection is equal to one projection alone ($\mathbb{P}^2 = \mathbb{P}$); its eigenvalues are therefore $\lambda = 0, 1$. Figure 4.1 defines the basic iteration scheme and the projections employed in both direct space ($\mathbb{P}_{DS}$) and reciprocal space ($\tilde{\mathbb{P}}_{RS}$).

The basic algorithm in Figure 4.1 is therefore formulated by two projections.

Direct Space Projection:

$$\mathbb{P}_{DS} f'_n = f_{n+1}$$

Reciprocal Space Projection:

$$\mathbb{P}_{RS} f_n = \mathcal{F} \, \tilde{\mathbb{P}}_{RS} F_n \, \mathcal{F}^{-1} = f'_n \qquad (4.4)$$

The $(n+1)^{th}$ iterate is therefore described as,

$$f_{n+1} = \mathbb{P}_{RS} \mathbb{P}_{DS} f_n$$

The reflection projection applies an additional second repetition projection, effectively reflecting it about a constraint set and is defined,

$$\mathbb{R} = I + 2[\mathbb{P} - I] = 2\mathbb{P} - I \qquad (4.5)$$

4.3.1 Reciprocal Space Projections

The measured intensity, the common reciprocal space constraint sees the calculated amplitudes replaced by the measured amplitudes.

$$F'_n = \frac{F_n}{|F_n|} |\sqrt{I_{meas}}|$$

The appreciation of a threshold variable where this constraint is applied for all those pixels

registering x scattered photons significantly improved the ability of the algorithms to avoid stagnation caused by fitting the noise in the measured amplitudes.

The threshold provides a lower bound, little has been tested regarding the associated error on the measured intensities. The statistical error ($\sqrt{no.of photons}$ [116]) for each pixel can be applied to relax the modulus constraint in the following form.

$$f_{n+1}(r) = \mathcal{F}^{-1} \begin{cases} \frac{F_n(r)}{|F_n(r)|+\epsilon}(\sqrt{I_0} + \sigma_{\sqrt{I_0}}) & if \quad F_n > \left[\sqrt{I_0} + \sigma_{\sqrt{I_0}}\right] \\ \\ \frac{F_n(r)}{|F_n(r)|+\epsilon}(\sqrt{I_0} - \sigma_{\sqrt{I_0}}) & if \quad F_n < \left[\sqrt{I_0} - \sigma_{\sqrt{I_0}}\right] \\ \\ F_n & otherwise \end{cases} \qquad (4.6)$$

where I_0 is the measured intensity, $\sigma_{\sqrt{I_0}}$ the error on the measured amplitudes and ϵ a small constant. A detailed analysis of this constraint has not been completed but the potential implications are discussed later in Section 5.3.

4.3.2   Direct Space Projections

A large variety of direct space projections have been formulated based on *a priori* knowledge of the crystal. The algorithms developed to date built on work by Gerchberg and Saxton [70] in electron microscopy. Fienup developed an x-ray compatible algorithm called Error Reduction (ER) [63] and later a Hybrid-Input-Output algorithm (HIO) [64] which has proved very successful. Extensions and variations of these methods will be introduced.

4.3.3 Gerchberg-Saxton Algorithm

The motivation of Gerchberg and Saxton (GS) was to find a method whereby the phase of a wavefunction may be recovered from simultaneous measurements in the image and diffraction planes [70]. It was proposed a similar method could be used in x-ray crystallography, however the technical difficulties involved in making an x-ray measurement in the image plane limited its application to electron microscopy.

In the GS algorithm there are two known constraints: (i) magnitude of the amplitudes in the image plane, (ii) magnitude of the amplitudes in the diffraction plane.

The algorithm operation is represented in the flow diagram in Figure 4.2, the algorithm iterates between direct and reciprocal space using the amplitudes in each space as the constraint for estimating the unknown phases from a random starting position. The feedback loop is instigated by a measure of the quality of the result and raises the question how does one test this?

The simple observation of the FFT of the result compared to the experimental provides a qualitative measure. Quantitatively an error metric E_{nmse}^2 is defined as the normalised mean squared difference between the reconstructed (A_{calc}) and measured amplitudes (A_{meas}) in reciprocal space [66].

$$E_{nmse}^2 = \frac{\sum |A_{calc}|^2 - |A_{meas}|^2}{\sum |A_{meas}|^2} \qquad (4.7)$$

Hence when the direct space reconstructed amplitudes match the experimental amplitudes $E_{nmse}^2 = 0$ the problem is solved.
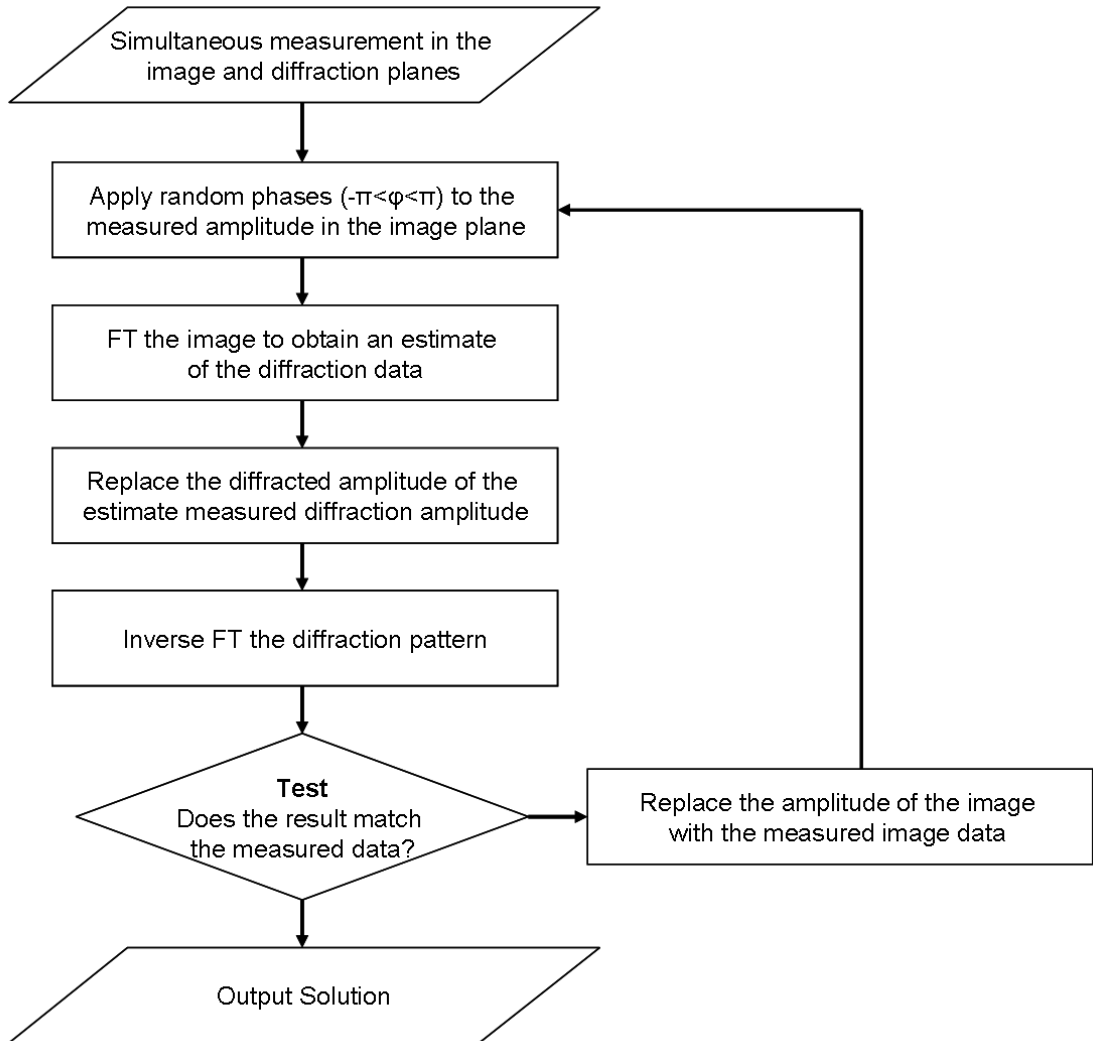
Figure 4.2: Flowchart of the Gerchberg Saxton(GS) algorithm operation

4.3.4 Error-Reduction (ER) Algorithm

Fienup suggested an extension to the GS algorithm in 1978 [63] whereby the intensity measurement is only made in reciprocal space. He proposed to use real-space constraints in place of the real-space intensity measurement. The most common constraints being:

1. Positivity - The real-space density should not be negative, which in the case of a perfect single crystal is physically expected.

$$f_{n+1}(r) = \mathbb{P}_{S+} f_n(r) \begin{cases} Re\{f_n(r)\} & if \ \ r \in S \ \ \& \ \ if \ \ Re\{f_n(r)\} > 0 \\ \\ 0 & otherwise \end{cases} \quad (4.8)$$

2. Finite support - The real-space density occupies a confined region within the volume of real-space measured by the diffraction data.

$$f_{n+1}(r) = \mathbb{P}_S f_n(r) = \begin{cases} f_n(r) & if \ \ r \in S \\ \\ 0 & if \ \ r \notin S \end{cases} \quad (4.9)$$

here, any amplitude or phase outside of the support region (S) is set to zero, as practically it cannot exist, the result is an estimate for the real space density $f_{n+1}(r)$.

Initially it was thought that both constraints were required, however Fienup later showed [64] using a sufficiently tight support constraint the complex problem is no harder. Allied to the original GS algorithm (Section 4.3.3), the reciprocal space constraint is the modulus set, $\mathbb{P}_m$.

The algorithm proceeds with the FT on an estimate of the real space density $f_n(r)$ to obtain $F_n(q)$. A copy of the chosen support is the best estimate of the diffracting object, the FFT of which is used as the starting point. The following steps are repeated; (i) Replace the magnitude of the reconstructed diffracted amplitude by the measured diffracted amplitudes $F'_n(q)$, (ii) IFT the result and (iii) project the solution onto the support set ($\mathbb{P}_S$) by setting all data outside of the support to zero. Test the quality of the reconstruction and repeat the process until a solution is found where the current iterate is the best estimate.

The algorithm operation is defined using the projection of the modulus set described in Equation (4.4):

$$f_{n+1}(r) = \mathbb{P}_S \mathbb{P}_M f_n(r) \tag{4.10}$$

The ER algorithm itself converges very slowly, once all of the amplitudes and phases lie within the support the algorithm will stagnate. The algorithm has no way of distinguishing between all solutions which contain phases and amplitude within the support, highlighting the problem of finding a unique solution in this case, and further compounded when the support is large relative to the object.

4.3.5   Hybrid Input Output (HIO) Algorithm

The slow convergence and stagnation tendency of the ER algorithm led to the formulation of alternate algorithms. One class of these is the Input Output algorithms, again developed by Fienup [63]; here the basic process of ER is maintained but the constraints are different,

the input is no longer the current best estimate of the dataset, it is in fact the driving function for the next output (derived from a combination of the current and previous iteration). This produces a large amount of variation in the following input, aiding the algorithm to avoid stagnation although it remains susceptible to it.

The constraint again applies outside the support; the current iterate $f_n(r)$ is used to drive the algorithm through combination with the current iterate after projection onto the modulus set.

$$f_{n+1}(r) = \mathbb{P}_S\mathbb{P}_M f_n(r) = \begin{cases} \mathbb{P}_M f'_n(r) & if \ \ r \in S \\ \\ f_n(r) - \beta\mathbb{P}_M f'_n(r) & if \ \ r \notin S \end{cases} \tag{4.11}$$

where β is a variable, we employ β=0.9 for all phasing operations. β values in the range 0.8-0.95 are common, any lower and the changes made are insufficient to move out of local minima in solution space and stagnation results. It is clear that, when $\beta = 1$ and the next iterate begins to replicate the current iterate (i.e stagnates), the algorithms operation approaches the ER algorithms regime; the amplitudes and phases outside of the support will be set to zero, see Equation 4.9. Beyond a value of 1, amplitudes and phases outside of the support will oscillate between positive and negative values forcing the algorithm further away from a solution.

4.3.6 Alternate Algorithms and Extensions

To date variations on the existing ER and HIO algorithms have been used as iterative approaches to the phase problem in the form of Millanes HIO [133] and Solvent Flipping (SF) [2]. Alternative algorithms include Difference Map (DM) [53], Averaged Successive Reflections (ASR) [19], Hybrid Projection Reflection (HPR) [18] and Relaxed Averaged Alternating Reflectors (RAAR) algorithm [115]. These algorithms are discussed fully by Marchesini [122] and after extensive testing he concludes HIO is the most effective algorithm at finding a solution and gradient based methods such as ER or SF can be used to polish up the solution. The operation of each of the algorithms will be introduced.

Solvent Flipping Solvent Flipping (Charge Flipping) is analogous to the ER algorithm, instead of setting the density outside of the support to zero it is forced negative.

$$\mathbb{P}_S\mathbb{P}_M f_n(r) \begin{cases} \mathbb{P}_M f_n(r) & if \ \ r \in S \\ \\ -\mathbb{P}_M f_n(r) & if \ \ r \notin S \end{cases} \tag{4.12}$$

The algorithm can be simplified using reflector notation, *see equation 4.5*, to

$$f_{n+1} = \mathbb{R}_S\mathbb{P}_M f_n \tag{4.13}$$

The SF algorithm is a gradient search with a larger step size compared to ER, the result is a faster convergence, however its application is only useful when refining a solution obtained using HIO. The difference between solutions produced with SF/ER after several

iterations of HIO is negligible.

Difference Map   The difference map method exploits the difference between elementary projections ($\mathbb{P}_M$ and $\mathbb{P}_S$) and converges to a fixed point at which both constraint sets are satisfied.

$$Df_n = [I + \Delta] f_n \tag{4.14}$$

The error metric is defined as

$$\Delta = [\beta\mathbb{P}_S\left((1+\gamma_S)\mathbb{P}_M - \gamma_S I\right) - \beta\mathbb{P}_M\left((1+\gamma_M)\mathbb{P}_S - \gamma_M I\right)] f_n \tag{4.15}$$

When the parameters are set to $\gamma_M = \beta^{-1}$ and $\gamma_S = -\beta^{-1}$, equation 4.14 can be simplified

$$Df_n = [1 + 2\mathbb{P}_S\mathbb{P}_M - \mathbb{P}_S - \beta\mathbb{P}_M] f_n \tag{4.16}$$

Rewriting the HIO algorithm defined in equation 4.11 as a pure projection operation and simplifying reproduces equation 4.16 and proves they in fact coincide.

$$f_{n+1} = \mathbb{P}_S\mathbb{P}_M f_n + [(1 - \mathbb{P}_S)(1 - \beta\mathbb{P}_M)] f_n \tag{4.17}$$

$$= [1 + 2\mathbb{P}_S\mathbb{P}_M - \mathbb{P}_S - \beta\mathbb{P}_M] f_n$$

A great deal of analysis was performed by Garth Williams [213] prior to this project identifying the best parameters for the DM algorithm. The difficulties encountered and the findings of Marchesini prompted focus on the HIO and variants (i.e additional constraints) discussed in Section 4.3.7.

Alternate Algorithms The remaining three algorithms are defined using projection notation.

Average Successive Reflections

$$f_{n+1} = \frac{1}{2}(\mathbb{R}_S\mathbb{R}_M + I)f_n \tag{4.18}$$

Hybrid Projection Reflections

$$f_{n+1} = \frac{1}{2}\left[\mathbb{R}_S(\mathbb{R}_M + (\beta - 1)\mathbb{P}_M) + I + (1 - \beta)\mathbb{P}_M\right] f_n \tag{4.19}$$

Relaxed Average Alternating Reflectors

$$f_{n+1} = \left[\frac{1}{2}\beta(\mathbb{R}_S\mathbb{R}_M + I) + (1 - \beta)\mathbb{P}_M\right] f_n \tag{4.20}$$

It can be shown that HIO also coincides with ASR, HPR and RAAR when $\beta = 1$ as

demonstrated previously with DM.

4.3.7 Algorithm Extensions

The basis for phasing in this work is built on that developed by Robinson et al. [147, 149, 213] and uses Fienups HIO and ER with additional phase constraints dubbed Phase Constrained HIO (PC-HIO) and Phase Only ER (PO-ER) introduced by Ross Harder [79].

PC-HIO sets maximum and minimum thresholds for the phase that the algorithm can assign in direct space. The method is often applied to crystals with relatively small phase variations and prevents the phases from rotating randomly. Additionally it prevents the formation of vortices as the phase is not allowed to form a 2π phase wrap. The presence of vortices in reconstructions can lead to impractical features in reconstructions and will be discussed later. Equation 4.11 is altered with an additional set of Phase constraints on the support set, we define the projection as $P_{s\phi}$ and rewrite the equation

$$
\mathbb{P}_{S\phi}\mathbb{P}_m f_n(r) = \begin{cases} \mathbb{P}_M f'_n(r) & if \quad r \in S \quad \cap \phi_r > \phi_{min} \quad \cap \phi_r < \phi_{max} \\[2ex] f_n(r) - \beta\mathbb{P}_M f'_n(r) & if \quad r \notin S \quad \cup \phi_r > \phi_{min} \quad \cup \phi_r < \phi_{max} \end{cases} \tag{4.21}
$$

PO-ER is the ER algorithm with an additional constraint; amplitude can exist outside the support region if its phase is zero. Practically the amplitude manifests as noise in the data and has proven advantageous in refining reconstructions whilst quenching vortices. Equation 4.9 becomes

$$\mathbb{P}_{S\phi}\mathbb{P}_M f_n(r) = \begin{cases} \mathbb{P}_M f_n(r) & if \quad r \in S \\ \pm |\mathbb{P}_M f_n(r)| & if \quad r \notin S \end{cases} \tag{4.22}$$

here the amplitudes are rotated to their nearest axis and $\pm$ defines the sign of the amplitude imposed by the phase range, i.e (-) in the range $(\frac{1}{2}\pi > \phi < \frac{3}{2}\pi)$, (+) in the range $(\frac{1}{2}\pi < \phi > \frac{3}{2}\pi)$.

Three methods that were not analysed by Marchesini are the voting method [65], guided HIO (gHIO) [37] and Shrinkwrap (SW) [123]. They focus on varying the constraints as opposed to the application of these constraints like those in PC-HIO and PO-ER. Both methods employ the normal HIO and ER algorithms. The voting method and gHIO attempt to maintain features from multiple random starts to seed further phasing operations (generations) until the solutions are equivalent. SW constrains the support around the current iterate after each phasing operation until the support and the object are consistent with each other. These methods were developed to overcome the uniqueness problem, we combine their best attributes with the variants of HIO and ER to build confidence in our results. In just 30-50 iterations of HIO followed by 10-20 iterations of ER or their variants a solution is reached. Stagnation, solution uniqueness and ambiguity are the key problems faced by the phase retrieval algorithms for finite crystal phase retrieval problems.

Fienup and Wackerman [65] observed from multiple starting points stripes were found to be prevalent in 2D reconstructions; different random starting points resulted in different orientations and frequencies of stripes. Originating from phase singularities (vortices) in

reciprocal space, vortices present, in pairs, centrosymmetrically in the image and with opposite phase wrapping, of total 2πn. Two methods; the 'voting method' and the 'patching method' are discussed. In the voting method three random reconstructions are made, of the two that correlate the most an average or combination is taken and used to drive the next fit. The patching method is an extension of the voting method, the stripes extend beyond the support and are used to locate the vortices and subsequently patch them out. In 3D vortices present as loops which are much rarer than 2D cases [213], the proposed solution is to reduce the background to prevent the algorithm assigning phase values large enough for vortices to form. A valid approach that neglects the scenario whereby large phase variations in a crystal are expected, distinguishing between an anomalous vortex and physical phase wrap in this case becomes problematic. Harder [78] found that a correlation between direct space vortices and the observed error metric minimum during HIO.

Guided HIO has been developed by Chen et al. [37] and builds on the principle of maintaining features from multiple solutions. Running the phasing algorithm through x number of random starting points, the best solution is sought and combined individually with all of the other solutions, these solutions then drive the next generation of solutions; the process is then repeated until the algorithm converges. A version of this algorithm was written for the Bragg scattering geometry, conclusions drawn were; the algorithm always tends towards the initial solution and suffers similar stagnation problems as HIO and ER methods. A useful method for the determination of ambiguous solutions via cross correlation, discussed further in Section 5.2.2.

Marchesini et al. [123] developed the SW algorithm for which no *a priori* knowledge is required, the support is built from the autocorrelation of the data and tightened until the algorithm converges. Briefly, a Gaussian is convolved in each dimension with the reconstructed object. This slowly reduces the size of the support used to constrain the result until it converges to the correct solution. It has to overcome the autocorrelation function as a potential solution and must converge when the solution has been found, if the support encroaches on the reconstruction an incorrect solution will result.

In order to identify ambiguous solutions we must overcome f($\pm$r-r$_0$)e$^{i\phi}$ solutions. The phase factor offset is required before the alignment correction and enantiomorph identification is completed.

4.3.8 Aligning Solutions

In order to align two reconstructions *g(x,y,z)* and *h(x,y,z)* after the phase offset correction has been implemented, we raster one solution relative to another by a shift $r_s(x_s, y_s, z_s)$ and maximise

$$\max_{r_s \ \in \ r_{supp}} \ \sum_{i \in N} g_i(r_s)h_i \tag{4.23}$$

where r$_{supp}$ defined the shift based on the dimensions of the support as the majority of amplitude is found here and N defines the number of voxels in the array. This is still computationally demanding and in complex problems can be applied to either the amplitudes or the phases or both simultaneously. If the average phase offset is not employed here in

rare cases the complex method will result in a misalignment.

In order to speed the operation up a cross correlation is employed which utilises a convolution to aid the computation. The only difference is the complex conjugate of one function is convolved with the other.

$$g * h = g^* \otimes h \tag{4.24}$$

we rewrite this according to the convolution theorem, eqns 2.3.

$$\mathcal{F}(g^* \otimes h) = \mathcal{F}\{g^*\} \, \mathcal{F}\{h\} \tag{4.25}$$

and calculate for a discretely sampled dataset over all voxels.

$$g * h = \sum_{i \in N} g_i^* h i \tag{4.26}$$

The cross correlation method is demonstrated in Figure 4.3. Combination of their Fourier Transforms provide a correlation map from which the required shift to map one image onto the other is extracted from the peak relative to the origin, shown on the right of Figure 4.3 by a wireframe representation of $g(x,y,z)$ now superimposed onto $h(x,y,z)$.
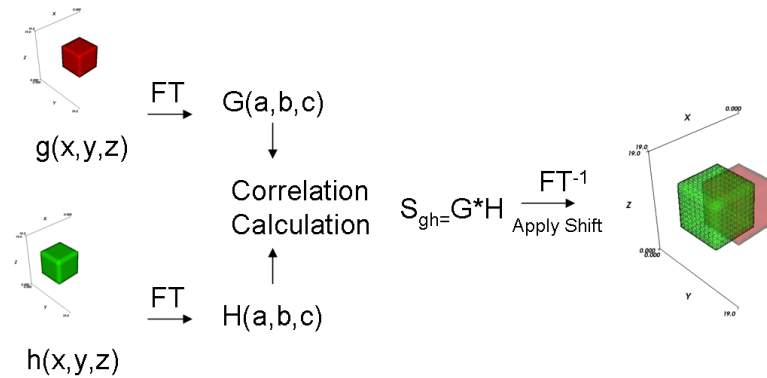
Figure 4.3: Convolution cross correlation method, two objects ($f(x,y,z)$ and $g(x,y,z)$) superimposed by the peak in the correlation map produced from the convolution of one object and the complex conjugate of the other, $\mathcal{F}^{-1}(\text{G*H})$

4.3.9 Enantiomorph Identification

A function $g(x,y,z)$ is aligned to a reference function $h(x,y,z)$ to produce, $g(x_1,y_1,z_1)$, it and its complex conjugate $g^*(x_1,y_1,z_1)$ are combined with the reference function according to the summation in equation 4.23. The maximum of the two identifies the solution which best represents the reference function and thus, if an enantiomorph has been identified.

A direct space error metric (E^2_{direct}) can now be applied to compare the solutions.

$$E^2_{direct} = \frac{\sum |\rho_a - \rho_b|^2}{\sum |A^{meas}|^2} \tag{4.27}$$

Again a summation over all voxels and equal to zero when in perfect agreement, can only be applied when ambiguous solutions have been identified and corrected for.

4.3.10 Phase Factor Offset

Fienup described a method to calculate the phase offset between two datasets using error metric minimization [66]. All solutions, be they twins or shifts should produce error metrics equal to zero. Building on the cross correlation method, whereby a maximisation of the cross correlation corresponds a minimised error metric between two images. The required phase offset is obtained by minimising the partial derivative of the error metric with respect to the associated phase factor and solving for it.

4.4 Summary

The algorithms used to solve the 'Phase problem' have been introduced in the favoured projection notation. Extensions to the algorithms employed by Robinson *et al.* [78,79,147, 149,213] prior to and during this project were introduced. The ambiguities of the found solutions and approaches towards their identification highlighted. The robustness of the algorithms can now be tested, correct average solutions generated and estimates from the PRTF made. An example of the implementation of the phasing procedure described and the constraint sets employed to successfully retrieve the lost phases for a diffraction pattern from a non-periodic finite crystal will be outlined in the next chapter.

The modulus constraint was limited and does not consider the error present in the measurement. The intensity measured in a Charge-Coupled Device detector is converted to Analog Digital Units (ADUs)[4] and does not directly translate to photon counts. We as-

---

[4]The voltage generated from the charge created by the absorption of a photon in a pixel is converted via a digital circuit into Analog Digital Units (ADU), the number is directly proportional to the voltage

sume approximately one photon is equal to 150ADU for our CCD detector (see Section

5.2.1 for determination of this quantity). The ADU count per photon varies poisson like,

hence the variance of each intensity measurement in photons (I_{ph}) is

$$\sigma_I(ph) = ((I(ADU))/150)^{1/2} \tag{4.28}$$

Thus the variance per pixel in ADU ($\sigma_I(ADU)$) can be formulated as

$$\sigma_I(ADU) = 150\sigma_I(ph) \tag{4.29}$$

The error in the constraint can be implemented using equation 4.6.

---

generated. In the CXDI case the photons have a very small bandwidth hence their generated voltage is approximately identical per photon within statistical errors.

Chapter 5

Phase Retrieval Implementation

A description of the data treament steps from the collection on the experiment through
to the phase retrieved reconstruction will be detailed in this chapter. The computational
framework will be described and a measured dataset worked through for illustration. The
constraints applied will be introduced and different phasing approaches attempted dis-
cussed.

5.1   Data Preparation

5.1.1   Computational Framework and Data Conversion

The Charge-Coupled Device (CCD) detector is read off into Winview data acquisition
software (Princeton, Roper Scientific[1]) and outputs files in SPE format (ASCII text file).
Data manipulation and analysis programming capabilities are being constantly improved

---

[1]http://www.princetoninstruments.com/

upon, hence only a brief outline of the current data treatment method will follow.

The SPE files are converted into the Sp4Array() file format introduced by Pitney [149]. A set of C-program libraries used to manipulate Sp4Arrays were developed and improved upon by Williams [213] and Pfeifer [147]. These C-program libraries were compiled for use in a python environment using a Simplified Wrapper and Interface Generator (SWIG)[2] by Harder [79]. For 3-dimensional visualisation the open source Visualization ToolKit (VTK)[3] combined with the MayaVi Data Visualizer[4] are used. The Enthought Python Distribution (EPD) has MayaVi built in and provides a maintained cross platform compatible base from which to build the phasing programs[5].

The Fourier Transform (FT) operation identified in eqn. 2.12 is used to move from the time domain to the frequency domain and vice versa. For a discretely sampled continuous function, such as the diffraction surrounding a Bragg reflection, a discrete FT is used. In practice it is computed efficiently using a Fast Fourier Transform (FFT) [150] and in our case uses the Fastest Fourier Transform in the West (FFT-W) source code[6].

For the phasing process to be successful several data preparation steps are undertaken. Firstly, the data is centered in the array, the symmetry of the FFT requires this step. Secondly, the data can be binned within reason to save time during data processing and can be used to improve statistics but is limited by the required oversampling ratio, see Section 4.2.2. Finally, spurious intensity in the detector unrelated to the measured crystal is identified and removed.

---

[2]http://www.swig.org
[3]http://www.vtk.org
[4]http://mayavi.sourceforge.net/
[5]http://www.enthought.com/products/epd.php
[6]www.fftw.org/

5.1.2 Centering

The FFT is a mathematical translation to reciprocal space units. Those points in the center of the array are moved to the edge and those those at edge move to the center, this is called 'wrapping'. If the data is not placed in the center of the array unpractical asymmetry is introduced into the data and leads to a gradient in the phase of the reconstructed image, this gradient can be used to identify if the data is centered correctly. By observing the autocorrelation function [150] (FFT of the measured intensity) of the data as a function of position the center is identified. The program 'dataCenter-5x5.py' maps the autocorrelation function by removing 2-dimensional slices of data in each dimension through the central point, and repeats the operation for shifts in the data's position of ± 2 in each dimension relative to the center. The ouput of the x-y, x-z and z-y 2D cross sections allows the required shift for a dataset to be identified quickly. In Figure 5.1, a region of flat phase can be seen at a (-1 in z, -2 in y) from the center of *(a)*, shifting the flat phase region by the shifts defined by the axes lead to the centered result in *(b)*. The region of flat phase is not always obvious. As reciprocal space is discretely sampled the actual center of reciprocal space can lie anywhere in the 3D space a single voxel encloses. Slight gradients are inevitable but minimised using this method. The gradients of large shifts (i.e ± 2) are larger and give a clearer representation of where the center actually is. Demonstrated in Figure 5.1 (b), moving clockwise around the largest shifts the gradients are radial to the centered position therefore the data is correctly centered.

When centering it is important to buffer the data array with voxels of value zero. If the CCDs region of interest is 200 x 200 pixels and center is at (100,126), such a large shift
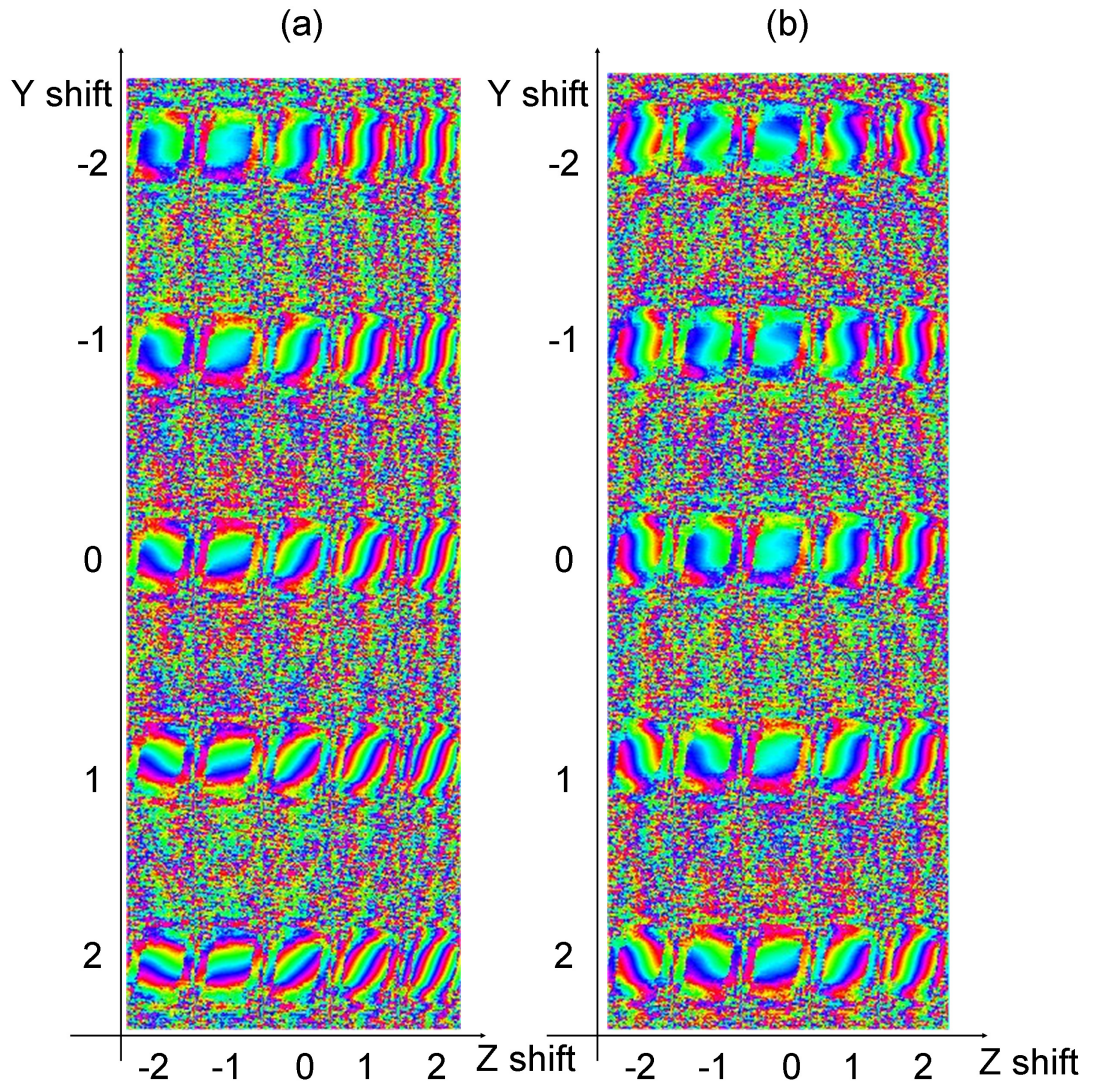
Figure 5.1: Autocorrelation of a 2D cross section of the 3D Dataset 27 in z-y plane pre (a) and post (b) centring, using 'dataCenter_5x5.py', a region of flat phase 'the center' is observed at z=-1,y=-2.
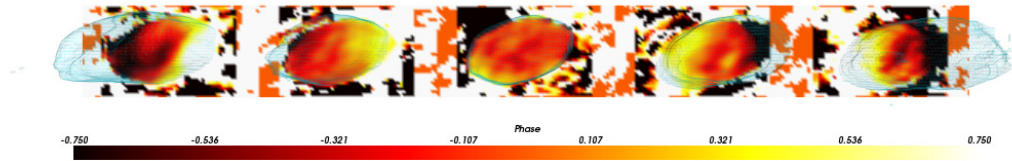
Figure 5.2: The reconstructed amplitude (translucent isosurface) and phases (2D scalar cut planes) for a phased dataset for shifts; -2,-1,0,1,2 about the central voxel along the x dimension

will see data far from the center wrap to the other side of the array. In this case the voxel at (190,190) will move to (190,16), it is necessary to buffer by at least 26 pixels in y, preferably more. The phase gradients reconstructed from an incorrectly centered dataset are demonstrated in Figure 5.2, large erroneous gradients from left to right appear across the reconstructed phase and the algorithm struggles to find a solution when ± 2 voxels away from the true center.

5.1.3 Binning

Once centered the analyst can decide whether or not to bin the data, this saves time in the data processing stage as the file size is decreased dramatically. There is no evidence to suggest that binning affects the quality of the reconstructed object. Binning requires the data array to possess an even number of pixels in each dimension and can be set in the data acquisition stage using Winview or in the data preparation stage. The Roper Scientific CCD can operate in two modes; FAST and SLOW Analog to Digital Conversion (ADC) rates, 1MHz and 100KHz respectively. The associated name defines the speed of readout and each have a different threshold at which the CCD pixels register a photon count and

saturate, a more limited dynamic range in fast operation mode but a five fold decrease in readout time. A high resolution comparison has not been made, but low resolution data has shown no difference between the two modes of operation, hence the fast ADC was used. Acquisition speed can be further maximised by binning the data to the point where the oversampling ratio is met but not violated (~3).

5.1.4 Scaling Diffracted Intensities

When large crystals are illuminated naturally their observed diffraction patterns are very intense and span a small region of reciprocal space. Maintaining the oversampling ratio, the exposure time is limited to 80% of the maximum intensity to prevent damage to the CCD using a fast shutter. When required exposure times dropped below the operation limit (4 milliseconds) of the fast shutter, either the detector was moved further away[7] or attenuators were introduced. Attenuators[8] are applied either to the entire diffraction pattern or to the brightest regions, known as 'beam stops' to obtain good statistics in the outer fringes of the diffraction pattern quickly. In both cases the different frames or different parts of frames of a diffraction pattern carry different weights, see Figure 5.3; a rocking curve taken through a ZnO Bragg reflection using attenuation of zero, 25μm Mo, 50μm Mo, 25μm Mo and zero attenuation moving from the center to the outer fringes respectively. Attempts to scale the dataset failed for three reasons:

1. The predicted scaling factor did not match the scaling factor required at correspond-

---

[7]The detector could be moved back to 3 metres, if the oversampling ratio was not met the crystal could not be measured

[8]Molybdenum or Aluminium, depending on attenuation factor required.

ing attenuation steps.

2. Where large attenuation and short exposures were used large amounts of data was lost at high spatial frequencies, it is impossible to scale a count rate of zero.

3. Drifting of the sample during measurement is non uniform because the number of accumulations and CCD exposure time were different for each attenuation.

The method for scaling was explored further with the use of beamstops. Beamstops create an equally difficult problem whereby the alignment of the beamstop to the CCD is imperfect and overlapping pixels make it difficult to scale accordingly. The ambiguity of the attenuation provided makes it very difficult to successfully match statistics accurately between frames of different attenuation and can completely suppress low intensity data in the outer fringes. Beam stops have been used successfully in CXD microscopy and incorporated into iterative phase retrieval algorithms [35, 81], however were not implemented here.

5.1.5 Aliens and their origins

After collection the data must be checked for 'aliens', erroneous intensity measurements due to cosmic rays, other crystals and air scatter must be removed as they too introduce asymmetry into the data, see Appendix B.1 for examples. These regions are simply cropped out by setting their value to zero, using 'alienExterminate.py', see Appendix G.1.5.

The influence of nearby crystal diffraction tends to only affect the unfocussed CXDI mode
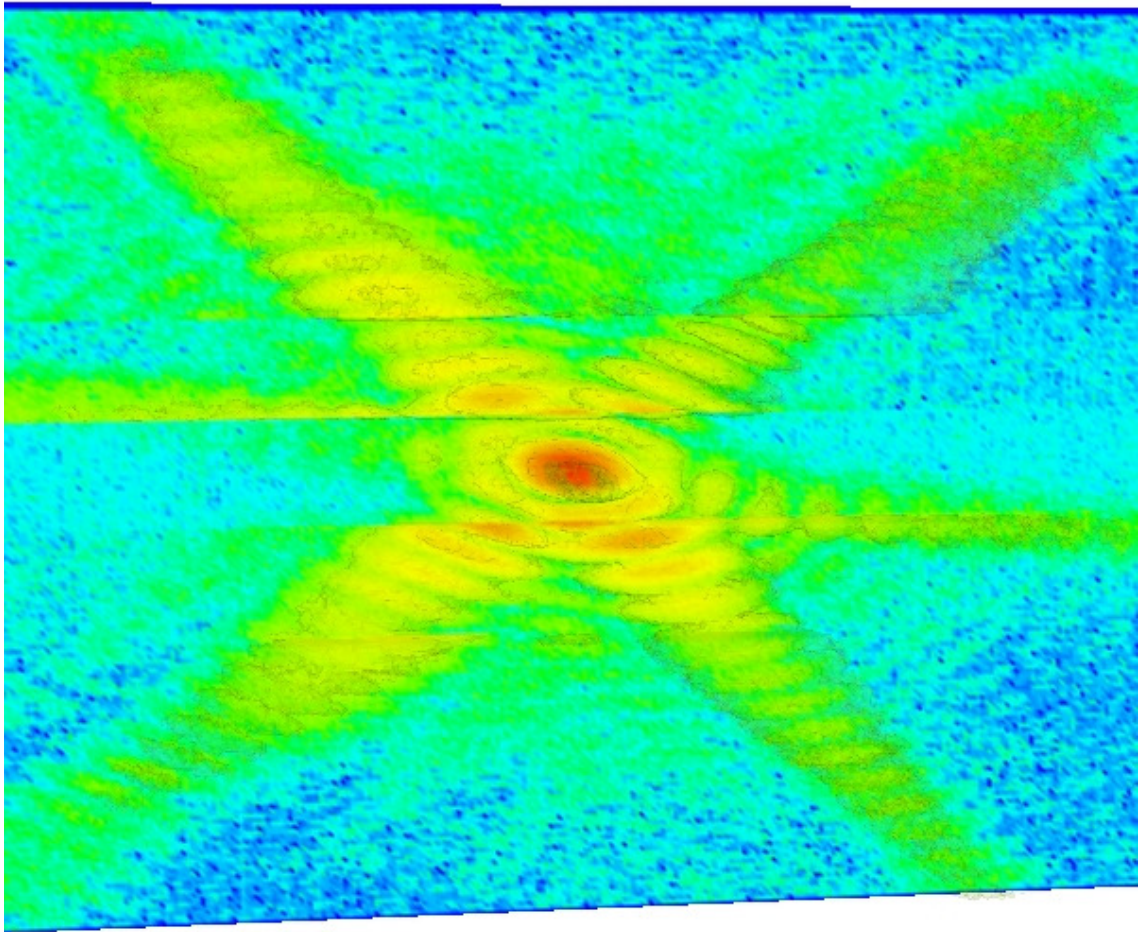
Figure 5.3: Scalar Cut Plane of the amplitude (log scale) across a concatenated diffraction pattern 3 levels of attenuation were applied (zero, 25μm Mo, 50μm Mo, 25μm Mo, Zero)

of operation and is reduced by reducing the size of the beam incident on the sample using the Roller Blade slits and translating the sample to keep the crystal of interest in the beam. Air scatter is minimised using either a helium filled or evacuated flight path from the sample to the CCD detector limiting the exposure of the beam to the scattering atmosphere.

Another factor which cannot be ignored is the presence of transparent materials (Beryllium(Be) and Kapton) in the flight path, which can affect the coherence of the incident beam and interfere with the diffracted beam. Observed in experiments where the window lay between the diffracting sample and the CCD, as the crystal was rocked in the beam a half-doughnut shaped artifact remained constant in position, seen in Figure 5.4 top left of the bragg peak. The artifact was present in every frame, was stationary relative to the sample but varied in intensity, hence, due to a stationary object in between the sample and the CCD. Both Kapton and Be exist in this region. The Kapton is attached to the detector arm hence its illuminated area remains approximately constant for all measurements. The Be window was large and stationary for the measurements, see Figure 3.9. Different Bragg reflections required different experimental geometries and so different parts of the Be window were illuminated for different crystals. Artifacts did not present in every diffraction pattern thus the Be was the source. Industrially manufactured Be has been found to exhibit Fe inclusions [96] and can account for these artifacts. To date the these artifacts have not been identified in the reconstructed datasets.

The data are now ready for phasing.
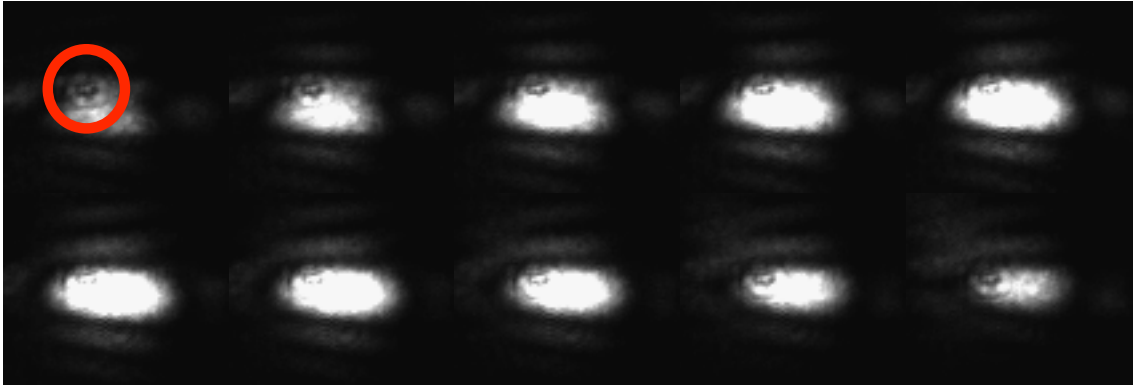
Figure 5.4: Ten CCD images at uniform ϕ steps about a Bragg reflection with a Beryllium window induced doughnut shape observable in the intensity distribution, top left of bragg spot due to an Fe inclusion indicated in the first image by a red circle.

5.2 Phasing Data

The user defined algorithm constraints will be discussed in this section.

5.2.1 Threshold

The threshold is an addition by Ross Harder, applied to the phasing algorithm so that all data below a certain value should be ignored by the algorithm. This threshold is determined by the user and is usually set to several photons. The CCD detector outputs the measured intensity in Analog to Digital Units (ADUs), a full discussion of the operation of a CCD detector was provided by Howell [85]. The gain of a CCD determines how the charge collected in each pixel will be assigned to a digital number. As the majority of intensity measured surrounds the Bragg peak, low intensity regions will register single photons. Histograms including voxels from these regions identify single photon and sometimes double photon peaks. Figure 5.5 illustrates a prominent single photon peak of the
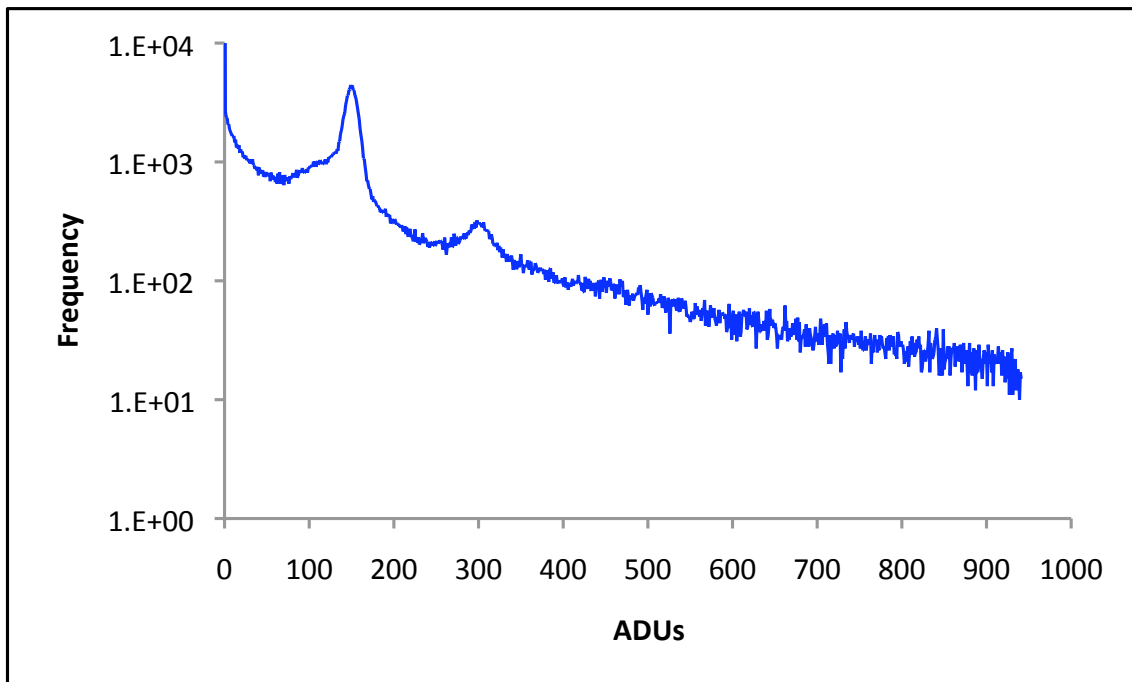
Figure 5.5: Histogram produced using 'histogram.py' for DS_{131} identifying the frequency of intensities measured on the CCD pixels, all 51 2D frames were considered

order 140-150 ADUs and a double photon peak (280-300 ADUs) observable only in the 2D slice taken through the (101) ZnO Bragg peak.

The effect of the threshold is very important. When set too low the algorithm is forced to represent a large number of low intensity pixels and often stagnates. If set too high the resolution of the image is compromised. This feature can be advantageous, by setting the threshold deliberately high the algorithm reconstructs a low resolution object. Fewer spatial frequencies converge faster due to fewer data points and provide a good starting point when approaching datasets that stagnate initially at lower thresholds when the defined support is still loose.

5.2.2 Start Point

The iterative algorithms employed require an initial guess of the density of the crystal. As mentioned previously a random starting point is the best method for identifying a robust calculation. These methods are built on the application of prior knowledge in the form of constraints. Therefore it is logical to implement a more accurate representation of the illuminated object rather than a uniform density with random phases. The technique is sensitive to small displacement fields and in the Bragg geometry a highly crystalline sample is required, thus a perfect crystal with a flat phase is more probable than a set of completely random phases. Discussion will continue related to this topic in Section 6.2.5.

5.2.3 Support Choice

The support for the data must now be chosen, this defines the region around the origin at which the reconstructed object is allowed to exist. The support construction is based around the volume enclosed by a set of analyst defined planes. From Section 4.2.2 the maximum size of the object is half the volume of the array. Generally, the datasets are oversampled by a factor of 3 in each dimension, so the support can be reduced to approximately $\frac{1}{27}^{th}$ of the volume of the array. By observing the autocorrelation function[9] in 3D one can estimate the size of a rough support for the object. From experience, figure 5.6, this is set to 2/3 the extents of the autocorrelation function in each dimension. Large enough to find a preliminary solution but not small enough to impinge on the reconstructed object. The support can then be tightened further until it encloses the

---

[9]FT of the measured intensity, $FT(\rho.\rho^*)$, is twice the size of the object
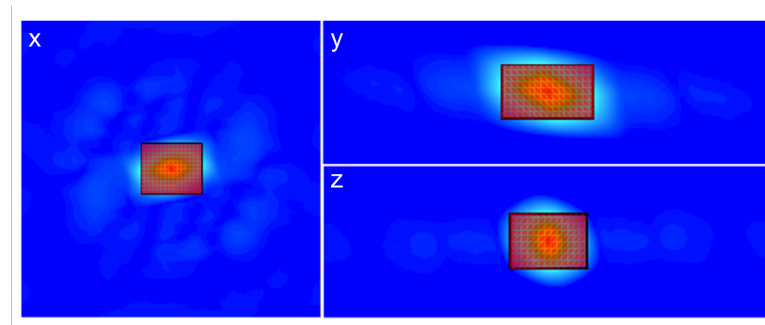
Figure 5.6: x, y and z slices through the autocorrelation function of a dataset and red wireframe isosurface of first guess at the support, approximately two thirds its size.

reconstructed object but does not interfere with its shape.

The reconstructed image is inspected and the support tightened or loosened depending on the effect of the support on the current output. This process has been sped up by feeding multiple supports to the phasing algorithm with variations of two voxel increases in each dimension (± 1 in the $\pm$ direction for each dimension to keep the support symmetric). Each dimension is approached independently, multiple dimensional variations in the support drastically alter reconstructions and lead to malsized supports and are difficult to converge. The programs used to complete this operation are 'varyXsupport.py','varyYsupport.py' and 'varyZsupport.py'.

The evaluation of the suitability of the chosen support is based primarily on the analysts intuition. To begin with the support is much larger than the object and hence can be changed dramatically to the analysts discretion. Once the analyst is no longer able to decide upon the variation required the error metric can be called upon but cannot be relied upon, equation 5.7. Figure 5.7 shows the progression of the error metric as the PC-HIO algorithm proceeds for 50 iterations with a further 20 iterations of ER for several

different sized supports, here B is the prime support, A is smaller than B by four pixels in each dimension, C is larger than B by two pixels in each dimension and D is larger than C by two pixels in each dimension. C and D both converge to a lower error metric than B, this is because the algorithms constraints are not enough for it to distinguish between solutions, a superposition of solutions result which can lower the error metric, see Figure 5.11. Only A does not exhibit a saddle point in the error metric, the constraints are too tight and force the solution to an erroneous state. B is determined to be the prime support as its reconstruction (Figure 5.9) has a relatively uniform amplitude distribution, well defined hexagonal facets and reasonably well defined ends, an estimate of the crystal dimension from the diffraction pattern also match the reconstruction, whereas C and D do not. Yet $E_{nmse}^2(D)$ and $E_{nmse}^2(C)$ are lower than $E_{nmse}^2(B)$ suggesting an overfitting of the noise.

Until this point the data is considered in voxel dimensions, in reality a geometric correction [79, 147] provides a meaningful lengthscale for the reconstructed image in both reciprocal and direct space dimensions.

At present, depending on the number of defined planes a large portion of the support will in fact remain empty. Therefore the algorithm has only the raw diffraction data to constrain it in these regions, in reality the constraint could be tighter. These regions of empty support become significant when the crystal lies at an angle to each of the voxel dimensions and in the worst case scenario at 45° to every dimension the support has a volume $\frac{3}{\sqrt{2}}$ times larger than the ideal scenario. Using rotated planes is time consuming and as expected significantly improves the convergence of the algorithm. This process
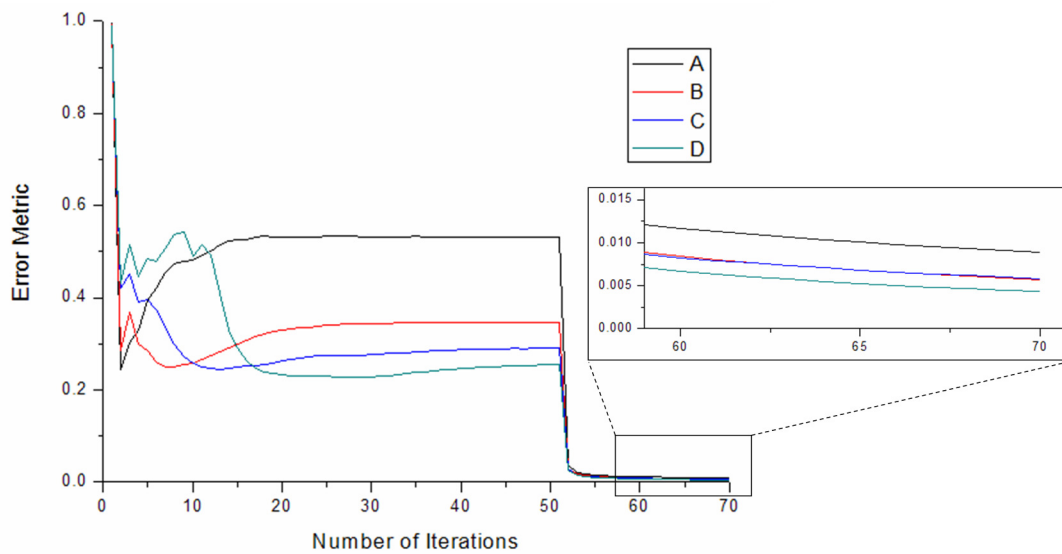
Figure 5.7: Tracking the error metric for a phasing operation with multiple supports, where A < B < C < D, switch to ER after 50 iteration of HIO.

is not automated at present. The proposed Shrinkwrap algorithm (SW) [123], uses the autocorrelation function to begin with and smooths the function, constantly updating the support relative to the solution. Ideally this should make the support as tight to the reconstructions shape as possible but has one significant drawback; updating the support relative to the solution produced from a support based on the autocorrelation function and the typical HIO and ER algorithms. The SW algorithm is susceptible to the optimisation of a local miminum. Effectively the robustness of this algorithm cannot be easily tested as the starting point is predetermined and the number of defined variables considerable. The variables for the smoothing of and building of the new support define the algorithms ability to move to other minima, it is not obvious what these should be determined to be. From experience the support has the most impact on the reconstruction and when asymmetric can favour previously ambiguous solutions. For the application of such an
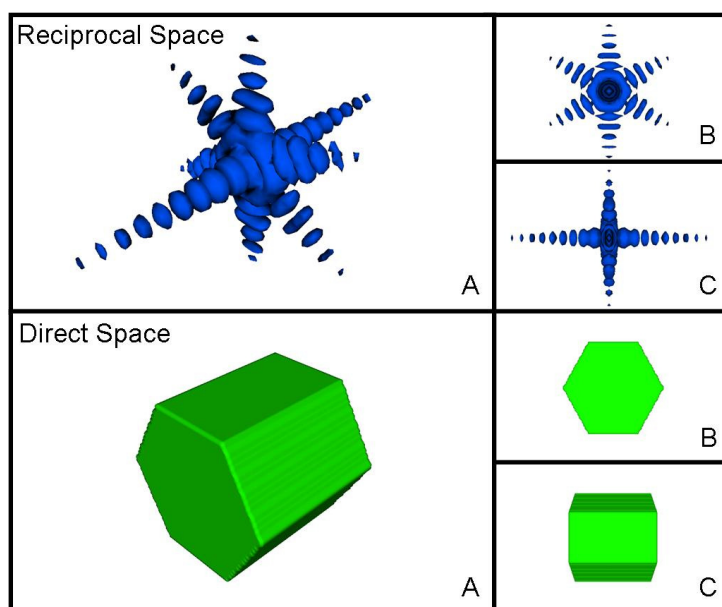
Figure 5.8: Theoretical reciprocal space diffraction pattern and corresponding direct space nanorod (a) Isometric View (b) Top View (c) Side View

asymmetry *a priori* knowledge is required, if it is not possible ambiguous solutions should be dealt with via cross correlation described in Section 4.3.8.

5.2.4   CXDI ZnO

Theoretical Data Treatment

A simple three-dimensional model of the diffraction pattern of a hexagonal faceted nanowire was produced by FFT; and is shown in Figure 5.8.

An experimental dataset is shown for comparison in Figure 5.9. The six fold symmetry due to the hexagonal cross section of the rod and two fold symmetry perpendicular are

evident, although in this particular case the two fold fringes are not well defined (are at the limit of oversampling).

The phasing method described thus far was applied to dataset 27 (April 2007). It encompasses a succession of improvements in the sample preparation, data collection and data analysis methods.

A 3-dimensional render of the experimental data obtained by stacking up the 2-dimensional data and viewed in Mayavi (three-dimensional imaging software) is shown in Figure 2.10, Diffraction Data. The morphology of the rod is well defined (A) and (B) respectively. The two fold and six fold symmetry are evident, as seen in SEM. Increased rocking curves enhanced the resolution of solutions in the z-dimension and smaller θ steps ensure oversampling. Subsequent 'alien' removal and phasing were carried out, the reconstruction is shown in Figure 5.9, Direct Space Inversion. The data was collected using the focussed beamline setup, see Section 2.2.5, with focusing mirrors, for an object greater in size in a single dimension than the beam, the beam itself defines the ends of the wire, implying the edges of the focused beam are not uniform in shape and intensity. The subsequent smearing of the fringes in the 002 crystal direction could be explained by a rod with one well defined end and one rough end; manifested either from the algorithm itself, an erroneous feature or, the beam incident on either the base/top of the rod in which case the rod defines one end of the beam and the rough focus smears out the fringes.

The preliminary results are very encouraging, a solid real object has been inverted from the diffraction data. Its dimensions have been estimated; width of uniform hexagonal facets between opposite parallel faces approximately 370nm and 700nm in length. This agrees
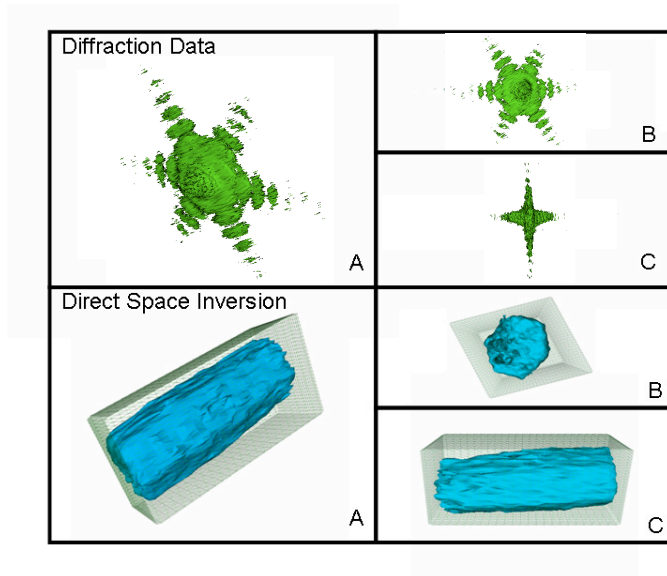
Figure 5.9: Diffraction pattern measured from a ZnO nanorod and corresponding direct space inversion (a) Isometric View (b) Top View (c) Side View

quantitatively with estimates for dimensions and aspect ratios from SEM characterisation[10]. Undulations in the surface of the reconstruction are of the order of the resolution of the image ∼50nm along the c axis and ∼35nm in the a-b plane.

The resolution of the dataset is estimated by the statistics in the nth order fringes, where n is an integer the resolution is defined by the crystal extents d in dimension of fringes divided by the number of observable fringes, $\frac{d}{n}$. The resolution is therefore set by the acquisition time in this case, through experimentation and the need for good statistics this was set to 200+ accumulations of each pixel at an exposure time defined by the brightest part of the bragg peak at 80% pixel saturation (∼350photons). It will later be shown this method is equivalent to the PRTF function defined in equation 4.3.

The error metric shows an interesting characterisitic, a saddle point observed after 17 HIO

---

[10]The exact crystal measured with CXDI cannot be identified as thousands of crystals are illuminated at any one time, only the orientation, a rod stood on end, is known.
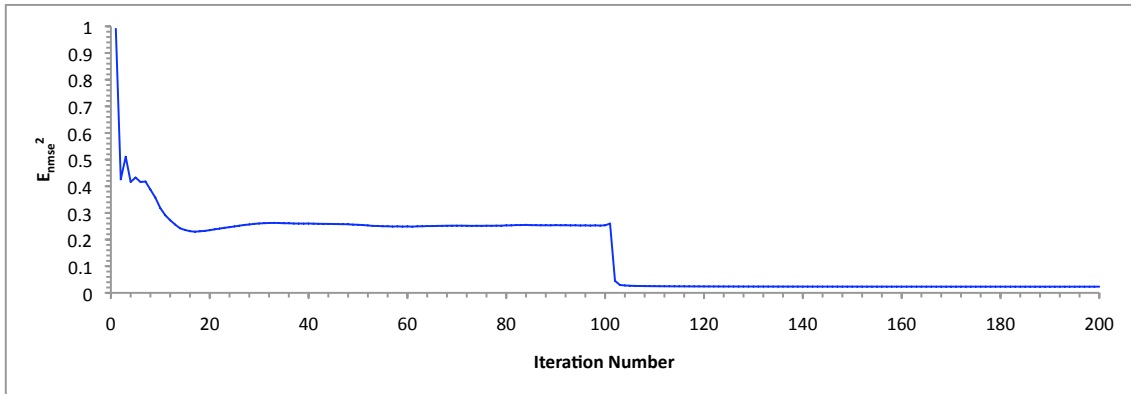
Figure 5.10: Normalised mean squared error metric at each iteration for the phasing of dataset 27 (April 2007), 100 iterations of PC-HIO ($\phi_c = \pm\frac{\pi}{2}$)followed by 100 iterations of ER

iterations, E^2_{nmse}=0.021, the error metric then increases and stabilises at a value 0.025. Subsequent iterations of the ER algorithm drop the error metric to 0.003. The saddle point was observed for multiple dataset when the support was fully optimised.

5.2.5   Iteration Number and Algorithm Choice

The best way to understand the algorithms operation is to observe its effect on the developing image, Figure 5.11 demonstrates the solution at every iteration in terms of both amplitude and phase. The error metric drops to a saddle point before stagnating, the value at which stagnation occurs is dataset dependent and a property of the amount of binning but does not scale with binning. The output of the algorithm at each iteration is shown in Figure 5.11A, beginning with a copy of the support the algorithm proceeds to a state of two overlapping solutions and then converges to one of these solutions. Cross sections of the amplitude, shown in Figure 5.11C, show two 'hot spots' (red) superimposed onto one another with a small offset, these 'hot spots' merge until the algorithm imposes

a change large enough to favour one of them (the other likely an enantiomorph). The reconstruction concludes a highly nonuniform amplitude distribution, the phase structure variations correlate to amplitude variations upon further iteration. We expect a uniform amplitude distribution and note attempts to enforce a uniform distribution within a small error were unsuccessful. The saddle point was used to identify a suitably tight support.

5.2.6   Phasing methods

Many variations on the phasing methods described were employed. It was not possible to identify an underlying phase method for definitive reconstruction of the diffracting object. A simple HIO followed by ER method allowed a solid 3D object to then be enhanced through constraint tightening. Increased iterations and consecutive repeats of the phasing operation did not improve the result. The choice of support has the greatest impact on the reconstructed object, to maintain objectivity a support incommensurate with the shape of the crystal (i.e a hexagonal prism in this case) was deemed suitable as not to influence the reconstruction. For highly symmetric crystal morphologies it was necessary maintain a symmetric support otherwise enantiomorphs were favoured. However, *a priori* knowledge can be applied to identify the correct orientation and this will be demonstrated in Chapter 7. Several variants of existing algorithms were employed and will be discussed as and when they apply to specific problems. Where suitable PC-HIO and PO-ER were generally advantageous.
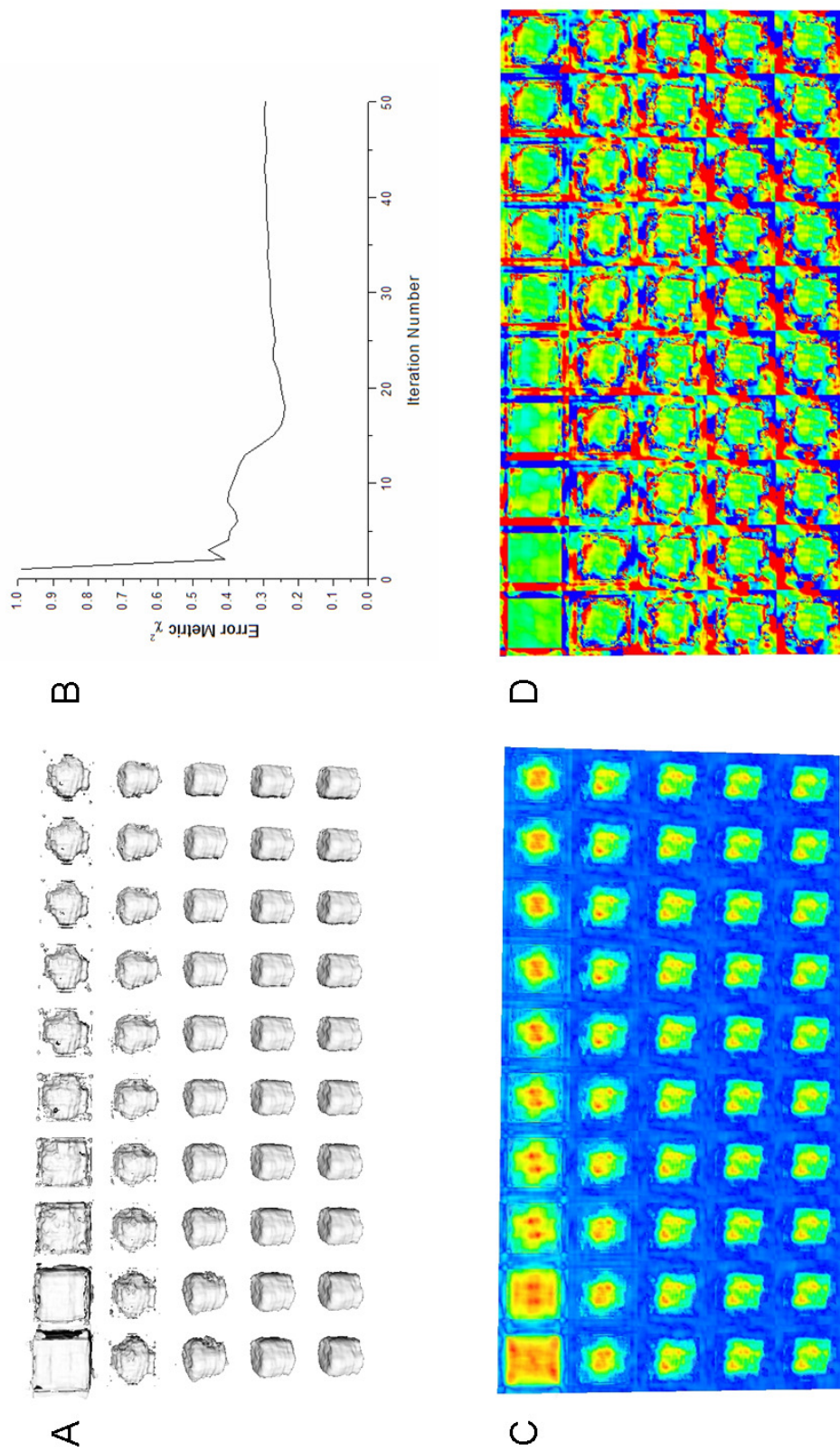
Figure 5.11: An isosurface of the amplitude (A), the error metric (B), scalar cut planes of the amplitude (C) and the phases (D) are displayed for every iteration of a 50 iteration HIO phasing operation carried out on dataset 62 (April 2008)

5.3   Summary

The phasing procedure from collection to reconstruction has been described. The support constraint has the greatest impact on the reconstructed crystal, should be symmetric and can take any shape, however, for consistency the support should avoid the shape of the reconstructions to prevent bias. The methods described in Chapter 4 can identify any ambiguous reconstructions that symmetry allows. The chosen starting point for the algorithms remains up for debate and will be approached in Chapter 6 for multiple datasets recorded from the same crystal. The HIO algorithm produces a saddle point in the error metric and was observed when the support was optimised.

Chapter 6

Solid State Diffusion studies

This chapter will summarise the results obtained for deposition and annealing experiments carried out on ZnO crystals coated with a layer of Fe, Ni and Co. The interpretation of the calculated phases will be introduced using the results of the dataset phased in Chapter 5. An approach to justify the reliability of the reconstructions will be implemented. The continuity of reconstructions of consecutive diffraction patterns measured from the same crystal annealed through several cycles will be presented and the practical origins of the phase modulations identified.

6.1   ZnO studied via CXDI

The key feature of the CXDI technique is the ability to map displacements within the crystal. The phase maps shown in Figure 6.1 demonstrate scalar cross sections of direct space phase through a translucent isosurface of the amplitude of a ZnO rod reconstructed
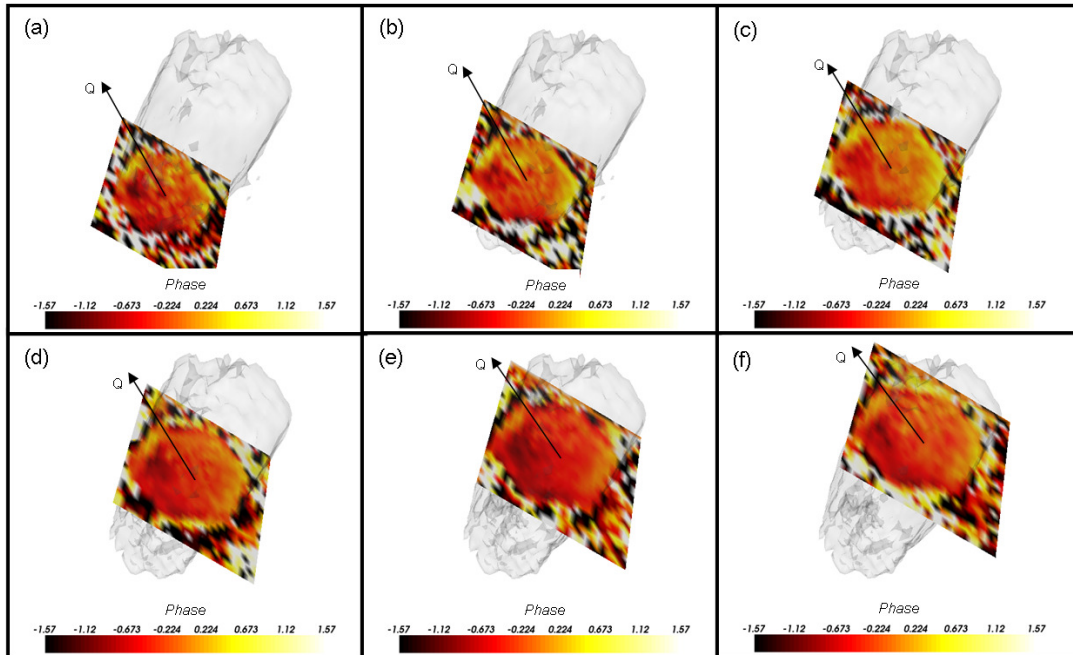
Figure 6.1: Phase map cross sections taken at 80nm intervals along the length of the rod (a)150nm → (f)550nm. The (101) Q vector direction is also shown.

in Section 5.2.4. The cross sections were taken at 80nm intervals along its length parallel to the Q vector.

Close inspection of the phase maps shown in Figure 6.1 along an extrapolated (101) Q vector highlight a phase modulation ranging from $+\pi/4$ to $-\pi/4$ to $+\pi/4$, a non-quadratic relationship, which is present in all phase maps along the length of a ZnO rod shown in Figure 6.1. A misalignment of the diffraction data due to pixelation can be ruled out as the origin of this feature as this would generate a linear phase ramp, previously discussed in Section 5.1.2. In this case a linear phase ramp was not evident however a linear feature can underly the observed phase modulation. A suitable method for implementing this correction has not been considered to date, however the centering process should limit its

impact on the result. This particular measurement was completed using KB focussing, hence, if a quadratic phase structure were to be generated the curvature of the wavefront would need to be considered as a possible source. The quadratic phase structure would see a smooth quadratic modulation in the phase from facet to facet along the sampled Q-vector, this was not observed. Any complicated phase modulation is likely to correspond to a strain in the crystal. The scalar cut planes slice through the phase perpendicular to the c-axis, hence of the six equivalent hexagonal 100 facets; the two along and against the Q-vector respectively exhibit the same sign, the remaining four which are less coupled to Q also exhibit modulation in the phase.

6.1.1 Interpreting the phase in direct space

In Section 2.2 we introduced CXDI experiments, the interpretation of the generated phase maps will be reiterated. In direct space, the calculated phase corresponds to the displacement along the Q vector relative to an underlying equilibrium crystal lattice, $\phi = \mathbf{Q}.\mathbf{u}(\mathbf{r})$. In the positive Q direction a positive phase corresponds to an expansion, a negative phase corresponds to a compression. In negative Q, a positive phase corresponds to a compression, a negative phase corresponds to an expansion. Fitting to the phase modulation will provide an insight into their physical origins.

The phase modulation seen in Figure 6.1 shows a positive phase on both 100 facets along and against the Q-vector. This represents an expansion in the positive Q direction and a compression in the opposite direction, the origins of which are undetermined. We expect the presence of oxygen and zinc vacancies, if they were to be uniformly distributed

throughout the centre of the rod the atomic spacing in the crystal would be constant throughout the crystal thus the Bragg peak would simply shift. If however a sample was placed in vacuum an increase in oxygen vacancies at the surface would lead to a contraction near the facet relative to the rest of the crystal [164]. Equally a contraction on the six hexagonal facets would not be expected as they are non polar and atomically flat with equal numbers of cations and anions in the surface plane. A contraction is predicted on the zinc face however the scale of contraction, 0.4Å, is likely below the resolution of the data, close to 50nm, so would not be observed. It is clear strains of some form have been observed and are considerably larger than the resolution of the direct space phase ($\sim$ 0.15rad) but their origins are not obvious.

6.1.2   How reliable is a reconstruction?

This is the primary cause for concern. The nature of the 'Phase problem', a problem with N unknowns and N knowns leads to not only the multiple ambiguous solutions discussed in Section 4.2.4, but a significant number of different solutions (local minima in solution space) if the constraints are insufficient. Two approaches exist to overcome these problems, first, ambiguous solution identification [20,213] and second, averaging [35,37,168]. A combination of the two will be implemented here as they are both advantageous for different reasons. The first makes the second applicable and averaging highlights reproducible phase features and averages out the erroneous phase features.

6.1.3 Phasing variables

The phasing variables discussed in section 4 provide the constraints for the phasing oper-
ation. The constraint with the largest impact on the solution is the support constraint.
The shrinkwrap method introduced by Marchesini et al. has proved very successful in
forward scattering phase retrieval experiments [35,36,123]. The algorithm begins with the
autocorrelation function as the first estimate of the illuminated object, several iterations
of HIO and ER are run and a support tailored to the current solution via a convolution
operation with a 3x3x3 voxel cube and smoothing with a gaussian function. Further it-
erations of HIO and ER follow, the support is updated after each set of iterations. The
algorithm converges when the support is found to be self consistent between algorithm
iterations ($<1\%$ variance in shape). For a detailed overview of the modified Shrinkwrap
algorithm see Appendix G.2.

Although a valid method, the shrinkwrap method outlined relies on the initial solution
of pre-existing algorithms with a very loose support constraint, an enlarged copy of the
autocorrelation function. In solution space a number of solutions are available with loose
constraints, and are subsequently optimised by shrinking the support around them. The
shrinkwrap method has optimised the solution based on the support constraint, it does
not definitively identify the global minimum. It simply identifies a solution based on a set
of loose constraints and optimises it. From random starting points we would expect and
observe a large variation in reconstructions but their supports are optimised. From this
position we can apply the two approaches mentioned previously and find a more reliable
average. In Section 5.2.2 an argument was put forward for using an object with a flat

phase variation as the starting point, thus a comparison will be made here.

6.1.4   Identifying ambiguous solutions

The random starting point leads to multiple different solutions, in order to combine them the average phase needs to be set to zero, solutions need to be overlaid, ambiguous solutions identified and made equivalent (i.e enantiomorphs) and finally averaged together. To identify ambiguous solutions we refer to Section 4.2.4. The solutions are now equivalent and can be averaged accordingly. The average solution must then be normalised before it is used to seed further phasing iterations.

6.2   Consecutive measurements from the same crystal

6.2.1   Raw Data

Initial observations of the Bragg peak of a ZnO nanorod post Fe deposition are shown in Figure 6.2. The stark contrast between diffraction from the same crystal annealed to a higher temperature is clear. The crystal has decreased in size as the interference fringes have become larger. Then a dramatic increase in exposure time from 0.1 to 2 seconds was required to obtain the same level of statistics and the need for a wider rocking curve confirms a solid state chemical reaction between Fe and ZnO has taken place on a relatively large scale.

The reaction proceeds at a relatively low temperature of 350°C. Bates *et al.* [16] observed a solubility of zero at 500°C increasing as a function of temperature to 7 at.% at 800°C. A
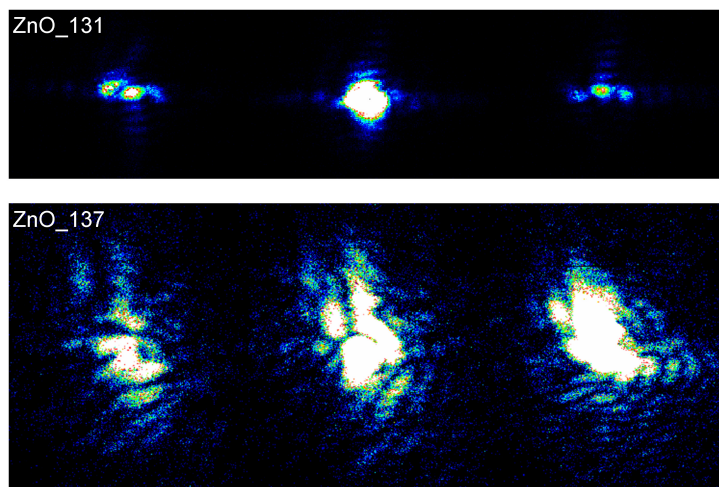
Figure 6.2: Diffraction data at -4,0,+4 frames offset from the bragg spot at (a) 298°C (DS$_{131}$) and (b) 358°C (DS$_{137}$) for sample 108A

solubility of this order does not explain the large variation in diffraction. We would expect a severe degradation due to the formation of Fe dominated crystal structures leading to fractured ZnO crystals. In one case, a crystal began to move away from its previously adhered location, it was tracked for an hour over 1.0° in angle. Its movement prevented a measurement but upon returning to its original location a remnant similar to that observed in Figure 6.2 DS$_{137}$ was observed suggesting part of the crystal detached.

The low reaction temperature observed can be explained by heating of the nanocrystal due to the illuminating beam and the presence of large errors in the temperature measurement. The thermocouple sits several millimetres away from the illuminated region of the sample. Inspection of the silicon as it began to conduct suggested a good temperature calibration as the sample began to glow orange at 600°C, see Appendix Figure A.1. The heating was asymmetric and large gradients were evident across the sample. The thermocouple resides on a mounting plate attached to a screw hence, measures a region of the sample

approximately 5mm from the illuminated sample region. An error in the thermocouple itself must also be considered, they are less sensitive at higher temperatures as they exhibit a negative exponential resistance to temperature relationship.

The structural change was later confirmed with SEM, see Figure 6.3. The sample was heated through to 358°C and post experiment SEM analysis shown in A and B confirms the presence of crystals coated with a layer of Fe but no obvious change in morphology. The shadow is due to the angle of evaporation and means only the top and three of the hexagonal facets are coated in metal. A second sample (No. 115) where similar diffraction changes were observed, see Figure B.2, was heated to 600°C was shown in (C) and (D). At this temperature the layer of Fe has dewetted the surface and the internal degradation of the crystals observed. This confirms the large variation in the x-ray diffraction data and highlights the ability of CXDI to observe the initial stages of the reaction before the morphology changes. It also emphasises the potential for CXDI of buried structures.

6.2.2 Goals

Having ascertained the basic parameters for the experiment further experiments were carried out with Fe, Ni and Co depositions ranging between ∼10-100nm. Several experimental methods were introduced to obtain the best data. The crystals were measured at a reference temperature (approximately 200-300°C), chosen from experience where no variation in diffraction was observed but close enough to the reaction temperature that the diffraction does not move completely out of the detector upon further annealing. Annealing proceeds for 5 and 10 minute periods, which will be referred to as 'steps', after
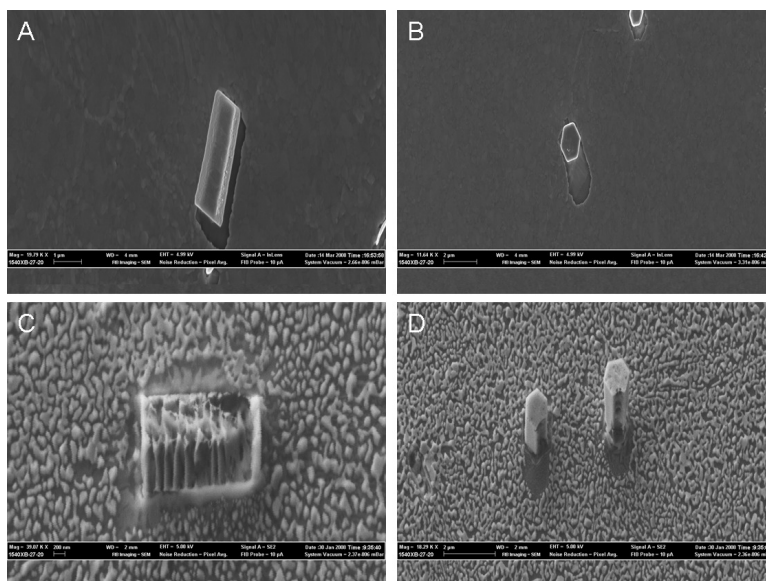
Figure 6.3: SEM from the sample heated to 358°C (A and B) in Figure 6.2 and the sample heated to 600°C (C and D) 6.2 for two different orientations ([002] perpendicular and parallel to the substrate) of ZnO crystal imaged by CXD

which the sample was cooled and measured at the reference temperature. This had three advantages; firstly, the crystal was not changing during measurement, secondly, the phasing parameters could be kept constant as thermal expansion effects can be neglected and thirdly, the Bragg spot proved highly reproducible, in the case of a large structural change the remaining crystal could be found and measured by returning to the logged motor positions for the previous measurement. In order to obtain sufficient statistics a 3 hour scan was required after each annealing step. By gradually altering the annealing step the onset of the solid state chemical reaction was sought, subsequent quenching to a reference temperature would prevent a continuation of the reaction while the measurement was made. The process was then repeated on a clean crystal to hone the parameters further.

Attempts were made to observe the crystal change during annealing using 2D analysis (1000 accumulations, 50 second total exposure). Any observable variation was difficult to

identify by eye, there was no guarantee at each temperature the same 2D slice through the crystals Bragg spot was measured. Subsequent reconstructions proved too slow to have an impact on the decision to cool the sample and suffered from inconsistencies due to the miscentering.[1].

The diffraction data for the experiments described previously for depositions and subsequent annealing of Fe, Ni and Co will now be discussed. The oversampling ratio was optimised to a factor of 3 or greater in all dimensions by binning the data and checks made to ensure the visibility of the fringes was not compromised.

6.2.3   Fe Deposition Diffraction Analysis

The diffraction patterns measured from a (101) Bragg peak for a ZnO crystal embedded in SiO_2 after annealing iterations is shown in Figure 6.4 (Sample 3 July 08).

The first datasets were measured before annealing, the following three annealing steps show no visible variation and the final step demonstrates a significant change. The integrated intensities, the total photons scattered into the detector from the crystal, for these datasets for the same exposure time are 5.67, 4.34, 3.99, 4.20, 4.70 $(x10^9 ADU)$[2]. We would expect a drop in intensity if the crystal structure was changed dramatically as observed previously. There are many error sources to consider; the long exposure time rules out beam intensity fluctuations; a beam refill (every 8 hours) could not account for

---

[1]Approximately 3 minutes per phasing operation where required to compare 2D datasets once the phasing variables had been optimised

[2]Based on the assumption a single photon produces 150ADU, the diffraction pattern consists of $3.73x10^7$ scattered photons of which $8x10^5$ are removed by a 10 photon threshold. A high threshold is set to enable the successful removal of alien scattering without accidentally removing scattered photons from the illuminated crystal
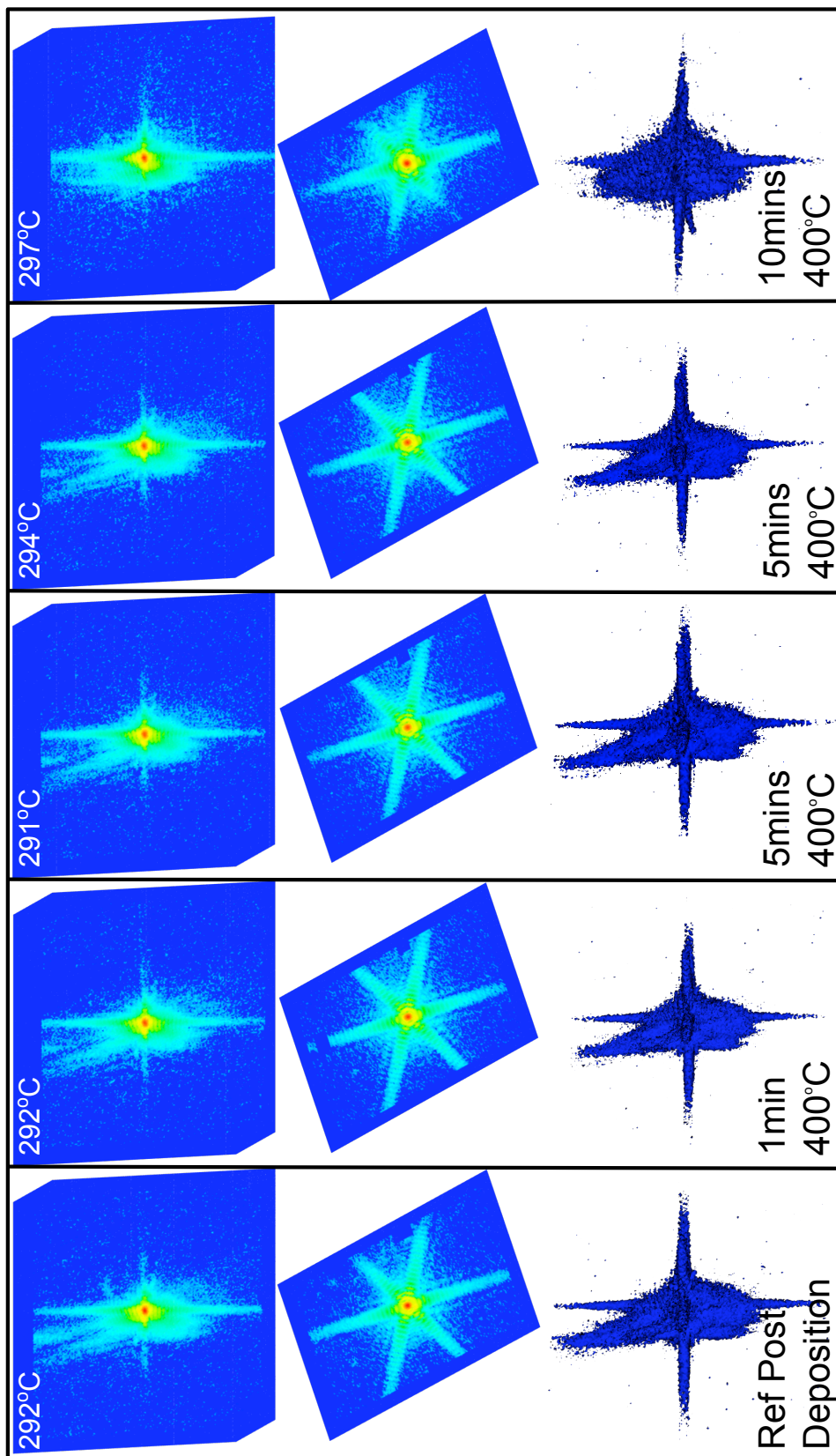
Figure 6.4: Left to right as a function of annealing step starting from a reference measurement Sample No.139c (July 08) with a 60nm deposited Fe layer, two log scale cut planes through the geometrically corrected measured intensities and a 3D render for comparison.

a 17% increase and we would see it twice as each dataset took 2hrs 30mins to acquire plus annealing and subsequent alignment delays. These datasets were acquired in the unfocussed mode, therefore any structure in the beam may become apparent. Realignment after each step may sample a slightly different distribution of intensity and could explain the modulations between datasets 2, 3 and 4. Note alien diffraction was removed and is evident from blocks of zero intensity in the hexagonal cross section of the reference dataset in Figure 6.4.

Table 6.1: Integrated Intensities before and after threshold was applied, corresponding photon flux discarded

Filename	DS_{54}	DS_{55}	DS_{59}	DS_{61}	DS_{64}
I_{Int}	5.67×10^9	4.34×10^9	3.99×10^9	4.20×10^9	4.70×10^9
$I_{Int}^{Threshold}$	5.55×10^9	4.23×10^9	3.87×10^9	4.08×10^9	4.56×10^9
Δ (Photon Number)	1.43×10^8	1.16×10^8	1.18×10^8	1.18×10^8	1.40×10^8

The visibility of the diffraction patterns was measured for each set of fringes and found to be consistently high (>90%) along every direction defined perpendicular to a set of parallel facets, see Table 6.1. Binning of the data did not compromise the visibility and an oversampling ratio of 3 was maintained in all dimensions. The importance of the visibility will be discussed further in Chapter 7 therefore the assumption of a perfect coherent illumination of the crystal was made.

Table 6.2: Observed visibilities for 5 datasets from Sample No.139c (July 08) measured along the both the a-axis and c-axis

Filename	DS_{54}	DS_{55}	DS_{59}	DS_{61}	DS_{64}
Visibility (002) (%)	95	96	95	98	92
Visibility (100) (%)	98	98	98	98	70

6.2.4   Ni and Co Deposition Diffraction Analysis

A similar observation was made when Ni was evaporated onto ZnO and annealed. The diffraction patterns are shown in Appendix 1 Figures (F.1, F.2) and (F.3, F.4). For two crystals covered with Ni and one crystal covered in Co a change was visible in the diffraction pattern, for the second Co covered crystal the experiment was unsuccessful, expected due to a failed Co deposition. A coherent illumination was confirmed via the fringe visibility and the integrated intensities were well correlated with the change in exposure times. See Tables 6.3 and 6.4 for Ni samples and Tables 6.5 and 6.6 for Co samples.

In both Ni depositions where a change in the crystal was observed the intensity remained relatively constant until the onset of the solid state chemical reaction; Ni Sample 115 (Mar 08), see Figure F.1, dropped by factor of 2 in intensity, Ni Sample 123 (Mar 08), see Figure F.2, dropped by 33%. In the first Co deposition the sample (Sample 113, Mar 08), see Figure F.3, remained constant over the first two annealing steps and then increased by 22% before returning to the level of the first two annealing steps, the diffraction patterns do not vary dramatically suggesting the crystal has not changed. The second Co deposition, Sample 115 (Mar 08), see Figure F.4, remained constant for the first two annealing steps and then increased by 5% before dropping to 87% of the level obtained in the first two annealing steps. Considering the aim of the experiment was to observe the onset of a solid state chemical reaction the variation in integrated intensity should remain constant for small displacements (less than the lattice parameter across the whole crystal). This was not observed, increasing intensity can be understood by the fluctuations in flux across the beam profile, equally the drops in intensity could also be attributed to similar effects.

The data shown were taken for the initial identification of the temperature at which the solid state reaction proceeds and have relatively low statistics. The lack of consistency in the measured temperature of the onset combined the irreproducibility of the cobalt and nickel film evaporation led to focus on the Fe deposition experiments, quenching and measurements at reference temperatures were not made for Ni and Co depositions.

Table 6.3: Experimental parameters for successive annealing steps for Sample 115 (Mar 08) with a Ni deposition

Filename	DS_{160}	DS_{161}	DS_{162}	DS_{164}	DS_{165}	DS_{166}	DS_{169}	DS_{170}
Temperature(°C)	203	203	211	303	351	382	382	403
Accumulations	300	100	50	100	100	100	50	50
Exposure Time (sec)	0.2	0.2	0.2	0.2	0.2	0.2	1.0	1.0
I_{Int} (x10^9)	2.82	1.39	0.73	1.35	1.23	1.34	1.55	1.49

Table 6.4: Experimental parameters for successive annealing steps for Sample 123 (Mar 08) with a Ni deposition

Filename	DS_{114}	DS_{116}	DS_{118}	DS_{120}
Temperature(°C)	200	307	408	501
Accumulations	100	100	100	40
Exposure Time (sec)	0.2	0.2	0.2	0.6
I_{Int}	2.15×10^9	2.43×10^9	2.51×10^9	2.03×10^9

Table 6.5: Experimental parameters for successive annealing steps for Sample 113 (Mar 08) with a Co deposition

Filename	DS_{62}	DS_{64}	DS_{65}	DS_{67}	DS_{68}
Temperature(°C)	200	303	350	401	451
Accumulations	200	200	200	200	200
Exposure Time (sec)	0.15	0.15	0.15	0.15	0.10
I_{Int}	1.73×10^9	1.69×10^9	1.75×10^9	2.13×10^9	1.25×10^9

6.2.5 Reconstructions of consecutive Bragg reflection data

The described diffraction patterns measured after annealing steps for Fe, Co and Ni depositions will now be 'phased' and the internal structure revealed. We have seen from the integrated intensities errors may be present and will propagate into the reconstructed so-

Table 6.6: Experimental parameters for successive annealing steps for Sample 115 (Mar 08) with a Co deposition

Filename	DS_{185}	DS_{188}	DS_{190}	DS_{192}	DS_{193}
Temperature(°C)	321	406	480	607	320
Accumulations	200	100	100	100	100
Exposure Time (sec)	0.3	0.3	0.3	0.2	0.3
I_{Int}	0, $6.08\text{x}10^9$	$3.10\text{x}10^9$	$3.20\text{x}10^9$	$2.30\text{x}10^9$	$2.77\text{x}10^9$

lutions. Based on the arguments and questions raised in Section 5.2.2, two starting points will be implemented; random start and a copy of the support. From a random starting point the reliability of the algorithms can be tested, hence 10 random starts will be used and the result averaged and normalised after considerations for ambiguous solutions have been made. Starting from a copy of the support will always lead to the same solution. The question of how much *a priori* knowledge can we apply? can be raised. With multiple diffraction patterns from the same crystal we have the capability of seeding phasing operations from solutions of any one of the diffraction patterns. Ideally this should be the reference reconstruction, however if the quality of the reconstruction was compromised an alternate seed solution would be used. There is also an algorithm independent test, by measuring the crystal at a reference temperature all experimental variables are approximately constant, hence we can apply constant constraints in the phasing operation so any variation in the generated solution is a property of the intensity distribution alone. The instance in which a slight variation in a crystal was expected lends itself to an alternate method of analsyses called the Differential Phase Map and will be compared alongside the individual diffraction pattern phasing methods employed.

The following phasing operation was applied. The datasets were individually phased using a copy of the support as the starting point to quickly hone in on the correct phasing

parameters with 50 iterations of PC-HIO followed by 20 iterations of ER. Ten random starts were run for each diffraction pattern and the solutions shifted via cross correlation, twins identified and phase offsets applied. Once satisfied the constraints were correct, the random start solutions were averaged and normalised to the measured diffraction intensity. Two seed reconstructions for each diffraction pattern result; the averaged solution from random starts and a solution from the copy of the support. Cross correlation of these solutions proceed, twins identified and a visual comparison completed to unify the seed solutions. A decision is now required with regards to which seed solution to use for the final phasing operation. If an obvious consistency between reconstructions was observed the solutions were used as seed solutions, however, if no obvious similarity was observed the three reconstructions with the lowest error metric were used as seed solutions for phasing with the diffraction data to produce the final result.

The phasing approach will be detailed for the Fe coated sample introduced previously. The final results of the same operation will be shown and discussed for Ni and Co depositions. An additional analytical tool will be employed, the Differential Phase map, described in Appendix D.1. Any region which is non zero has changed between experimental steps, this allows very subtle variations of phase in an image to be identified. Side by side individual reconstructions are difficult to interpret when the variation is small (a phase variation), hence this method will be applied to try to identify the small scale changes in phase expected.
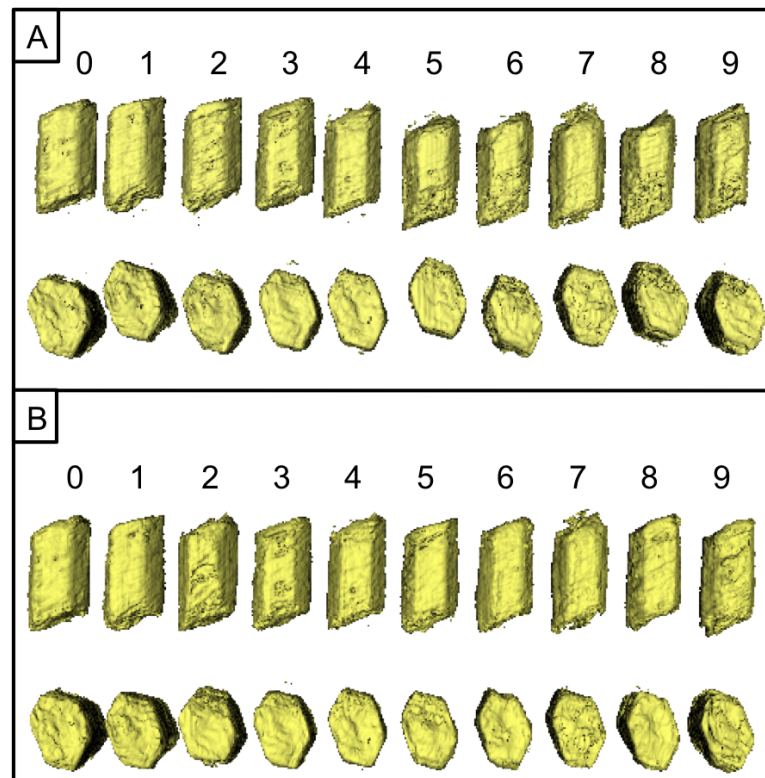
Figure 6.5: (A) 3D isosurface renders of solutions from DS_{54} Sample 139c for 10 random starting points, cross correlation identifies 5 twins (2,3,5,8,9 numbered left to right starting from zero), the shifted solutions and complex conjugates of twins for visual comparison are shown in (B)

Fe *in-situ* reconstruction analysis

The first two stages of the phasing process are demonstrated in Figures 6.5 and 6.6 [3].

In Figure 6.5 ten random starting points were used to obtain 10 solutions (A) using a generic parallelpiped support generated in the initial parameter identification steps. These solutions were phase offset corrected and cross correlated (B) to obtain and implement the correct shift, twins identified and complex conjugates used where necessary when averaging. The phase constraint of $\pm\frac{\pi}{2}$ were used initially to obtain a solid density, the

---

[3]The solutions demonstrated here have not been geometrically corrected and appear skewed as a result.

phase constraints were later relaxed if the algorithm utilised the whole phase range in the reconstruction. Solutions 2, 3, 5, 8 and 9 (numbered left to right starting from zero) were found to be twins, see 'CrossCorrelation.py' output in Appendix B.3 and are visibly inverted in (B). The solutions were then averaged together to produce a seed solution with which further phasing operations were run, akin to the gHIO method [37]. For comparison a copy of the support was used to seed phase retrieval for each dataset as well. In this case five diffraction datasets were phased, each dataset had individual seeds generated (one random average generated without a phase offset correction and one copy of the support). In Figure C.1(A) from left to right, the average solution seed, and copy support seed for consecutive diffraction patterns (DS_{54}, DS_{55}, DS_{59}, DS_{61} and DS_{64}) are shown. The solutions have had their supports optimised with the SW algorithm and were cross correlated to align for visual comparison in (B). If we compare solutions all seeded from average solutions from random starting points for different diffraction patterns, a trend emerges. In (A) (0,2,4,6,8) the reconstructions appear smooth and possess well defined facets, subsequent iterations of the SW support optimisation break the facets up. Alternately phasing from a copy of the support (1,3,5,7,9) produce broken up facets initially and support optimisation smoothes the amplitude, the reason for which is not clear. The phase responds as one would expect, for the average solutions some but not all of the phase features are maintained, solutions from the copy of support maintain their features and change very slightly. The exception to this trend is reconstruction 9, for which the phase is very different after support optimisation and may be due to the complex nature of the crystal structure in the degraded region.

Figure 6.6 shows the same random start solutions with the phase offset correction before

averaging. The results are very different. Large phase modulations are observed and few, if any consistencies between reconstructions are observed. The average amplitudes also vary, with DS_{59} particularly rough compared with DS_{61} suggesting an unknown noise source during DS_{59} measurement. The smoothing trend of the amplitude after SW optimisation remains clear after the addition of the phase offset correction.
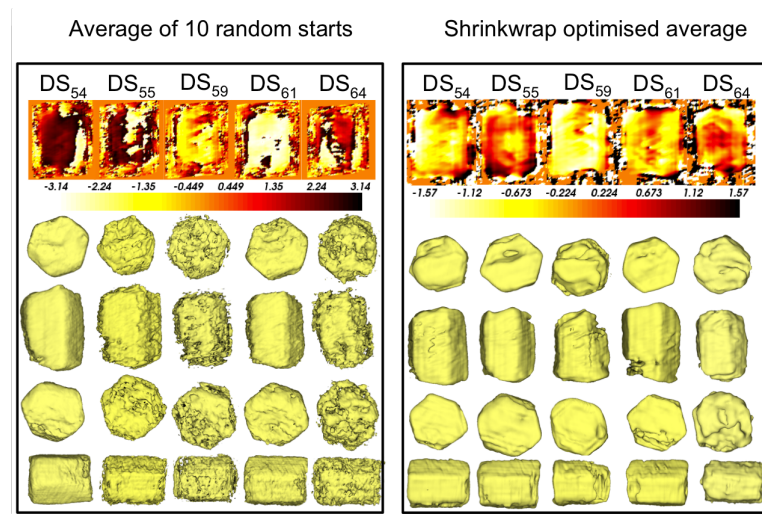
Figure 6.6: From Sample 139c for DS_{54}, DS_{55}, DS_{59}, DS_{61}, DS_{64}, at reference temperature 292°C, after a 1 minute anneal to 400°C, and additional annealing steps of 5,5 and 10 minutes. Cut planes through the phase and multiple views (+y,+z,-y, +x) of 3D renderings of the amplitude isosurface at 18% for both the average of 10 random starts and after support optimisation with the Shrinkwrap algorithm.

Ideally for consistency between shrunk supports to be achieved the solution needs to be enlarged by approximately the resolution of the image, the parameters used for SW in this case are found in Appendix C.1. The lowest E_{nmse}^2 was used to identify the best solution, in this case solution 0, 6 and 7 in (B) at 0.005923, 0.005871 and 0.005726 respectively. There was very little variation in the final nmse values across all reconstructions, in the range, 0.005923 - 0.007250, the PC-HIO E_{nmse}^2 did not impact which dataset produced the lowest error. The three solutions were then used to seed the phasing of all diffraction

patterns. The quality of the reconstructions were compared both with E^2_{nmse} and via visual comparison, renderings of the amplitude distribution and cut planes of the phase are shown with geometric correction applied in Figures 6.7 and 6.8 respectively.

Uniform crystal morphology

The morphology of the crystal was uniform, geometric corrections found the crystal to be 1520nm in length and the three parallel inter facet diameters from the hexagonal cross section 1176nm, 1095nm and 1141nm. The resolution of the datasets at a threshold of 1600ADU were 100nm along its length and 70nm across its width according to the fringe counting approximation. All facets are well defined for the first four annealing steps. The final annealing step shows the breakdown of several facets to an extent, a change greater than the resolution of the data. Accompanied by a variation in the internal phase modulation, see Figure 6.8, of the crystal confirms its physical existence and was not due to noise in the diffraction data.
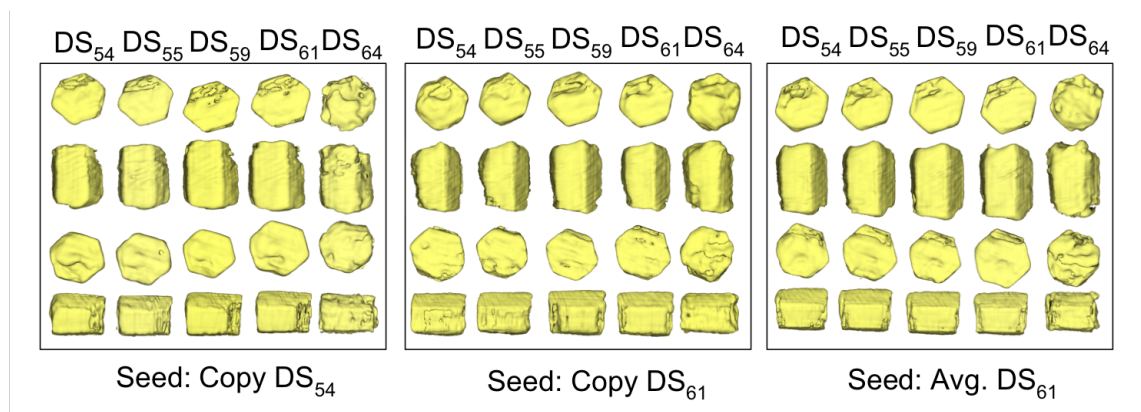
Figure 6.7: 3D renderings of the amplitude isosurface for five annealing steps using solutions DS_{54} Copy, DS_{61} Copy and DS_{61} Avg as seeds for five measured diffraction patterns at different stages of annealing. Note all renderings are not on a commensurate scale.

The phase cut planes shown in Figure 6.8 are taken along the Q vector direction. A consis-

tent phase variation was observed below the origin of the Q vector, the two distinct phase gradients are observed at the top and base of the crystal. The orientation was not definitive, the twin solution may in fact be the correct orientation as the crystal morphology was symmetric[4]. An interaction was expected between the crystal and the substrate, zinc diffusion into the SiO_2 layer was discussed in Section 3.4. In the reconstructions this would exhibit as an asymmetric feature on one of the $00l$ facets in the direct space reconstruction. We observe large phase modulations on both facets therefore cannot distinguish the correct orientation of the crystal. Phase modulations on the $00l$ facets were also inconsistent between different crystals. An Fe coating was expected on the left and top facets from the readers perspective, due to the evaporation angle. Diffusion of Fe into the ZnO structure would lead to an expansion on the Fe coated facets. The last reconstruction for each seed shows a considerable variation in the phase structure compared to the previous four reconstructions, as expected from the diffraction data in Figure 6.4. Previous experiments observed heavy crystal degradation, to the point where the diffraction patterns were too complex to reconstruct.[5] It is concluded that Fe is scavenging oxygen from the crystal and forming Iron oxide phases as opposed to diffusing into the ZnO crystal.

If we were to observe the expected diffraction intensities of the reconstructions (FFT^{-1}) the E_{nmse}^2 values show they are very similar. By thresholding the solution and recalculating the measured intensities, one can establish if the variation in diffraction corresponds to noise or a specific physical feature in the reconstruction. For these data this was not possible, the change was too small to pinpoint a physical feature that corresponded to the

---

[4]The twinned solution would demonstrate the same physical attributes, its phases are conjugated and the Q vector inverted.

[5]Too little crystal remained to achieve sufficient statistics in the measured diffraction patterns post annealing iterations.
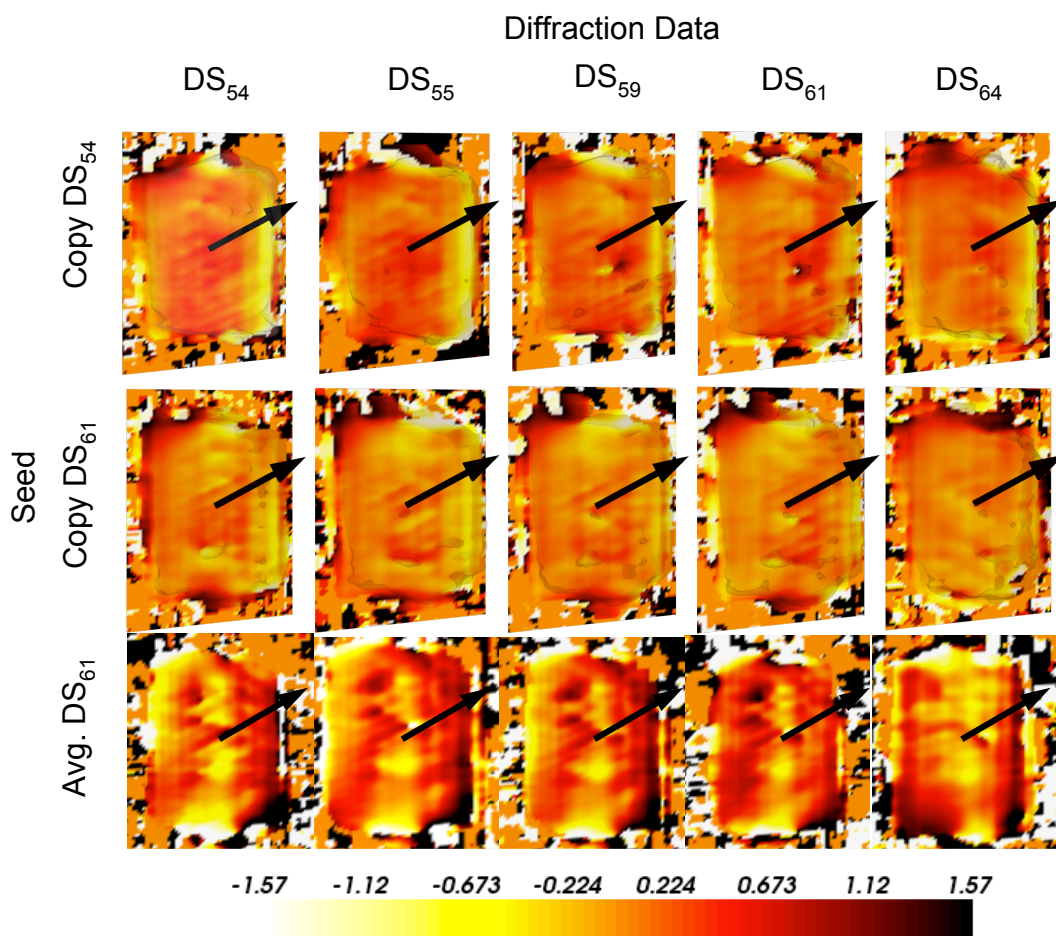
Figure 6.8: Phase cut planes along the Q vector direction (arrow) for three seeds 0, 6 and 7 used as starting points for the reconstruction of 5 diffraction datasets (left to right increasing annealing steps)

diffraction change.

The phase variation between reconstructions observed thus far appears small. In this scenario a Differential Phase map approach can be applied to try to reconstruct the variation due to each annealing step. The calculated reciprocal space phases for each diffraction pattern are used as the missing phases for the other four measured diffraction patterns. The results are shown in Figure 6.9, the data has been geometrically corrected, the modulus of the difference was plotted.
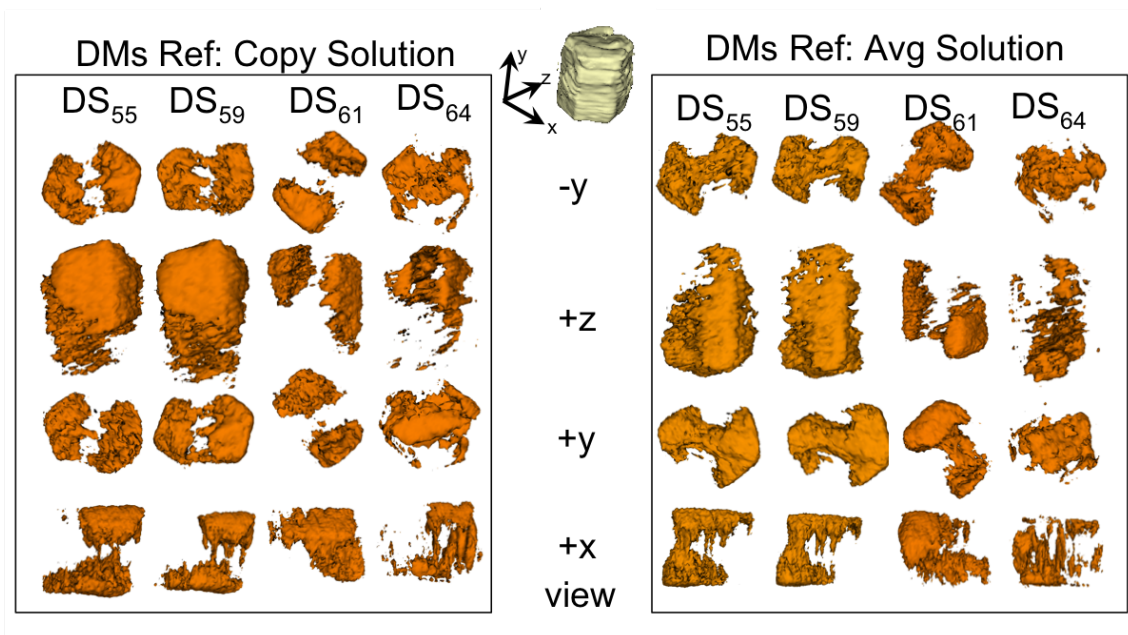
Figure 6.9: Differential Phase maps using both Copy and Avg. seed solutions from DS_{54} as the reference reconstruction for the remaining four annealing iterations of Sample 139c.

The interpretation of the differential phase maps for both starting points produce are the same. Two regions of density opposite one another suggest a change in the crystal structure on both sides of the crystal. The crystal in question had a layer of Fe deposited from one position hence a change would only be expected on one side of the crystal. This can be interpreted as a miscentering of the two datasets relative to one another, the resulting gradient in the phase between the two would exhibit as two positive lobes in the plotted modulus. In our case the first three annealing steps demonstrate variations of the two lobed structure, the third DS_{61} has a rotated lobe feature attributed to miscentering in multiple dimensions. The final dataset does not show the lobe features instead modulations are observed throughout one end of the crystal. The modulation is not uniform and is unlikely to be due to diffusion effects, the formation of iron oxide phase cannot be ruled out.

As the data has been binned it could be shifted with sub-pixel resolution to recenter the data and remove this gradient. This process was implemented for the data in Figure 6.9. It remains possible an underlying gradient will remain. The solution is to interpolate the data. As we expect to observe a phase modulation which is non linear this step is not required until quantitative analyses are made. We conclude from the lack of observed phase modulation evolution between annealing steps the Differential Phase map approach is unsuitable for these particular problems.

Ni *in-situ* reconstruction analysis

The final reconstructions for Ni data is shown in Figure 6.10.

Sample 115 demonstrates a general trend towards crystal degradation and was expected from the diffraction data, the reconstructions are however very inconsistent. The amplitude distribution is very asymmetric and is not expected for single crystal rods. The source of this feature in the reconstructions will be discussed fully in Section 7.1.

Sample 123 shows a large change after the final annealing step. The algorithms struggle to find a uniform direct space amplitude distribution. Agreement was observed between the phase modulation before the onset of the reaction after which the crystal had changed so much an evolution would not be seen.

The low solubility of Ni in ZnO suggests changes of this nature are unlikely a result of Ni integration into the ZnO lattice but rather NiO cluster formation.
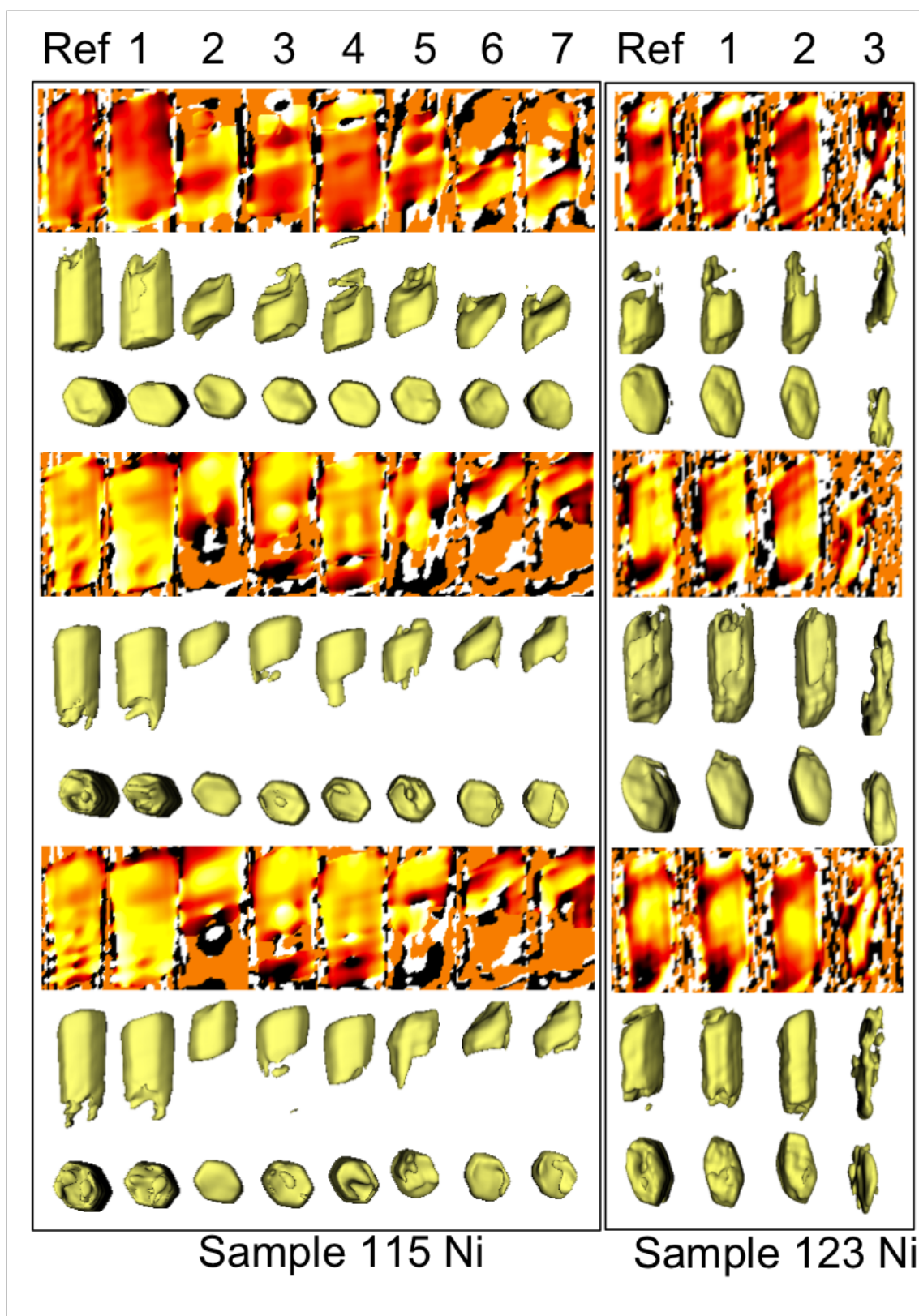
Figure 6.10: Phase retrieval solutions from three different seeds for two crystals (Sample 115 Ni, Sample 123 Ni) deposited with Nickel and annealed and quenched through several steps. The geometric correction was not implemented.

Co *in-situ* reconstruction analysis

The final reconstructions for Co data is shown in Figure 6.11.

Sample 113 demonstrates no change upon annealing with a deposited Co layer. Very little change was observed between reconstructions and agrees with the minimal changes (of the order of the noise) observed in the diffraction patterns.

Sample 115 shows a similar amplitude distribution observed for a Ni deposition on sample grown under identical conditions. The larger aspect ratio of crystals means that each scatterer is no longer coherent relative to every other scatterer of the crystal. A partial coherent illumination results and the phase retrieval process leads to erroneous amplitude modulation, again this will be covered in more detail in Section 7.1. The 3D renderings of the diffraction data showed a very slight variation, the reconstructions do not provide sufficient consistency to conclude the crystal has in fact changed in some way.

Multiple Bragg peaks from a single crystal

It is important to highlight the experiments discussed thus far have measured a single Bragg peak from a ZnO crystal and are only sensitive to displacements in the measured crystal in one dimension. Improvements in experimental technique have allowed us to measure multiple Bragg peaks from a single crystal. This method, initially only possible in the unfocussed mode of operation identified important consequences for the longitudinal coherence properties of the illuminating x-ray beam. It also opens the door to multi-dimensional displacement fields from the same crystal, displacement fields with overlapping
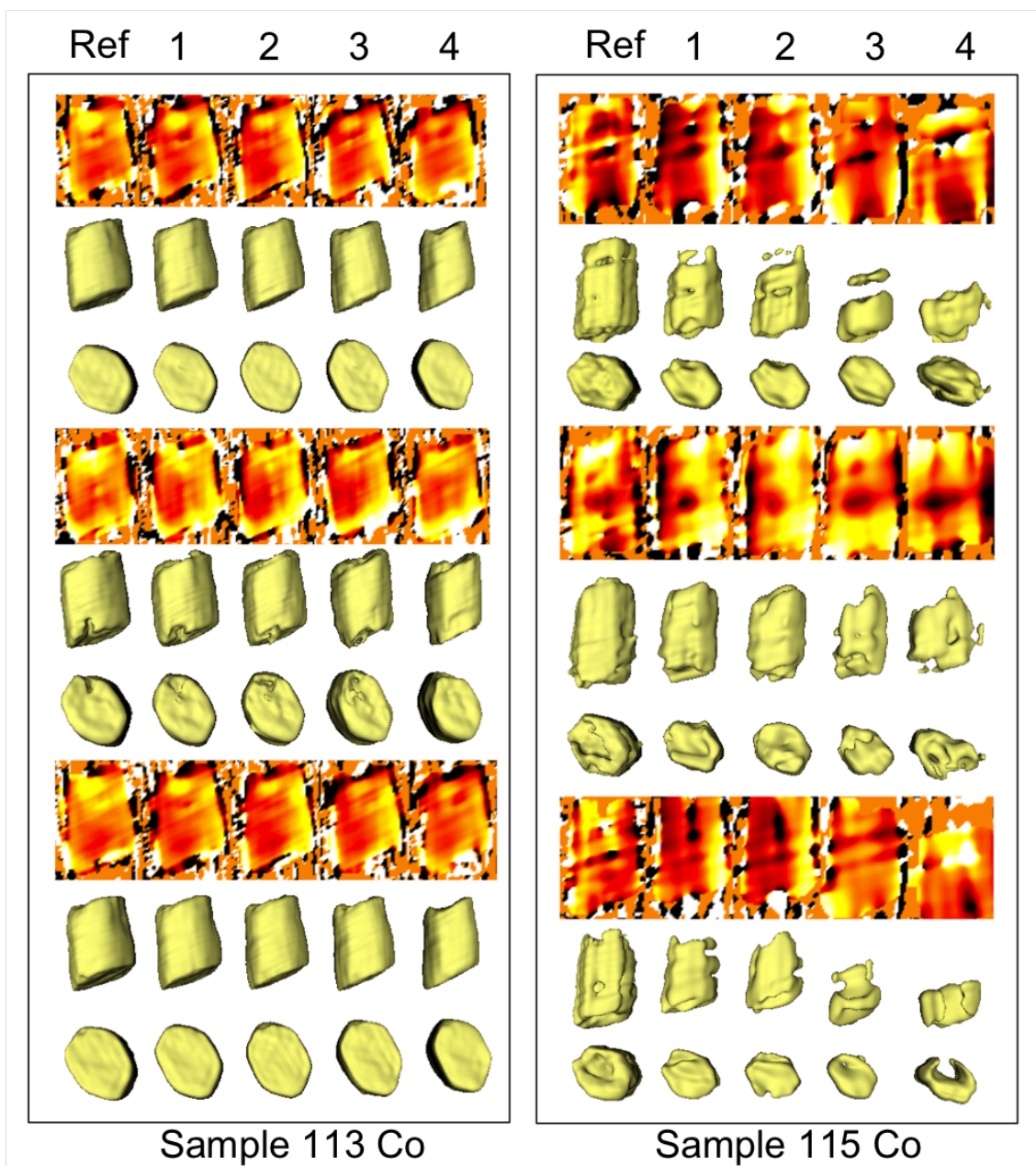
Figure 6.11: Phase retrieval solutions from three different seeds for two crystals (Sample 113 Co, Sample 115 Co) deposited with Cobalt and annealed and quenched through several steps

components can also be used to verify the quality of the reconstructed solution. This will be comprehensively described in Chapter 7.

6.2.6 Refraction Correction

Refraction occurs when a wave travels from one material to another where the refractive indices of the two mediums are different. In our experiments there are three mediums to consider; air, vacuum and ZnO crystal. At 8.9KeV the refractive index difference between x-rays in air and vacuum is negligible. We apply a correction to the recovered phases in direct space according to the method exhibited by Harder et al. [79].

$$n = 1 - \delta - i\beta \qquad (6.1)$$

For ZnO the real part of the refractive index, n, is less than unity by δ=1.308x10^{-5} [6], relative to an x-ray in vacuum in parallel to that passing through the crystal the maximum phase difference ($\Delta\phi$) can be calculated using the following equation:

$$\Delta\phi = kd\delta \qquad (6.2)$$

where d is the path length for an x-ray through the crystal. For a 1μm ZnO crystal, $\delta\phi$=0.59rad. The attenuation over the path length is $\sim$1% ($kd\beta$, where β=2.24x10^{-7}) therefore absorption can be neglected. In actuality the experimental geometry increases

---

[6]http://henke.lbl.gov/optical-constants, were used to calculate both δ and β for ZnO, ρ_{ZnO}=5.67gm/cm^3, at 8.9 KeV (λ=0.138nm, $k=\frac{2\pi}{\lambda}$=45nm^{-1})

the optical path length difference for a crystal of a specific dimension.

The refraction effect is exacerbated by the amount of crystal the illuminating beam has to pass through. The majority of the reconstructions correspond to a crystal stood on end, i.e the short dimension determines the refraction correction for a 1μm ZnO crystal. A rod laying on its side with long axis parallel to the beam would see a significant impact due to refraction. In Figures 6.12 and 6.13 the generated reconstruction of DS_{54} has had its direct space phases set to zero, the refraction correction is then applied to demonstrate the relative offset. The crystals morphology is shown by a translucent isosurface, scalar cut planes through the corrected phase at regular intervals are shown along the length and the width of the ZnO rod in Figures 6.12 and 6.13 respectively. For a 1.5μm crystal the maximum phase offset was 0.849 radians observed to the left of the center of the rod where the maximum optical path length through the crystal for scattered x-rays is found. Moving towards the edge of the crystal along the positive Q-vector direction the path length is decreased and equally in the negative Q-vector direction beyond the observed maximum the path length decreases.

In Figure 6.13 the top view of the ZnO rod is shown and scalar cut planes of phase modulation corrections are uniform between cut planes as the optical path length remains approximately identical for each slice of scatterers[7]. The observed phase corrections again demonstrate an asymmetric phase modulation, the maximum was observed left of the center of the crystal along the negative Q-vector direction and matching gradients to those seen previously from the side view.

---

[7]When the $001/00\bar{1}$ are approached the phase retardation will decrease as the optical path length difference decreases.
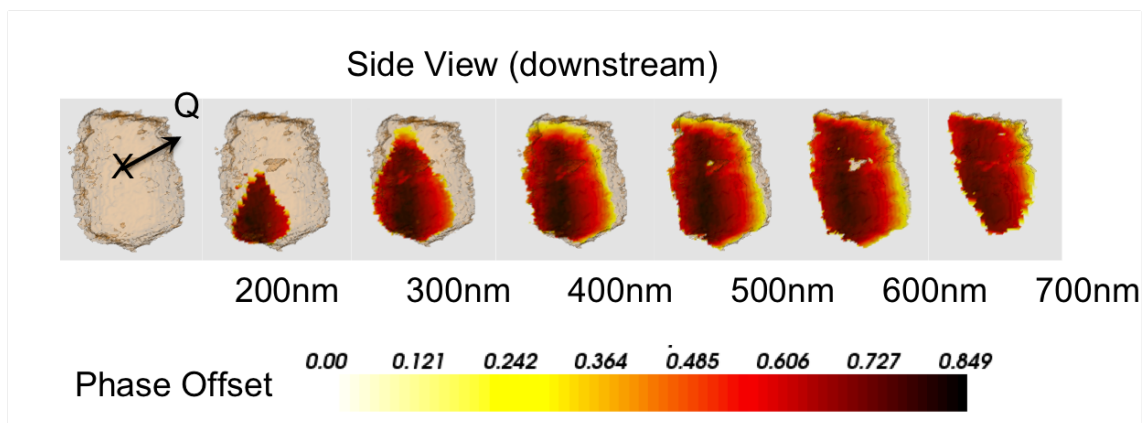
Figure 6.12: A side view of a reconstructed ZnO rod (DS$_{54}$, 1.5μm x 1.0μm) stood on end from the illuminating source perspective, scalar cut planes through the refraction corrected phase at regular intervals along the incident beam direction.
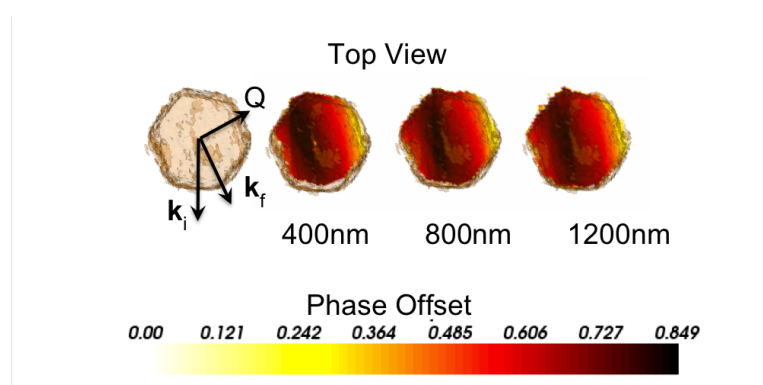
Figure 6.13: A top view of a reconstructed ZnO rod (DS$_{54}$, 1.5μm x 1.0μm) stood on end, scalar cut planes through the refraction corrected phase at regular intervals along the crystals c-axis
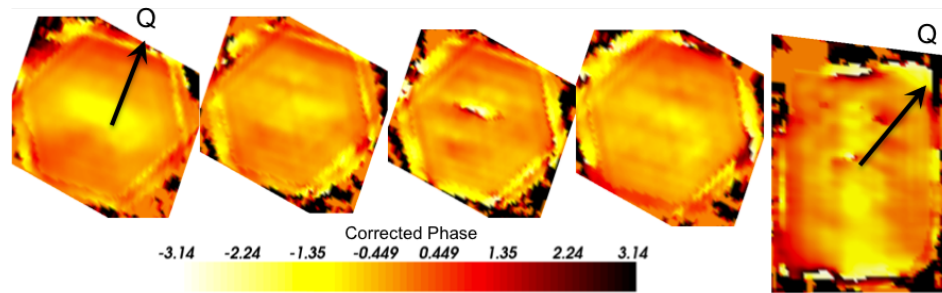
Figure 6.14: Cut planes through the refraction corrected phase at regular intervals (bottom to top) along the crystals c-axis and a side view equivalent to *Figure 6.8* Avg. DS_{61} Seeded phase retrieval of DS_{61}.

The refraction correction was considerable and provides an insight into the origins of some of the phase modulations observed in unprocessed crystals. It does not detract from the evolution of the crystal morphology discussed in the *in-situ* experiments as the offset correction is identical for each measurement.

The refraction phase correction was applied to DS_{61} Fe Sample 139c, see Figure 6.8. No change was expected upon this iteration so a phase corrected reconstruction would demonstrate the crystal in its as grown state. Cut planes through the phase are shown in Figure 6.14. The phase modulations observed previously have been removed, along the positive Q vector direction a positive phase shift of π represents an expansion and a smaller positive phase shift, $5/8\pi$, in the negative Q direction describes a contraction. The expansion remains relatively constant along the length of the rod and the contraction decrease in size towards the top. Again it is difficult to attribute any of the observed phase modulations with practical origins.

6.3 Resolution

When we discuss resolution we separate the phases and amplitudes. A single wrap in the phase across a crystal corresponds to a shift from the equilibrium lattice by a single lattice parameter. The resolution of the phase is difficult to quantify and is defined by the asymmetry around a Bragg reflection. The signal to noise ratio defines the ability to determine asymmetry. On average phase changes of the order 0.15rad are resolvable corresponding to 1/40th of a ZnO lattice parameter. The phase modulation describes the shift of a portion of crystal i.e the size of which is defined by the resolution of the amplitude. The resolution of the amplitude can be estimated by the size of the crystal divided by the number of resolvable crystal fringes along that dimension. The ability to reconstruct the outer fringes defines the resolution and the reconstructed phases have the greatest impact on the resolution of the image. When multiple solutions have been measured it is common to define the Phase Retrieval Transfer Function (PRTF) of the data equivalent to the Modulation Transfer Function for a lens, defined in Equation 4.3.

If a perfect average reconstruction were generated a step function would be expected, PRTF = 1 for all spatial frequencies up to a cutoff frequency, the resolution limit, where PRTF = 0. The PRTF function for a solution generated from a copy of the support is shown in Figure 6.15, the PRTF is close to 1 for all values up to a cutoff frequency of 0.018nm^{-1} corresponding to a $\sim 28\text{nm}$ half period. This is not an acid test for the associated error on the resolution of our reconstructed solution, it does demonstrate the resolution limit. By taking an average solution from many random starting points the reproducibility of the phases reconstructed at higher frequencies is tested.
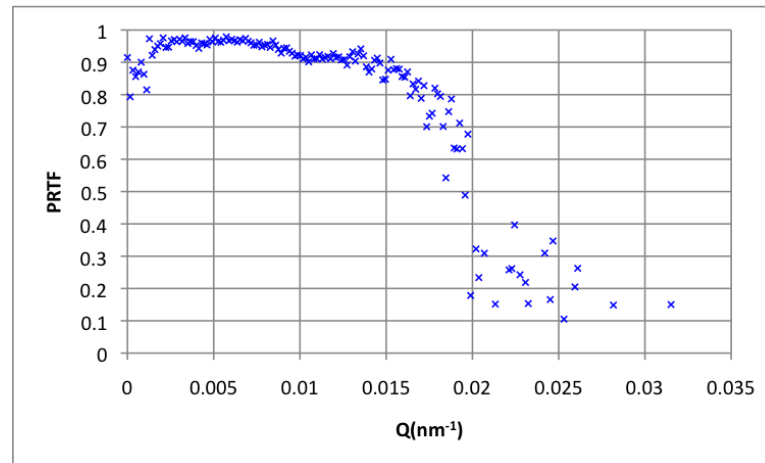
Figure 6.15: PRTF of a reconstructed solution generated from DS_{54} Sample 139c (July 08) using a copy of the support as a starting point and the SW algorithm for support optimisation.

Figure 6.16 demonstrates the PRTF generated from the average of 10 random start re-constructed solutions for the same dataset (Sample 139c (July 08)). The reconstructed crystal is 1.5μm in length and 1μm in width (hexagonal parallel facet separation), the threshold was set to approximately 10 photons (1600 ADUs). At low Q (low frequencies in direct space) the PRTF is low, we would expect it to be closer to 1, and likely due to a lack of statistics, the first datapoint considers only 7 voxels compared to 45,000 voxels at higher frequencies. The peak of the PRTF is observed at 0.6 (0.0025nm^{-1}) corresponding to a 161nm half period in direct space. The PRTF slowly drops and several peaks are observed at 86nm, 56nm and 38nm half periods. The 56nm peak is large, the likely source are the phases corresponding to the fringes generated due to the hexagonal facets. Here three sets of parallel facets of equivalent resolution will correspond to a larger number of voxels, compared to the set of fringes due to the parallel facets perpendicular to the c-axis. As the crystal is large along the c-axis we would expect lower resolution along the length of the crystal, hence the PRTF would be expected to drop due to irreproducible
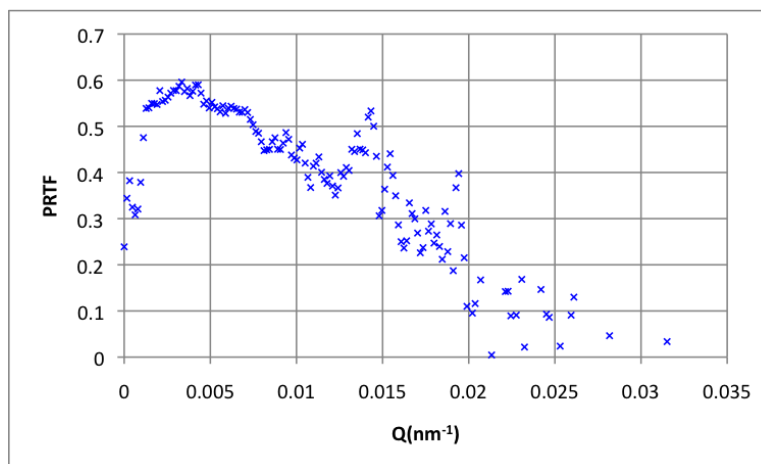
Figure 6.16: PRTF of an solution generated from 10 random starts for DS_{54} Sample 139c (July 08)

phases at higher frequencies and a peak observed where the phases corresponding to the reconstructed hexagonal parallel facets dominate. The python code used to generate the PRTF function can be found in Appendix G.4

6.3.1 Summary

The *in-situ* experiments involving an Fe deposition routinely changed the crystal morphology at a temperature of 400°C for 10-20minutes. The observed modulation in the amplitude suggested a more vigorous solid state reaction than diffusion, the formation of secondary phase of iron oxide has been observed previously in experiments of this nature [16,200] and is the likely source of the effects observed in this study. As a direct result of the lack of phase modulation evolution the interpretation of the Differential Phase maps proved difficult and deemed unsuitable for analysis of crystal variation of this order.

The *in-situ* experiments annealing ZnO with a deposited Ni layer confirmed a solid state

reaction consistent with a scavenging type process observed previously upon annealing with an Fe layer. The formation of NiO clusters destroys the ZnO lattice.

The *in-situ* experiments involving an evaporated Co layer upon annealing showed no evidence for a solid state reaction and was somewhat surprising considering the previous reports of a high Co solubility in ZnO.

The refraction correction was found to be considerable for ZnO crystals on the micron length scale. Application of the refraction correction to reconstructed data proved inconclusive, however did reduce the reconstructed phase modulations.

The formulation of the PRTF function confirms the phases in the low intensity fringes are considerably harder to reconstruct and limits the resolution to fringes with considerable statistics.

Chapter 7

Multiple Bragg Reflections

The coherent diffraction patterns surrounding five Bragg peaks of the same ZnO micro-crystal have been measured for the first time. For a large aspect ratio (4:1) ZnO crystal the degree of coherence can be determined via the visibility providing a coherence estimate on a different length scale for each Bragg peak. Combined with eleven Bragg reflections from a small aspect ratio crystal (3:2) the longitudinal coherence function of the incident radiation was mapped. Two illumination regimes were studied; fully coherent and partially coherent illumination, the consequences of a partially coherent illumination for the reconstruction of a crystal are discussed [102]. Sufficiently coherent diffraction patterns were combined to produce a two dimensional displacement field of the crystal studied. A three dimensional displacement field was later generated [138], based on the observed coherence effects a suitably smaller crystal was imaged.
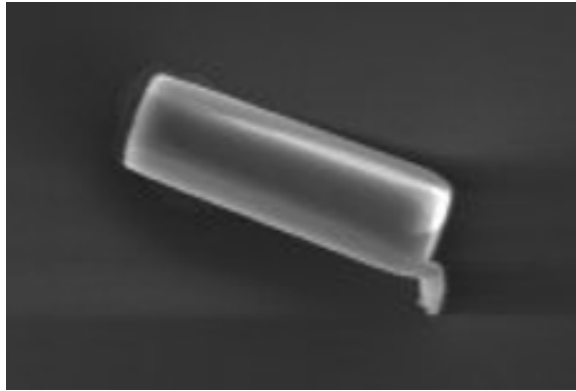
Figure 7.1: Scanning Electron Micrograph of the crystal from which 5 Bragg reflections were measured, the field of view is 4μm x 6μm, a slight taper is evident and the bright feature on the 100 facet parallel to the substrate on top of the crystal is due to charging effects in the SEM

7.1 Multiple Bragg Reflections from a ZnO crystal

The large aspect ratio ZnO microcrystal was prepared via micromanipulation as described in Section 3.4.1 on a silicon (100) substrate, using the unfocused mode of operation an orientation matrix obtained and five different Bragg reflections were measured from the crystal; (100), (010), (011), (101) and (002). The sample was characterised using SEM, Figure 7.1 and is shown during micromanipulation stages in Figure 3.7, the crystal has well defined facets and a halo observed post oxide growth corresponding to Zn diffusion into the SiO_2 layer during thermal oxide growth. The crystals dimensions were measured to be 4.08μm x 1.10μm commensurate with the fringe spacing from the observed diffraction patterns.

The longitudinal coherence length of the incident x-ray beam is of the order 0.7μm, the transverse coherence components are larger than the crystal dimensions ($>10\mu$m). For different Bragg reflections the optical path length difference (OPLD) between incident
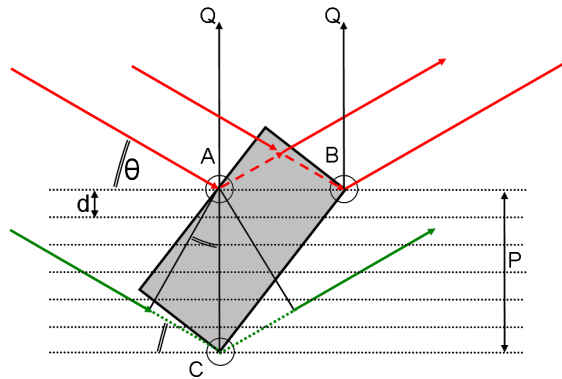
Figure 7.2: Schematic of diffraction from point scatters A,B and C for OPLD calculation; $\text{OPLD}_{AB} = 0$, $\text{OPLD}_{AC} = 2\text{BC}\sin\theta$

x-rays scattering from the extents of the crystal will change. When the OPLD exceeds the longitudinal coherence length the crystal is defined as under a partial coherent illumination. Upon a partial coherent illumination of a crystal the distribution of intensities is no longer a full contrast interference pattern. A combination of interference between coherent components and addition between incoherent components results and is quantified by a drop in the fringe visibility, equation 2.16.

Figure 7.2 shows a crystal (grey rectangle) illuminated at the angle satisfying Braggs Law for a set of lattice planes that lie perpendicular to the reciprocal lattice vector Q. The OPLD between two coherent x-rays scattering from points within the same plane (A and B) will be zero, hence the longitudinal coherence is independent to the length of the crystal perpendicular to the Q-vector. If two scatterers (B and C) are positioned at the extreme extents of the crystal, the OPLD (dotted line through point C) in this scenario is simply the product of the plane layer spacing d with the number of planes between the two scattering points with an additional angular scaling given by Braggs law [23]. This

length equates to the projection of the long axis of the crystal onto the Q-vector and is therefore the maximum OPLD of the measurement. Hence, measurement of a finite crystal in the Bragg geometry using CXDI is viable if the longitudinal coherence is greater than the projection of each of the crystals dimensions onto the Q-vector. If the inequality is violated the fringes will become less visible in, at least, that direction.

Multiple values of the OPLD are probed for a given crystal by the simple expedient varying Q by observing multiple Bragg peaks. The visibility of the same c-axis data can be compared among these measurements. Diffraction data were sampled by extracting a line of points through the measured distribution of the Bragg peak oriented along the 002 crystal direction in reciprocal space. The results for the 5 Bragg reflections are shown in Figure 7.3 and the sampled points (green line) for each diffraction pattern highlighted in the corresponding 3D renderings of the isosurface (blue diffracted intensities).

The fringes are clearly visible in the 100 and 010 reflection, less visible for 101 and 011 and not visible for the 002. The interference between two facets is equivalent to the 1D slit function derived in Chapter 2 shown in Figure 2.5 (c). We fit Lorentzian functions using MATLAB[1] to the maxima and minima of the fringes to obtain the visibility, see Figure 7.4. The decrease in fringe visibility as a function of the projection of the crystals c-axis along the Q-vector allows us to map out the coherence function of the source.

Figure 7.5 shows these data combined with 11 additional Bragg reflections from a small aspect ratio ZnO crystal, dimensions 1.6μm x 1μm. Sampled points for the additional

---

[1]The Mathworks, MATLAB Version 7.7, R2008b. Fits were determined at high Q either side of the bragg peak independently to avoid asymmetry due to strain in the interference pattern impinging on the estimate of the degree of coherence
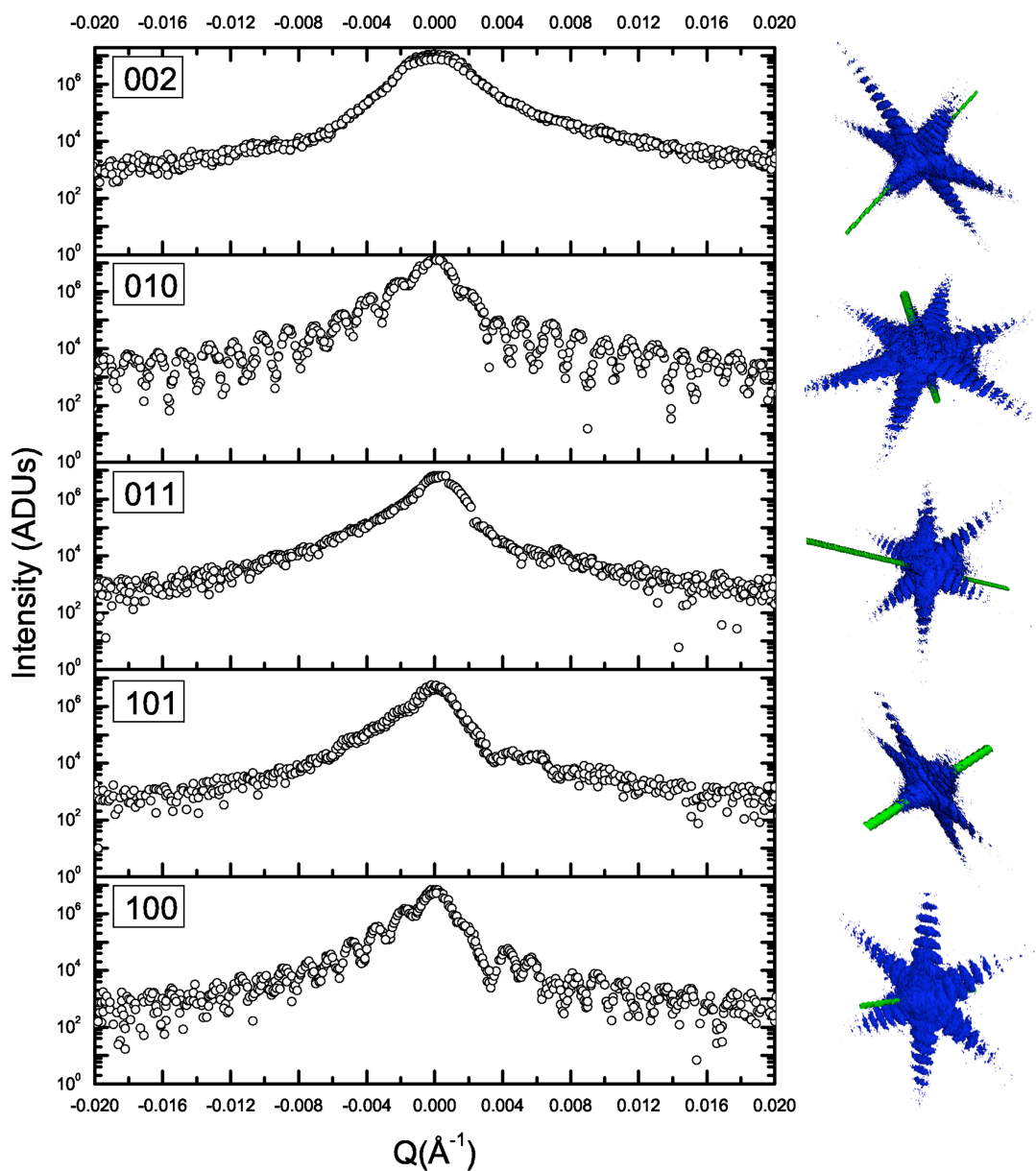
Figure 7.3: Measured intensity as a function of momentum transfer deviation along the 002 crystal direction (reciprocal space) demonstrating the 002 fringe visibility for 5 different Bragg peaks from the first ZnO nanocrystal (Left). The data points sampled are highlighted (Right) as a green solid line through the measured diffraction data, blue iso-surface
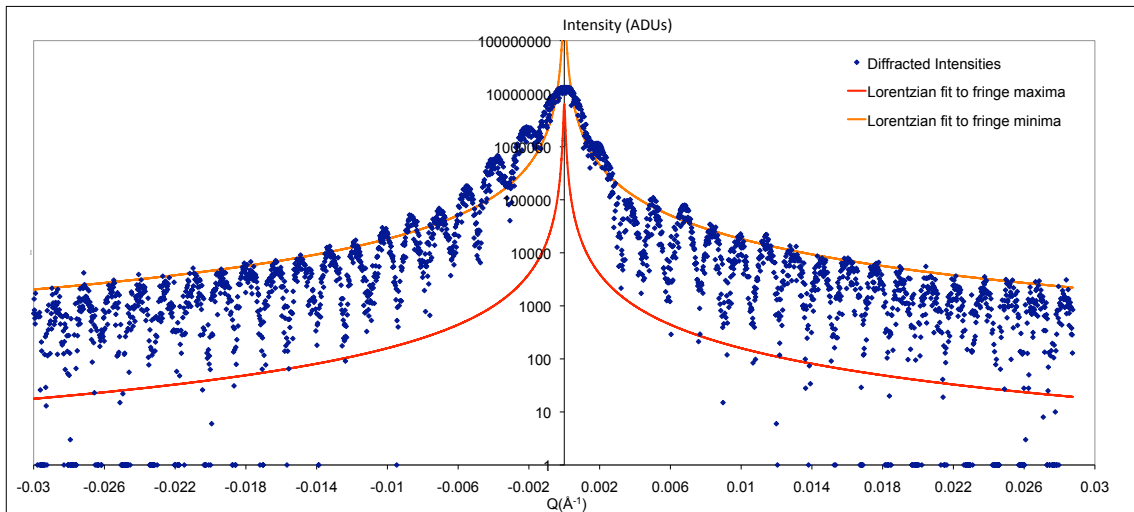
Figure 7.4: Lorentzian fits to the maxima and minima of the fringe system generated along the 002 crystal direction measured at the 100 Bragg reflection

reflections can be found in Appendix 1 E.1. A Gaussian function fitted to the coherence function has a Half Width Half Maximum (HWHM) of $0.66\pm0.02\mu$m, we take this width as an estimate of ξ_L it implies a wavelength spread; $\Delta\lambda/\lambda$=1.07x10$^{-4}\pm$0.16x10^{-4} and is within the expected range (1.0-2.9x10^{-4}) for a Si(111) monochromator at 9keV [7,38].

The effect of a partially coherent illumination on the ability of the phasing algorithms to reconstruct the electron density was investigated. The direct space reconstructions of both 010 and 101 reflections of crystal 1 are shown in Figure 7.6, the raw data possess visibilities of 96$\pm$3% and 25$\pm$10% representing both the fully coherent (010) and partially coherent (101) geometries. The coherent 010 reconstruction has well defined facets with a uniform amplitude distribution and the region of low amplitude in the bottom right corner was attributed to a strained region of the crystal. The partially coherent 101 reconstruction has one well defined facet and one rough end and is an incorrect solution for the diffraction data according to the uniform morphology identified using SEM and
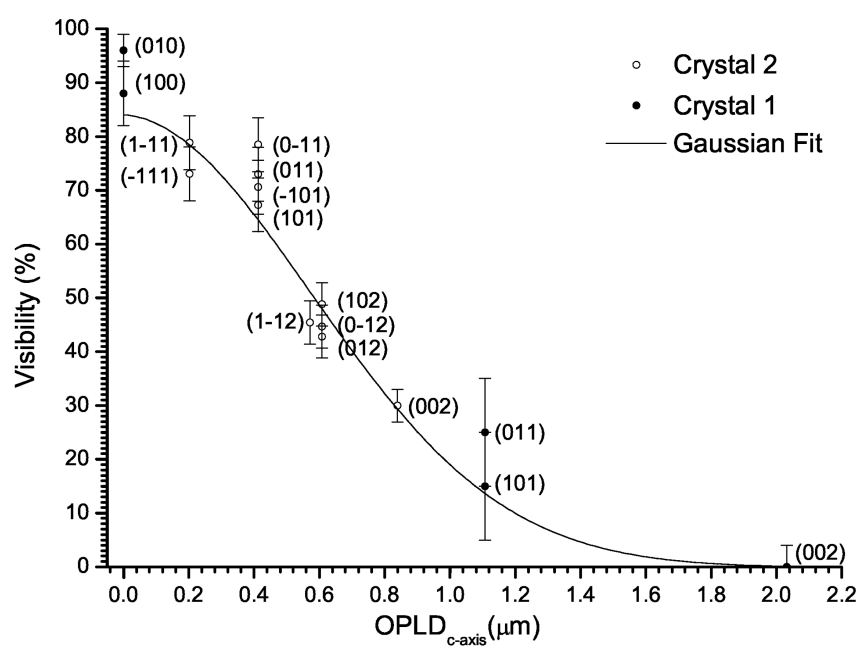
Figure 7.5: Visibility as a function of OPLD for 16 Bragg reflections measured from 2 separate ZnO crystals.
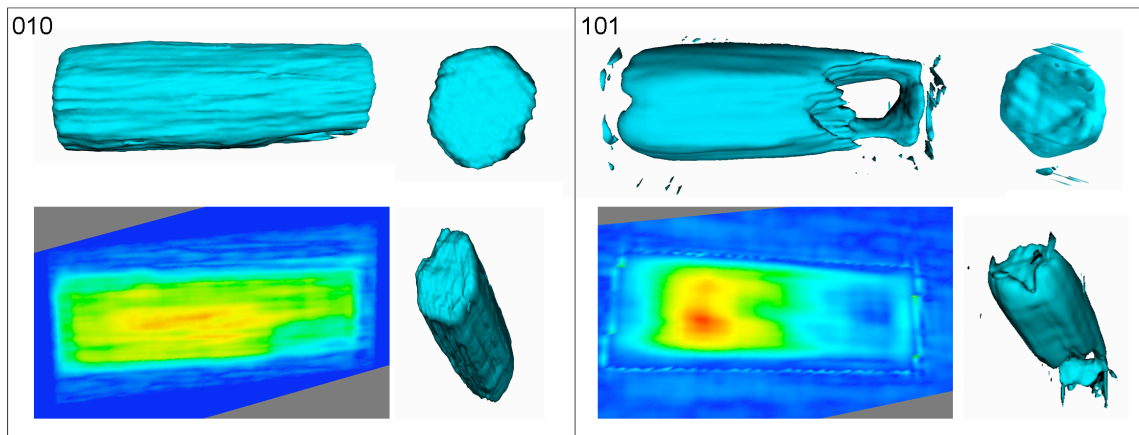
Figure 7.6: Corresponding isosurface and scalar cut planes of the reconstructed density of crystal 1 using diffraction data surrounding the 010 and 101 Bragg reflections, as labeled.

fully coherent reconstructions. The spacing of interference fringes defines the size of the object and the number of fringes defines the resolution of the image obtained. When this information has been smeared out by a lack of coherence, the phasing algorithm seeks a solution which would mimic this behavior. Practically, this could manifest as a crystal with two facets along the direction of interest, one flat and the other rough.

Scanning Electron Micrographs and fully coherent Bragg reflections confirmed the crystal size for the two reflections to be 4.08μm x 1.10μm. In the 010 case the reconstruction accurately reproduced the crystal dimensions and in the 101 case the reconstruction was less than half the size of the actual crystal (2μm) with the high amplitude region superimposed on a lower amplitude correct representation of the crystal. Features of this type were coined 'hot spots' and were first predicted by Vartanyants *et al.* [190], and observed in 2D reconstructions from Au nanocrystals by Williams *et al.* [212]. As the fringe visibility drops, the algorithm finds a superposition solution of a low amplitude fringe pattern and high amplitude fringeless pattern creating a 'double image; this appears in direct space as

a low amplitude full size representation of the object and a superimposed, foreshortened 'hot spot. From the five measured reflections only two, the (100) and (010) are sufficiently coherent to reconstruct an accurate representation of the crystal.

7.2 Combining reconstructions

The independent reconstructions of the (100) and (010) can be combined to generate a two dimensional displacement field. In order to measure multiple Bragg reflections a crystal must be manipulated over large angles with high precision in order to satisfy different Bragg conditions. Therefore the reconstructions are misoriented in the lab reference frame in both morphology and consequently voxel axes. Hence a reverse rotation around the goniometer angles measured at each reflection brought the reconstructions into alignment, an interpolation was required to resample the rotated solution onto a uniform voxel grid (50nm voxel dimensions) and finally a real cross correlation (amplitude only) was required to overlay the reconstructions via a simple translation (ambiguous solution).

Reconstructed amplitudes for the two reflections are shown in Figure 7.7 and phases in Figures 7.8 and 7.9 for the (010) and (100) respectively, they were produced using the Shrinkwrap method with a scaled version of the autocorrelation function of the diffracted intensities as a starting point [138].

For analysis of the reconstructions it is necessary to employ the Bravais-Miller (h, k, i, l) notation, see Appendix B.4. We define the facet in contact with the substrate $(\bar{1},0,1,0)$ and the smallest end of the crystal the $(0,0,0,\bar{1})$.
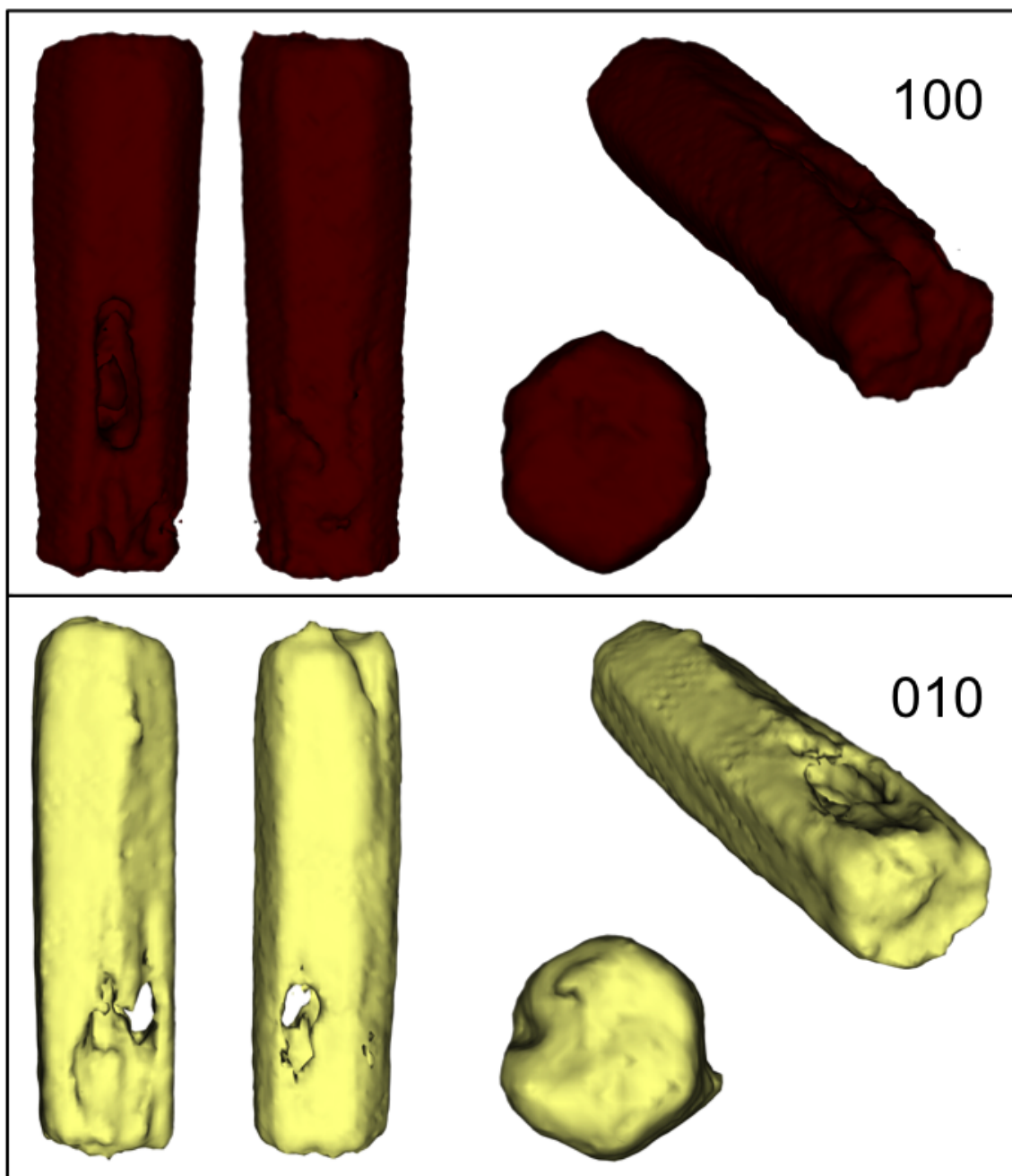
Figure 7.7: Corresponding 3D renders of the amplitude of the reconstructed density from diffracted intensities measured at the 100 and 010 Bragg reflections, as labeled. Note a manual rotation was used to compare the two reconstructions.
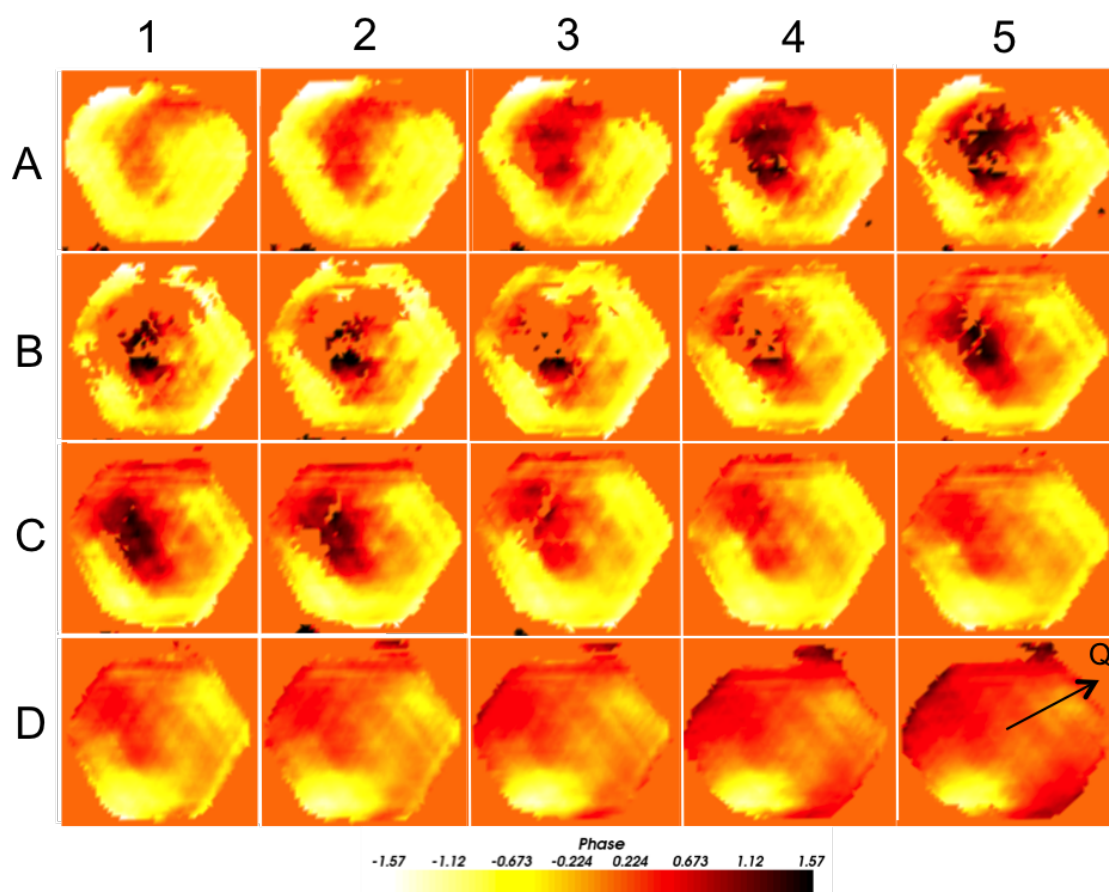
Figure 7.8: From left to right (numbered, 1-5) and top to bottom (letters, A-D) Scalar cut planes through the phase of the (010) reconstruction perpendicular to the c-axis at 200nm intervals along the length of the rod beginning at the smallest end of the tapered rod, A1, and finishing at the largest end, D5.
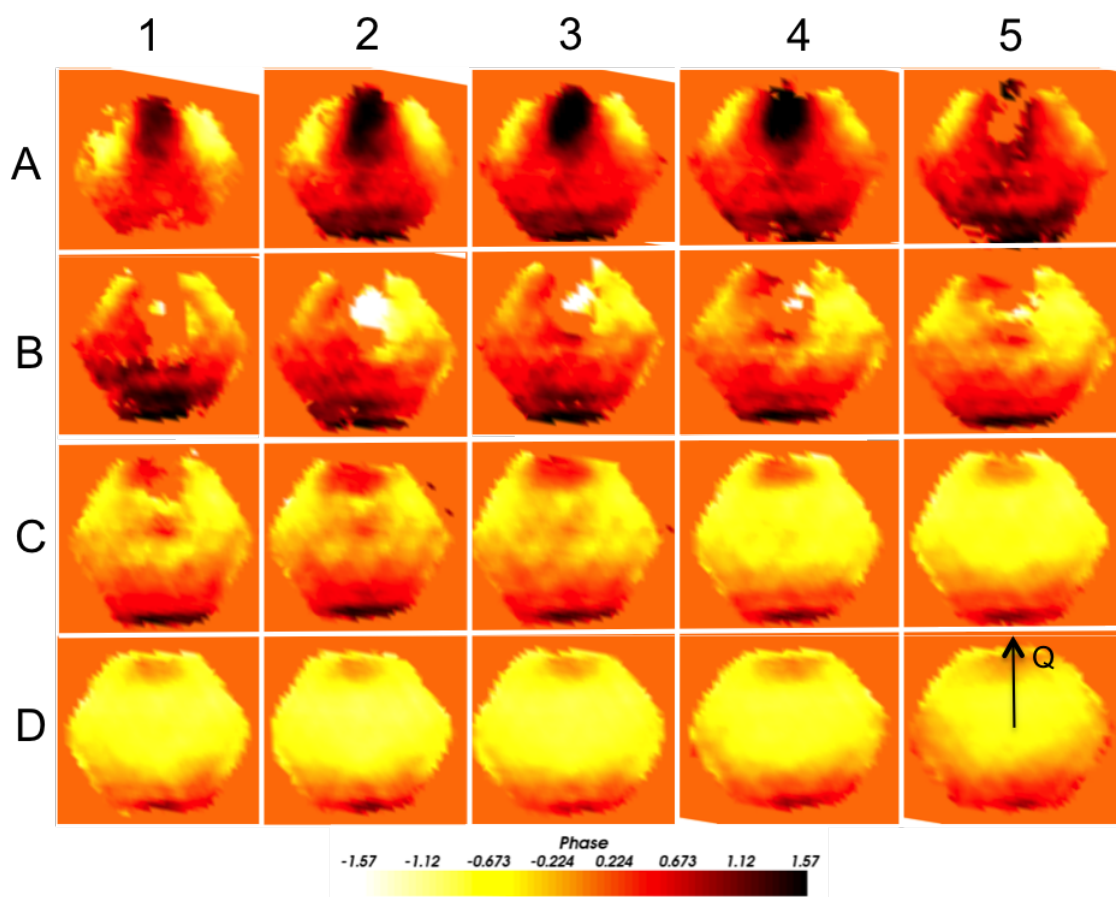
Figure 7.9: From left to right (numbered, 1-5) and top to bottom (letters, A-D) Scalar cut planes through the phase of the (100) reconstruction perpendicular to the c-axis at 200nm intervals along the length of the rod beginning at the smallest end of the tapered rod, A1, and finishing at the largest end, D5.

A distinct low amplitude region presents in both reconstructions at the smallest end $(0,0,0,\bar{1})$ of the tapered large aspect ratio microcrystal. In the 100 reconstruction a region of missing density was observed on the $(1,0,\bar{1},0)$ facet and on the $(1,0,\bar{1},0)$ and $(0,1,\bar{1},0)$ for the 010 reconstruction. The missing density extends through to the base $(\bar{1},0,1,0)$ facet of the 010 reconstruction. The 100 $(\bar{1},0,1,0)$ facet is not as well defined near the $(0,0,0,\bar{1})$ facet beneath the low density region.

The phase maps shown combine 15% amplitude thresholded data, hence regions of zero phase are found in the centre of the reconstruction where very low amplitudes were reconstructed. The phase maps from the 100 reconstruction at 200nm intervals along the c-axis show a consistent phase feature on the base of the crystal, $(\bar{1},0,1,0)$ facet and corresponds to a compression of the $0.81\mathring{A}$ relative to the equilibrium lattice which decays to $0.20\mathring{A}$ over 150nm depth. An expansion was observed consistently across the $(1,0,\bar{1},0)$ facet, over a 1.4μm section approximately 800nm from the $(0,0,0,\bar{1})$ facet of the crystal a region of missing amplitude was observed accompanied by a large phase feature. In B2,B3,B4 a wrapping of the phase was not observed but is inferred, the phase increases radially towards the $(1,0,\bar{1},0)$ facet and in the region of low amplitude switches to a large negative phase. Upon relaxation of the phase constraint the algorithm still failed to reconstruct this region the total phase range required was ±2.5rad. If the phase were to wrap a full 2π variation would be expected, therefore the crystal is highly strained with regions of both expansion and compression in this region. Either side of the missing density the phase gradient relaxes and a solid density observed with a well defined phase feature. Towards the $(1,0,\bar{1},0)$ facet the expansion is accompanied by a compression on the adjoining $(1,\bar{1},0,0)$ and $(0,1,\bar{1},0)$.

The 010 reconstruction shows a similar missing density over a 1.8μm region 0.6μm from the $(0,0,0,\bar{1})$ facet. An expansion was observed consistently on the left hand side of the base of the crystal. Both expansions and compressions are observed in the region of low amplitude. B5, C1-6 and D1-6 all demonstrate oscillation in the phase consistent with artifacts observed by fienup [65], in fienups case striping was observed in different directions from different random starts, here oscillations are observed parallel to each facet and correspond to the resolution limit of the reconstructed data.

We expect a substrate-crystal strain, but that observed on the top facet of the crystal is likely due to damage caused in the manipulation of the sample. A plastic deformation has left large strain gradients in the crystal. In the SEM image a small piece of crystal is seen at one end of the rod, this feature presented after micro manipulation and is unique to this sample and was not observed post oxide growth.

The consistency between the two reconstructions of the defect structure allows us to confidently (overcome ambiguous solutions) superimpose the reconstructions to generate a 2D displacement field. The result of the rotation, realignment, resampling and overlay operation is shown in Figure 7.10.

The agreement between the alignment of the two reconstructions is qualitatively very good. A slight gradient along the length of the crystal was observed, the resolution of the data is approximately 65nm in the hexagonal plane and 200nm perpendicular (c-axis), a direct space voxel has dimensions (50nm in each dimension) so the translation error is lower than the resolution and should not impinge on the result. The two displacement fields are then combined using 'BuildDField.py' written by Marcus Newton, the two dimensional
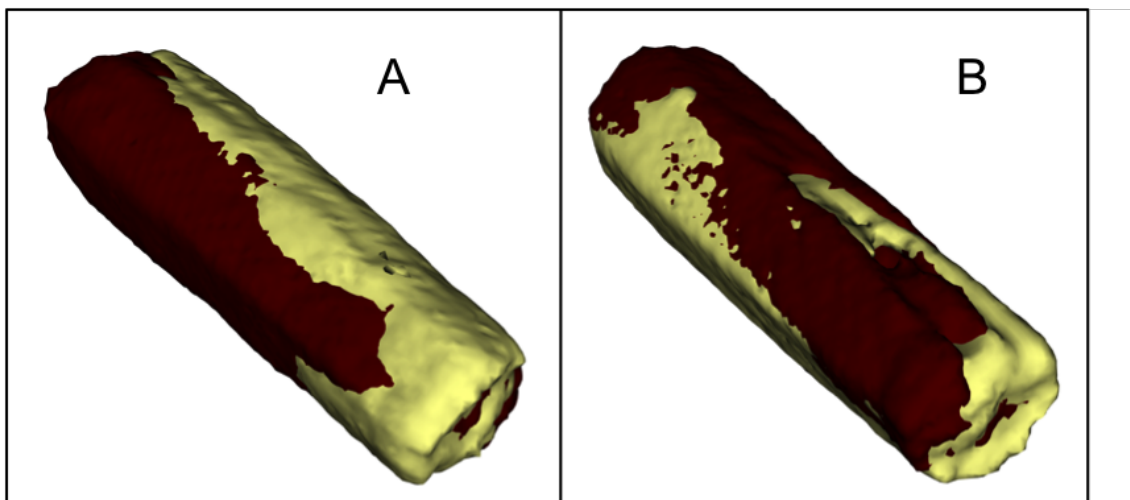
Figure 7.10: 3D renders of the 100 (maroon) and 010 (cream) reconstructions superimposed via a rotation alignment, interpolation and shift operation.

displacement field was calculated and three 2D slices taken through the defect region of the crystal, see Figure 7.11.

The 2D displacement field highlights the compression at the substrate and a large displacement either side of the low amplitude defect region providing a practical demonstration of the displacements observed in the phase maps previously. The maximum displacements are 1.03Å 0.72Å and 0.88Å for the 2D slices (left to right).

7.3 Summary

Multiple CXDI Bragg reflections from a single crystal have been measured for the first time by manually isolating a crystal. We have shown that the longitudinal coherence length can be determined by measuring the visibility of the fringe system (generated by the illumination of a finite crystal with x-rays) relative to the projection of the corresponding
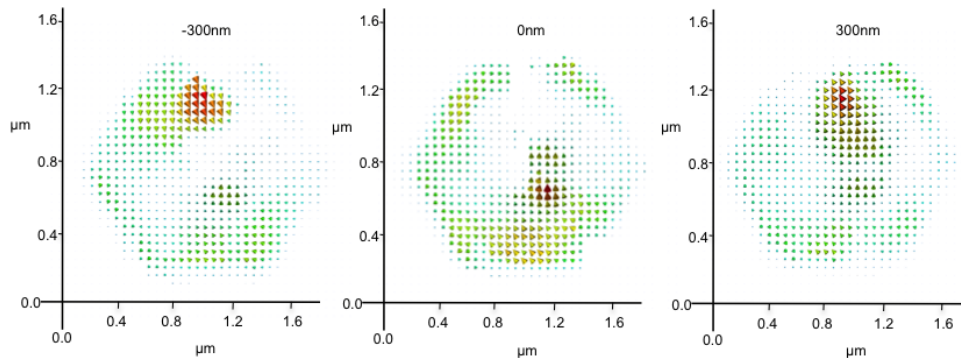
Figure 7.11: 2D displacement fields at the defect site and ±300nm constructed perpendicular to the c-axis of the crystal, the displacement direction is identified by the cone shaped arrows, the magnitude of the displacement vector is defined by their size and emphasised by their colour for consecutive images. The maximum displacement in each plane is 1.03Å, 0.72Å and 0.88Å.

dimension onto the Q-vector. At the Advanced Photon Source (APS) 34-ID-C beamline the longitudinal coherence was shown to be gaussian shaped and the coherence length measured to be, ξ_L=0.66±0.02μm. The phase retrieval from partially coherent Bragg reflections was compromised by the visibility of the observed fringe pattern. False solutions resulted and led to features in the reconstructions such as hot spots of amplitude and combinations of well defined and rough facets deemed incorrect by the reconstructions from the fully coherent geometries. It is vital to know the coherence lengths of the incident radiation and ensure they are larger than the OPLD for any measured Bragg reflection. This confirms that any smearing present in the diffraction pattern is a property of the crystal alone, i.e due to internal strains.

Two fully coherent illumination Bragg peaks (010) and (100) were combined to produce a 2D displacement field. In this case the slight taper along the length provides sufficient

asymmetry to identify the correct orientation of the crystal characterised previously by SEM. The observed defect structure was confirmed by both independent reconstructions raising several avenues for further investigation.

By rotating, translating and interpolating the two reconstructions onto a regular cartesian grid, independent reconstructions could be used to seed the phasing operation for different Bragg peaks, the method implemented in Section 6.2.5. Consideration would have to be made for the components of the displacement field observed in the additional reflections. In the case where the measured displacement fields are orthogonal only the crystals shape can be applied as a priori constraint.

Multiple Bragg reflections will also play a significant role validating strain fields observed in crystals, independent reconstruction provide an acid test of reconstructed features.

The results discussed were obtained for large crystals in an unfocussed mode of operation, ensuring the crystal was illuminated was relatively easy with a 100μm x 100μm [2]. Moving to the nanoscale requires a focused beam and a more precise method for crystal alignment has been realised via the integration of a confocal microscope into the setup, an approach outlined in Section 3.5. Manipulation with this level of precision opens the CXDI technique to 3D displacement fields and regular recovery of the full 3D strain tensor assuming the longitudinal coherence is sufficient for all reflections [138]. Additionally the strain fields in two different crystal structures on either side of an interface could be achieved.

---

[2]Scored lines on the substrate provide features large enough to identify to guarantee illumination of the crystal

Chapter 8

Conclusion

8.1   Zinc Oxide Nanocrystal Synthesis

The aim of the ZnO synthesis was to grow uniform ZnO nanocrystalline samples suitable for device applications and characterisation with CXDI. It was shown in Chapter 3 the synthesis method produced high yields of equiproportioned single crystal ZnO nanorods (up to 100%) loose on substrates. A source material of Zinc Carbonate to Carbon weight ratio 10:1 heated to 900°C in an atmosphere of Argon (6.4% Oxygen) deposits ZnO nanorods on a substrate positioned at 150°C. The crystals were successfully adhered to substrates via the growth of a thermal oxide layer. Zinc diffusion was observed from the crystals into the SiO_2 substrates. Other morphologies including the tetrapod and nanowire were fabricated, however their growth parameters were not optimised for further experimentation. As the device applications for ZnO nanocrystalline samples continues to grow the need for sensitive characterisation increases as the origins of the variation of properties are sought.

The potential for further study is huge and will be discussed after the CXDI results have been reviewed.

8.2 Coherent X-ray Diffraction Imaging

8.2.1 Experiments

In Chapters 4 and 5 we provided a detailed description of the methods employed to solve the phase problem specific to CXDI in the Bragg geometry. The data processing has been advanced to a state whereby a diffraction pattern can be measured and within half an hour of acquisition a first rough reconstruction of the crystal can be achieved[1]. At which point a judgement on the quality of the crystal is possible for further measurements, i.e higher resolution analysis, in-situ measurements or even moving onto a new sample. The choice of the crystal is the first of many assumptions made from data collection to solution generation and objectivity is difficult.

CXDI was implemented in an unfocussed mode of operation to study the solid state reaction and attempt to dope the ZnO to tailor their properties. A solid state reaction between Fe and ZnO was observed repeatably upon annealing, the onset of the reaction was observed after being held between 10 and 20 minutes at 400°C. An inability to measure the illuminated crystals temperature accurately prevented the onset of the reaction being accurately identified. Two dimensional phasing was used to identify variations around the Bragg peak, these proved unsuccessful due to thermal expansion making it very difficult

---

[1]A typical synchrotron experiment allocates between 3-6 days of continuous beam access, prior to this project analysis was carried out after the allocated time

to track and measure the same slice of the reciprocal space. CXDI measurements were taken at a reference temperature of 300°C where the reaction was known not proceed from experience. The sample was quenched to the reference state after each annealing step to maintain objectivity in the phasing process and ensure the reaction had ceased during measurements. The origins of the observed phase modulations was not identified and refraction effects were insufficient to account for them. Formation of secondary phases as opposed to integration into the ZnO lattice, $Zn_{1-x}Fe_xO$, was expected.

Experiments with Ni and Co depositions produced inconsistent results. The Ni depositions were likely to produce the smallest observable change in the crystals due to its low solubility in ZnO, yet showed a large change in the diffraction data. This confirmed a vigorous reaction process than diffusion alone. Co was expected to produce the largest change yet very little variation was observed in the diffraction patterns. Solid state reaction experiments with Ni did not create reproducible changes in the crystal structure.

The measurement of multiple Bragg reflections from an isolated crystal was demonstrated for the first time. Improvements in the sample fabrication method allowed a single ZnO crystal to be isolated and adhered to a substrate in a known location, SEM characterisation of the orientation allowed multiple Bragg reflections to be measured.

We have shown that the longitudinal coherence length can be determined by measuring the visibility of the fringe system (generated by the illumination of a finite crystal with x-rays) relative to the projection of the corresponding dimension onto the Q-vector. At the Advanced Photon Source (APS) 34-ID-C beamline the longitudinal coherence was measured to be, $\xi_L = 0.66 \pm 0.02\mu m$. In the phase retrieval process false solutions resulted

from a partially coherent illumination and led to features in the reconstructions such as hot spots of amplitude and combinations of well defined and rough facets deemed incorrect by the reconstructed solutions from the fully coherent Bragg geometries. Our work confirms the notion that it is vital to know the coherence lengths of the incident radiation and ensure they are larger than the OPLD for any measured Bragg reflection. This also confirms that any smearing present in the diffraction pattern is a property of the crystal alone, i.e due to internal strains. This result will have consequences for thin film characterization methods, films with a thickness close to the longitudinal coherence in the specular geometry will result in smearing in the non-specular reflections (depending on the size of the beam footprint and penetration depth).

The identified fully coherent Bragg reflections were combined to produce a 2D displacement map of the measured crystal. The independent reconstruction of the reflections showed commensurate phase structures. The integration of a confocal microscope into the beamline has opened up CXDI to regular 3D displacement field imaging of nanocrystals and led to the recovery of the full 3D displacement field and strain tensor in a ZnO rod [138].

CXDI Outlook

The level of control now available gives CXDI the capability to characterise individual devices during operation and study the impact of fabrication methods such as FIB and e-beam lithography currently used to fabricate these morphologies into devices. The improved sample manipulation for multiple Bragg reflections potentially allows the inves-

tigation of both sides of a crystalline interface i.e. ZnO tetrapod zinc blende core and wurtzite arm interface, and the strains created in buried structures by host materials. The additional advantages provided by independent measurements of the same crystal for the phase retrieval will be discussed in the next section. For further *in-situ* experiments a separate mobile vacuum chamber could add the multiple Bragg reflection method to aid the characterisation and speed up the sample loading process.

8.2.2 Phase Retrieval

While it is clear there is no definitive general phasing method that solves every dataset, to date attempts at phasing approximately 160 different datasets have identified no obvious advantage between specific algorithms or their order of implementation. The general approach which guarantees a finite solution was described in Chapter 5, some form of HIO algorithm (30-50 iterations) to identify a solution followed by an a ER type algorithm (10-20) to clean up the result. This provides a suitable starting point from which to hone the phasing parameters. The acknowledgement that the phase retrieval is specific to each problem means objectivity in the phase retrieval process is lost to an extent. We aimed to maintain objectivity and identified several generic problems which manifest in the phasing retrieval process.

The choice of support provided the largest variation in results in the phase retrieval process. When too large multiple non ambiguous solutions result and when too small the support defines the shape of reconstructed object and creates false features in the reconstructions. Supports should remain incommensurate with the shape of the object once

an initial solution has been obtain, at which point the support can be tightened to the minimum, within the resolution of the crystal in each dimension thus should match its shape closely. Where possible the support should remain symmetric as not to favour particular orientations of solution (unless prior knowledge can be applied), it is conceivable an asymmetric support will favour one of two equivalent enantiomorph solutions.

As we have discovered from the multitude of solutions created from random starting points, *a priori* information is very important. It begs the question; How valid is a random starting point? The interference pattern around a Bragg peak suggests the crystal structure is not random, the application of a phase constraint adds weight to this argument, if the variation is small and it is constrained to be small the reconstructions improve. The choice of starting point remains debateable. The illuminated crystals are approximately single crystal (flat phase object) therefore to begin from a set of random phases effectively loosens the constraints on the solution. In the case of several random starts in order to correctly average the solutions and scale them ambiguous solutions must be indentified and accounted for via cross correlation, for twin and shift identification, and the phase factor offset to adjust for the arbitrary phase origin. When a crystal was tracked through some form of processing, subtle variation in the diffraction patterns are seen. The corresponding changes in direct space should be identifiable by phasing all datasets in the same way, using the same support, same phase constraint if there is one and when the crystal experiences the same conditions[2]. Starting independent phasing operations on each diffraction pattern in this way proved inconsistent. The reconstructions did not reproduce amplitude distribution and phase modulation for every annealing step although some agreement was

---

[2]Only applicable when the CXDI measurements are all obtained at a reference point, i.e the same experimental conditions, hence variation in the recontructed solution is independent of the phasing operation

observed >50%. To solve this problem the introduction of further *a priori* knowledge in the form of seeds proved relatively successful. A combination of the guided HIO algorithm and the Shrinkwrap algorithm produced agreement between reconstructions of consecutive annealing steps. Sources of discrepancy were identified in the data handling stages and minimised by centering the data correctly and intensity unrelated to the illuminated crystal removed. Constant phase modulation due to refraction of the scattering x-rays was corrected for.

Several algorithms were introduced and discussed. Their best attributes were harnessed for the analysis presented in this thesis. The potential drawback of the Shrinkwrap algorithm was identified when the autocorrelation function was used as the initial support, the SW algorithm always produced the same solution from random starting points. The constraints applied initially were very loose and quickly tighten and force the algorithm into a local minimum where the change implemented by the algorithm is too small to escape. The obvious advantage of the PC-HIO is the additional constraint when required and supports the argument of a flat phase object as a starting point. The PO-ER algorithm allows amplitude to exist outside the support so provides a better representation of the noise in the data.

Outlook

There are many avenues of investigation to pursue with regards to the phase retrieval operation. The Shrinkwrap algorithm would improve its objectivity if it were to shrink the support and symmetrize it about the origin. A sample with 5 fully visible (100%) Bragg

reflections would provide a test bed for the reliabiility of the individual reconstructions, like those discussed in Chapter 7 [138]. Each reconstructed Bragg reflection will sample the same components of the displacement field in the crystal as other reflections hence provide an independent test of the reliability of the reconstructions.

8.2.3   Laser Experiments

Preliminary experiments have been completed for pump probe CXDI measurements building on the groundwork in this thesis. The premice for the measurement is to maintain a crystal in an x-ray beam, excite it in some way using laser light and measure it during its excited state. A laser of frequency (88MHz) at beamline ID-7 is commensurate with the frequency of x-ray pulses produced by a 324 bunch mode operation at the APS. An accurate alignment of the pulses within 20picoseconds allows us to probe the distortion produced by the incident laser. In this case a thermally induced shockwave. The experimental set up, a ZnO crystal illuminated with a 800nm laser, was measured at incremental offsets from alignment up to the expected dissipation time of a shockwave produced by the incident radiation. In this case the ZnO is transparent to the laser due its large band gap so a thin layer of Ni was deposited to absorb the laser light and initiate the shockwave. Cut planes through the same slice of phases are shown for 3 offsets at 0ps, 100ps and 200ps [3] in Figure 8.1. The symmetric shape of the crystal makes it difficult to assess which twin is actually the correct solution. The substrate may in fact reside at the other end of the rod. The position defined is based on our interpretation of the phase modulation. At 0ps a band of phase was evident in the center of the rod, corresponding to an expansion of

---

[3]Corresponding datasets DS_{144}, DS_{146} and DS_{148} for the respective 0ps, 100ps and 200ps offsets.

approximately $\frac{3}{8}\pi$ relative to the rest of the crystal, this distortion was present throughout the hexagonal cross section of the crystal. The band at the center of the crystal suggests the offset between laser pulse and x-rays is not as accurate as expected. Thus if we expect the shockwave to propagate through the rod in approximately 200ps from the top facet the third reconstruction will show very little distortion. At 100ps and 200ps a band of positive phase was observed at the top of the crystal, the overall phase modulation in the crystal is $\frac{1}{8}\pi$ larger in the 100ps reconstruction, suggesting a distortion was still present. This analysis suggests the original state of the crystal has been measured at an offset of 200ps and a distinct phase structure was already present in the crystal. At 100ps a slight deviation in the phase was seen near the substrate throughout the crystal which may relate to the tail of the shockwave passing through the crystal and the top end has returned to its original state.

Further experiments are required to confirm the phase modulation observed. This experiment outines the potential for CXDI experiments in the Bragg geometry in pump probe modes of operation looking at phenomena on the sub nanosecond timescale and emphasises its potential with the soon to be realised fourth generation X-ray Free Electron Laser sources.
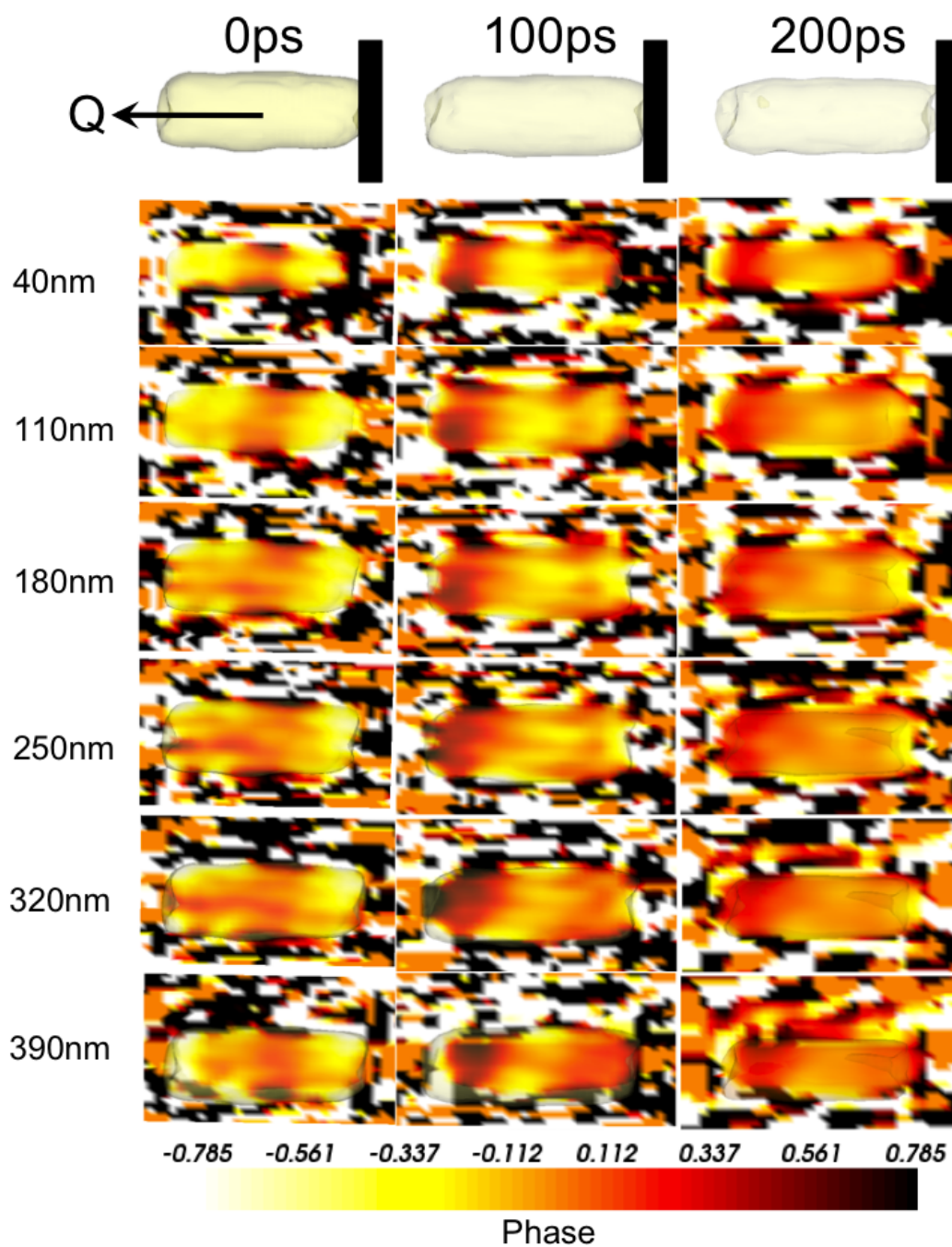
Figure 8.1: The reconstructed solutions at a laser to x-ray offset of 0ps, 100ps and 200ps, the translucent solid object shows the direct space amplitudes, the black bar represents the expected location of the substrate. Cut planes through the phase are shown at regular intervals along the beam direction, the crystals dimensions are 1.5μm x 0.5μm.

Appendix A

A.1 Asymmetric Sample Heating

The gradients observed are a result of non uniform contact between the clamp and the substrate.
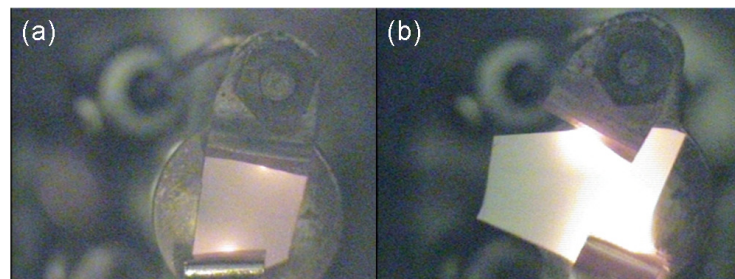
Figure A.1: Silicon wafer mounted and heated to approximately (a) 600°C and (b) 780°C

A.2 Diffraction Geometry

The experiment itself requires an intimate knowledge of the sample orientation and detector position and orientation relative to the sample. The sample sits on kinematic mounts with horizontal translations both parallel (z) and perpendicular (x) to the incident beam (k_i), where downstream and outboard translations are positive respectively and a vertical translation (y). The kinematic mounts reside on a six circle diffractometer, five circles are used, χ rotates around $\mathbf{k}_i$, θ a rotation about the surface normal and ϕ a rotation about the x-axis. χ and ϕ are used to orient the sample perpendicular to the laboratory z axis (i.e flat), relative to this a rotation of ϕ about the x axis and determines the incident angle (α) of the beam. The 2D detector sits on an extendable arm aligned perpendicular to the incident beam ($\mathbf{k}_i$) with rotation around both the surface normal (δ) and the x axis (γ). Combination of ϕ, δ and γ define the $\theta_{Bragg} - 2\theta_{Bragg}$ Bragg geometry for the measurements.
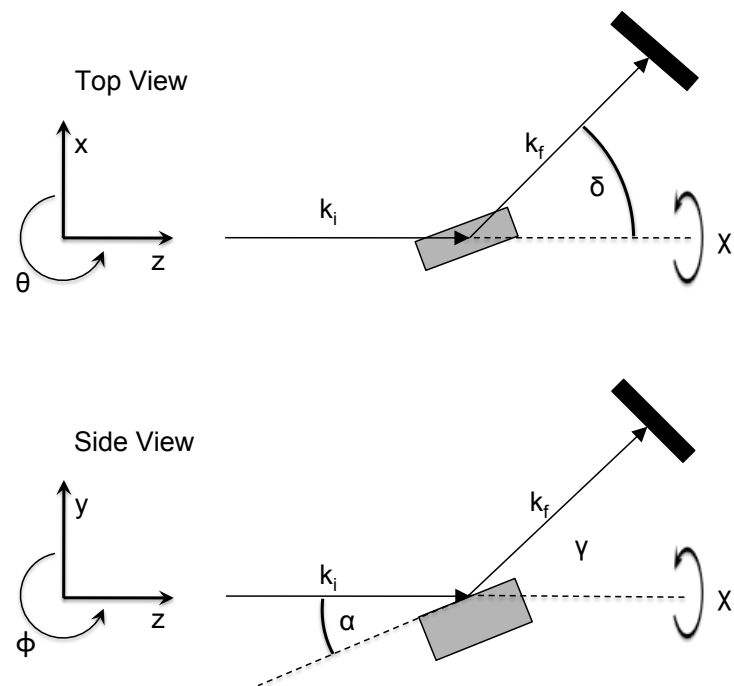
Figure A.2: Schematics of both top view and side view perspectives of the diffractometer geometry, incident beam $\mathbf{k}_i$ and refracted beam $\mathbf{k}_f$, detector rotations δ and γ and sample rotations θ, χ and ϕ

A.3   Convolution

The convolution theorem is useful, in part, because it gives us a way to simplify many calculations. Convolutions can be very difficult to calculate directly, but are often much easier to calculate using Fourier transforms and multiplication.

$$f * g = f^* \otimes g \tag{A.1}$$

$$\mathcal{F}(f \otimes g) = \mathcal{F}(f).\mathcal{F}(g) \tag{A.2}$$

$$f * g = \sum_m^\infty f^* g \tag{A.3}$$

The correlation theorem can be stated in words as follows: the Fourier tranform of a correlation integral is equal to the product of the complex conjugate of the Fourier transform of the first function and the Fourier transform of the second function. The only difference with the convolution theorem is in the presence of a complex conjugate, which reverses the phase and corresponds to the inversion of the argument u-x.

A.4 Geometric Series

The geometric series is defined as a series with a constant ratio between successive terms, $\frac{a_{n+1}}{a_n}$, over the summation. When the series starts from 1 the sum can be written as

$$S_N = \sum_{n=0}^{N-1} a_n = \frac{1 - a^N}{1 - a} \qquad \text{(A.4)}$$

Where $N \to \infty$, the sum converges if $|a| < 1$, thus

$$S_\infty = \lim_{N \to \infty} S_N = \sum_{n=0}^{\infty} a^n = \frac{1}{1 - a} \qquad \text{(A.5)}$$

Geometric series are common in crystallography in the summation of phase factors.

$$
\begin{aligned}
S_n = \sum_{n=0}^{N-1} e^{iQr.n} &= \frac{1 - e^{iQr.N}}{1 - e^{iQr}} \\
&= \frac{(e^{-i\frac{Qr.N}{2}} - e^{i\frac{Qr.N}{2}})}{(e^{-i\frac{Qr}{2}} - e^{i\frac{Qr}{2}})} \cdot \frac{e^{i\frac{Qr.N}{2}}}{e^{i\frac{Qr}{2}}} \\
&= \frac{sin(\frac{NQr}{2})}{sin(\frac{Qr}{2})} \cdot e^{i\frac{(N-1)Qr}{2}}
\end{aligned}
\qquad \text{(A.6)}
$$

A.5 Wave interference calculations

A.5.1 Two Point Scatterers

Consider two equivalent waves (ψ_1, ψ_2) scattered from electrons, one at the origin and the other a position $\mathbf{r}$, are of the form,

$$\psi_1 = Ae^{ik.x} \quad ; \quad \psi_2 = Ae^{ik.x}e^{iQ.r} \tag{A.7}$$

where A is the amplitude, $\mathbf{k}$ the wavevector and $e^{iQ.r}$ is an additional phase factor.

The total scattered amplitude at a point is then written,

$$A_{scattered}(Q) = \psi_1 + \psi_2 = Ae^{ik.x}(1 + e^{iQ.r}) \tag{A.8}$$

and the observed intensity,

$$I(Q) = |A_{scattered}|^2 = A_{scattered}.A_{scattered}^* \tag{A.9}$$

$$= A^2 e^{ik.x}e^{-ik.x}(1 + e^{iQ.r})(1 + e^{-iQ.r})$$

$$= 2A^2(1 + cos(Q.r))$$

Plotted in Figure 2.5(a) where $\mathbf{Q}$ is parallel to $\mathbf{r}$.

A.5.2   Finite Crystal

A finite crystal is built from the convolution of a lattice and a unit cell. Assuming a perfect crystal lattice and a perfectly coherent illuminating beam the scattered amplitude can be written

$$A_{scattered}(Q) = F(Q) \sum_{R_n}^{lattice} e^{iQ.R_n} \tag{A.10}$$

where F(Q) is the structure factor. The structure factor describes the Fourier Transform of the electron density inside the unit cell. As F(Q) is a constant we simply solve the sum using a geometric series approach, *see Appendix A.4*, assuming a finite crystal of N_1,N_2 and N_3 unit cells along **a**,**b** and **c** respectively the summation becomes

$$\sum_{R_n}^{lattice} e^{iQ.R_n} = \sum_{x=0}^{N_1-1} \sum_{y=0}^{N_2-1} \sum_{z=0}^{N_3-1} e^{iQ.(x\mathbf{a}+y\mathbf{b}+z\mathbf{c})} \tag{A.11}$$

$$= \frac{sin(N_1 Qa)}{sin(Qa)}.e^{i\frac{(N_1-1)Qa}{2}}.\frac{sin(N_2 Qb)}{sin(Qb)}.e^{i\frac{(N_2-1)Qb}{2}}.\frac{sin(N_3 Qc)}{sin(Qc)}.e^{i\frac{(N_3-1)Qc}{2}}$$

The intensity is therefore proportional to

$$I(Q) \propto \frac{sin^2(\frac{N_1 Qa}{2})}{sin^2(\frac{Qa}{2})}.\frac{sin^2(\frac{N_2 Qb}{2})}{sin^2(\frac{Qb}{2})}.\frac{sin^2(\frac{N_3 Qc}{2})}{sin^2(\frac{Qc}{2})} \tag{A.12}$$

This is similar to the 'sinc' function and demonstrated in 1D in Figure 2.5 (b) and (c).

A.6   X-ray Free Electron Laser sources

A Free Electron Laser (FEL) is a laser that shares the same optical properties as conventional lasers. Emitting a beam consisting of coherent electromagnetic radiation capable of reaching high power. The European XFEL[1] expects to produce a brilliance billions times stronger than third generation synchrotron at its brightest intensity and 10^4 times brighter on average across the whole beam. Its operation is very different compared to gas, liquid or solid-state lasers, which rely on bound atomic or molecular states, the 'free electron' term arises from the use of a relativistic electron beam as the lasing medium. This gives them the widest frequency range of any laser type, and makes many of them widely tunable, currently ranging in wavelength from infrared ISIR, Osaka University, through to soft X-rays at the FLASH facility, at the Deutsches Elektronen-Synchrotron (DESY) in Hamburg. The potential of FEL sources for CXDI has already been shown by Chapman *et al.*; initially in the reconstruction of a test object [34] and later x-ray holography of polystyrene spheres as they are vaporised by the incident beam [36]. The proposed European XFEL will produce pulses of less than 100 femtoseconds providing the time resolution to probe chemical and physical processes with precision yet to be achieved by other characterization methods. The speed at which the measurements are taken is problematic itself and there are many engineering hurdles to overcome, but the potential in the fields of CXDI and Holography are clear [191].

---

[1]http://xfelinfo.desy.de/en/start/2/index.html

A.7 Furnace cleaning procedure

The furnace system was cleaned with acetone and isopropanol and purged for a 30 minute period to ensure the concentration of contaminants was reduced by a factor of 10^5 and is calculated using equation A.13. The furnace took 36 minutes to reach 900°C and growth periods ranged from 1-20mins.

$$Cn = C_0 e^{\frac{-Q_{flow}t}{V}} \tag{A.13}$$

Cn = Concentration of dust particles and contaminants after time t C_0 = Initial concentration of dust particles and contaminants Q_{flow} = Flow rate of gas (Nitrogen 500sccm) t = Time V = Volume of furnace tube (2748sccm)

Appendix B

B.1 Aliens reconstructed
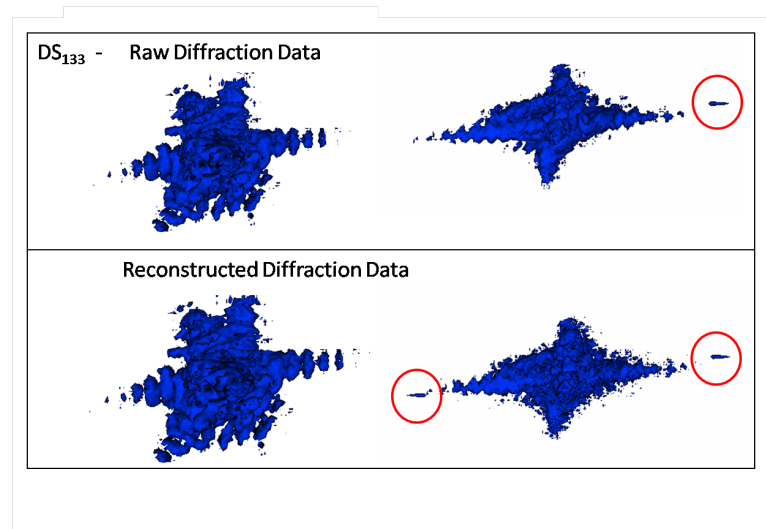
Figure B.1: Example of reconstruction of cosmic ray strike total 7 pixels

B.2 Initial Fe deposition annealing diffraction data
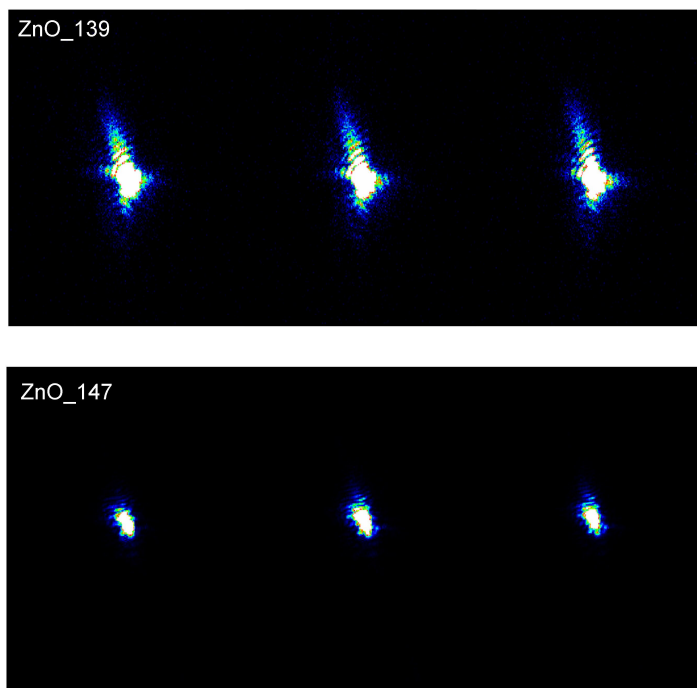
Figure B.2: Diffraction data at -1,0,+1 frames offset from the bragg spot at (a) 230°C (DS$_{139}$)(b) 400°C (DS$_{147}$) for sample 115

B.3   Cross Correlation output for Figure 6.5 A

The python script used to generate this output can be found in Appendix G.3.1

```
FFTmethodCross Correlation between:   shiftedSequence0dist0070_bd_54.sp4, Sequence0dist0070_bd_54.sp4

Shift required to achieve best correlation: (7,5,-7)

FFTmethodCross Correlation between:  shiftedSequence0dist0070_bd_54.sp4, Sequence0dist0070_bd_54Transpose.sp4

Shift required to achieve best correlation: (-3,8,-1)

Normal orientation had a stronger correlation, filename: 0.sp4

FFTmethodCross Correlation between:  shiftedSequence0dist0070_bd_54.sp4, Sequence1dist0070_bd_54.sp4

Shift required to achieve best correlation: (-4,4,-5)

FFTmethodCross Correlation between:  shiftedSequence0dist0070_bd_54.sp4,  Sequence1dist0070_bd_54Transpose.sp4

Shift required to achieve best correlation: (8,15,-3)

Normal orientation had a stronger correlation, filename: 1.sp4

FFTmethodCross Correlation between:  shiftedSequence0dist0070_bd_54.sp4, Sequence2dist0070_bd_54.sp4

Shift required to achieve best correlation: (4,4,-7)

FFTmethodCross Correlation between:  shiftedSequence0dist0070_bd_54.sp4,  Sequence2dist0070_bd_54Transpose.sp4

Shift required to achieve best correlation: (0,17,-1)

Possible Twin Identified, filename: 2.sp4

FFTmethodCross Correlation between:  shiftedSequence0dist0070_bd_54.sp4, Sequence3dist0070_bd_54.sp4

Shift required to achieve best correlation: (2,3,-7)

FFTmethodCross Correlation between:  shiftedSequence0dist0070_bd_54.sp4,  Sequence3dist0070_bd_54Transpose.sp4

Shift required to achieve best correlation: (0,11,-1)

Normal orientation had a stronger correlation, filename: 3.sp4

FFTmethodCross Correlation between:  shiftedSequence0dist0070_bd_54.sp4,  Sequence4dist0070_bd_54.sp4

Shift required to achieve best correlation: (3,9,-2)

FFTmethodCross Correlation between:  shiftedSequence0dist0070_bd_54.sp4,  Sequence4dist0070_bd_54Transpose.sp4

Shift required to achieve best correlation: (1,8,-6)

Normal orientation had a stronger correlation, filename: 4.sp4

FFTmethodCross Correlation between:  shiftedSequence0dist0070_bd_54.sp4,   Sequence5dist0070_bd_54.sp4

Shift required to achieve best correlation: (-6,13,-5)

FFTmethodCross Correlation between:  shiftedSequence0dist0070_bd_54.sp4,   Sequence5dist0070_bd_54Transpose.sp4

Shift required to achieve best correlation: (8,3,-3)

Possible Twin Identified, filename: 5.sp4

FFTmethodCross Correlation between:   shiftedSequence0dist0070_bd_54.sp4,   Sequence6dist0070_bd_54.sp4

Shift required to achieve best correlation: (6,3,-6)

FFTmethodCross Correlation between:   shiftedSequence0dist0070_bd_54.sp4,   Sequence6dist0070_bd_54Transpose.sp4

Shift required to achieve best correlation: (-2,6,-2)

Possible Twin Identified, filename: 6.sp4

FFTmethodCross Correlation between:   shiftedSequence0dist0070_bd_54.sp4,   Sequence7dist0070_bd_54.sp4

Shift required to achieve best correlation: (-2,13,-4)

FFTmethodCross Correlation between:   shiftedSequence0dist0070_bd_54.sp4,   Sequence7dist0070_bd_54Transpose.sp4

Shift required to achieve best correlation: (6,4,-4)
```

```
Normal orientation had a stronger correlation, filename: 7.sp4

FFTmethodCross Correlation between:   shiftedSequence0dist0070_bd_54.sp4,   Sequence8dist0070_bd_54.sp4

Shift required to achieve best correlation: (-4,12,-2)

FFTmethodCross Correlation between:   shiftedSequence0dist0070_bd_54.sp4,   Sequence8dist0070_bd_54Transpose.sp4

Shift required to achieve best correlation: (7,7,-6)

Possible Twin Identified, filename: 8.sp4

FFTmethodCross Correlation between:   shiftedSequence0dist0070_bd_54.sp4,   Sequence9dist0070_bd_54.sp4

Shift required to achieve best correlation: (2,8,-4)

FFTmethodCross Correlation between:   shiftedSequence0dist0070_bd_54.sp4,   Sequence9dist0070_bd_54Transpose.sp4

Shift required to achieve best correlation: (0,9,-4)

Possible Twin Identified, filename: 9.sp4
```

B.4 Bravais-Miller index

The facets on ZnO can be referred to using a four coordinate {hkil} indexing system, where $h + k = i$, to distinguish all facets on a hexagonal crystal.
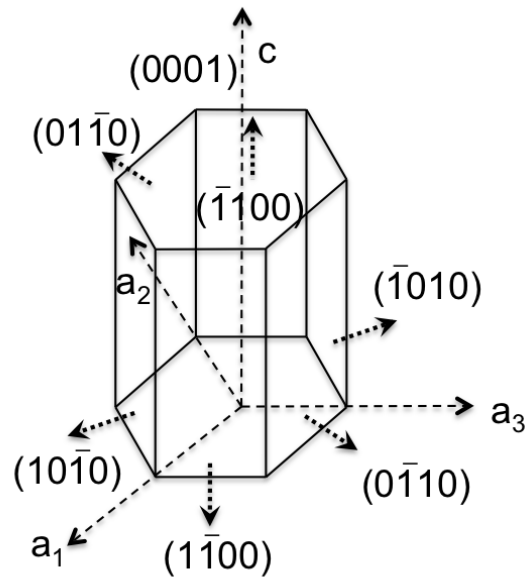
Figure B.3: Silicon wafer mounted and heated to approximately (a) 600°C and (b) 780°C

Appendix C

C.1 The Shrinkwrap Method

The Shrinkwrap algorithm implemented was written by Marcus Newton and based on Marchesini [123]. The implementation from raw data to phased solution is a three step process, this will be introduced and modifications made outlined based on the experience gained through data analysis.

C.1.1 Stage 1: Data Preparation

The data is prepared based on the handling methods described in Section 5.1, the data is centered, aliens removed, buffered with additional voxels and binned to the oversampling limit. This file will be named 'BD-data.sp4'.

C.1.2 Stage 2: Initial Support Generation

Usage in terminal: python AutoArray2Support.py BD-data.sp4

An automated method 'AutoArray2Support.py' was written to generate a support from the autocorrelation function of the measured data. The autocorrelation function has a 2D slice removed. An applied threshold produces a 2D solid shape. The 2D shape is copied at every voxel in the third dimension where the brightest pixel in the 2D slice lies above the defined threshold, the 2D shape is copied onto the brightest pixel. The result is a finite 3D object which approximately describes the autocorrelation function.

Scaling the Autocorrelation function to a percentage of the maximum allows a generic value to e used for all datasets. The python script 'AC_diff_percent.py' carries out this operation and the output viewed in Mayavi to optimise the threshold used

The user defined variables and typical values are:

```
Support_Axis = 3
Support_LengthThreshold = 30.0
Support_WidthThreshold = 10.0
Support_CrossSectionSmoothing = 0.5
Support_Smoothing = 1.0
```

Choose *Support_axis*

For high aspect ratio crystals choose axis approximately perpendicular to longest dimension. In reality you need to know something about your crystal and can be estimated by the longest (pixel number) dimension of the autocorrelation function.

```
1 = x-axis (yz plane)
2 = y-axis (xz plane)
3 = z-axis (xy plane)
```

Choose *Support_lengthThreshold: (%)*

This variable changes the dimension of the 3D object perpendicular to the plane of the

chosen slice set by the *Support_axis* variable.

Observe the autocorrelation function on a percentage scale, by decreasing threshold on the isosurface when lobes begin to appear use this % as the threshold. Note, this variable is dependent on the smoothing for the value defined approximately 20% more should be added to this.

Choose *Support_widthThreshold: (%)*

Effectively identical to *Support_lengthThreshold*, a slightly larger threshold than set for *Support_lengthThreshold* ensures multiple 3D objects are not created as a support.

Choose Smoothing Parameters

> Choose Support_CrossSectionSmoothing = 0.5
> Choose Support_Smoothing = 1.0

The smoothing variables appear not to have a massive impact on the smoothness of the support. Both use a c-program 'Sp4ArraySmoothIPfft.c' to convolve with a Gaussian of width σ defined by the variable. This effectively increases the width of the 3D object (*Support_CrossSectionSmoothing*) and the length (*Support_Smoothing*).

Once the correct variables have been identified and 'AutoArray2Support.py' run an Sp4Array file is generated with a binary support built from the autocorrelation function.

C.1.3   Stage 3: Phasing

The final step carries out the phasing operation, tightening the support at every iteration.

> Usage: python Shrinkwrap.py BD-data.sp4

The python script in appendix G.2 has been modified to surpass stages 1 and 2. In this case the starting support is generated using an alternate method however the phasing operation remains the same. All associated variables are declared in the 'ParamsShrinkwrap.py' file.

A log file is generated with all user defined variables inputted, the additional input to the support file is the raw centered intensities,The square root is taken to obtain the amplitudes and a phasing operation initiated using the support file, the number of iterations are defined by the variables ($numERiter\_Initial$ and $numHIOiter\_Initial$). The solution is then convolved with the a binary cube of the analysts choice which makes it larger and is then smoothed, this new object commensurate with the solution is used as the new support. The phasing operation is repeated and the number of iterations defined by the variables ($numHIOiter\_ShrinkWrap$ and $numERiter\_ShrinkWrap$), a new support is then generated using the convolution method described in the previous step. The consistency between the new support and the old support is tested, when this falls below the required consistency the final phasing operation is carried out ($numHIOiter\_Final$ and $numERiter\_Final$) and all of the vtk files are generated for viewing in Mayavi.

The typical variables employed and their magnitudes are:

```
# Number of iterations of each algorithm with initial support
numERiter_Initial = 2
numHIOiter_Initial = 20

# Numer of ShrinkWrap iterations within each loop
numHIOiter_ShrinkWrap = 10
numERiter_ShrinkWrap = 2

# Number of iterations after the final support
numHIOiter_Final = 20
numERiter_Final = 5
```

Choose *Initial_iterations*

Initial iterations requires some finite object to begin support optimisation anything from 20-35 iterations of HIO and a few ER should be sufficient.

Choose *Shrinkwrap_iterations*

Select the number of iterations of each algorithm during the support shrinking process, the more you select the lower the probability of consistency being achieved.

Choose *Final_iterations*

Arbitrary, could make equal to Initial_iteration cycle, once the algorithm has decided on a minimum it is likely to find it very quickly once the support has been shrunk, 20-35 iterations and a few ER is sufficient.

Self consistency variables and typical values:

```
# Self Consistence loop threshold value. Percentage value <1% is good.
SelfConsistenceThreshold = 1.0

# Self Consistency Smoothing variables for Sp4ArrayAverageIPfft:
AverageWidth = 3
AverageIter = 3

# Self Consistency Smoothing variables for Sp4ArraySmoothIPfft:
SmoothSigma = 0.35

# Self Consistency data cutoff threshold. 20.0 is normal
Array2SupportThreshold = 19.5
```

Choose *SelfConsistenceThreshold*

This value defines the variation between supports for shrinking cycles, a value below 1% is sufficient to achieve a reasonable reconstruction, the lower this variable the longer it will

take to converge to a consistent solution if at all. A 10 iteration limit has been placed on the shrinking process, it can also be manually exited via keyboard command e.

Choose *SelfConsistencySmoothing* variables

The AverageWidth is the size of the cube to convolve the solution with, as you increase this you decrease the size of the support, the required purpose of this operation is to broaden the support. The AverageIter is the number of times to carry out the convolution.

Choose *SmoothSigma*

The width of the Gaussian with which to smooth the support.

Choose *Array2SupportThreshold* (%)

The percentage threshold at which to define the function to be the support.

C.2   Fe deposition: Preliminary phasing steps

The average reconstructions demonstrated in Figure C.1 does not include a phase offset correction.
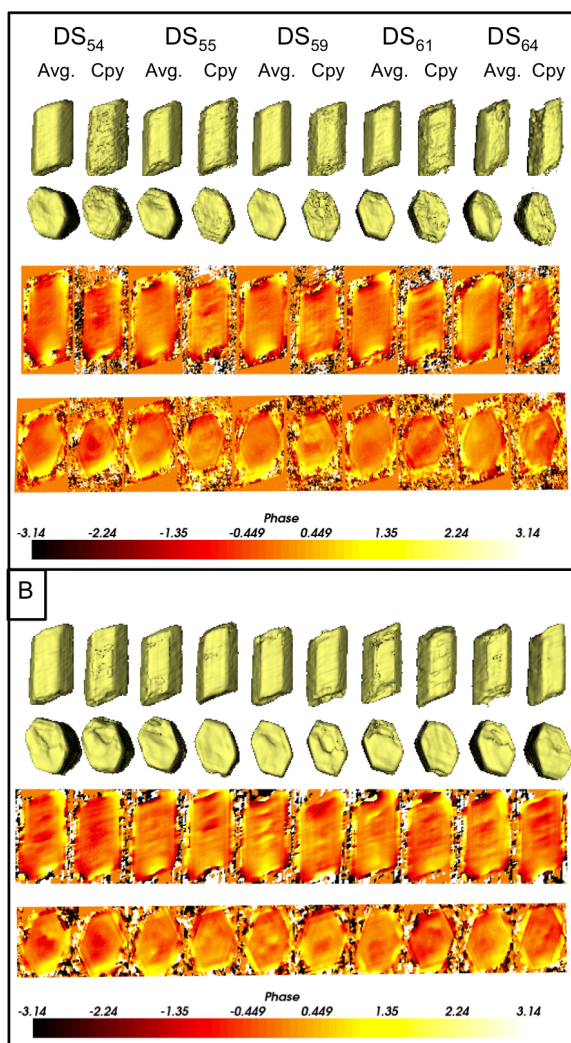
Figure C.1: From Sample 139c for DS_{54}, DS_{55}, DS_{59}, DS_{61}, DS_{64}, at reference temperature 292°C, after a 1 minute anneal to 400°C, and additional steps of 5, 5 and 10 minutes. (A) 3D isosurface renders for average solutions from random starts and copy of support phased solutions for each of the datasets, (B) the reconstructions after further support optimisation with the Shrinkwrap algorithm

Appendix D

D.1 Differential Phase Map
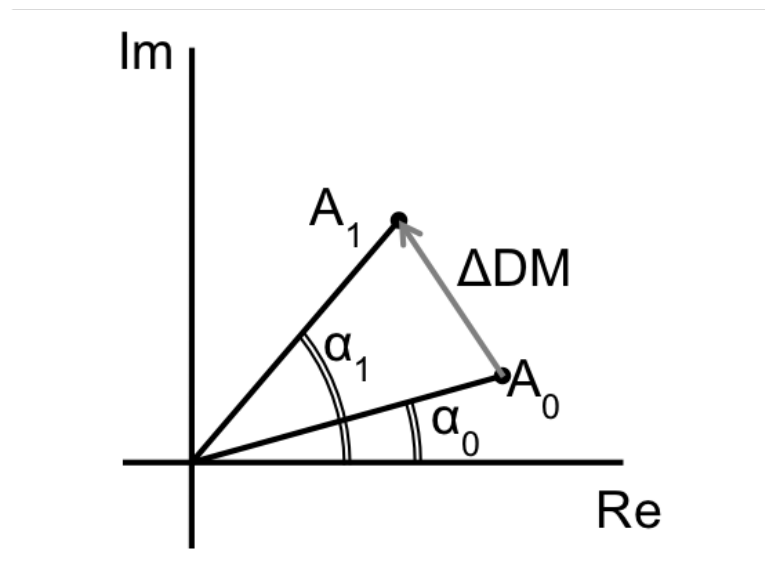
Figure D.1: The observed difference map between two images, the initial state, $f_0(r)$, and the final state after a small change in phase in an isolated region, $f_1(r)$. Where the corresponding amplitudes and phases are (A_0, α_0) and (A_1, α_1) respectively and the modulus of the difference (Δ DM) the observed difference map

The differential phase map applies for a small change in a crystal. The crystal is measured

in its initial state $f_0(r)$ and after an induced change $f_1(r)$, for the majority of the crystal

$f_0(r) \simeq f_1(r)$ except for a local region of displacement.

$$f_0(r) - f_1(r) = \mathcal{F}^{-1}\{F_0(q) - F_1(q)\} \tag{D.1}$$

where $\mathcal{F}$ and $\mathcal{F}^{-1}$ represent for Fourier Transform and its inverse respectively. When the change is small the measured intensities are approximately equal, $I_0(q) \simeq I_1(q)$, hence the measured amplitudes ($\sqrt{I}_{0,1}$) and phases ($\alpha_{0,1}$) are approximately equal. We can separate the displaced region through subtraction and view as a differential phase map (the modulus of the difference), see Figure D.1. and rewrite equation D.1 as:

$$f_0(r) - f_1(r) \simeq \mathcal{F}\{\sqrt{I_0 - I_1}e^{i\alpha_0(q)}\} \tag{D.2}$$

$$\simeq \mathcal{F}\{\sqrt{I_0 - I_1}e^{i\alpha_1(q)}\} \tag{D.3}$$

The python scripts were developed by Dr. Moyu Watari and the visualisation module for Mayavi was developed by Dr. Ross Harder. The method is very sensitive to small variations in phase between consecutive diffraction patterns.

Appendix E

E.1   Visibility of Bragg reflections from second ZnO crystal

A total of 11 Bragg reflections from a second ZnO crystal of dimensions 1.6μm in length and 1μm in width were measured. The extracted lines of data corresponding to the 002 crystal direction in reciprocal space are shown in Figure E.1.
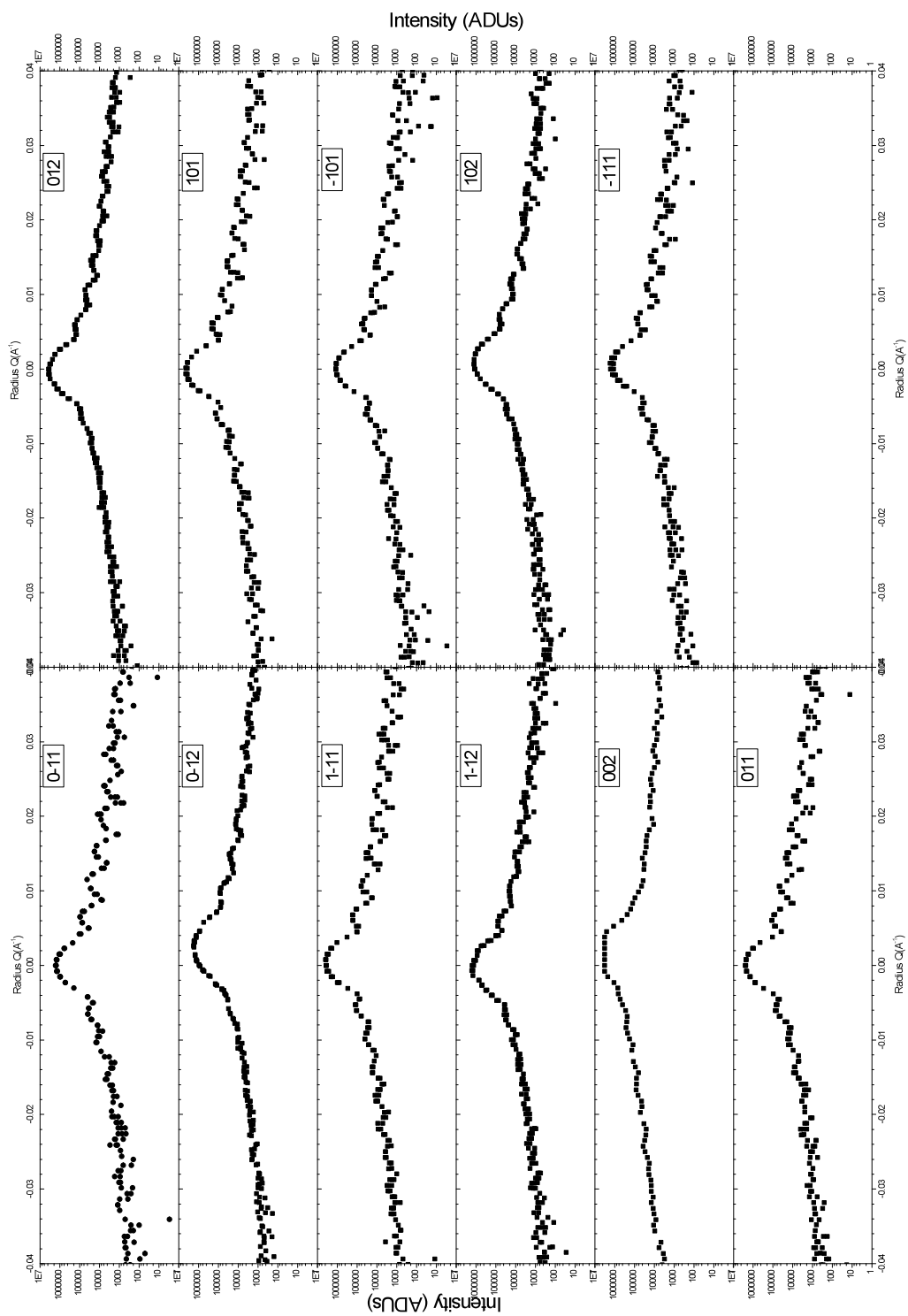
Figure E.1: Measured intensity as a function of momentum transfer deviation along the 002 crystal direction (reciprocal space) demonstrating the 002 fringe visibility for 11 different Bragg peaks from the second ZnO nanocrystal (1.6μm x 1μm).

Appendix F

F.1 Ni deposition diffraction data

Diffraction data obtained from annealing steps on ZnO rods with a layer of Nickel deposited on them.
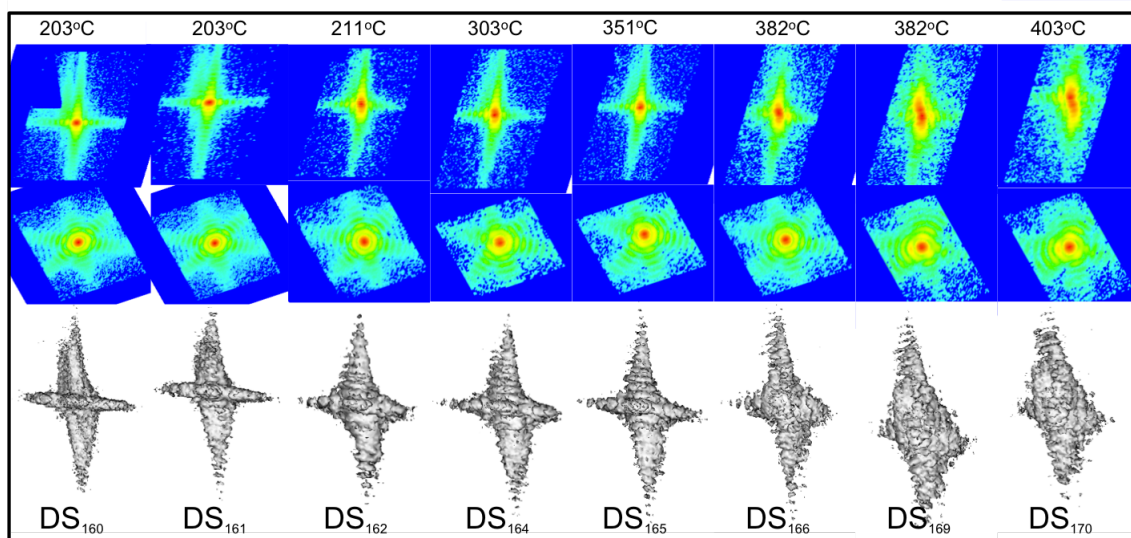
Figure F.1: Cut planes and isosurface renderings of the diffraction measured upon annealing steps for Sample 115 Ni
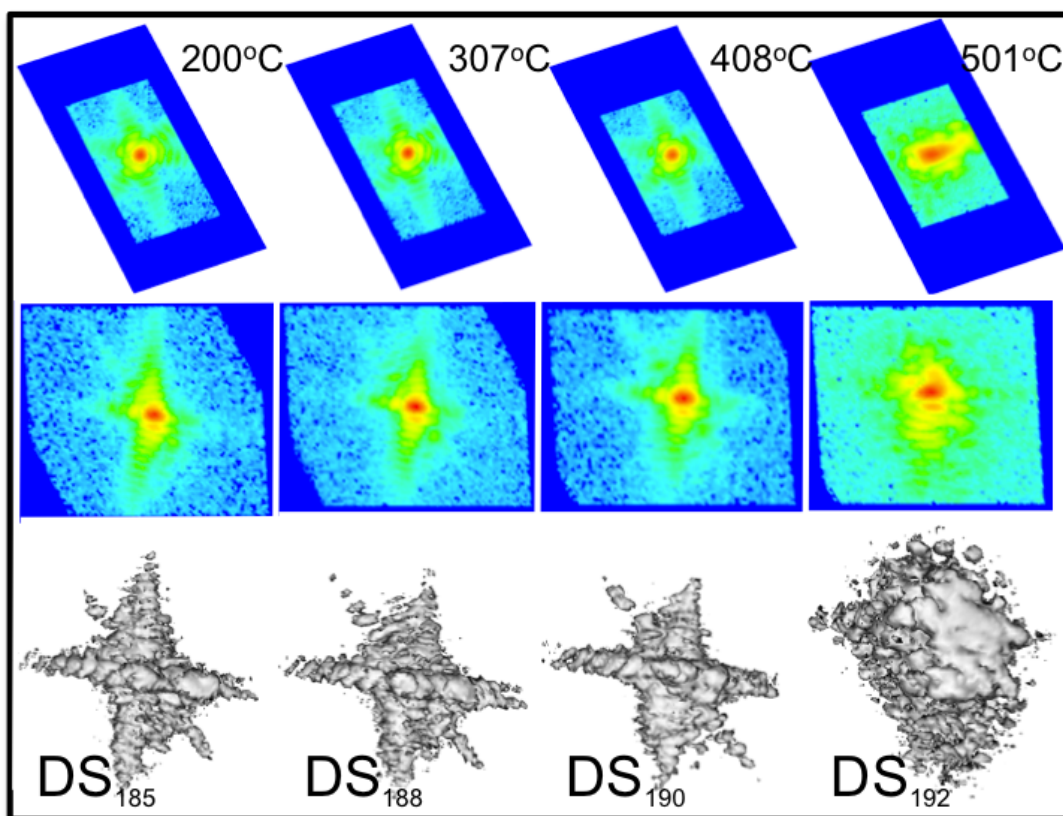
Figure F.2: Cut planes and isosurface renderings of the diffraction measured upon annealing steps for Sample 123 Ni

F.2 Co deposition diffraction data

Diffraction data obtained from annealing steps on ZnO rods with a layer of Cobalt deposited on them.
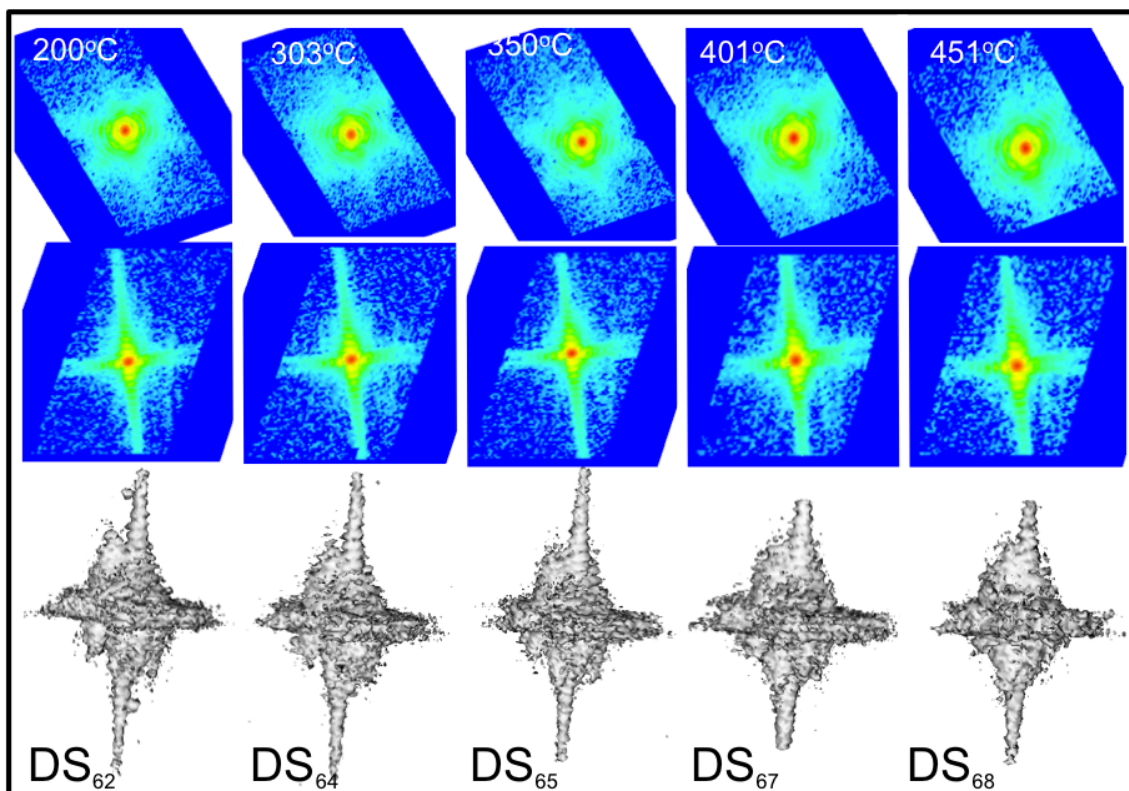
Figure F.3: Cut planes and isosurface renderings of the diffraction measured upon annealing steps for Sample 113 Co
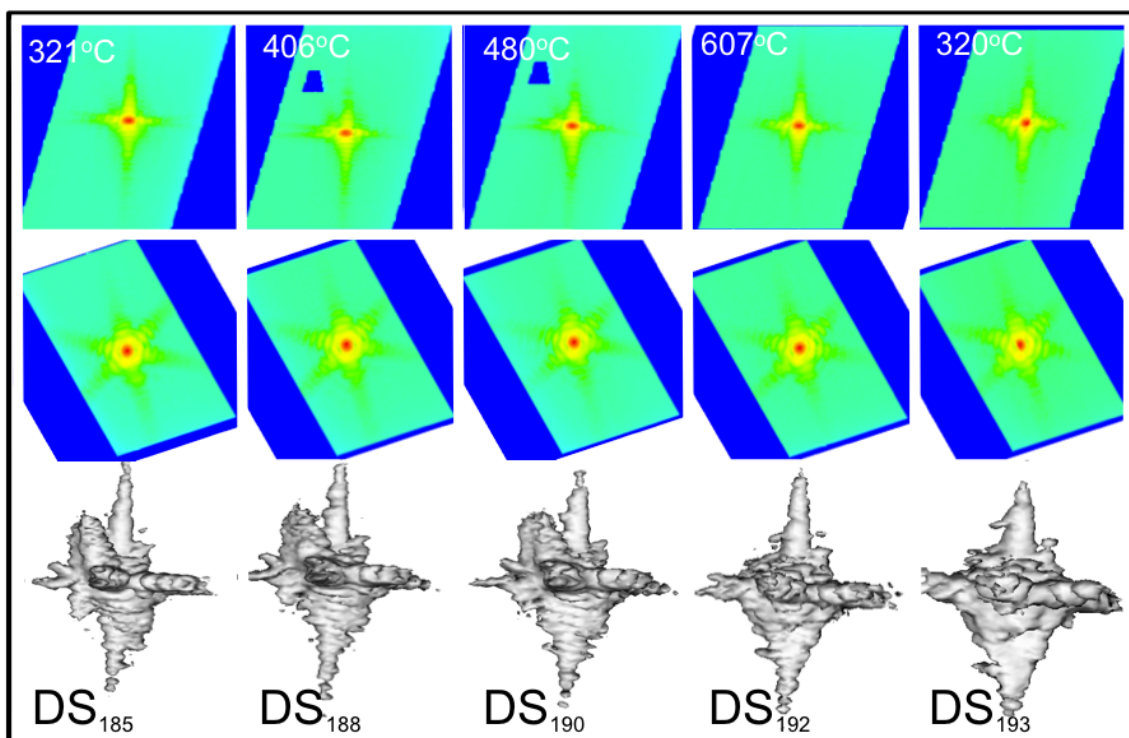
Figure F.4: Cut planes and isosurface renderings of the diffraction measured upon annealing steps for Sample 115 Co

Appendix G

G.1 Basic Phasing Operation

Documented Python scripts for phasing operations. 'Phase.py' file runs all other programs

internally and are separated for ease editing. Adapted from scripts written by Ross Harder.

G.1.1 PhasingParams.py

```
######################################################################
# Variables file required to run Phase.py phasing file
######################################################################

# import the required libraries
import math

# Constants required for calculations
pi=math.pi
deg2rad = pi/180.0000
phasingparamsexecuted=True

######################################################################
# Datafile identifier no.
######################################################################

SequenceNumber=0                # File identifier, ends up in filename
scaleArrayPercentAmps=True       # Scale the output amplitude array

######################################################################
# Data Preprocessing
######################################################################

# Define the min and max of the data amplitudes that are used in the phasing
minthresh = 50
maxthresh = 9000000000

# Set to true to output the data in various file formats
outputdatavtk=True
outputdataspe=True
outputdatasp4=True

# If True the program will exit after the data preparation stage
stopdataprep=False

######################################################################
# Phasing Parameters
######################################################################
```

```
beta = .9

#####################################################################
# Iteration variables for each Algorithm run in the phasing operation
#####################################################################

numHIOiter = 50
numERiter2 = 20

ID='\%dHIO\_\%dER'\%(numERiter1,numHIOiter,numERiter2)

#####################################################################
# The Phase Constrained HIO phase constraint must be defined here when used.
#####################################################################

phmin = -pi*.500
phmax = pi*.500

#####################################################################
# Planes defined to enclose a 3D region of space defined as the support
#####################################################################

planeList=[]
planeList.append([19,0,0])
planeList.append([-19,0,0])
planeList.append([-2,37,-2])
planeList.append([2,-37,2])
planeList.append([0,0,16])
planeList.append([0,0,-16])

#####################################################################
# Detector and scan variables
#####################################################################

pixelx=2*(22.50e-6)            #Total pixel size, binning factor x pixel size (in meters)
pixely=2*(22.50e-6)            #Total pixel size, binning factor x pixel size (in meters)
arm = 2.145                    #Detector distance from sample (units are m)
lam = 0.139                    #Wavelength of x-ray (units in nm)
delta = 29.502 * deg2rad       #Detector angle delta
gam = 14.7472 * deg2rad        #Detector angle gamma
dth = 0.0025 * deg2rad         #rocking curve step size in theta orientation
dtilt = 0.00 * deg2rad         #rocking curve step size in tilt (phi) orientation
dpx=pixelx/arm                 #pixel size in radians
dpy=pixely/arm                 #pixel size in radians

#####################################################################
```

G.1.2 Phase.py

```
####################################################################

# Function for scaling amplitude in an array to a percentage of the maximum amplitude
def Scale(Array,ScaledArray):
        c.Sp4ArrayGetModulus(ScaledArray,Array)
        max=c.Sp4ArrayGetMax(ScaledArray,c.AMP)
        nontuple=max[1]
        factor = 100.0/nontuple
        c.Sp4ArrayScale(ScaledArray,factor)

####################################################################
# User defined variables:
# i)   Iterations of Phase Constrained HIO + Phase Only ER
# ii)  Support dimensions
# iii) Equipment positions for correct geometric correction
####################################################################

# import the necessary libraries
import cstuff as c
import mycstuff as mc
import sys
import SequenceClass as sc
import vtkStructuredGridMaker as vs
import vtkImageImportFromArray as iia
import vtk
import SpeFile as spe
import math
import os

# Generate Sp4 arrays
diffData=c.Sp4Array()
dDcrop=c.Sp4Array()
supcrop=c.Sp4Array()
support=c.Sp4Array()
NewCoords=c.Sp4Array()

# execute necessary python scripts
execfile("phasingparams.py")
execfile("DataPrep.py")

n=SequenceNumber

####################################################################
# Update log file
####################################################################

list = ['File Identifier =\%d \n'\%n,'Raw Data file: BD-data-'+fID+'.sp4\n','Support \n']

stringPlanes=''
for i in range(len(planeList)):
        stringPlanes+='\%d \%d \%d\n'\%(planeList[i][0],planeList[i][1],planeList[i][2])
list+=stringPlanes

append=ID

s = fID1+'\%d\_Support\_'\%n+append
s1 = fID1+'\%d\_'\%n+append

list+= ['Datamask Threshold: \%d\n'\%(minthresh),'Copy of Support to start\n',
        'Filenames Produced:\n',s1,'\n',s,'\n','########################################\n']

data = []
if os.path.exists("PhasingLog\%d.txt"\%n):
  data=open("PhasingLog\%d.txt"\%n).readlines()
filename='PhasingLog\%d.txt'\%n
outfile=open(filename, "w")

for i in range (len(data)):
    outfile.write(data[i])
for j in range (len(list)):
    outfile.write(list[j])
####################################################################

max=c.Sp4ArrayGetMax(bd,c.AMP)          #find max amplitude in raw processed data array
dims=c.Sp4ArrayGetDims(bd)[1:]          #find dimensions of raw processed data array
print max[1], dims                      #print for the user benefit, error checking

####################################################################
# Generate the support
####################################################################

string = 'supportconf\%d'\%(n)          #support planes conf filename
file = open(string, 'w' )              #open new conf file
file.write (stringPlanes)              #write user defined planes to conf file
```

```
file.close()                          #close conf file

c.Sp4ArrayInitAsOther(support,bd)        #give the support the same attributes of the data array
c.Sp4ArrayZero(support)                        #zero the support
c.Makepoly(support, string, 0.0,0.0,0.0)         #make a polygon for the support

c.Sp4ArraySave(support,'support.sp4')        #save the support file


########################################################################
# Run algorithms
########################################################################

execfile("Algorithms.py")
# run a set of user defined algorithms from a different file
# the phasing parameters and result are saved in a SequenceData structure

diffData=seqdata.dist                           #copy the current result to a new array
max=c.Sp4ArrayGetMax(diffData,c.AMP)         #find the maximum amplitude
# save the maximum amplitude to the log file
outfile.write("Maximum Amplitude in reconstruction: \%d\n"\%max[1] )
########################################################################
# Crop data for reduced output
########################################################################

# locate the dimensions of the reconstructed object, needs to be a binary array
cropDims=mc.Sp4ArrayFindCropDims(support,3)
print cropDims                                      #print the crop dimensions for the users reference

# Test that the crop dimensions calculated do not exceed the size of the data array
arrayDims=c.Sp4ArrayGetDims(support)

if (abs(cropDims[1]*2)+cropDims[2])>arrayDims[1]:
  cropDims[1]=0
  cropDims[2]=arrayDims[1]

if (abs(cropDims[3]*2)+cropDims[4])>arrayDims[2]:
  cropDims[3]=0
  cropDims[4]=arrayDims[2]

if (abs(cropDims[5]*2)+cropDims[6])>arrayDims[3]:
  cropDims[5]=0
  cropDims[6]=arrayDims[3]

print cropDims                                          #print the crop dimensions for the users reference

# Extract an array  surrounding the reconstructed object based on cropDims
c.ExtractArray(diffData, dDcrop, cropDims[1], cropDims[2], cropDims[3], cropDims[4], cropDims[5], cropDims[6])
c.ExtractArray(support, supcrop, cropDims[1], cropDims[2], cropDims[3], cropDims[4], cropDims[5], cropDims[6])


########################################################################
# Generate a coordinate system
########################################################################

# get the cropped array dimensions
size1 = c.Sp4ArrayGetDim(dDcrop,0)[1]
size2 = c.Sp4ArrayGetDim(dDcrop,1)[1]
size3 = c.Sp4ArrayGetDim(dDcrop,2)[1]

# define the dimensions in real space
dx = 1.0/c.Sp4ArrayGetDim(diffData,0)[1]
dy = 1.0/c.Sp4ArrayGetDim(diffData,1)[1]
dz = 1.0/c.Sp4ArrayGetDim(diffData,2)[1]

# Generate a coordinate system in direct space
if dtilt ==0.0:
  c.ThCoordTrans(NewCoords, size1, size2, size3, lam, delta, gam, dpx, dpy, dth,dx ,dy,dz,c.DIRECT)
  print "theta rocking curve coordinate tranform"
elif dth == 0.0:
  c.TiltCoordTrans(NewCoords, size1, size2, size3, lam, delta, gam, dpx, dpy, dtilt,dx,dy,dz,c.DIRECT)
  print "chi rocking curve coordinate transform"
else:
  print "dth/dtilt has been set incorrectly"


########################################################################
# Generate output files
########################################################################

# Ross Harder added the Q-vector output 3/08
# Generates a vtk file visualised with Glyph module in Mayavi

c.ShiftCoordOrigin(NewCoords, size1/2, size2/2, size3/2)

Qlabcenter1 = math.sin(delta)*math.cos(gam)*(2*3.14159265)/lam;
Qlabcenter2 = math.sin(gam)*(2*3.14159265)/lam;
Qlabcenter3 = (math.cos(delta)*math.cos(gam)-1.0)*(2*3.14159265)/lam;
ki=(0.0,0.0,(2*3.14159265)/lam)
kf= ( math.sin(delta)*math.cos(gam)*(2*3.14159265)/lam,
       math.sin(gam)*(2*3.14159265)/lam, math.cos(delta)*math.cos(gam)*(2*3.14159265)/lam )
```

```
vectorarr = vtk.vtkDoubleArray()
vectorarr.SetNumberOfComponents(3)
vectorarr.SetNumberOfTuples(3)
vectorarr.SetComponent(0,0,Qlabcenter1)
vectorarr.SetComponent(0,1,Qlabcenter2)
vectorarr.SetComponent(0,2,Qlabcenter3)
vectorarr.SetComponent(1,0,ki[0])
vectorarr.SetComponent(1,1,ki[1])
vectorarr.SetComponent(1,2,ki[2])
vectorarr.SetComponent(2,0,kf[0])
vectorarr.SetComponent(2,1,kf[1])
vectorarr.SetComponent(2,2,kf[2])

vectorpoints=vtk.vtkPoints()
vectorpoints.SetDataTypeToDouble()
vectorpoints.SetNumberOfPoints(3)
vectorpoints.SetPoint(0, (0.0,0.0,0.0) )
vectorpoints.SetPoint(1, (0.0,0.0,0.0) )
vectorpoints.SetPoint(2, (0.0,0.0,0.0) )

vectorgrid = vtk.vtkUnstructuredGrid()
vectorgrid.SetPoints(vectorpoints)
vectorgrid.GetPointData().SetVectors(vectorarr)

# Define filenames to save output files
s1=seqdata.filenameroot+"dist\%04d"\%seqdata.iterationscompleted+'\_bd\_'+fID

c.Sp4ArraySave(diffData,s1+'.sp4')
s=seqdata.filenameroot+"\_Support"

# output calculated phases
dDphaseGM=vs.vtkStructuredGridMaker(NewCoords, dDcrop, c.PHASE)
dDphaseGM.WriteStructuredGrid(s1+'\_phase.vtk')

# scale the amplitudes
ScaledArray=c.Sp4Array()
c.Sp4ArrayInitAsOther(ScaledArray,dDcrop)
Scale(dDcrop,ScaledArray)

c.Sp4ArrayCopy(dDcrop,ScaledArray,'')

# output reconstructed amplitudes
dDampsGM=vs.vtkStructuredGridMaker(NewCoords, dDcrop, c.AMP)
dDampsGM.WriteStructuredGrid(s1+'\_amp.vtk')

# output support vtk file
supampsGM=vs.vtkStructuredGridMaker(NewCoords, supcrop, c.AMP)
supampsGM.WriteStructuredGrid(s+'\_amp.vtk')

# output Q vector vtk file
usgridwriter=vtk.vtkUnstructuredGridWriter()
usgridwriter.SetFileName('Qvector.vtk')
usgridwriter.SetFileTypeToASCII()
usgridwriter.SetInput(vectorgrid)
usgridwriter.Write()

# Remove following three lines if a datamask vtk file is not required.
iimport=iia.vtkImageImportFromSp4Array()
iimport.SetArray(datamask, c.AMP)
iimport.WriteImageData('datamask_amp.vtk')

########################################################################
```

G.1.3 DataPrep.py

```
######################################################################
# Data preparation steps
######################################################################

# import required libraries
import cstuff as c
import sys
import vtkImageImportFromArray as iia
import vtk
import SpeFile as spe
import math

# generate Sp4 arrays
bd=c.Sp4Array()
datamask=c.Sp4Array()

# test to ensure phasing parameters have been defined
if not phasingparamsexecuted:
  execfile("phasingparams.py")

c.Sp4ArrayLoad(bd,datafilename)            #Load the diffraction data
c.Sp4ArraySqrt(bd)                           #Square root the diffraction intensities

# Read the dimensions of the data array
size1 = c.Sp4ArrayGetDim(bd,0)[1]
size2 = c.Sp4ArrayGetDim(bd,1)[1]
size3 = c.Sp4ArrayGetDim(bd,2)[1]

# output vtk files if requested
if outputdatavtk:
  iimport=iia.vtkImageImportFromSp4Array()
  iimport.SetArray(bd, c.AMP)
  cleandatafilename=fID+"Sequence\%i"\%SequenceNumber+"\_processeddata.vtk"
  iimport.WriteImageData(cleandatafilename)

# output sp4 arrays if requested
if outputdatasp4:
  cleandatafilename=fID+"Sequence\%i"\%SequenceNumber+"\_processeddata.sp4"
  c.Sp4ArraySave(bd, cleandatafilename)

# set thresholds on the diffracted amplitudes
c.MinMaxThreshMask(datamask, bd, minthresh, maxthresh)

# place the data in wrap around format for correct Fourier transform operation
c.Sp4ArrayWrap(datamask)
c.Sp4ArrayWrap(bd)

######################################################################
```

G.1.4 Algorithms.py

```
########################################################################
# Set up data structures
########################################################################

# create a sequenceData structure to hold information about the reconstruction produced in phasing
seqdata=sc.SequenceData(SequenceNumber, './')

# choose to initialise the algorithm with a random starting point or user defined starting point
c.InitializeSequence_COPY(seqdata, support)
c.InitializeSequence_dsRANDOM_REAL(seqdata, support)

########################################################################
# Algorithms
########################################################################

c.PhaseConstrainedHIO(seqdata, bd, support, datamask, beta, phmin, phmax, numHIOiter)
c.DoER_support(seqdata, bd, support, numERiter2)

# output the contents of the data structure
seqdata.Write()

########################################################################
```

G.1.5 AlienExterminate.py

```
#######################################################################
# Use to remove aliens from datasets
# Removes user defined cuboids / setting region defined to zero
# RectAlienRemoval(array,xmax,xmin,ymax,ymin,zmax,xmin)
#######################################################################

import cstuff as c
import mycstuff as mc
import sys
import vtkImageImportFromArray as iia

array=c.Sp4Array()
c.Sp4ArrayLoad(array,sys.argv[1])

# Apply multiple instances of the next line, drawing boxes around known alien scattering
mc.CuboidAlienRemoval(array,xmax,xmin,ymax,ymin,zmax,xmin) #

# Export the required files
c.Sp4ArraySave(array,'AlienRM'+sys.argv[1])

iimport=iia.vtkImageImportFromSp4Array()
iimport.SetArray(array, c.AMP)
iimport.WriteImageData('alienRM_amp.vtk')

#######################################################################
```

G.2 Shrinkwrap Phasing Operation

The shrinkwrap code has been adapted to a single python file from a script written by
Marcus Newton.

G.2.1 ShrinkWrap.py

```
def Scale(Array,ScaledArray):
        c.Sp4ArrayGetModulus(ScaledArray,Array)
        max=c.Sp4ArrayGetMax(ScaledArray,c.AMP)
        nontuple=max[1]
        factor = 100.0/nontuple
        c.Sp4ArrayScale(ScaledArray,factor)

#####################################################################%
# Performs phase reconstruction with a Shrink Wrapped support.
# For attended execution, the shrink wrap loop can be safely broken with user input character 'e'
# Inputs: AutoArray.sp4, Support.sp4
# Outputs: ShrinkWrap.log, Final.sp4, SupportSW.sp4, FinalCrop.sp4, SupportSWCrop.sp4, NewCoords.sp4,
# Object.vtk, Support_Initial.vtk, Support.vtk
%#
%# Usage:# python ShrinkWrap.py
%# c dependences: "cstuff": tree
%# c dependences: "mycstuff": Sp4ArrayThresholdRemoveLow.c, Sp4ArrayAverageIPfft.c, Sp4ArraySmoothIPfft.c,
%# Array2Support.c, Sp4ArrayAutoCrop.c.
%# python dependences: PhasingVariables.py
#####################################################################

# import required libraries
import cstuff as c
import mycstuff as mc
import sys
import SequenceClass as sc
import vtkStructuredGridMaker as vs
import vtkImageImportFromArray as iia
import math
import os
import time
import select
import tty
import termios

# generate the required arrays
InputArray=c.Sp4Array()
iD='001'

Support=c.Sp4Array()
ScaledAC=c.Sp4Array()
DataMask=c.Sp4Array()
OutputArray=c.Sp4Array()
OutputArrayNew=c.Sp4Array()
FinalArray=c.Sp4Array()
NewCoords=c.Sp4Array()
FinalArrayCrop=c.Sp4Array()
SupportCrop=c.Sp4Array()
OutputArrayCrop=c.Sp4Array()
execfile("ParamsShrinkwrap.py")

# Load Centred Intensity Data
c.Sp4ArrayLoad(InputArray,sys.argv[1])

#####################################################################
# Generate Support
#####################################################################

c.Sp4ArrayCopy(Support,InputArray,'')
c.Sp4ArrayFFT(Support,1,1)
c.Sp4ArrayWrap(Support)

supFN='Support.vtk'
acFN='AC_scaled.vtk'

Scale(Support,ScaledAC)
print c.Sp4ArrayGetDims(Support)
c.Sp4ArraySave(Support,'ACfunction.sp4')
```

```
mc.Sp4ArrayAC2Block(Support,Support_Axis,Support_WidthThreshold,Support_LengthThreshold,Support_CrossSectionSmoothing)
mc.Sp4ArraySmoothIPfft(Support,Support_Smoothing)
mc.Array2Support(Support,0.000001)
c.Sp4ArraySave(Support,'Support.sp4')

# output autocorrelation function
iimport=iia.vtkImageImportFromSp4Array()
iimport.SetArray(ScaledAC, c.AMP)
iimport.WriteImageData(acFN)
c.Sp4ArrayDestroy(ScaledAC)

# output support generated form autocorrelation function
iimport=iia.vtkImageImportFromSp4Array()
iimport.SetArray(Support, c.AMP)
iimport.WriteImageData(supFN)

if stopSupportPrep:
        print '\nSupport Generated:',supFN,'\nScript terminated for further support preparation
                \nRefer to file: ',acFN,'for percentage scale autocorrelation function\n'
        sys.exit()
else:
        print 'Support Generated'

print 'testing'
c.Sp4ArraySqrt(InputArray)

########################################################################
# Update log file
########################################################################

sw_log = open("ShrinkWrap\%d.log"\%n, "a")
sw_log.write(time.strftime("\n\%H:\%M:\%S \%a \%d-\%m-\%y", time.localtime()))
sw_log.writelines("\n\nIterations:"+"\nnumHIOiter_Initial = "+str(numHIOiter_Initial)+
    "\nnumERiter_Initial = "+str(numERiter_Initial)+ "\nnumHIOiter_ShrinkWrap =
    "+str(numHIOiter_ShrinkWrap)+ "\nnumERiter_ShrinkWrap = "+str(numERiter_ShrinkWrap
    +"\nnumHIOiter_Final = "+str(numHIOiter_Final)+ "\nnumERiter_Final = "+str(numERiter_Final))
sw_log.writelines("\n\nSelf Consistency:" + "\nSelfConsistenceThreshold = "+ str(SelfConsistenceThreshold))
sw_log.writelines("\n\nSp4ArrayAverage:" +"\nAverage Width = "+str(AverageWidth) +"\nAverageIter = "+str(AverageIter))
sw_log.writelines("\n\nSp4ArraySmoothIPfft:" +"\nSmoothSigma = "+str(SmoothSigma))
sw_log.writelines("\n\nData Cutoff Threshold:"+"\nArray2SupportThreshold = "+str(Array2SupportThreshold))

########################################################################
# Initial Phasing
########################################################################

# Create and save DataMask if u like
c.MinMaxThreshMask(DataMask, InputArray, minthresh, maxthresh)

# Wrap:
c.Sp4ArrayWrap(InputArray)
c.Sp4ArrayWrap(DataMask)

execfile("Phasing_Initial.py")

c.Sp4ArrayInitAsOther(OutputArray,InputArray)
c.Sp4ArrayZero(OutputArray)
c.Sp4ArrayInitAsOther(OutputArrayNew,InputArray)
c.Sp4ArrayZero(OutputArrayNew)

########################################################################
# Self Consistent Shrink Wrapped Phasing
########################################################################
error_abs=100.0

sw_log.write("\n\nSelf consistency error values: \n")

c.Sp4ArrayFastCopy(OutputArray,seqdata.dist)
mc.Sp4ArrayThresholdRemoveLow(OutputArray,Array2SupportThreshold)
mc.Sp4ArrayAverageIPfft(OutputArray,AverageWidth,AverageIter)
mc.Sp4ArraySmoothIPfft(OutputArray,SmoothSigma)
mc.Array2Support(OutputArray,0.000001)

# Check that tty session is active from user input
# Shrink wrap can be exited cleanly with user input
# This is useful for testing the shrink wrap conditions
# during attended execution
iter=0
if sys.stdin.isatty():
        def tty_input():
                # boolean return on stdin pool.  no timeout.
                return select.select([sys.stdin], [], [], 0) == ([sys.stdin], [], [])

        # Grab current tty mode
        old_tty_settings = termios.tcgetattr(sys.stdin)
        try:
                # Set file descriptor to break
                tty.setcbreak(sys.stdin.fileno())
```

```
                   while error_abs > SelfConsistenceThreshold:
                           execfile("Phasing_ShrinkingSupport.py")
                           # Self consistent part:
                           c.Sp4ArrayFastCopy(OutputArrayNew,seqdata.dist)
                           mc.Sp4ArrayThresholdRemoveLow(OutputArrayNew,Array2SupportThreshold)
                           mc.Sp4ArrayAverageIPfft(OutputArrayNew,AverageWidth,AverageIter)
                           mc.Sp4ArraySmoothIPfft(OutputArrayNew,SmoothSigma)
                           mc.Array2Support(OutputArrayNew,0.000001)
                           sum_old=c.Sp4ArraySelectSum(OutputArray,c.REAL)[1] + c.Sp4ArraySelectSum(OutputArray,c.IMAG)[1]
                           sum_new=c.Sp4ArraySelectSum(OutputArrayNew,c.REAL)[1] + c.Sp4ArraySelectSum(OutputArrayNew,c.IMAG)[1]
                           error=100.0 * (sum_new*sum_new - sum_old*sum_old)/(sum_old*sum_old)
                           error_abs= abs(error)
                           sw_log.writelines(str(error) + "\n")
                           print "Self-consistency error is \%.5f" \%error

                           c.Sp4ArrayFastCopy(OutputArray,OutputArrayNew)
                           if iter==10:
                                   break
                           iter+=1
                           # Break loop with 'e' key
                           if tty_input():
                                   user_key = sys.stdin.read(1)
                                   if user_key == 'e':          # x1b is ESC
                                           break

           finally:
                   #restore tty settings
                   termios.tcsetattr(sys.stdin, termios.TCSADRAIN, old_tty_settings)

else:
           while error_abs > SelfConsistenceThreshold:
                           execfile("Phasing_ShrinkingSupport.py")
                           # Self consistent part:
                           c.Sp4ArrayFastCopy(OutputArrayNew,seqdata.dist)
                           mc.Sp4ArrayThresholdRemoveLow(OutputArrayNew,Array2SupportThreshold)
                           mc.Sp4ArrayAverageIPfft(OutputArrayNew,AverageWidth,AverageIter)
                           mc.Sp4ArraySmoothIPfft(OutputArrayNew,SmoothSigma)
                           mc.Array2Support(OutputArrayNew,0.000001)
                           sum_old=c.Sp4ArraySelectSum(OutputArray,c.REAL)[1] + c.Sp4ArraySelectSum(OutputArray,c.IMAG)[1]
                           sum_new=c.Sp4ArraySelectSum(OutputArrayNew,c.REAL)[1] + c.Sp4ArraySelectSum(OutputArrayNew,c.IMAG)[1]
                           error=100.0 * (sum_new*sum_new - sum_old*sum_old)/(sum_old*sum_old)
                           error_abs= abs(error)
                           sw_log.writelines(str(error) + "\n")
                           print "Self-consistency error is \%.5f" \%error

                           c.Sp4ArrayFastCopy(OutputArray,OutputArrayNew)

# close file
sw_log.close()

#######################################################################
# Final Phasing
#######################################################################

execfile("Phasing_Final.py")
FinalArray=seqdata.dist

CropDims=mc.Sp4ArrayFindCropDims(OutputArray,3)
print CropDims
print 'Change this if you want to look at the original support'

# Reduce the size of the output array
c.ExtractArray(FinalArray, FinalArrayCrop, CropDims[1], CropDims[2], CropDims[3], CropDims[4], CropDims[5], CropDims[6])
c.ExtractArray(Support, SupportCrop, CropDims[1], CropDims[2], CropDims[3], CropDims[4], CropDims[5], CropDims[6])
c.ExtractArray(OutputArray, OutputArrayCrop, CropDims[1], CropDims[2], CropDims[3], CropDims[4], CropDims[5], CropDims[6])

ScaledArray=c.Sp4Array()
c.Sp4ArrayInitAsOther(ScaledArray,FinalArrayCrop)
if scaleArrayPercentAmps:
        Scale(FinalArrayCrop,ScaledArray)
else:
        c.Sp4ArrayCopy(ScaledArray,FinalArrayCrop,'')

# Name some files
PhaseNameSupportInitial='\%d_sw_Support_fromAC'\%(n)
PhaseNameSupport='\%d_sw_Support_Final'\%(n)
PhaseName='\%d_sw_ReconstructedObject'\%(n)

if outputdatasp4:
        c.Sp4ArraySave(OutputArray,PhaseNameSupport+'.sp4')
        c.Sp4ArraySave(Support,PhaseNameSupportInitial+'.sp4')

if outputdatavtkvoxeldims:
        iimport=iia.vtkImageImportFromSp4Array()
        iimport.SetArray(ScaledArray, c.AMP)
        iimport.WriteImageData(PhaseName+'VDamp.vtk')

        iimport=iia.vtkImageImportFromSp4Array()
```

```
        iimport.SetArray(FinalArray, c.PHASE)
        iimport.WriteImageData(PhaseName+'VDph.vtk')

        iimport=iia.vtkImageImportFromSp4Array()
        iimport.SetArray(OutputArray, c.AMP)
        iimport.WriteImageData(PhaseNameSupport+'VD.vtk')

        iimport=iia.vtkImageImportFromSp4Array()
        iimport.SetArray(Support, c.AMP)
        iimport.WriteImageData(PhaseNameSupportInitial+'VD.vtk')

#####################################################################
# Geometric correction
#####################################################################

size1 = c.Sp4ArrayGetDim(FinalArrayCrop,0)[1]
size2 = c.Sp4ArrayGetDim(FinalArrayCrop,1)[1]
size3 = c.Sp4ArrayGetDim(FinalArrayCrop,2)[1]

# define the dimensions in real space
dx = 1.0/c.Sp4ArrayGetDim(FinalArrayCrop,0)[1]
dy = 1.0/c.Sp4ArrayGetDim(FinalArrayCrop,1)[1]
dz = 1.0/c.Sp4ArrayGetDim(FinalArrayCrop,2)[1]

# Translate coordinates
if dtilt ==0.0:
  c.ThCoordTrans(NewCoords, size1, size2, size3, lam, delta, gam, dpx, dpy, dth,dx ,dy,dz,c.DIRECT)
  print "theta rocking curve coordinate tranform"
elif dth == 0.0:
  c.TiltCoordTrans(NewCoords, size1, size2, size3, lam, delta, gam, dpx, dpy, dtilt,dx,dy,dz,c.DIRECT)
  print "chi rocking curve coordinate transform"
else:
  print "dth/dtilt has been set incorrectly"

#####################################################################
# Output  vtk files
#####################################################################

if outputdatavtkgeocorr:
        dDampsGM=vs.vtkStructuredGridMaker(NewCoords, ScaledArray, c.AMP)
        dDampsGM.WriteStructuredGrid(PhaseName+'_amp.vtk')

        dDphaseGM=vs.vtkStructuredGridMaker(NewCoords, FinalArrayCrop, c.PHASE)
        dDphaseGM.WriteStructuredGrid(PhaseName+'_phase.vtk')

        supampsGM=vs.vtkStructuredGridMaker(NewCoords, SupportCrop, c.AMP)
        supampsGM.WriteStructuredGrid(PhaseNameSupportInitial+'_amp.vtk')

        supampsGM=vs.vtkStructuredGridMaker(NewCoords, OutputArrayCrop, c.AMP)
        supampsGM.WriteStructuredGrid(PhaseNameSupport+'_amp.vtk')

#####################################################################
```

G.2.2 ParamsShrinkwrap.py

```
import math
# define constants
pi=math.pi
deg2rad = pi/180.0000

######################################################################
# Filename: ShrinkwrapParams.py
# Contains Variables for the Shrinkwrap method
######################################################################

# File Identifier
n=0

# Set to true to output the data in various file formats
generateSupport=True
scaleArrayPercentAmps=False
outputdatavtkgeocorr=True
outputdatavtkvoxeldims=False
outputdatasp4=True

# declare some Phasing variables
beta = .9

# Threshold for datamask
minthresh = 50
maxthresh = 9000000

# Phase Constraints set for PhaseConHIO
phmin = -pi * 2/4
phmax = pi * 2/4

######################################################################
# Support from Autocorrelation variables
######################################################################
Support_Axis=2
Support_LengthThreshold=90.0
Support_WidthThreshold=40.0
Support_CrossSectionSmoothing=2.0
Support_Smoothing=2.0
# If stopSupportPrep=True the program will exit after the support preparation stage.
# stopSupportPrep=True
stopSupportPrep=False

######################################################################
# Algorithm parameters
######################################################################

# Number of iterations of each algorithm with initial support
numERiter_Initial = 12
numHIOiter_Initial = 60

# Numer of ShrinkWrap iterations within each loop
numHIOiter_ShrinkWrap = 10
numERiter_ShrinkWrap = 2

# Number of iterations after the final support
numHIOiter_Final = 60
numERiter_Final = 12

######################################################################
# Self consistent support generation variables
######################################################################

# Self Consistence threshold, when the support changes by less than the threshold exit
SelfConsistenceThreshold=1.0

# Self Consistency Smoothing variables for Sp4ArrayAverageIPfft:
AverageWidth=3
AverageIter=3

# Self Consistency Smoothing variables for Sp4ArraySmoothIPfft:
SmoothSigma=0.35

# Self Consistency data cutoff threshold
Array2SupportThreshold=19.5

######################################################################
# Experimental variables
######################################################################

pixelx=2*(22.50e-6)
pixely=2*(22.50e-6)
arm = 2.145
lam = 0.139
```

```
delta = 29.502 * deg2rad
gam = 14.7472 * deg2rad
dth = 0.0025 * deg2rad
dtilt = 0.00 * deg2rad
dpx=pixelx/arm
dpy=pixely/arm

#####################################################################
```

G.2.3 Phasing_Initial.py

```
######################################################################
# Phasing Initial Support
######################################################################

seqdata=sc.SequenceData(n, './')
# c.InitializeSequence_COPY(seqdata, Support)
c.InitializeSequence_dsRANDOM_REAL(seqdata, Support)

######################################################################
# Run algorithms
######################################################################

c.PhaseConstrainedHIO(seqdata, InputArray, Support, DataMask, beta, phmin, phmax, numHIOiter_Final)
mc.DofER_maskedzero(seqdata, InputArray, Support, DataMask, numERiter_Initial)

######################################################################
```

G.2.4 Phasing_Final.py

```
######################################################################
# Algorithms for final phasing operation
######################################################################

c.PhaseConstrainedHIO(seqdata, InputArray, OutputArray, DataMask, beta, phmin, phmax, numHIOiter_Final)
mc.DofER_maskedzero(seqdata, InputArray, OutputArray, DataMask, numERiter_Final)

######################################################################

# Output results
seqdata.Write()

######################################################################
```

G.2.5 Phasing_ShrinkingSupport.py

```
######################################################################
# Algorithms for shrinking support
######################################################################

c.PhaseConstrainedHIO(seqdata, InputArray, OutputArray, DataMask, beta, phmin, phmax, numHIOiter_ShrinkWrap)
mc.DofER_maskedzero(seqdata, InputArray, OutputArray, DataMask, numERiter_ShrinkWrap)

######################################################################
```

G.3 Cross Correlation Operation

G.3.1 CrossCorrelation.py

```
########################################################################
#FFT cross correlation method
#N squared cross correlation method
#plus transpose and shift array functions to identify twins
########################################################################

# import required libraries
import cstuff as c
import mycstuff as mc
import os
import string
import vtkImageImportFromArray as iia
import sys

# generate required Sp4 arrays
tempRI=c.Sp4Array()
RI=c.Sp4Array()
mult=c.Sp4Array()
mod=c.Sp4Array()
array=c.Sp4Array()
transposeArray=c.Sp4Array()

########################################################################
#FFT cross correlation method
########################################################################

def CrossCorrelationFastFFT(templateFilename,RIFilename):

        c.Sp4ArrayLoad(tempRI,templateFilename)
        c.Sp4ArrayLoad(RI,RIFilename)

        c.Sp4ArrayFFT(tempRI,1,1)
        c.Sp4ArrayFFT(RI,1,1)
        mc.Sp4ArrayConjugate(RI)

        c.Sp4ArrayInitAsOther(mult,tempRI)
        c.Sp4ArrayFastMult(tempRI,RI,mult)
        c.Sp4ArrayFFT(mult,1,1)
        c.Sp4ArrayWrap(mult)
        c.Sp4ArrayGetModulus(mod,mult)

        size1 = c.Sp4ArrayGetDim(tempRI,0)[1]
        size2 = c.Sp4ArrayGetDim(tempRI,1)[1]
        size3 = c.Sp4ArrayGetDim(tempRI,2)[1]

        cenx=size1/2
        ceny=size2/2
        cenz=size3/2

        max=mc.Sp4ArrayLocateMax(mod)

        shiftX=max[1]-cenx
        shiftY=max[2]-ceny
        shiftZ=max[3]-cenz

        print 'The FFT method shifts the RI (\%d,\%d,\%d) to match to the template'\%(-shiftX,-shiftY,-shiftZ)
        totalShift = [-shiftX,-shiftY,-shiftZ]
        ################################################################
# Update log file        ################################################################
        list = ['FFTmethod','Cross Correlation between:\n','   '+templateFilename,'\n','   '+RIFilename,'\n','Shift required to achieve best correlation:\
        data = []
        if os.path.exists("CrossCorrelations.txt"):
                data=open("CrossCorrelations.txt").readlines()
        outfile=open("CrossCorrelations.txt", "w")

        for k in range (len(data)):
                outfile.write(data[k])
        for j in range (len(list)):
                outfile.write(list[j])

        return totalShift

########################################################################
# N squared cross correlation method
########################################################################

def CrossCorrelationN2(templateRIFilename,RIFilename,shiftRange):

        # set the shiftRange to 1 to calculate a single N2 value
```

```
        c.Sp4ArrayLoad(tempRI,templateRIFilename)
        c.Sp4ArrayLoad(RI,RIFilename)

        MaxSum = 0.0
        MaxCoords = []
        counter = 0

        for x in range (shiftRange):
                for y in range (shiftRange):
                        for z in range (shiftRange):
                                shiftX = x - (shiftRange-1)/2
                                c.Sp4ArrayShift(RI,1,shiftX)

                                shiftY = y - (shiftRange-1)/2
                                c.Sp4ArrayShift(RI,2,shiftY)

                                shiftZ = z - (shiftRange-1)/2
                                c.Sp4ArrayShift(RI,3,shiftZ)

                                c.Sp4ArrayInitAsOther(mult,tempRI)
                                c.Sp4ArrayFastMult(RI,tempRI,mult)

                                sum = mc.Sp4ArraySum(mult)
                                if sum[1] >= MaxSum:
                                        MaxSum=sum[1]
                                        MaxCoords=[-shiftX,-shiftY,-shiftZ]
                                        #print MaxSum
                                counter+=1

        if (shiftRange>1):
                print 'The RI was shifted by \%d voxels in each dimension around its current position'\%(shiftRange-1/2)
                print 'The maximum was found to be \%d at a shift of (\%d,\%d,\%d)'\%(MaxSum,MaxCoords[0],MaxCoords[1],MaxCoords[2])

        totalShift=MaxCoords[0:]
        totalShift.append(MaxSum)
        return totalShift


#####################################################################
# Function: shift array in 3 dimensions
#####################################################################

def ShiftArray(Filename,shift):
        c.Sp4ArrayLoad(array,Filename)
        c.Sp4ArrayShift(array,1,shift[0])
        c.Sp4ArrayShift(array,2,shift[1])
        c.Sp4ArrayShift(array,3,shift[2])
        return array


#####################################################################
# Transpose array function
#####################################################################

def TransposeArray(RIFilename):
        c.Sp4ArrayLoad(array,RIFilename)
        c.Sp4ArrayInitAsOther(transposeArray,array)
        mc.Sp4Array3DTransposeComplex(array,transposeArray)
        c.Sp4ArraySave(transposeArray,string.split(RIFilename, '.')[0]+'Transpose.sp4')
        return transposeArray


#####################################################################
# Usage
#####################################################################

print 'multiple files'
niter=0
for i in range(5):
        i+=5
        templateFilename=sys.argv[1]
        RIFilename='Seq\%d.sp4'\%i
        print RIFilename
        shift=CrossCorrelationFastFFT(templateFilename,RIFilename)
        RIshiftFilename=string.split(RIFilename, '.')[0]+'Shifted.sp4'
        print RIshiftFilename
        c.Sp4ArraySave(ShiftArray(RIFilename,shift),RIshiftFilename)
        N2=CrossCorrelationN2(templateFilename,RIshiftFilename,1)[3]
        print N2
        TransposeArray(RIFilename)
        RItranFilename='Seq\%dTranspose.sp4'\%i
        RItranShiftFilename=string.split(RItranFilename, '.')[0]+'Shifted.sp4'
        c.Sp4ArraySave(ShiftArray(RItranFilename,CrossCorrelationFastFFT(templateFilename,RItranFilename)),RItranShiftFilename)
        print RItranShiftFilename
        N2tran=CrossCorrelationN2(templateFilename,RItranShiftFilename,1)[3]
        print N2tran
        if os.path.exists("CrossCorrelations.txt"):
                data=open("CrossCorrelations.txt").readlines()
        outfile=open("CrossCorrelations.txt", "w")
        for k in range (len(data)):
```

```
        outfile.write(data[k])

if N2tran>N2:
        s='Possible Twin Identified, filename: \%d.sp4\n'\%i
        print s
        outfile.write(s)
if N2>N2tran:
        s1='Normal orientation had a stronger correlation, filename: \%d.sp4\n'\%i
        print s1
        outfile.write(s1)
outfile.close()

#####################################################################
```

G.3.2   Phase offset correction

```
####################################################################
# Calculate the phase offset required to align the phase modulation around a common origin
####################################################################
import cstuff as c
import mycstuff as mc
import sys

import os
files=os.listdir("./")

ref=c.Sp4Array()
recon=c.Sp4Array()
cpRecon=c.Sp4Array()

def ApplyOffset(refFilename,reconFilename):
        c.Sp4ArrayLoad(ref,refFilename)
        c.Sp4ArrayLoad(recon,reconFilename)
        offset=mc.Sp4ArrayFindPhaseOffsetFienup1(ref,recon,cpRecon)
        #mc.Sp4ArrayAddPhaseOffset(recon,offset[1],1.0)
        c.Sp4ArraySave(cpRecon,'CP'+reconFilename)
        #print offset
        return offset


####################################################################
# Usage
####################################################################

refFilename=sys.argv[1]
reconFilename=sys.argv[2]

ApplyOffset(refFilename,reconFilename)

####################################################################
```

G.4   PRTF

```
import cstuff as c
import mycstuff as mc
import sys
import vtkStructuredGridMaker as vs
import math as m

# Define Constants
pi=m.pi
deg2rad = pi/180.0000

########################################################################
# Define required data arrays
########################################################################

arg1=sys.argv[1] # Raw intensities
arg2=sys.argv[2] # Reconstructed result

rawInt=c.Sp4Array()
reconRes=c.Sp4Array()
c.Sp4ArrayLoad(rawInt,arg1)
c.Sp4ArrayLoad(reconRes,arg2)

c.Sp4ArrayFFT(reconRes,1,1)
c.Sp4ArrayWrap(reconRes)

########################################################################
# Variables
########################################################################

# Set Threshold
minthresh=1600
maxthresh=900000000

# Experimental Parameters
pixelx=4*(22.50e-6)  #Total pixel size including binning (in meters)
pixely=4*(22.50e-6)
arm = 2.792              #Detector distance from sample (units are m)
lam = 0.139             #Wavelength of x-ray (units in nm)
delta = 29.14 * deg2rad
gam = 15.4 * deg2rad
dth = 0.005 * deg2rad
dtilt = 0.00 * deg2rad
dpx=pixelx/arm
dpy=pixely/arm

# Generate datamask based on the defined threshold
datamask=c.Sp4Array()
c.MinMaxThreshMask(datamask, rawInt, minthresh, maxthresh)

# Generate coordinate system
NewCoords=c.Sp4Array()
size1 = c.Sp4ArrayGetDim(rawInt,0)[1]
size2 = c.Sp4ArrayGetDim(rawInt,1)[1]
size3 = c.Sp4ArrayGetDim(rawInt,2)[1]
dx = 1.0/c.Sp4ArrayGetDim(rawInt,0)[1]
dy = 1.0/c.Sp4ArrayGetDim(rawInt,1)[1]
dz = 1.0/c.Sp4ArrayGetDim(rawInt,2)[1]

if dtilt ==0.0:
  c.ThCoordTrans(NewCoords, size1, size2, size3, lam, delta, gam, dpx, dpy, dth,dx ,dy,dz,c.RECIP)
  print "theta rocking curve coordinate tranform"
elif dth == 0.0:
  c.TiltCoordTrans(NewCoords, size1, size2, size3, lam, delta, gam, dpx, dpy, dtilt,dx,dy,dz,c.RECIP)
  print "chi rocking curve coordinate transform"
else:
  print "dth/dtilt has been set incorrectly"

# Calculate q for each point from origin

c.ShiftCoordOrigin(NewCoords,size1/2,size2/2,size3/3)

dDampsGM=vs.vtkStructuredGridMaker(NewCoords, reconRes, c.AMP)
dDampsGM.WriteStructuredGrid('Coords_amp.vtk')
dDphGM=vs.vtkStructuredGridMaker(NewCoords, reconRes, c.PHASE)
dDphGM.WriteStructuredGrid('Coords_ph.vtk')
dDampsGM=vs.vtkStructuredGridMaker(NewCoords, datamask, c.AMP)
dDampsGM.WriteStructuredGrid('DatamaskCoords_amp.vtk')

# Convert sp4 arrays into strings of doubles
rawIntdouble = mc.doubleArray.frompointer(rawInt.data)
reconResdouble = mc.doubleArray.frompointer(reconRes.data)
NewCoordsdouble = mc.doubleArray.frompointer(NewCoords.data)
datamaskdouble=mc.doubleArray.frompointer(datamask.data)
```

```
# Generate bins and defined variable ranges
dataList=[]
cnt=0
cnt1=0
for a1 in range(size1):
        for a2 in range(size2):
                for a3 in range(size3):
                        cnt+=1
                        # index for coordinate array
                        coordIndex = 3*( a3 + size3*(a2 + size2*a1) )
                        # index for data array
                        dataIndex = 2*( a3 + size3*(a2 + size2*a1) )
                        if datamaskdouble[dataIndex]>0:
                                cnt1+=1
                                #get values of h,r and theta, amps and phase
                                q=m.sqrt(NewCoordsdouble[coordIndex]**2+NewCoordsdouble[coordIndex+1]**2+NewCoordsdouble[coordIndex+2]**2)
                                calcAmps = m.sqrt((reconResdouble[dataIndex+1]**2) + (reconResdouble[dataIndex]**2))
                                rawAmps = m.sqrt(rawIntdouble[dataIndex])
                                PRTF=calcAmps/rawAmps
                                dataList.append([q,PRTF])


print 'voxels considered:%d, voxels in datamask :%d'%(cnt,cnt1)

# output sp4 for reference
c.Sp4ArraySave(datamask,'datamask.sp4')

qMax=0
print len(dataList)
for i in range (len(dataList)):
        if dataList[i][0]>qMax:
                qMax=dataList[i][0]

print qMax

# Assume 300 bins in 0.001 increments

binsList=[]
for i in range (300):
        binsList.append([0.001*i,0,0])

for i in range (len(dataList)):
        bin=int(round((dataList[i][0])/0.001))
        binsList[bin][1]+=dataList[i][1]
        binsList[bin][2]+=1

resList=[]
string=''

for i in range(len(binsList)):
        if binsList[i][2]>0:
                q=binsList[i][0]
                PRTF=binsList[i][1]/binsList[i][2]
                resList.append([q,PRTF])
                string+='\%.10f          \%.10f\n'\%(q,PRTF)


#####################################################################
# Generate a text file output, (q, PRTF) written on every line
#####################################################################
outfile1=open("PRTF.txt", "w")
outfile1.write(string)
```

Bibliography

[1] B. Abbey, K. A. Nugent, G. J. Williams, J. N. Clark, A. G. Peele, M. A. Pfeifer, M. de Jonge, and I. McNulty, *Keyhole coherent diffractive imaging*, Nat Phys **4** (2008), no. 5, 394–398.

[2] J. P. Abrahams and A. G. W. Leslie, *Methods used in the structure determination of bovine mitochondrial f1 atpase*, Acta. Crystallography D **52** (1996), 30–42.

[3] G. Y. Ahn, S-I Park, S. J. Kim, and C. S. Kim, *Ferromagnetic properties of fe-substituted zno-based magnetic semiconductor*, Journal of Magnetism and Magnetic Materials **304** (2006), no. 2, 498–500.

[4] G. Y. Ahn, S-I Park, S. J. Kim, B. W. Lee, and C. S. Kim, *Preparation of fe-doped zno ferromagnetic semiconductor by sol-gel method with hydrogen treatment*, Magnetics, IEEE Transactions on **41** (2005), no. 10, 2730–2732.

[5] N. Akdogan, H. Zabel, A. Nefedov, K. Westerholt, H-W. Becker, S. Gok, R. Khaibullin, and L. Tagirov, *Dose dependence of ferromagnetism in co-implanted zno*, Journal of Applied Physics **105** (2009), no. 4, 043907.

[6] A. A. Allred, *Electronegativity values from thermochemical data*, J. Inorg. Nucl. Chem. **17** (1961), no. 215, 215–221.

[7] J. Als-Nielsen and D. McMorrow, *Elements of modern x-ray physics*, WILEY, 2001.

[8] M. Andres-Verges, A. Mifsud, and C. J. Serna, *Formation of rod-like zinc oxide microscrystals in homogeneous solutions*, J. Chem. Soc. FARADAY TRANS. **86** (1990), 959–963.

[9] S. R. Andrews and R. A. Cowley, *Scattering of x-rays from crystal surfaces*, Journal of Physics C: Solid State Physics **18** (1985), no. 35, 6427–6439.

[10] A. B. M. A. Ashrafi, A. Ueta, A. Avramescu, H. Kumano, I. Suemune, Y-W. Ok, and T-Y. Seong, *Growth and characterization of hypothetical zinc-blende zno films on gaas(001) substrates with zns buffer layers*, Appl. Phys. Lett. **76** (2000), no. 5, 550–552.

[11] S. Baek, J. Song, and S. Lim, *Improvement of the optical properties of zno nanorods by fe doping*, Physica B: Condensed Matter **399** (2007), no. 2, 101 – 104.

[12] A. Baikova, *Solution of phase retrieval problem by a maximum entropy method*, Radiophysics and Quantum Electronics **39** (1996), no. 4, 321–327.

[13] J. Bao, M. A. Zimmler, F. Capasso, X. Wang, and Z. F. Ren, *Broadband zno single-nanowire light-emitting diode*, Nano Letters **6** (2006), no. 8, 1719–1722.

[14] R. Barakat and G. Newsam, *Necessary conditions for a unique solution to two dimensional phase recovery*, J. Math. Phys. **25** (1984), 3190–3193.

[15] A. Barty, S. Marchesini, H. N. Chapman, C. Cui, M. R. Howells, D. A. Shapiro, A. M. Minor, J. C. H. Spence, U. Weierstall, J. Ilavsky, A. Noy, S. P. Hau-Riege,

A. B. Artyukhin, T. Baumann, T. Willey, J. Stolken, T. van Buuren, and J. K. Kinney, *Three-dimensional coherent x-ray diffraction imaging of a ceramic nanofoam: Determination of structural deformation mechanisms*, Physical Review Letters **101** (2008), no. 5, 055501.

[16] C. H. Bates, W. B. White, and R. Roy, *The solubility of transition metal oxides in zinc oxide and the reflectance spectra of mn2+ and fe2+ in tetrahedral fields*, J. Inorg. Nucl. Chem. **28** (1966), 297–405.

[17] R. H. T. Bates, *Uniqueness of solutions of two-dimensional fourier phase problems for localized and positive images*, Computer Vision, Graphics, And Image Processing **25** (1984), 205–217.

[18] H. H. Bauschke, P. L. Combettes, and D. Luke, *Hybrid projection reflection method for phase retrieval*, J. Opt. Soc. Am **20** (2003), 1025–1034.

[19] H. H. Bauschke, P. L. Combettes, and D. R. Luke, *Phase retrieval, error reduction algorithm, and fienup variants: a view from convex optimization*, J. Opt. Soc. Am. A **19** (2002), no. 7, 1334–1345.

[20] J. B. Baxter and C. A. Schmuttenmaer, *Conductivity of zno nanowires, nanoparticles, and thin films using time-resolved terahertz spectroscopy*, The Journal of Physical Chemistry B **110** (2006), no. 50, 25229–25239.

[21] D. J. Binks, *Computational modelling of zinc oxide and related oxide ceramics*, Ph.D. thesis, University of Surrey, 1994.

[22] J. Blasco, F. Bartolome, L. M. Garcia, and J. Garcia, *Extrinsic origin of ferromagnetism in doped zno*, Journal of Materials Chemistry **16** (2006), no. 23, 2282–2288.

[23] W. L. Bragg, *The diffraction of short electromagnetic waves by a crystal*, Proc. Camb. Philos. Soc. **17** (1913), 43–57.

[24] Bricogne and G., *Maximum entropy and the foundations of direct methods*, Acta Crystallographica Section A **40** (1984), no. 4, 410–445.

[25] G. Bricogne and C. J. Gilmore, *A multisolution method of phase determination by combined maximization of entropy and likelihood. i. theory, algorithms and strategy*, Acta Crystallographica Section A **46** (1990), no. 4, 284–297.

[26] Y. M. Bruck and L. G. Sodin, *On the ambiguity of the image reconstruction problem*, Optics Communications **30** (1979), no. 3, 304–308.

[27] Y. Cao, L. Miao, S. Tanemura, M. Tanemura, Y. Kuno, and Y. Hayashi, *Low resistivity p-zno films fabricated by sol-gel spin coating*, Appl. Phys. Lett. **88** (2006), no. 25, 251116–3.

[28] M. Catti, Y. Noel, and R. Dovesi, *Full piezoelectric tensors of wurtzite and zinc blende zno and zns by first-principles calculations*, Journal of Physics and Chemistry of Solids **64** (2003), no. 11, 2183–2190.

[29] J. Cembrero and David Busquets-Mataix, *Zno crystals obtained by electrodeposition: Statistical analysis of most important process variables*, Thin Solid Films **517** (2009), no. 9, 2859–2864.

[30] J. Cembrero, A. Elmanouni, B. Hartiti, M. Mollar, and B. Mar, *Nanocolumnar zno films for photovoltaic applications*, Thin Solid Films **451-452** (2004), 198–202.

[31] V. Chamard, J. Stangl, S. Labat, B. Mandl, R. T. Lechner, and T. H. Metzger, *Evidence of stacking-fault distribution along an inas nanowire using micro-focused coherent x-ray diffraction*, Journal of Applied Crystallography **41** (2008), no. 2, 272–280.

[32] R. Chander and A.K. Raychaudhuri, *Electrodeposition of aligned arrays of zno nanorods in aqueous solution*, Solid State Communications **145** (2008), no. 1-2, 81–85.

[33] S-C. Chang and P. Mark, *The crystallography of the polar (0001) zn and (000-1)o surfaces of zinc oxides*, Surface Science **46** (1974), no. 1, 293–300.

[34] H. N. Chapman, A. Barty, M. J. Bogan, S. Boutet, M. Frank, S. P. Hau-Riege, S. Marchesini, B. W. Woods, S. Bajt, W. Henry Benner, R. A. London, E. Plonjes, M. Kuhlmann, R. Treusch, S. Dusterer, T. Tschentscher, J. R. Schneider, E. Spiller, T. Moller, C. Bostedt, M. Hoener, D. A. Shapiro, K. O. Hodgson, D. van der Spoel, F. Burmeister, M. Bergh, C. Caleman, G. Huldt, M. Marvin Seibert, F. R. N. C. Maia, R. W. Lee, A. Szoke, N. Timneanu, and J. Hajdu, *Femtosecond diffractive imaging with a soft-x-ray free-electron laser*, arXiv:physics/0610044v2 (2006), 1–6.

[35] H. N. Chapman, A. Barty, S. Marchesini, A. Noy, S. P. Hau-Riege, C. Cui, M. R. Howells, R. Rosen, H. He, J. C. H. Spence, U. Weierstall, T. Beetz, C. Jacobsen, and D. Shapiro, *High-resolution ab initio three-dimensional x-ray diffraction microscopy*, J. Opt. Soc. Am. A **23** (2006), no. 5, 1179–1200.

[36] H. N. Chapman, S. P. Hau-Riege, M. J. Bogan, S. Bajt, A. Barty, S. Boutet, S. Marchesini, M. Frank, B. W. Woods, W. H. Benner, R. A. London, U. Rohner, A. Szoke, E. Spiller, T. Moller, C. Bostedt, D. A. Shapiro, M. Kuhlmann, R. Treusch, E. Plonjes, F. Burmeister, M. Bergh, C. Caleman, G. Huldt, M. M. Seibert, and J. Hajdu, *Femtosecond time-delay x-ray holography*, Nature **448** (2007), 676–680.

[37] C. C. Chen, J. Miao, C. W. Wang, and T. K. Lee, *Application of optimization technique to noncrystalline x-ray diffraction microscopy: Guided hybrid input-output method*, Physical Review B (Condensed Matter and Materials Physics) **76** (2007), no. 6, 064113.

[38] A. I. Chumakov, A. Q. R. Baron, R. Ruffer, H. F. Grunsteudel, and A. Meyer, *Nuclear resonance energy analysis of inelastic x-ray scattering*, Phys. Rev. Lett. **76** (1996), no. 22, 4258–4261.

[39] M.F. Chung and H.E. Farnsworth, *Investigations of surface stability of ii-vi wurtzite compounds by leed*, Surface Science **22** (1970), no. 1, 93–110.

[40] P. Coppens, D. Cox, E Vlieg, and I. K. Robinson, *Synchrotron radiation crystallography*, Academic Press, London, 1992.

[41] J. F. Cordaro, C. E. Shipway, and J. T. Schott, *Radiation hardness of zinc oxide varistors*, J. Appl. Phys. **61** (1987), no. 1, 429–431.

[42] R. Crowther, *The use of non-crystallographic symmetry for phase determination*, Acta Crystallographica Section B **25** (1969), no. 12, 2571–2580.

[43] Y. Dai, Y. Zhang, Q. K. Li, and C. W. Nan, *Synthesis and optical properties of tetrapod-like zinc oxide nanorods*, Chemical Physics Letters **358** (2002), no. 1-2, 83 – 86.

[44] E. A. Dalchiele, P. Giorgi, R. E. Marotti, F. Martn, J. R. Ramos-Barrado, R. Ayouci, and D. Leinen, *Electrodeposition of zno thin films on n-si(100)*, Solar Energy Materials and Solar Cells **70** (2001), no. 3, 245–254.

[45] Ryan P. Davies, C. R. Abernathy, S. J. Pearton, D. P. Norton, M. P. Ivill, and F. Ren, *Review of recent advances in transition and lanthanide metaldoped gan and zno*, Chemical Engineering Communications **196** (2009), no. 9, 1030–1053.

[46] A. I. Demidov and I. A. Markelov, *Thermodynamics of reaction of carbon with oxygen*, Russian Journal of Applied Chemistry **78** (2005), no. 5, 707–710.

[47] S. Desgreniers, *High-density phases of zno: Structural and compressive parameters*, Phys. Rev. B **58** (1998), no. 21, 14102–.

[48] T. Dietl, F. Matsukura, and H. Ohno, *Ferromagnetism of magnetic semiconductors: Zhang-rice limit*, Phys. Rev. B **66** (2002), no. 3, 033203–.

[49] Y. Ding, Z. L. Wang, T. Sun, and J. Qiu, *Zinc-blende zno and its role in nucleating wurtzite tetrapods and twinned nanowires*, Applied Physics Letters **90** (2007), no. 15, 153510.

[50] M. T. Dove, *Structure and dynamics*, Oxford University Press, 2003.

[51] J. Dumont, T. Seldrum, S. Couet, C. Moisson, D. Turover, and R. Sporken, *Thermal diffusion of co into atomically flat zno(000-1) surfaces investigated by scanning probe*

microscopies and low energy electron diffraction, J. Vac. Sci. Technol. B, vol. 24, AVS, July 2006, pp. 2124–2131.

[52] S. Eisebitt, J. Luning, W. Schlotter, M. Lorgen, O. Hellwig, W. Eberhardt, and J. Stohr, *Direct holographic inversion 1.59nm rcp diffraction from magnetised film and pinhole*, Nature **432** (2004), 885–888.

[53] V. Elser, *Phase retrieval by iterated projections*, J. Opt. Soc. Am. A **20** (2003), no. 1, 40–55.

[54] M. Fahoume, O. Maghfoul, M. Aggour, B. Hartiti, F. Chrabi, and A. Ennaoui, *Growth and characterization of zno thin films prepared by electrodeposition technique*, Solar Energy Materials and Solar Cells **90** (2006), no. 10, 1437–1444.

[55] H. J. Fan, A. S. Barnard, and M. Zacharias, *Zno nanowires and nanobelts: Shape selection and thermodynamic modeling*, Applied Physics Letters **90** (2007), no. 14, 143116.

[56] H. J. Fan, B. Fuhrmann, R. Scholz, C. Himcinschi, A. Berger, H. Leipner, A. Dadgar, A. Krost, S. Christiansen, S. Gosele, and M. Zacharias, *Vapour-transport-deposition growth of zno nanostructures: switch between c-axial wires and a-axial belts by indium doping*, Nanotechnology **17** (2006), no. 11, S231–S239.

[57] H. J. Fan, W. Lee, R. Scholz, A. Dadgar, A. Krost, K. Nielsch, and M. Zacharias, *Arrays of vertically aligned and hexagonally arranged zno nanowires: a new template-directed approach*, Nanotechnology **16** (2005), no. 6, 913–917.

[58] Z Fan and J. G. Lu, *Gate-refreshable nanowire chemical sensors*, Appl. Phys. Lett. **86** (2005), no. 12, 123510–3.

[59] Z. Fan, D. Wang, P-C Chang, W-Y Tseng, and J. G. Lu, *Zno nanowire field-effect transistor and oxygen sensing property*, Appl. Phys. Lett. **85** (2004), no. 24, 5923–5925.

[60] M. Farnsworth and C. H. Kline, *Zinc chemicals*, Zinc Development Association, 1973.

[61] H. M. L. Faulkner and J. M. Rodenburg, *Movable aperture lensless transmission microscopy: A novel phase retrieval algorithm*, Phys. Rev. Lett. **93** (2004), no. 2, 023903.

[62] V. Favre-Nicolin, J. Eymery, R. Koester, and P. Gentile, *Coherent-diffraction imaging of single nanowires of diameter 95 nanometers*, Physical Review B (Condensed Matter and Materials Physics) **79** (2009), no. 19, 195401.

[63] J. R. Fienup, *Reconstruction of an object from the modulus of its fourier transform*, Optics Letters (1978), no. 3, 27–29.

[64] J. R. Fienup, *Reconstruction of a complex-valued object from the modulus of its fourier transform using a support constraint*, J. Opt. Soc. Am. A **4** (1987), no. 1, 118–123.

[65] J. R. Fienup and C. C. Wackerman, *Phase-retrieval stagnation problems and solutions*, J. Opt. Soc. Am. A **3** (1986), no. 11, 1897–1907.

[66] James R. Fienup, *Invariant error metrics for image reconstruction*, Appl. Opt. **36** (1997), no. 32, 8352–8357.

[67] M. Francon, *Holography*, Academic Press, New York, 1974.

[68] T. Fujita and M. R. McCartney, *Phase recovery for electron holography using gerchberg-papoulis iterative algorithm*, Ultramicroscopy **102** (2005), 279–286.

[69] P. X. Gao, Y. Ding, and Z. L. Wang, *Crystallographic orientation-aligned zno nanorods grown by a tin catalyst*, Nano Letters **3** (2003), no. 9, 1315–1320.

[70] R. W. Gerchberg and W. O. Saxton, *A practical algorithm for the determination of phase from image and diffraction plane pictures*, Optik **35** (1972), 237–246.

[71] C. J. Gilmore, G. Bricogne, and C. Bannister, *A multisolution method of phase determination by combined maximization of entropy and likelihood. ii. application to small molecules*, Acta Crystallographica Section A **46** (1990), no. 4, 297–308.

[72] W. Gopel, R.S. Bauer, and G. Hansson, *Ultraviolet photoemission studies of chemisorption and point defect formation on zno nonpolar surfaces*, Surface Science **99** (1980), no. 1, 138–156.

[73] L. E. Greene, M. Law, D. H. Tan, M. Montano, J. Goldberger, G. Somorjai, and P. Yang, *General route to vertical zno nanowire arrays using textured zno seeds*, Nano Letters **5** (2005), no. 7, 1231–1236.

[74] E. C. Greyson, Y. Babayan, and T. W. Odom, *Directed growth of ordered arrays of small-diameter zno nanowires*, Advanced Materials **16** (2004), no. 15, 1348–1352.

[75] G. Grubel, D. Abernathy, G. Vignaud, M. Sanchez del Rio, and A. Freund, *A diamond double-crystal transmission monochromator for the troika ii station at esrf*, Review of Scientific Instruments **67** (1996), no. 9, 1–4.

[76] A. Guinier, *X-ray diffraction: In crystals, imperfect crystals and amorphous bodies*, Dover Publications, New York, 1994.

[77] H. Haneda, I. Sakaguchi, A. Watanabe, and J. Tanaka, *Oxygen grain boundary diffusion in zinc oxide ceramics*, Defect and Diffusion Forum **143-147** (1996), 1219–1224.

[78] R. Harder, M. Liang, Y. Sun, Y. Xia, and I. K. Robinson, *Imaging of complex density in silver nanocubes by coherent x-ray diffraction*, New Journal of Physics SPECIAL ISSUE: X-ray Beams with High Coherence.

[79] R. Harder, M. A. Pfeifer, G. J. Williams, I. A. Vartaniants, and I. K. Robinson, *Orientation variation of surface strain*, Physical Review B (Condensed Matter and Materials Physics) **76** (2007), no. 11, 115425.

[80] H. He, S. Marchesini, M. Howells, U. Weierstall, H. Chapman, S. Hau-Riege, A. Noy, and J. C. H. Spence, *Inversion of x-ray diffuse scattering to images using prepared objects*, Phys. Rev. B **67** (2003), no. 17, 174114–.

[81] H. He, S. Marchesini, M. Howells, U. Weierstall, G. Hembree, and H. Spence, *Experimental lensless soft x-ray imaging using iterative algorithms: phase diffuse scattering*, Acta Crystallographica A **59** (2003), 143–152.

[82] V. E. Henrich and P. A. Cox, *The surface science of metal oxides*, Cambridge University Press, 1994.

[83] Y. W. Heo, V. Varadarajan, M. Kaufman, K. Kim, D. P. Norton, F. Ren, and P. H. Fleming, *Site-specific growth of zno nanorods using catalysis-driven molecular-beam epitaxy*, Applied Physics Letters **81** (2002), no. 16, 3046–3048.

[84] M.A. Hernandez-Fenollosa, L.C. Damonte, and B. Mar, *Defects in electron irradiated zno single crystals*, Superlattices and Microstructures **38** (2005), no. 4-6, 336–343.

[85] Steve B. Howell, *Handbook of ccd astronomy*, Cambridge University Press, 2006.

[86] C-C. Hsiao, K-Y Huang, and Hu Y-C, *Fabrication of a zno pyroelectric sensor*, Sensors **8** (2008), 185–192.

[87] M. H. Huang, Y. Wu, H. Feick, N. Tran, E. Weber, and P. Yang, *Catalytic growth of zinc oxide nanowires by vapor transport*, Advanced Materials **13** (2001), no. 2, 113–116.

[88] Y. Huang, X. Bai, and Y. Zhang, *In-situ mechanical properties of individual zno nanowires and the mass measurement of nanoparticles*, Journal of Physics: Condensed Matter **18** (2006), no. 15, L179–L184.

[89] J. E. Jaffe, J. A. Snyder, Z. Lin, and A. C. Hess, *Lda and gga calculations for high-pressure phase transitions in zno and mgo*, Phys. Rev. B **62** (2000), no. 3, 1660–.

[90] A. Janotti and C. G. Van de Walle, *Oxygen vacancies in zno*, Applied Physics Letters **87** (2005), no. 12, 122102.

[91] N. Jedrecy, S. Gallini, M. Sauvage-Simkin, and R. Pinchaux, *The zno non-polar (1010) surface: an x-ray structural investigation*, Surface Science **460** (2000), no. 1-3, 136–143.

[92] Huaidong Jiang, Damien Ramunno-Johnson, Changyong Song, Bagrat Amirbekian, Yoshiki Kohmura, Yoshinori Nishino, Yukio Takahashi, Tetsuya Ishikawa, and Jianwei Miao, *Nanoscale imaging of mineral crystals inside biological composite materials using x-ray diffraction microscopy*, Physical Review Letters **100** (2008), no. 3, 038103.

[93] Z. Jin, T. Fukumura, M. Kawasaki, K. Ando, H. Saito, T. Sekiguchi, Y. Z. Yoo, M. Murakami, Y. Matsumoto, T. Hasegawa, and H. Koinuma, *High throughput fabrication of transition-metal-doped epitaxial zno thin films: A series of oxide-diluted magnetic semiconductors and their properties*, Applied Physics Letters **78** (2001), no. 24, 3824–3826.

[94] H. Karzel, W. Potzel, M. Kfferlein, W. Schiessl, M. Steiner, U. Hiller, G. M. Kalvius, D. W. Mitchell, T. P. Das, P. Blaha, K. Schwarz, and M. P. Pasternak, *Lattice dynamics and hyperfine interactions in zno and znse at high external pressures*, Phys. Rev. B **53** (1996), no. 17, 11425–.

[95] Rohit Khanna, K. Ip, K. Allums, K. Baik, C. Abernathy, S. Pearton, Y. Heo, D. Norton, F. Ren, S. Shojah-Ardalan, and R. Wilkins, *Proton irradiation of zno schottky diodes*, Journal of Electronic Materials **34** (2005), no. 4, 395–398.

[96] V. Kiiko, L. Zolotukhina, E. Zabolotskaya, I. Dmitriev, and Yu Makurin, *Defects in beryllium ceramics*, Glass and Ceramics **56** (1999), no. 11, 346–349.

[97] E. H. Kisi and M. M. Elcombe, *u parameters for the wurtzite structure of zns and zno using powder neutron diffraction*, Acta Crystallographica Section C **45** (1989), no. 12, 1867–1870.

[98] A. F. Kohan, G. Ceder, D. Morgan, and Chris G. Van de Walle, *First-principles study of native point defects in zno*, Phys. Rev. B **61** (2000), no. 22, 15019–15027.

[99] G. Kresse, O. Dulub, and U. Diebold, *Competing stabilization mechanism for the polar zno(0001)-zn surface*, Phys. Rev. B **68** (2003), no. 24, 245409–.

[100] S. O. Kucheyev, J. S. Williams, C. Jagadish, J. Zou, Cheryl Evans, A. J. Nelson, and A. V. Hamza, *Ion-beam-produced structural defects in zno*, Phys. Rev. B **67** (2003), no. 9, 094115–.

[101] M. Kunat, St. Gil Girol, Th. Becker, U. Burghaus, and Ch. Wll, *Stability of the polar surfaces of zno: A reinvestigation using he-atom scattering*, Phys. Rev. B **66** (2002), no. 8, 081402–.

[102] Steven J. Leake, Marcus C. Newton, Ross Harder, and Ian K. Robinson, *Longitudinal coherence function in x-ray imaging of crystals*, Opt. Express **17** (2009), no. 18, 15853–15859.

[103] C. J. Lee, T. J. Lee, S. C. Lyu, Y. Zhang, H. Ruh, and H. J. Lee, *Field emission from well-aligned zinc oxide nanowires grown at low temperature*, Applied Physics Letters **81** (2002), no. 19, 3648–3650.

[104] S. H. Lee, S. S. Lee, J.-J. Choi, J. U. Jeon, and K. Ro, *Fabrication of a zno piezo-electric micro cantilever with a high-aspect-ratio nano tip*, Microsystem Technologies **11** (2005), no. 6, 416–423.

[105] W Lee, M-C Jeong, and J-M Myoung, *Fabrication and application potential of zno nanowires grown on gaas(002) substrates by metal–organic chemical vapour deposition*, Nanotechnology **15** (2004), no. 3, 254–259.

[106] A. Levi and H. Stark, *Image restoration by the method of generalized projections with application to restoration from magnitude*, Journal of Optical Society of America: A **1** (1984), 932–943.

[107] J. D. Levine, A. Willis, W.R. Bottoms, and P. Mark, *Correlation of electronic, leed, and auger diagnostics on zno surfaces*, Surface Science **29** (1972), no. 1, 144–164.

[108] W. Y. Liang and A. D. Yoffe, *Transmission spectra of zno single crystals*, Phys. Rev. Lett. **20** (1968), no. 2, 59–.

[109] L. Liao, H. B. Lu, J. C. Li, H. He, D. F. Wang, D. J. Fu, C. Liu, and W. F. Zhang, *Size dependence of gas sensitivity of zno nanorods*, The Journal of Physical Chemistry C **111** (2007), no. 5, 1900–1903.

[110] C. Lin, H. Lin, J. Li, and X. Li, *Electrodeposition preparation of zno nanobelt array films and application to dye-sensitized solar cells*, Journal of Alloys and Compounds **462** (2008), no. 1-2, 175–180.

[111] D. C. Look, *Electrical and optical properties of p-type zno*, Semiconductor Science and Technology **20** (2005), no. 4, S55–S61.

[112] D. C. Look, J. W. Hemsky, and J. R. Sizelove, *Residual native shallow donor in zno*, Phys. Rev. Lett. **82** (1999), no. 12, 2552–.

[113] D. C. Look, D. C. Reynolds, C. W. Litton, R. L. Jones, D. B. Eason, and G. Cantwell, *Characterization of homoepitaxial p-type zno grown by molecular beam epitaxy*, Appl. Phys. Lett. **81** (2002), no. 10, 1830–1832.

[114] Ming-Pei Lu, Jinhui Song, Ming-Yen Lu, Min-Teng Chen, Yifan Gao, Lih-Juann Chen, and Zhong Lin Wang, *Piezoelectric nanogenerator using p-type zno nanowire arrays*, Nano Letters **9** (2009), no. 3, 1223–1227.

[115] D. R. Luke, *Relaxed averaged alternating reflections for diffraction imaging*, Inverse Problems **21** (2005), no. 1, 37–50.

[116] L. Lyons, *Data analysis fo physical science students*, Cambridge University Press, 1991.

[117] D. W. Ma, Z. Z. Ye, and L. L. Chen, *Dependence of structural and optical properties of zn(1x)cd(x)o films on the cd composition*, Phys. Stat. Solidi A **201** (2004), 2929–2933.

[118] G. D. Mahan, *Intrinsic defects in zno varistors*, J. Appl. Phys. **54** (1983), no. 7, 3825–3832.

[119] T. Makino, Y. Segawa, M. Kawasaki, A. Ohtomo, R. Shiroki, K. Tamura, T. Yasuda, and H. Koinuma, *Band gap engineering based on mg[sub x]zn[sub 1 - x]o and cd[sub y]zn[sub 1 - y]o ternary alloy films*, Appl. Phys. Lett. **78** (2001), no. 9, 1237–1239.

[120] S. K. Mandal, A. K. Das, T. K. Nath, and D. Karmakar, *Temperature dependence of solubility limits of transition metals (co, mn, fe, and ni) in zno nanoparticles*, Applied Physics Letters **89** (2006), no. 14, 144105.

[121] L. Manna, D. J. Milliron, A. Meisel, E. C. Scher, and P. A. Alivisatos, *Controlled growth of terapod-branched inorganic nanocrystals*, Nature Materials **2** (2003), 382–385.

[122] S. Marchesini, *Invited article: A unified evaluation of iterative projection algorithms for phase retrieval*, Review of Scientific Instruments **78** (2007), no. 1, 011301.

[123] S. Marchesini, H. He, H. N. Chapman, S. P. Hau-Riege, A. Noy, M. R. Howells, U. Weierstall, and J. C. H. Spence, *X-ray image reconstruction from a diffraction pattern alone*, Phys. Rev. B **68** (2003), no. 14, 140101.

[124] B. Mar, M. Mollar, A. Mechkour, B. Hartiti, M. Perales, and J. Cembrero, *Optical properties of nanocolumnar zno crystals*, Microelectronics Journal **35** (2004), no. 1, 79–82.

[125] X.Q. Meng, D.Z. Shen, J.Y. Zhang, D.X. Zhao, Y.M. Lu, L. Dong, Z.Z. Zhang, Y.C. Liu, and X.W. Fan, *The structural and optical properties of zno nanorod arrays*, Solid State Communications **135** (2005), no. 3, 179–182.

[126] X.Q. Meng, D.X. Zhao, J.Y. Zhang, D.Z. Shen, Y.M. Lu, Y.C. Liu, and X.W. Fan, *Growth temperature controlled shape variety of zno nanowires*, Chemical Physics Letters **407** (2005), no. 1-3, 91 – 94.

[127] C. F. Meyer, *The diffraction of light, x-rays, and material particles*, The University of Chicago Press, 1934.

[128] J. Miao, H. N. Chapman, and D. Sayre, *Image reconstruction from the oversampled diffraction pattern*, Microscopy Microanalysis **Suppl. 2** (1997), 1155–1156.

[129] J. Miao, P. Charalambous, J. Kirz, and D. Sayre, *Extending the methodolgy of x-ray crystallography to allow imaging of micrometre-sized non-crystalline specimens*, Nature **400** (1999), 342–344.

[130] J. Miao, D. Sayre, and H. N. Chapman, *Phase retrieval from the magnitude of the fourier transforms of nonperiodic objects*, J. Opt. Soc. Am. A **15** (1998), no. 6, 1662–1669.

[131] Jianwei Miao, Tetsuya Ishikawa, Bart Johnson, Erik H. Anderson, Barry Lai, and Keith O. Hodgson, *High resolution 3d x-ray diffraction microscopy*, Phys. Rev. Lett. **89** (2002), no. 8, 088303.

[132] R. P. Millane, *Phase retrieval in crystallography and optics*, J. Opt. Soc. Am. A **7** (1990), no. 3, 394–411.

[133] R. P. Millane and W. J. Stroud, *Reconstructing symmetric images from their undersampled fourier intensities*, J. Opt. Soc. Am. A **14** (1997), no. 3, 568–579.

[134] A. A. Minkevich, M. Gailhanou, J.-S. Micha, B. Charlet, V. Chamard, and O. Thomas, *Inversion of the diffraction pattern from an inhomogeneously strained crystal using an iterative algorithm*, Physical Review B (Condensed Matter and Materials Physics) **76** (2007), no. 10, 104106.

[135] H. Morkoc and H Ozgur, *Zinc oxide: Fundamentals, materials and device technology*, WILEY-VCH, 2009.

[136] M. C. Newton, *Zinc oxide tetrapod nanocrystal diodes*, Ph.D. thesis, University College London, 2007.

[137] M. C. Newton, S. Firth, T. Matsuura, and P. A. Warburton, *Synthesis and characterisation of zinc oxide tetrapod nanocrystals*, Journal of Physics: Conference Series **26** (2006), 251–255.

[138] M. C. Newton, S. J. Leake, R. Harder, and I. K. Robinson, *Three-dimensional imaging of strain in a single zno danorod*, Nature Materials Letters **Advance online publication** (2009), Accepted for Publication Nature Materials December 2009.

[139] M. C. Newton and P. A. Warburton, *Zno tetrapod nanocrystals*, Materials Today **10** (2007), no. 5, 50 – 54.

[140] H. T. Ng, B. Chen, J. Li, J. Han, M. Meyyappan, J. Wu, S. X. Li, and E. E. Haller, *Optical properties of single-crystalline zno nanowires on m-sapphire*, Appl. Phys. Lett. **82** (2003), no. 13, 2023–2025.

[141] Y. Nishino, Y. Takahashi, N. Imamoto, T. Ishikawa, and K. Maeshima, *Three-dimensional visualization of a human chromosome using coherent x-ray diffraction*, Phys. Rev. Lett. **102** (2009), no. 1, 018101–4.

[142] D. P. Norton, M. Ivill, Y. Li, Y.W. Kwon, J. M. Erie, H. S. Kim, K. Ip, S. J. Pearton, Y. W. Heo, S. Kim, B. S. Kang, F. Ren, A. F. Hebard, and J. Kelly, *Charge carrier and spin doping in zno thin films*, Thin Solid Films **496** (2006), 160–168.

[143] A. Ohtomo, M. Kawasaki, T. Koida, K. Masubuchi, H. Koinuma, Y. Sakurai, Y. Yoshida, T. Yasuda, and Y. Segawa, *Mgzno as a ii–vi widegap semiconductor alloy*, Appl. Phys. Lett. **72** (1998), no. 19, 2466–2468.

[144] U. Ozgur, Ya. I. Alivov, C. Liu, A. Teke, M. A. Reshchikov, S. Dogan, V. Avrutin, S.-J. Cho, and H. Morkoc, *A comprehensive review of zno materials and devices*, J. Appl. Phys. **98** (2005), no. 4, 041301–103.

[145] Z. W. Pan, Z. R. Dai, and Z. L. Wang, *Nanobelts of semiconducting oxides*, Science **291** (2001), no. 5510, 1947–1949.

[146] L. Pauling, *The nature of the chemical bond*, Cornell University Press, 1960.

[147] M. A. Pfeifer, *Structural studies of lead nanocrystals using coherent x-ray diffraction*, Ph.D. thesis, University of Illinois, 2005.

[148] M. A. Pfeifer, G. J. Williams, I. A. Vartanyants, R. Harder, and I. K. Robinson, *Three-dimensional mapping of a deformation field inside a nanocrystal*, Nature **442** (2006), no. 7098, 63–66.

[149] J. A. Pitney, *Coherent x-ray diffraction*, Ph.D. thesis, University of Illinois, 2000.

[150] W. H. Press, B. P. Flannery, S. A. Teukolsky, and W. T. Vetterling, *Numerical recipes in c: The art of scientific computing*, Cambridge University Press, 1988.

[151] Y. Qin, X. Wang, and Z. L. Wang, *Microfibre-nanowire hybrid structure for energy scavenging*, Nature **451** (2008), no. 7180, 809–813.

[152] R. R. Reeber, *Lattice parameters of zno from 4.2k to 296k*, Journal of Applied Physics **41** (1970), no. 13, 5063–5066.

[153] I. K. Robinson, *Crystal truncation rods and surface roughness*, Phys. Rev. B **33** (1986), no. 6, 3830–3836.

[154] I. K. Robinson, C. A. Kenney-Benson, and I. A. Vartanyants, *Sources of decoherence in beamline optics*, Physica. B, Condensed matter **336** (2003), no. 1-2, 236.

[155] I. K. Robinson, J. L. Libbert, I. A. Vartanyants, J. A. Pitney, D. M. Smilgies, D. L. Abernathy, and G. Grbel, *Coherent x-ray diffraction imaging of silicon oxide growth*, Phys. Rev. B **60** (1999), no. 14, 9965–.

[156] I. K. Robinson and I. A. Vartanyants, *Use of coherent x-ray diffraction to map strain fields in nanocrystals*, Applied Surface Science **182** (2001), no. 3-4, 186 – 191.

[157] I. K. Robinson, I. A. Vartanyants, G. J. Williams, M. A. Pfeifer, and J. A. Pitney, *Reconstruction of the shapes of gold nanocrystals using coherent x-ray diffraction*, Phys. Rev. Lett. **87** (2001), no. 19, 195505.

[158] J. M. Rodenburg and H. M. L. Faulkner, *A phase retrieval algorithm for shifting illumination*, Applied Physics Letters **85** (2004), no. 20, 4795–4797.

[159] W. C. Roentgen, *On a new kind of rays*, Nature **53** (1896), no. 1369, 274–296.

[160] C. S. Rout, A.R. Raju, A. Govindaraj, and C.N.R. Rao, *Hydrogen sensors based on zno nanoparticles*, Solid State Communications **138** (2006), no. 3, 136–138.

[161] A. C. S. Sabioni, *About the oxygen diffusion mechanism in zno*, Solid State Ionics **170** (2004), no. 1-2, 145 – 148.

[162] A. C. S. Sabioni, M. J. F. Ramos, and W. B. Ferraz, *Oxygen diffusion in pure and doped zno*, Mat. Res. **6** (2003), no. 2, 173–178.

[163] D. Sayre, *Some implications of a theorem due to shannon*, Acta Crystallographica **5** (1952), no. 6, 843.

[164] O. Schmidt, P. Kiesel, C. G. Van de Walle, N. M. Johnson, J. Nause, and G. H. Doumhler, *Effects of an electrically conducting layer at the zinc oxide surface*, JAPANESE JOURNAL OF APPLIED PHYSICS **44** (2005), no. 10, 7271–7274.

[165] L. Schmidt-Mende and J. L. MacManus-Driscoll, *Zno - nanostructures, defects, and devices*, Materials Today **10** (2007), no. 5, 40 – 48.

[166] C. G. Schroer, P. Boye, J. M. Feldkamp, J. Patommel, A. Schropp, A. Schwab, S. Stephan, M. Burghammer, S. Schoder, and C. Riekel, *Coherent x-ray diffraction imaging with nanofocused illumination*, Physical Review Letters **101** (2008), no. 9, 090801.

[167] C. E. Shannon, *Communication in the presence of noise*, Proc. Inst. Radio Engrs. **37** (1949), no. 10, 1–21.

[168] D. Shapiro, P. Thibault, T. Beetz, V. Elser, M. Howells, C. Jacobsen, J. Kirz, E. Lima, H. Miao, A. M. Neiman, and S. Sayre, *Biological imaging by soft x-ray diffraction microscopy*, PNAS **102** (2005), no. 43, 15343–15346.

[169] A. A. Sokol, S. A. French, S. T. Bromley, H. J. J. Catlow, C. R. A. van Dam, and P. Sherwood, *Point defects in zno*, Faraday Discussions **134** (2007), 267–282.

[170] Changyong Song, Raymond Bergstrom, Damien Ramunno-Johnson, Huaidong Jiang, David Paterson, Martin D. de Jonge, Ian McNulty, Jooyoung Lee, Kang L. Wang, and Jianwei Miao, *Nanoscale imaging of buried structures with elemental*

specificity using resonant x-ray diffraction microscopy, Physical Review Letters **100** (2008), no. 2, 025504.

[171] Changyong Song, Huaidong Jiang, Adrian Mancuso, Bagrat Amirbekian, Li Peng, Ren Sun, Sanket S. Shah, Z. Hong Zhou, Tetsuya Ishikawa, and Jianwei Miao, *Quantitative imaging of single, unstained viruses with coherent x rays*, Phys. Rev. Lett. **101** (2008), no. 15, 158101–4.

[172] J. Song, J. Zhou, and Z. L. Wang, *Piezoelectric and semiconducting coupled power generating process of a single zno belt/wire. a technology for harvesting electricity from the environment*, Nano Letters **6** (2006), no. 8, 1656–1662.

[173] W. W. Song, E Riedo, and Z. L. Wang, *Systematic study on experimental conditions for large-scale growth of aligned zno nanwires on nitrides*, The Journal of Physical Chemistry B **109** (2005), no. 20, 9869–9872.

[174] Y. Sun, D. J. Riley, and M. N. R. Ashfold, *Mechanism of zno nanotube growth by hydrothermal methods on zno film-coated si substrates*, The Journal of Physical Chemistry B **110** (2006), no. 31, 15186–15192.

[175] M. S. Sze, *Physics of semiconductor devices*, 2nd ed., Wiley-Interscience, New York, 1981.

[176] Y. Takahashi, Y. Nishino, R. Tsutsumi, H. Kubo, H. Furukawa, H. Mimura, S. Matsuyama, N. Zettsu, E. Matsubara, T. Ishikawa, and K. Yamauchi, *High-resolution diffraction microscopy using the plane-wave field of a nearly diffraction limited focused x-ray beam*, Phys. Rev. B **80** (2009), no. 5, 054103–5.

[177] Yukio Takahashi, Yoshinori Nishino, Hidekazu Mimura, Ryosuke Tsutsumi, Hideto Kubo, Tetsuya Ishikawa, and Kazuto Yamauchi, *Feasibility study of high-resolution coherent diffraction microscopy using synchrotron x rays focused by kirkpatrick–baez mirrors*, J. Appl. Phys. **105** (2009), no. 8, 083106–5.

[178] C. W. Teng, J. F. Muth, U. Ozgur, M. J. Bergmann, H. O. Everitt, A. K. Sharma, C. Jin, and J. Narayan, *Refractive indices and absorption coefficients of mg[sub x]zn[sub 1 - x]o alloys*, Appl. Phys. Lett. **76** (2000), no. 8, 979–981.

[179] P. Thibault, M. Dierolf, A. Menzel, O. Bunk, C. David, and F. Pfeiffer, *High-resolution scanning x-ray diffraction microscopy*, Science **321** (2008), no. 5887, 379–382.

[180] G. W. Tomlins, J. L. Routbort, and T. O. Mason, *Oxygen diffusion in single-crystal zinc oxide*, Journal of the American Ceramic Society **81** (1998), no. 4, 869–876.

[181] Gregory W. Tomlins, Jules L. Routbort, and Thomas O. Mason, *Zinc self-diffusion, electrical properties, and defect structure of undoped, single crystal zinc oxide*, J. Appl. Phys. **87** (2000), no. 1, 117–123.

[182] F. Tuomisto, D.C. Look, and G.C. Farlow, *Defect studies in electron-irradiated zno and gan*, Physica B: Condensed Matter **401-402** (2007), 604–608.

[183] F. Tuomisto, K. Saarinendagger, K. Grasza, and A. Mycielski, *Observation of zn vacancies in zno grown by chemical vapor transport*, physica status solidi (b) **243** (2006), no. 4, 794–798.

[184] K. Ueda, H. Tabata, and T. Kawai, *Magnetic and electric properties of transition-metal-doped zno films*, Appl. Phys. Lett. **79** (2001), no. 7, 988–990.

[185] Chris G. Van de Walle, *Hydrogen as a cause of doping in zinc oxide*, Phys. Rev. Lett. **85** (2000), no. 5, 1012–.

[186] Friso van der Veen and Franz Pfeiffer, *Coherent x-ray scattering*, Journal of Physics: Condensed Matter **16** (2004), no. 28, 5003–5030.

[187] H. van Hove and R. Leysen, *Leed study on the polar surfaces of zno*, Physica Status Solidi (a) **9** (1972), no. 1, 361–367.

[188] I. Vartanyants, C. Ern, W. Donner, H. Dosch, and W. Caliebe, *Strain profiles in epitaxial films from x-ray bragg diffraction phases*, Appl. Phys. Lett. **77** (2000), no. 24, 3929–3931.

[189] I. A. Vartanyants, J. A. Pitney, J. L. Libbert, and I. K. Robinson, *Reconstruction of surface morphology from coherent x-ray reflectivity*, Phys. Rev. B **55** (1997), no. 19, 13193–.

[190] I. A. Vartanyants and I. K. Robinson, *Partial coherence effects on the imaging of small crystals using coherent x-ray diffraction*, Journal of Physics: Condensed Matter **13** (2001), no. 47, 10593–10611.

[191] I. A. Vartanyants, I. K. Robinson, I. McNulty, C. David, P. Wochner, and T. Tschentscher, *Coherent x-ray scattering and lensless imaging at the european xfel facility*, J. Synchrotron Rad. **14** (2007), 453–470.

[192] E. M. Vartiainen, K.-E. Peiponen, H. Kishida, and T. Koda, *Phase retrieval in nonlinear optical spectroscopy by the maximum-entropy method: an application to the x(3) spectra of polysilane*, J. Opt. Soc. Am. B **13** (1996), no. 10, 2106–2114.

[193] L. Vayssieres, K. Keis, S-E. Lindquist, and A. Hagfeldt, *Purpose-built anisotropic metal oxide material: 3d highly oriented microrod array of zno*, The Journal of Physical Chemistry B **105** (2001), no. 17, 3350–3352.

[194] O. Vigil, L. Vaillant, F. Cruz, G. Santana, A. Morales-Acevedo, and G. Contreras-Puente, *Spray pyrolysis deposition of cadmium-zinc oxide thin films*, Thin Solid Films **361-362** (2000), 53–55.

[195] D. Vogel, P. Kruger, and J. Pollmann, *Ab initio electronic-structure calculations for ii-vi semiconductors using self-interaction-corrected pseudopotentials*, Phys. Rev. B **52** (1995), no. 20, R14316–.

[196] R. S. Wagner and W. C. Ellis, *Vapor-liquid-solid mechanism of single crystal growth*, Applied Physics Letters **4** (1964), no. 5, 89–90.

[197] Q. Wan, Q. H. Li, Y. J. Chen, T. H. Wang, X. L. He, J. P. Li, and C. L. Lin, *Fabrication and ethanol sensing characteristics of zno nanowire gas sensors*, Appl. Phys. Lett. **84** (2004), no. 18, 3654–3656.

[198] Bi-Chen Wang, *Resolution of phase ambiguity in macromolecular crystallography*, Methods in Enzymology **115** (1985), 90–112.

[199] H. T. Wang, B. S. Kang, F. Ren, L. C. Tien, P. W. Sadik, D. P. Norton, S. J. Pearton, and Jenshan Lin, *Hydrogen-selective sensing at room temperature with zno nanorods*, Applied Physics Letters **86** (2005), no. 24, 243503.

[200] R. Wang, A. W. Sleight, and M. A. Subramanian, *An unusual iron site in iron-doped zinc oxide*, Journal of Solid State Chemistry **125** (1996), no. 2, 224 – 227.

[201] X. Wang, J. Song, P. Li, J. H. Ryou, R. D. Dupuis, C. J. Summers, and Z. L. Wang, *Growth of uniformly aligned zno nanowire heterojunction arrays on gan, aln, and al0.5ga0.5n substrates*, Journal of the American Chemical Society **127** (2005), no. 21, 7920–7923.

[202] X. Wang, C. J. Summers, and Z L Wang, *Large-scale hexagonal-patterned growth of aligned zno nanorods for nano-optoelectronics and nanosensor arrays*, Nano Letters **4** (2004), no. 3, 423–426.

[203] X. J. Wang, L. S. Vlasenko, S. J. Pearton, W. M. Chen, and I. A. Buyanova, *Oxygen and zinc vacancies in as-grown zno single crystals*, Journal of Physics D: Applied Physics **42** (2009), no. 17, 175411–.

[204] Z. L. Wang, *Nanostructures of zinc oxide*, Materials Today **7** (2004), no. 6, 26 – 33.

[205] Z. L. Wang, *Zinc oxide nanostructures: growth, properties and applications*, Journal of Physics: Condensed Matter **16** (2004), no. 25, R829–R858.

[206] Z. L. Wang, X. Y. Kong, Y. Ding, P. Gao, W. L. Hughes, R. Yang, and Y. Zhang, *Semiconducting and piezoelectric oxide nanostructures induced by polar surfaces*, Advanced Functional Materials **14** (2004), 943–956.

[207] Zhong Lin Wang, *The new field of nanopiezotronics*, Materials Today **10** (2007), no. 5, 20 – 28.

[208] B. Evgueni Warren, *X-ray diffraction*, Dover Publications, New York, 1990.

[209] A. Wei, X. W. Sun, J. X. Wang, Y. Lei, X. P. Cai, C. M. Li, Z. L. Dong, and W. Huang, *Enzymatic glucose biosensor based on zno nanorod array grown by hydrothermal decomposition*, Appl. Phys. Lett. **89** (2006), no. 12, 123902–3.

[210] X. X. Wei, C. Song, K. W. Geng, F. Zeng, B. He, and F. Pan, *Local fe structure and ferromagnetism in fe-doped zno films*, Journal of Physics: Condensed Matter **18** (2006), no. 31, 7471–7479.

[211] G. J. Williams, M. A. Pfeifer, I. A. Vartanyants, and I. K. Robinson, *Three-dimensional imaging of microstructure in au nanocrystals*, Phys. Rev. Lett. **90** (2003), no. 17, 175501.

[212] G. J. Williams, M. A. Pfeifer, I. A. Vartanyants, and I. K. Robinson, *Internal structure in small au crystals resolved by three-dimensional inversion of coherent x-ray diffraction*, Physical Review B (Condensed Matter and Materials Physics) **73** (2006), no. 9, 094112.

[213] Garth J. Williams, *Microscopy of gold microcrystals by coherent x-ray diffractive imaging*, Ph.D. thesis, University of Illinois, 2005.

[214] B. Xiang, P. Wang, X. Zhang, S. A. Dayeh, D. P. R. Aplin, C. Soci, D. Yu, and D. Wang, *Rational synthesis of p-type zinc oxide nanowire arrays using simple chemical vapor deposition*, Nano Letters **7** (2007), no. 2, 323–328.

[215] P. Yang and C. M. Lieber, *Nanostructured high-temperature superconductors: Creation of strong-pinning columnar defects in nanorod/superconductor composites*, J. Mat. Res. **12** (1996), 2981–2996.

[216] B. D. Yao, Y. F. Chan, and N. Wang, *Formation of zno nanostructures by a simple way of thermal evaporation*, Applied Physics Letters **81** (2002), no. 4, 757–759.

[217] G-C. Yi, C. Wang, and W. I. Park, *Zno nanorods: synthesis, characterization and applications*, Semiconductor Science and Technology **20** (2005), no. 4, S22–S34.

[218] Q. X. Zhao, M. Willander, R. E. Morjan, Q-H. Hu, and E. E. B. Campbell, *Optical recombination of zno nanowires grown on sapphire and si substrates*, Appl. Phys. Lett. **83** (2003), no. 1, 165–167.

[219] J. Zhou, N.S. Xu, and Z.L. Wang, *Dissolving behavior and stability of zno wires in biofluids: A study on biodegradability and biocompatibility of zno nanostructures*, Advanced Materials **18** (2006), no. 18, 2432–2435.

[220] J. M. Zuo, *Atomic resolution imaging of a carbon nanotube from diffraction intensities*, Science **300** (2003), 1419–1421.